

A Levelized Comparison of Pulsed and Steady-State Tokamaks

by

Daniel Joseph Segal

B.S. Engineering Physics, University of Wisconsin (2014)

Submitted to the Department of Nuclear Science and Engineering
in partial fulfillment of the requirements for the degree of

Master of Science in Nuclear Science and Engineering

at the

MASSACHUSETTS INSTITUTE OF TECHNOLOGY

February 2018

© Massachusetts Institute of Technology 2018. All rights reserved.

Author

Department of Nuclear Science and Engineering

December 25, 2018

Certified by

Jeffrey P. Freidberg

KEPCO Professor Emeritus

Thesis Supervisor

Certified by

Anne E. White

Cecil and Ida Green Associate Professor

Thesis Reader

Accepted by

Ju Li

Battelle Energy Alliance Professor

Chair, Department Committee on Graduate Students

A Levelized Comparison of Pulsed and Steady-State Tokamaks

by

Daniel Joseph Segal

Submitted to the Department of Nuclear Science and Engineering
on December 25, 2018, in partial fulfillment of the
requirements for the degree of
Master of Science in Nuclear Science and Engineering

Abstract

The goal of fusion energy research is to build an economically competitive reactor. This is difficult due to the complicated system composing a reactor and the nonlinearities it entails. Practically, to even get to the neighborhood of an economic reactor requires hundreds of simulations – which in turn necessitate quick running fusion systems codes. Moving towards these economic reactors then involves finding what design parameters provide the most leverage in lowering reactor costs.

As highlighted by the difference between European and American designs, however, the most important decision for tokamaks is whether to run them as *pulsed* or *steady-state*. This paper aims to fairly compare the two modes of operation using a single, comprehensive model. Benchmarked against other codes, this model actually shows that no fusion reactor is achievable without some technological advancements. This can be seen through every referenced design using nonstandard values of H and N_G .

The interesting result this paper shows is that developing high-temperature superconducting (HTS) tape could actually make both steady-state and pulsed tokamaks economically competitive against solar and coal. Further, this HTS tape actually has different best uses for the two modes of operation, appearing in the magnet structures of: TF coils for steady state and the central solenoid for pulsed. Developments in this technology should produce economic reactors within the coming decade.

Thesis Supervisor: Jeffrey P. Freidberg

Title: Professor of Nuclear Science and Engineering (Emeritus)

Contents

29	1	Introducing Fusion Reactor Design	17
30	1.1	Distinguishing Pulsed from Steady-State	18
31	1.2	Pricing a Fusion Reactor	19
32	1.3	Modeling Fusion Systems	21
33	1.4	Discussing HTS Magnet Technology	22
34	2	Designing a Steady-State Tokamak	25
35	2.1	Defining Plasma Parameters	26
36	2.1.1	Understanding Tokamak Geometry	26
37	2.1.2	Prescribing Plasma Profiles	28
38	2.2	Solving the Steady Current	31
39	2.2.1	Enforcing the Greenwald Density Limit	31
40	2.2.2	Declaring the Bootstrap Current	34
41	2.2.3	Deriving the Fusion Power	35
42	2.2.4	Using Current Drive	37
43	2.2.5	Completing the Steady Current	38
44	2.3	Handling Current Drive Self-Consistently	39
45	3	Formalizing the Systems Model	41
46	3.1	Explaining Static Variables	42
47	3.2	Connecting Dynamic Variables	42
48	3.3	Enforcing Power Balance	46
49	3.3.1	Collecting Power Sources	46
50	3.3.2	Approximating Radiation Losses	48

51	3.3.3	Estimating Heat Conduction Losses	49
52	3.3.4	Writing the Lawson Parameter	51
53	3.3.5	Finalizing the Primary Constraint	53
54	3.4	Collecting Limiting Constraints	56
55	3.4.1	Introducing the Beta Limit	57
56	3.4.2	Giving the Kink Safety Factor	58
57	3.4.3	Working under the Wall Loading Limit	59
58	3.4.4	Setting a Maximum Power Cap	60
59	3.4.5	Listing the Heat Loading Limit	61
60	3.5	Summarizing the Fusion Systems Model	62
61	4	Designing a Pulsed Tokamak	65
62	4.1	Modeling Plasmas as Circuits	66
63	4.1.1	Drawing the Circuit Diagram	66
64	4.1.2	Plotting Pulse Profiles	68
65	4.1.3	Specifying Circuit Variables	73
66	4.1.4	Constructing the Pulse Length	77
67	4.2	Producing Flux Balance	78
68	4.2.1	Rearranging the Circuit Equation	78
69	4.2.2	Adding Poloidal Field Coils	79
70	4.3	Improving Tokamak Geometry	81
71	4.3.1	Defining Central Solenoid Dimensions	81
72	4.3.2	Calculating Component Thicknesses	82
73	4.3.3	Revisiting Central Solenoid Dimensions	85
74	4.4	Piecing Together the Generalized Current	87
75	4.5	Simplifying the Generalized Current	88
76	4.5.1	Recovering the Steady Current	89
77	4.5.2	Extracting the Pulsed Current	89
78	4.5.3	Rationalizing the Generalized Current	91

79	5	Completing the Systems Model	93
80	5.1	Describing a Simple Algebra	93
81	5.2	Generalizing Previous Equations	95
82	5.2.1	Including Limiting Constraints	95
83	5.2.2	Minimizing Intermediate Quantities	97
84	5.2.3	Pinning Dynamic Variables	98
85	5.2.4	Detailing the Equation Solver	98
86	5.3	Wrapping up the Logic	101
87	6	Presenting the Code Results	103
88	6.1	Testing the Code against other Models	104
89	6.1.1	Comparing with the PSFC ARC Reactor	105
90	6.1.2	Contrasting with the ARIES ACT Studies	106
91	6.1.3	Benchmarking with the Process DEMO Designs	108
92	6.2	Developing Prototype Reactors	115
93	6.2.1	Navigating around Charybdis	119
94	6.2.2	Pinning down Proteus	119
95	6.2.3	Highlighting Operation Differences	120
96	6.3	Learning from the Data	120
97	6.3.1	Picking a Design Point	120
98	6.3.2	Utilizing High Field Magnets	125
99	6.3.3	Looking at Design Alternatives	128
100	7	Planning Future Work for the Model	135
101	7.1	Incorporating Stellarator Technology – Ladon	135
102	7.2	Making a Composite Reactor – Janus	136
103	7.3	Bridging Confinement Scalings – Daedalus	137
104	7.4	Addressing Model Shortcomings	138
105	7.4.1	Integrating Pedestal Temperature Profiles	139
106	7.4.2	Expanding the Radiation Loss Term	139
107	7.4.3	Taking Flux Sources Seriously	139

108	8 Concluding Reactor Discussion	141
109	A Cataloging Model Variables	143
110	A.1 Static Variables	143
111	A.2 Dynamic Variables	144
112	A.3 Intermediate Variables	144
113	B Simulating with Fussy.jl	145
114	B.1 Getting the Code to Work	145
115	B.2 Sorting out the Codebase	146
116	B.2.1 Typing out Structures	147
117	B.2.2 Referencing Input Decks and Solutions	149
118	B.2.3 Acknowledging Utility Functions	149
119	B.2.4 Mentioning Base Level Files	149
120	B.3 Delving into Reactor Methods	150
121	B.4 Demonstrating Code Usage	151
122	B.4.1 Initializing the Workspace	152
123	B.4.2 Running a Study	152
124	B.4.3 Extracting Results	153
125	B.4.4 Plotting Curves	154
126	C Discussing Fusion Power	159
127	C.1 Theoretical Background	159
128	C.2 Bosch-Hale Reactivity	161
129	D Selecting Plasma Profiles	165
130	D.1 Density – n	165
131	D.2 Temperature – T	167
132	D.3 Pressure – p	169
133	D.4 Bootstrap Current – f_{BS}	169
134	D.5 Volume Averaged Powers	171

135	E Determining Plasma Flux Surfaces	173
136	E.1 Flux Surface Coordinates	174
137	E.2 Cross-sectional Area and Volume	175
138	E.3 Surface and Volume Integrals	176
139	F Expanding on the Bootstrap Current	179
140	F.1 Summarized Results	179
141	F.2 Detailed Analysis	181
142	G Elaborating on the Current Drive	187
143	G.1 Summarized Results	187
144	G.2 Detailed Analysis	188
145	H Compending Code Plots	197
146	H.1 Magnet Strength Scans	198
147	H.2 Cost Sensitivity Studies	219
148	References	235

149 List of Figures

150	1-1	Cut-Away of Tokamak Reactor	18
151	1-2	Comparison of Pulsed and Steady-State Current	19
152	1-3	Steady State Magnet Components	23
153	1-4	Pulsed Magnet Components	23
154	2-1	Geometry of a Tokamak	27
155	2-2	Geometric Parameters	28
156	2-3	Radial Plasma Profiles	29
157	2-4	Greenwald Density Limit	33
158	3-1	Current Balance in a Tokamak	45
159	3-2	Power Balance in a Reactor	52
160	3-3	H-Mode Confinement Time Scaling	54
161	4-1	A Simple Plasma Transformer Description	67
162	4-2	Time Evolution of Circuit Profiles	69
163	4-3	Dimensions of Tokamak Cross-Section	82
164	5-1	Equation Selection for Fusion System	94
165	5-2	Minimize Cost Step II/III – Optimize Reactor	99
166	6-1	ARC and ACT Studies Cost Dependence on the H Factor	107
167	6-2	ARC Model Comparison	110
168	6-3	ARIES ACT I Model Comparison	111
169	6-4	ARIES ACT II Model Comparison	112
170	6-5	DEMO Steady Model Comparison	113

171	6-6 DEMO Pulsed Model Comparison	114
172	6-7 Designing Reactor Prototypes	116
173	6-8 Steady State Prototype Comparison	117
174	6-9 Pulsed Prototype Comparison	118
175	6-10 Limiting Constraint Regimes	121
176	6-11 Steady State Cost Curves	123
177	6-12 Pulsed Cost Curves	124
178	6-13 Pulsed B_{CS} Sensitivities	126
179	6-14 Pulsed Monte Carlo Sampling	127
180	6-15 Bootstrap Current Monte Carlo Sampling	129
181	6-16 Internal Inductance Sensitivities	130
182	6-17 Pulsed H Sensitivities	132
183	6-18 Steady State Current Drive Efficiency	133
184	6-19 Current Drive Efficiency vs Launch Angle	134
185	7-1 Cut-Away of Stellarator Reactor	136
186	7-2 Current Balance in a Tokamak	137
187	B-1 A Blank Plot	155
188	B-2 An Empty Plot	156
189	B-3 An Unscaled Plot	156
190	B-4 A Scaled Plot	157
191	C-1 Comparing Nuclear Fusion and Fission	160
192	C-2 The D-T Fusion Reaction	161
193	D-1 Radial Plasma Profiles	165
194	E-1 Cut-Away of Tokamak Reactor	173
195	E-2 Dimensions of Tokamak Cross-Section	176

196 List of Tables

197	3.1	Dynamic Variables	42
198	4.1	Piecewise Linear Scheme for Pulsed Operation	69
199	4.2	Example TF Coils and Central Solenoid Critical Values	85
200	5.1	Main Equation Bank	96
201	6.1	ARC Variables	110
202	6.2	ACT I Variables	111
203	6.3	ACT II Variables	112
204	6.4	DEMO Steady Variables	113
205	6.5	DEMO Pulsed Variables	114
206	6.6	Charybdis Variables	117
207	6.7	Proteus Variables	118
208	6.8	Proteus and Charybdis Comparison	119
209	A.1	List of Static Variables	143
210	A.2	List of Dynamic Variables	144
211	A.3	List of Intermediate Variables (Noncomprehensive)	144
212	C.1	Bosch-Hale Parametrization Coefficients	163
213	C.2	Tabulated Bosch-Hale Reactivities	163

List of Equations

215	1.1	Magnetic Energy – W_M	20
216	1.3	Cost-per-Watt – C_W	21
217	2.1	Minor Radius – a	27
218	2.2	Density Profile – n	29
219	2.4	Temperature Profile – T	30
220	2.5	Current Density Profile – J	30
221	2.6	Normalized Poloidal Magnetic Field – b_p	31
222	2.7	Current Balance – I	31
223	2.10	Greenwald Density – \bar{n}	32
224	2.14	Bootstrap Current – I_{BS}	35
225	2.19	Dilution Factor – f_D	36
226	2.21	Fusion Power – P_F	36
227	2.25	Heating Power – P_H	38
228	2.26	Current Drive – I_{CD}	38
229	2.28	Steady Current – I_P	39
230	2.29	Current Drive Efficiency – η_{CD}	40
231	3.1	Scanned Temperature – \bar{T}	43
232	3.3	Current Fractions – f	44
233	3.6	Power Balance – P	46
234	3.8	Plasma Resistance – R_P	47
235	3.10	Ohmic Power – P_Ω	47
236	3.15	Bremsstrahlung Power – P_{BR}	49
237	3.20	Heat Conduction Losses – P_κ	50
238	3.23	Triple Product – $\bar{n} \cdot \bar{T} \cdot \tau_E$	53

239	3.25	Generalized Confinement Time Scaling Law – τ_E	54
240	3.26	Loss Power – P_{src}	55
241	3.27	ELMy H-Mode Confinement Time Scaling Law – τ_E^H	55
242	3.28	Primary Constraint – B_0	56
243	3.35	Plasma Pressure – \bar{p}	57
244	3.38	Troyon Beta Limit – β_N	58
245	3.41	Kink Safety Factor – q_*	59
246	3.43	Surface Area – S_P	59
247	3.45	Wall Loading Limit – P_W	60
248	3.47	Electric Power – P_E	60
249	3.51	Maximum Power Limit – P_{max}	61
250	3.55	Heat Loading Limit – q_{DV}	62
251	4.12	Ramp-Up Time – τ_{RU}	70
252	4.16	Flat-top Time – τ_{FT}	71
253	4.17	Ramp-Down Time – τ_{RD}	72
254	4.19	Dwell Time – τ_{DW}	72
255	4.20	Duty Factor – f_{duty}	73
256	4.23	Inductive Current – I_{ID}	74
257	4.26	Central Solenoid Inductance – L_1	75
258	4.29	Plasma Inductance – L_2	76
259	4.34	Mutual Inductance – M	76
260	4.40	Central Solenoid Flux – Φ_{CS}	78
261	4.42	Ramp-Up Flux – Φ_{RU}	79
262	4.43	Flat-top Flux – Φ_{FT}	79
263	4.44	PF Coil Flux – Φ_{PF}	79
264	4.48	Plasma Perimeter – l_p	80
265	4.50	Vertical Field Strength – B_V	80
266	4.53	Flux Balance – Φ	81
267	4.56	Blanket Thickness – b	83
268	4.57	TF Coil Thickness – c	84

269	4.61	Central Solenoid Thickness – d	84
270	4.64	Central Solenoid Height – h_{CS}	86
271	4.65	Central Solenoid Inner Radius – R_{CS}	86
272	4.75	Generalized Current – I_P	88
273	5.3	General Model Equation – $G(\overline{T})$	95
274	5.10	General Model Solution – $\gamma_{RB\{I,T\}}$	100
275	7.1	L-Mode Confinement Time Scaling Law – τ_E^L	138
276	7.2	I-Mode Confinement Time Scaling Law – τ_E^I	138
277	C.2	Fusion Energy – E_F	160
278	C.3	Neutron Power – P_n	160
279	C.4	Alpha Power – P_α	160
280	C.9	Bosch-Hale Reactivity – $\langle\sigma v\rangle$	162
281	E.14	Shaping Parameter – g	175
282	E.24	Volume Integral – Q_V	177
283	E.25	Surface Integral – Q_S	177
284	F.7	Internal Inductance – l_i	180

Chapter 1

Introducing Fusion Reactor Design

The central goal of fusion energy research is to build an economically competitive nuclear reactor. It has long been joked, though, that fusion power will always be twenty years away. This is mainly due to the nonlinearities inherent to a reactor system and the high upfront cost of building new machines. The model developed for this paper uses standard theory and empirical fits to find cost trends from this nonlinear system. An important conclusion is that building an economic reactor using existing technology would be impossible. One solution may be improving magnet technology – as MIT is exploring with high-temperature superconducting (HTS) tape.

As can be seen by comparing the European and American/Asian fusion reactor design efforts, though, one of the most important decisions is whether to run the reactor as pulsed (EU^{1,2}) or steady-state (US³ and Korea⁴). The distinction between the two mainly manifests itself in the choice of auxiliary current drive: inductive for pulsed and lower hybrid for steady-state.⁵ With the model built for this thesis, it is possible to perform a direct comparison of these two modes of operations.

Due to the speed and simplicity of the model, hundreds of reactors can be simulated in minutes. Further, the model has been benchmarked against other ones from the literature,^{3,6–8} allowing it to answer several critical questions regarding the comparison of the two modes of operation. A major finding of this is that HTS tape should ap-

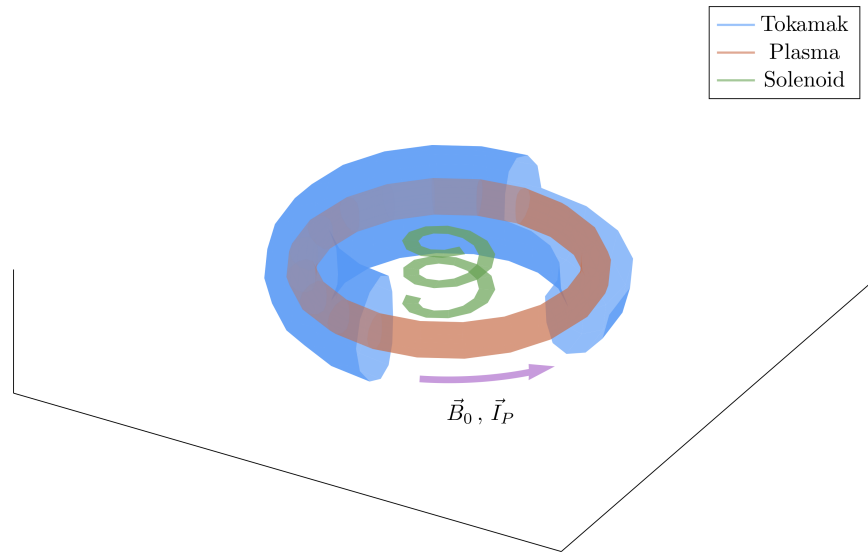


Figure 1-1: Cut-Away of Tokamak Reactor

The three main components of a magnetic fusion reactor are: the tokamak structure, the plasma fuel, and the spring-like solenoid at the center. Here, the directions of the magnetic field (B_0) and plasma current (I_P) variables are shown to be in the toroidal direction.

pear in different places for the two modes of operation: within the central solenoid for pulsed machines and inside the TF coil magnets for steady-state ones. A more basic finding is that pulsed can be competitive and the US should investigate it further.

1.1 Distinguishing Pulsed from Steady-State

The leading candidate for the first economic, power-producing fusion reactor is a tokamak. As shown in Fig. 1-1, tokamaks are doughnut-shaped metal structures that use magnets to confine their fusion-grade plasmas. The challenge in building such a device comes from the various physics and engineering constraints it must satisfy – i.e. not surpassing acceptable levels of neutron damage, plasma pressure, etc.

One of the most contentious points of reactor design, however, is whether to run it as: pulsed (the European effort^{1,2}) or steady-state (the American/Asian approach^{3,4}). Here, pulsed operation refers to how a reactor is ramped up and down several times

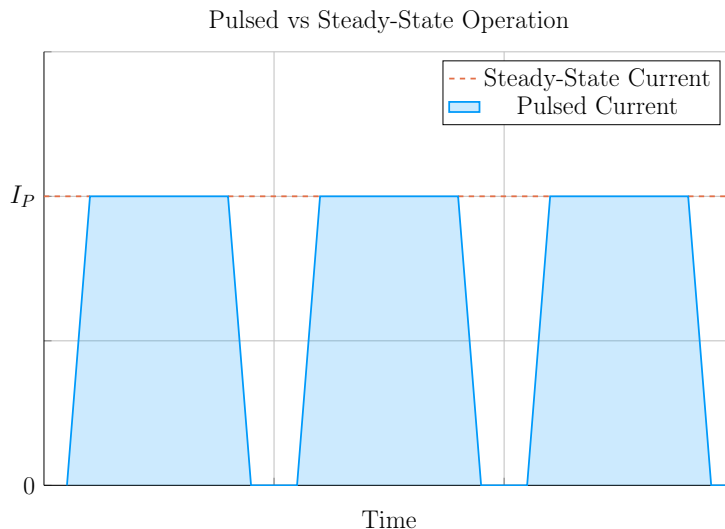


Figure 1-2: Comparison of Pulsed and Steady-State Current

Inside a pulsed reactor, current is ramped up and down several times a day – with downtime in-between. Steady state reactors are meant to remain on for weeks or months.

317 a day. Whereas steady-state implies a machine is functionally kept ramped up the
 318 entirety of its fifty-year campaign. These behaviors are shown in Fig. 1-2. The
 319 difficulties involves with the two modes of operation are then: cyclical stresses for
 320 pulsed and expensive current drive for steady state.⁵

321 The main way these two modes of operation, *pulsed* and *steady-state*, influence reactor
 322 design, though, is through the current balance equation (derived later). What this
 323 means practically is a tokamak plasma requires some current to stay in equilibrium
 324 and this current has to be partially generated by auxiliary systems: inductively for
 325 pulsed and non-inductively for steady-state. To fairly compare the two modes of
 326 operation thus requires a generalized handling of current balance that can incorporate
 327 both auxiliary systems.

328 1.2 Pricing a Fusion Reactor

329 To truly compare tokamaks used as fusion reactors, though, the obvious metrics are
 330 costs. ITER – the most expensive experiment in the world^{9,10} – has a history full of

331 countries backing out for high construction costs and rejoining only after they finally
 332 get lowered.⁵ The problem is \$20B is a lot of money and 20 years is a long time.
 333 Moreover, approximating true costs is difficult due to the need to project (or neglect)
 334 economies-of-scale for expensive components, such as the superconducting magnets
 335 and irradiated materials.

336 Therefore, this paper adopts stand-ins for the conventional capital cost and cost-
 337 per-watt metrics. This is done for simplicity, both in: formulating the relations and
 338 conveying the two metrics to physicists. The approximation for the capital cost –
 339 how much a tokamak costs to build – is the magnetic energy.¹¹

$$W_M \propto R^3 B^2 \tag{1.1}$$

340 In this magnetic energy proportion relation, the tokamak’s major radius – R – is
 341 involved in a volumetric term (R^3) and B is the strength (in Teslas) of the toroidal
 342 magnetic field. This quantity simply states that the two surefire ways to make a
 343 machine more expensive are to build it bigger and to use stronger magnets. As these
 344 terms also improve confinement, this cost introduces a trade-off between size and
 345 magnet technology. This is why the proposed ARC reactor – designed with HTS tape
 346 – could be half the size of ITER, which uses conventional LTS technology.

347 The next metric, the cost-per-watt, is defined by dividing the capital cost (i.e. the
 348 magnetic energy) by the main source of power output. For a tokamak, this source
 349 of power is fusion – discussed in more detail in Appendix C. The cost-per-watt thus
 350 measures how economically competitive a reactor will be once it is build. This is how
 351 to compare the rate of return for different base-load power sources (e.g. fission, coal,
 352 and solar).

$$\tilde{C}_W = \frac{W_M}{P_F} \tag{1.2}$$

353 A final correction can be made on the cost-per-watt to account for reactor downtime,
 354 which is fundamental to pulsed operation. This is handled through the duty factor
 355 (f_{duty}) that is defined as the ratio of a reactor’s quasi-steady-state flattop duration

356 to the entire pulse length of a tokamak. In the context of the cost-per-watt, it scales
 357 down the fusion power:

$$C_W = \frac{W_M}{f_{duty} \cdot P_F} \quad (1.3)$$

358 For a steady-state reactor, this duty factor is assumed to be held at one. Pulsed
 359 machines, on the other hand, can see around thirty minutes of downtime,⁸ which
 360 leads to duty factors around 80%. Analysis in Section 4.1.4, however, shows that
 361 pulsed reactors may also have duty factors near unity.

362 Combined, these two cost metrics allow designers to pinpoint economically competi-
 363 tive tokamaks within reactor space. Although not rigorous in an engineering context,
 364 these capital cost and cost-per-watt approximations do provide true physics meaning
 365 while comparing different machines – whether they run as pulsed or steady-state.

366 1.3 Modeling Fusion Systems

367 Before reactors can be priced, though, they have to be modeled. Therefore the first
 368 half of this thesis is devoted to the theory behind tokamak design. Emphasis is placed
 369 more on a physicist’s intuition than an engineer’s costing rigor. This is justified by
 370 the nonlinearities inherent to fusion systems and rationalized by this paper’s results
 371 matching more sophisticated models with high fidelity.

372 Stepping back, a fusion systems model is an approach to designing reactors based on
 373 satisfying various physics and engineering constraints. There are many of these models
 374 in the field.^{6,7,12–18} Zero-dimensional (0-D) systems models are then a particular
 375 subclass of these that reduce the inherently 3-D problem of design to a collection of
 376 scalar, averaged values. This reduction in complexity allows models to be orders of
 377 magnitude faster. The natural corollary of this is that hundreds of reactors can be
 378 simulated in minutes.

379 Within the context of reactor design, these 0-D systems models serve an important
380 role due to their speed and simplicity. Although not truly self-consistent,* these
381 models are capable of exploring large areas of reactor space. This is especially impor-
382 tant in the early stages of tokamak planning when researchers are selecting a design
383 point. These models also have use in finding general costing trends – as shown in this
384 document.

385 What makes this paper’s systems model different from other ones, though, is its gen-
386 eralized handling of both modes of tokamak operation: pulsed and steady-state. This
387 was necessitated by a desire to fairly compare the two. The most fundamental result
388 of this analysis is that both modes are actually capable of leading to economically
389 competitive reactors – assuming some technological advancements.

390 1.4 Discussing HTS Magnet Technology

391 As mentioned, no economically competitive fusion reactor can be built using existing
392 technology – regardless of whether it runs as pulsed or steady-state. This is why
393 MIT has been exploring HTS magnet technology for their ARC reactor in an effort to
394 nearly double the maximum achievable field strength. What this paper shows is that
395 this logic is indeed correct and HTS may be the final magnet advancement needed
396 for the conventional fusion paradigm (i.e. D-T fuel, H-Mode, etc.)

397 More concretely, this paper shows that new HTS technology is capable of lowering
398 reactor costs – both for pulsed and steady-state operation. Further, this HTS tape
399 has different uses within the two modes of operation – as set by cost concerns (see
400 Figs. 1-3 and 1-4). This analysis shows that HTS should be employed in the TF coils
401 for steady-state reactors *and* in the central solenoid for pulsed ones. This is because
402 pulsed machines require lower toroidal field strengths, which are achievable with less
403 expensive LTS magnets.

*For speed concerns, 0-D fusion systems models often ignore self consistency in quantities like pres-
sure profiles and use empirical fits to estimate values such as the confinement time.

Now that the problem has been thoroughly introduced, we will go over the theory behind steady-state and, then, pulsed tokamaks. A couple detours will be taken along the way to show how the model can be incorporated into a fusion systems code. This code – Fussy.jl – is the topic of Appendix B and is freely available at:

git.io/tokamak

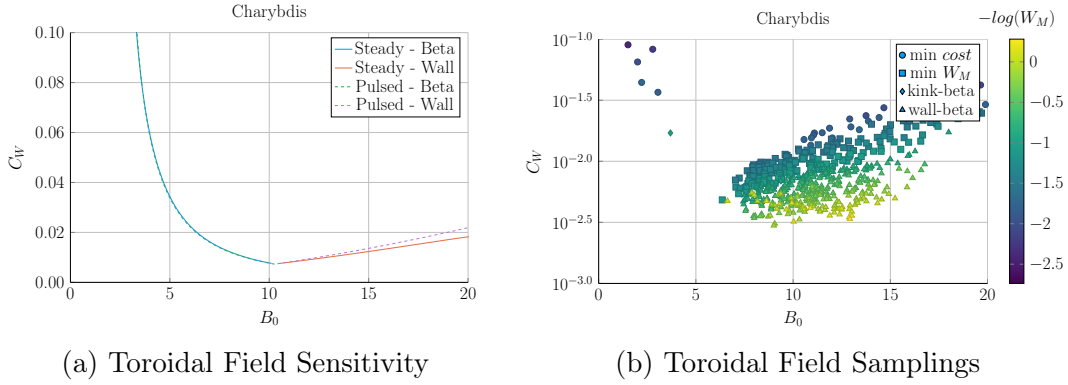


Figure 1-3: Steady State Magnet Components

Steady-state reactors benefit from increased toroidal field strength until neutron wall loading starts to dominate design (at around 10-15 T for Charybdis). This is well within the range accessible to HTS magnets.

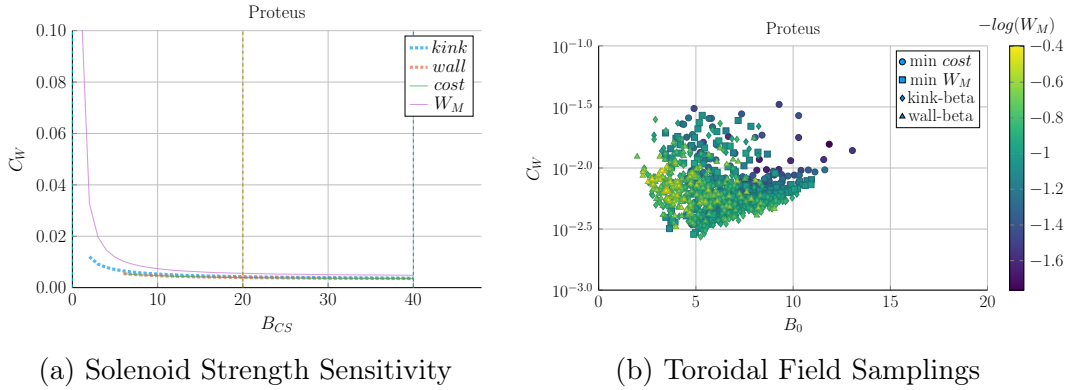


Figure 1-4: Pulsed Magnet Components

Pulsed reactors are shown to receive strong decreases in reactor cost as the central solenoid field strength is increased, until around 20 T. However, the TF coils do not receive the same cost reduction with field strength – as shown by the minimum cost appearing at 5 T.

Chapter 2

Designing a Steady-State Tokamak

This chapter explores a simple model for designing steady-state tokamaks. In the next couple chapters, the model is first formalized for use in a systems code and then generalized to handle pulsed operation. These derivations highlight that the only difference between the two modes of operation is how they generate their auxiliary plasma current: lower-hybrid current drive (LHCD) for steady-state operation and inductive sources for when a reactor is purely pulsed.

Along the way, equations will be derived that get rather complicated. To remedy the situation, a distinction between dynamic and static values is now given, which will allow splitting most equations into static and dynamic parts. Dynamic values – i.e. the tokamak’s major radius (R_0) and magnet strength (B_0), as well as the plasma’s current (I_P), temperature (\bar{T}), and density (\bar{n}) – are first-class variables in the model (see Table 3.1). Everything is derived to relate them. Static values, on the other hand, can be treated as code inputs, which remain constant throughout a reactor solve. These most obviously include the various geometric and profile parameters introduced next section.

The overall structure of this chapter, then, is built around developing an equation for plasma current in a steady-state tokamak. It is shown that this value arises from balancing current in a reactor using both a plasma’s own bootstrap current (I_{BS}),

430 as well the tokamak's auxiliary driven current (I_{CD}). These relations necessitate
431 geometric parameters and plasma profiles, which will be given shortly. Along the
432 way, definitions will also be needed for the Greenwald density (N_G) and the fusion
433 power (P_F). What is shown is that the current does not actually depend directly
434 on the major radius (R_0) or magnet strength (B_0) of a tokamak – allowing these
435 variables to be put off until next chapter.

436 2.1 Defining Plasma Parameters

437 As mentioned previously, the zero-dimensional model derived here can closely approx-
438 imate solutions from higher-dimensional codes that might take many hours to run.
439 The essence of boiling down three-dimensional behaviors to one dimensional profiles
440 – and zero-dimensional averaged values – begins with defining the most important
441 plasma parameters. These are the: current density (J), temperature (T), and density
442 (n) of a plasma.

443 Solving this problem most generally usually involves decoupling the geometry of the
444 plasma from the shaping of its nearly parabolic radial-profiles – both of which will be
445 explained shortly.

446 2.1.1 Understanding Tokamak Geometry

447 The first thing people see when they look at a tokamak is its geometry – see Fig. 2-1.
448 How big is it? Is it stretched out like a bicycle tire or compressed to the point of being
449 nearly spherical? Would a slice across the major radius result in two cross-sections
450 that were: circular, elliptic, or triangular?

451 These questions lend themselves to the three important geometric variables – the
452 inverse aspect ratio (ϵ), the elongation (κ), and the triangularity (δ). The inverse

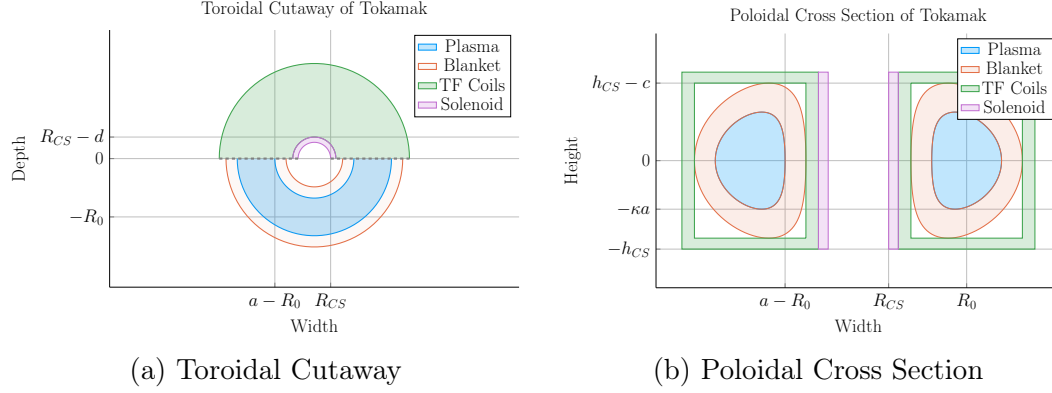


Figure 2-1: Geometry of a Tokamak

This diagram is of a tokamak's toroidal (top) view and the poloidal cross section of a slice across the major axis. Included are the four components of a reactor: the plasma, its metallic blanket, the toroidal field magnets surrounding them, and the central solenoid. These have thicknesses of a , b , c and d , respectively. R_{CS} is where the solenoid starts.

aspect ratio is a measure of how stretched out the device is, or formulaically:

$$a = \epsilon \cdot R_0 \quad (2.1)$$

This says that the minor radius (a), measured in meters, is related to the major radius of the machine (R_0) through ϵ . Or more tangibly, the minor radius is related to the two small cross-sections that result from a slice across the major radius of the machine.

The remaining two geometric parameters – κ and δ – are related to the shape of the torn halves. As the name hints, elongation (κ) is a measure of how stretched out the tokamak is vertically – is the cross-section a circle or an oval? The triangularity (δ) is then how much the cross-sections point outward from the center of the device. All three's effects can be seen in Fig. 2-2. Their exact usage within describing flux surfaces is shown in Appendix E.

These geometric factors allow the volumetric and surface integrals governing fusion power and bootstrap current to be condensed to simple radial ones – see Eqs. (E.24) and (E.25). The only remaining step is to define the radial profiles for: the density,

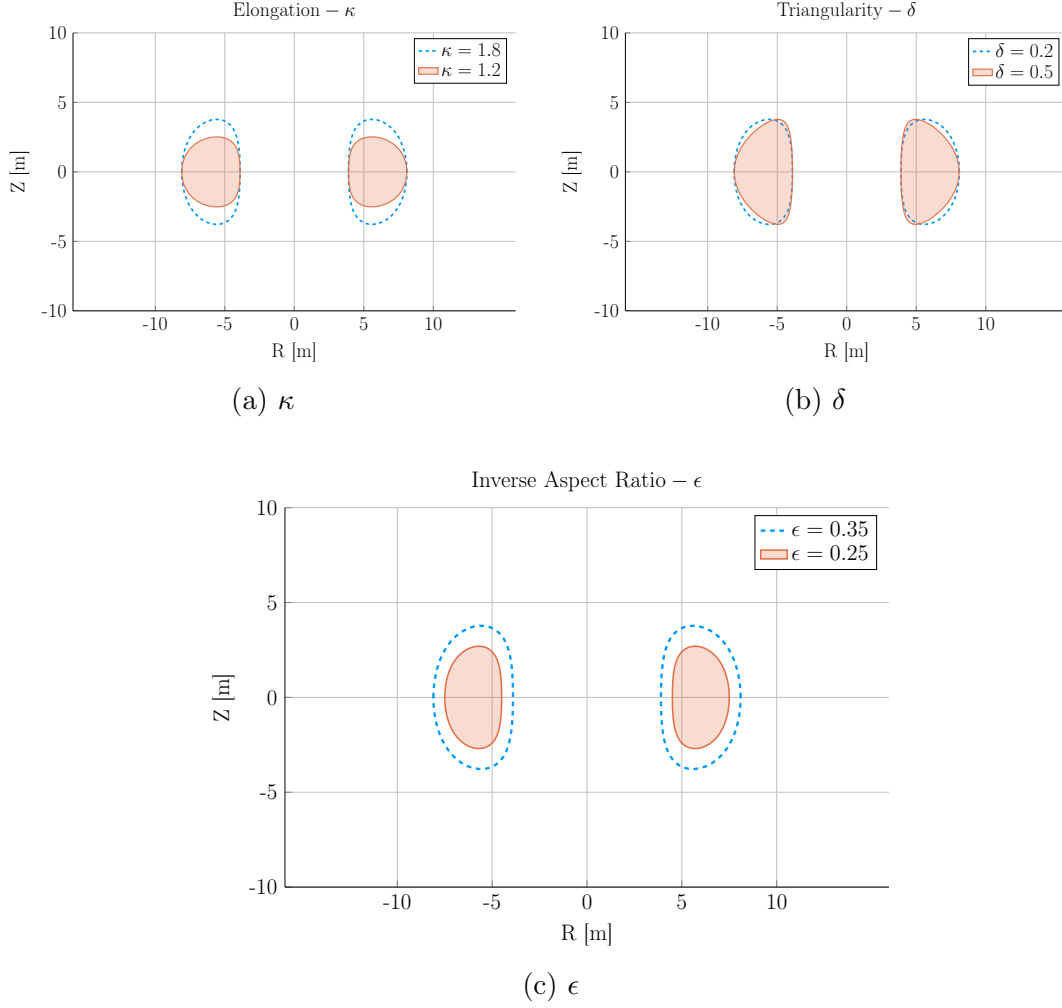


Figure 2-2: Geometric Parameters

These three geometric parameters allow the toroidal cross-sections to scale radially, stretch vertically, and become more triangular – thus improving upon simple circular slices.

467 temperature, and current density of a plasma.

468 2.1.2 Prescribing Plasma Profiles

469 The first step in defining radial profiles is realizing that all three quantities are essen-
 470 tially parabolas – i.e. the temperature, density and current density, shown in Fig. 2-3,
 471 are peaked at some radius (usually the center) and then decay to zero somewhere be-
 472 fore the walls of the tokamak enclosure.

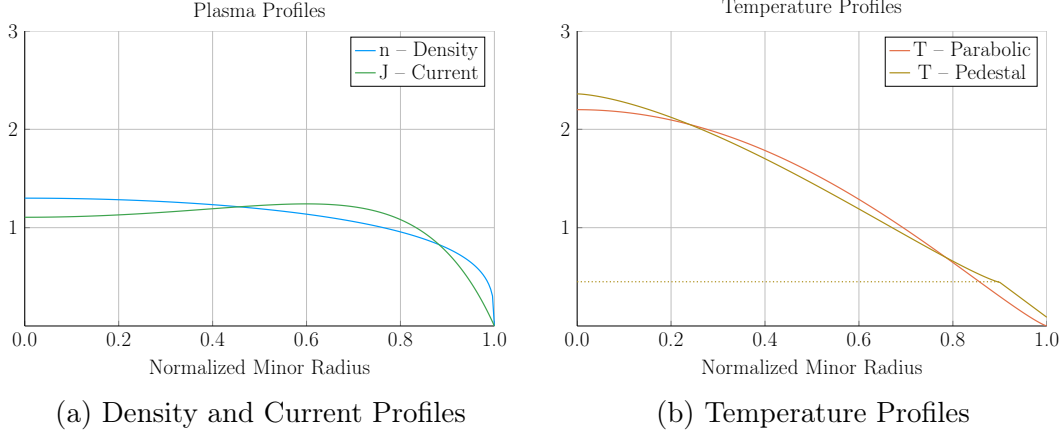


Figure 2-3: Radial Plasma Profiles

The three most fundamental profiles of a fusion plasma are its temperature, density, and current. These allow the model to reduce from three dimensions to just half of one.

Although not self-consistent, these profiles do capture enough of the physics to approximate relevant phenomenon, such as transport and fusion power.¹⁹

The Density Profile

To begin, density has the simplest profile. This is because it is relatively flat, remaining near the average value – \bar{n} – throughout the body of the plasma until quickly decaying to zero near the edge of the plasma.* For this reason, a parabolic profile with a very low peaking factor – ν_n – is well suited.

$$n(\rho) = \bar{n} \cdot (1 + \nu_n) \cdot (1 - \rho^2)^{\nu_n} \quad (2.2)$$

Here, ρ is a normalized radial-like flux label, with $\rho = 0$ at the magnetic axis and $\rho = 1$ at the outer plasma surface (i.e. the 95% surface). While \bar{n} is referred to as the volume-averaged density because using the volume integral – given by Eq. (E.24) – over the density profile results in that value after dividing through by the volume

*Even in H-Mode plasmas where density profiles have a pedestal,²⁰ they usually have much less of a peak than temperatures²¹ – especially so in a reactor setting.²²

484 (V):

$$\bar{n} = \frac{\int n(\mathbf{r}) d\mathbf{r}}{V} \quad (2.3)$$

485 A final point to make is this parabolic profile allows for a short closed-form relation
486 for the Greenwald density limit – substantially simplifying this fusion systems model.

487 The Temperature Profile

488 The use of a parabolic profile for the plasma temperature is slightly more dubious.
489 This is because H-Mode plasmas are actually highly peaked at the center, decaying
490 to a non-zero pedestal temperature near the edge before finally dropping sharply to
491 zero. This model chooses to forego this pedestal representation for a simple parabolic
492 one – although the pedestal approach is discussed in Appendix D. Analogous to the
493 density, the profile treats \bar{T} as the average value and ν_T as the peaking parameter.

$$T(\rho) = \bar{T} \cdot (1 + \nu_T) \cdot (1 - \rho^2)^{\nu_T} \quad (2.4)$$

494

495 The Current Density Profile

496 The plasma current density is the third profile and cannot safely be represented by a
497 simple parabola. This is because having an adequate bootstrap current relies heavily
498 on a profile being peaked off-axis – i.e. at some radius not at the center. This hollow
499 profile can then be modeled with the commonly given plasma internal inductance (l_i).
500 Concretely, the current's hollow profile is described by:

$$J(\rho) = \bar{J} \cdot \frac{\gamma^2 \cdot (1 - \rho^2) \cdot e^{\gamma \rho^2}}{e^\gamma - 1 - \gamma} \quad (2.5)$$

501 The intermediate γ quantity can then be numerically solved for from the plasma
502 internal inductance using the following relations – with b_p representing the normalized

503 poloidal magnetic field. These are derived in Appendix F.

$$l_i = \frac{4\kappa}{1 + \kappa^2} \int_0^1 b_p^2 \rho d\rho \quad (\text{F.7})$$

504

$$b_p(\rho) = \frac{-e^{\gamma\rho^2}(\gamma\rho^2 - 1 - \gamma) - 1 - \gamma}{\rho(e^\gamma - 1 - \gamma)} \quad (2.6)$$

505

506 Combined, these three geometric parameters and profiles lay the foundation for this
507 zero-dimensional fusion systems model.

508 2.2 Solving the Steady Current

509 As suggested, one of the most important equations in a fusion reactor is current
510 balance. In steady-state operation, all of a plasma's current (I_P) must come from
511 a combination of its own bootstrap current (I_{BS}), as well as auxiliary current drive
512 (I_{CD}). This can be represented mathematically as:

$$I_P = I_{BS} + I_{CD} \quad (2.7)$$

513 The goal is then to write equations for bootstrap current and driven current. This will
514 make heavy use of the Greenwald density limit. The steady current will then be shown
515 to be only a function of temperature! In other words, this current is independent of
516 a tokamak's geometry and magnet strength. As will be pointed out then, though, a
517 subtlety arises that will bring the two back into the picture – self-consistency in the
518 current drive efficiency (η_{CD}).

519 2.2.1 Enforcing the Greenwald Density Limit

520 The Greenwald density limit is a density limit that applies to all tokamaks It sets a
521 hard limit on the density and how it scales with current and reactor size. Although

522 currently lacking a true first-principles theoretical explanation, it does have a real
 523 meaning within the design context. Operate at too low a density and run the risk of
 524 never entering H-Mode. Run the density too high, and cause the tokamak's plasma
 525 to disrupt. Fig. 2-4 shows how most shots exist within the regime between the two.
 526 As no theoretical backing exists, the Greenwald density limit can simply be written
 527 (with citation) as:²³

$$\hat{n} = N_G \cdot \left(\frac{I_P}{\pi a^2} \right) \quad (2.8)$$

528 Here, \hat{n} has units of $10^{20} \frac{\text{particles}}{\text{m}^3}$, N_G is the Greenwald density fraction, and I_P is
 529 again the plasma current (measured in mega-amps). The final variable is then the
 530 minor radius – a – which was previously defined through:

$$a = \epsilon \cdot R_0 \quad (2.1)$$

531 The next step is transforming the *line-averaged* density (\hat{n}) into the *volume-averaged*
 532 version (\bar{n}) used in this model. Harnessing the simplicity of the density's parabolic
 533 profile allows this relation to be written in a closed form as:

$$\hat{n} = \frac{\sqrt{\pi}}{2} \cdot \left(\frac{\Gamma(\nu_n + 2)}{\Gamma(\nu_n + \frac{3}{2})} \right) \cdot \bar{n} \quad (2.9)$$

534 Where $\Gamma(\dots)$ represents the gamma function: the non-integer analogue of the facto-
 535 rial function.

536 Combining these pieces allows the volume-averaged density to be written in standard-
 537 ized units as:

$$\bar{n} = K_n \cdot \left(\frac{I_P}{R_0^2} \right) \quad (2.10)$$

538

$$K_n = \frac{2N_G}{\epsilon^2 \pi^{3/2}} \cdot \left(\frac{\Gamma(\nu_n + \frac{3}{2})}{\Gamma(\nu_n + 2)} \right) \quad (2.11)$$

539 The format of the previous equation pair will be used throughout the remainder of
 540 the paper. The top equation relates dynamic variables (i.e. \bar{n} , I_P , and R_0), while the

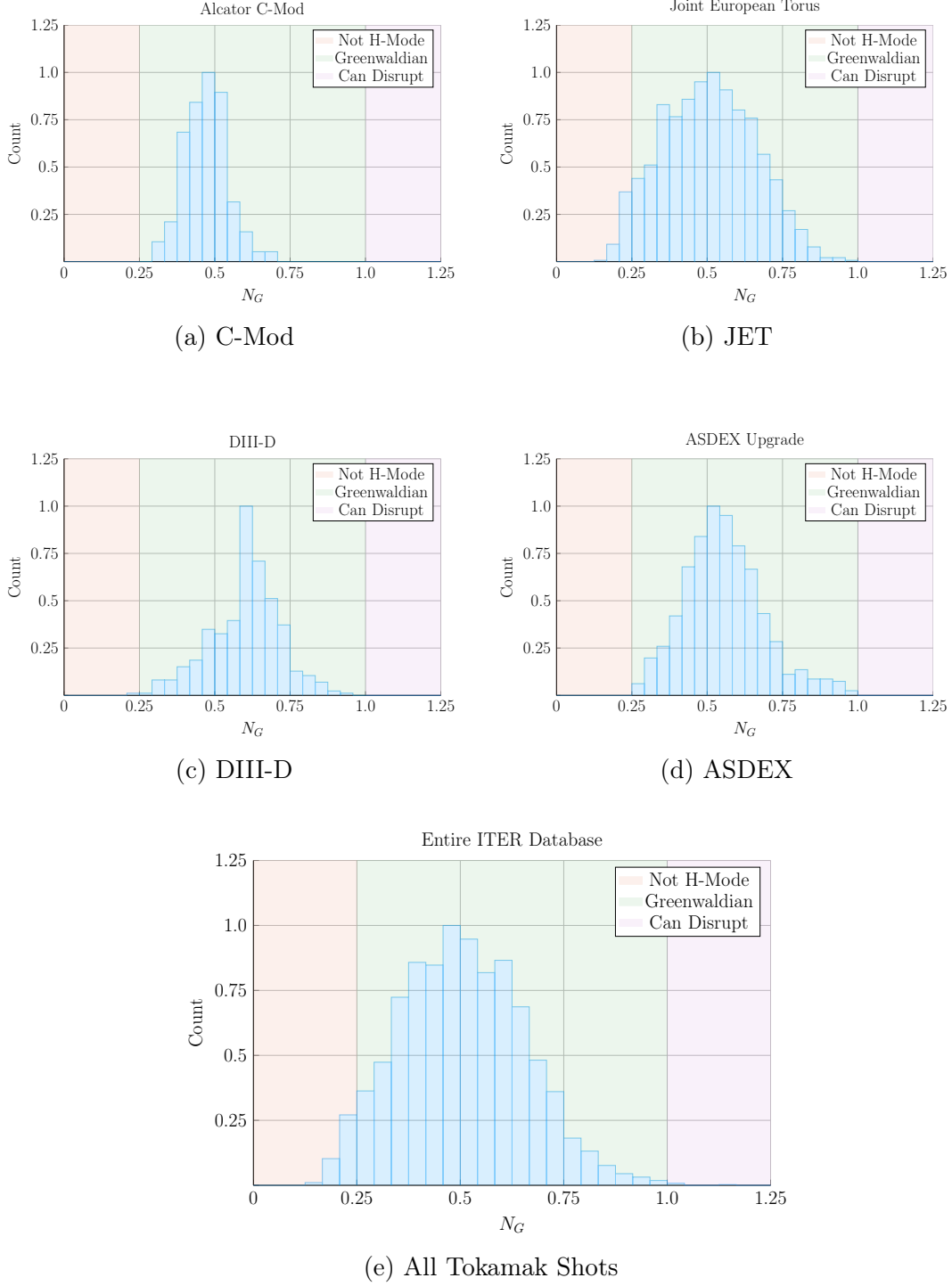


Figure 2-4: Greenwald Density Limit

The Greenwald Limit is a robust metric of what densities an H-Mode plasma can attain – here referred to as a *Greenwaldian* region. Although empirical in nature, it accurately predicts when a tokamak will undergo degraded plasma transport.^{23,24}

static-value coefficient (K_n) lumps together static quantities, such as: N_G , ϵ , 2, π ,
and ν_n .

2.2.2 Declaring the Bootstrap Current

The first term to define in current balance, Eq. (2.7), is the bootstrap current. This bootstrap current is a mechanism of tokamak plasmas that helps supply some of the current needed to keep a plasma in equilibrium. Its underlying behavior stems from particles stuck in banana-shaped orbits on the outer edges of the device propelling the majority species along their helical trajectories around the tokamak.

Utilizing the surface integral from Eq. (E.25), the bootstrap current (I_{BS}) can be written in terms of the temperature and density profiles:

$$I_{BS} = 2\pi a^2 \kappa g \int_0^1 J_{BS} \rho d\rho \quad (2.12)$$

551

$$\begin{aligned} J_{BS} &= f\left(n, T, \frac{dn}{d\rho}, \frac{dT}{d\rho}\right) \\ &\equiv -4.85 \cdot n \cdot T \cdot \frac{R_0 \sqrt{\epsilon} \rho}{d\psi/d\rho} \cdot \left(\frac{1}{n} \frac{dn}{d\rho} + 0.54 \frac{1}{T} \frac{dT}{d\rho}\right) \end{aligned} \quad (2.13)$$

Here, g is a geometric factor (of order 1) given by Eq. (E.14). While the second definition for the bootstrap current density – J_{BS} – comes from using well known theoretical results plus several simplifying assumptions, including the large aspect limit. The value of $d\psi/d\rho$ is given in Appendix F.

As shown later in the results, bootstrap fractions are often under-predicted by this model. This is due to parabolic profiles (i.e. for temperature) having much less steep declines near the edge (i.e. in their derivatives) than characteristic H-Mode profiles with pedestals. This implies that the area most positively impacted by a pedestal profile for temperature would be the bootstrap current derivation. The instructions

561 to do so are given in Appendix D.4.

562 Finally, summarizing the results of Appendix F, the bootstrap current is found to be
 563 only a function of temperature and static variables! In standardized units, it can be
 564 written as:

$$I_{BS} = K_{BS} \cdot \bar{T} \quad (2.14)$$

565

$$K_{BS} = 4.879 \cdot K_n \cdot \left(\frac{1 + \kappa^2}{2} \right) \cdot \epsilon^{5/2} \cdot H_{BS} \quad (2.15)$$

566

$$H_{BS} = (1 + \nu_n)(1 + \nu_T)(\nu_n + 0.054\nu_T) \int_0^1 \frac{\rho^{5/2} (1 - \rho^2)^{\nu_n + \nu_T - 1}}{b_p} d\rho \quad (2.16)$$

567 Quickly noting, this H_{BS} term serves as the analogue of static-value coefficients (e.g.
 568 K_{BS} and K_n) when they contain an integral. And b_p represents the poloidal magnet
 569 strength given by Eq. 2.6.

570 2.2.3 Deriving the Fusion Power

571 The next segue on our journey to solving for the steady current is deriving the fusion
 572 power (P_F), which appears in current drive. A comprehensive introduction to this is
 573 given in Appendix C. Summarized, though, a formula for fusion power from a D-T
 574 reaction – in megawatts – is given by the following volume integral:²⁵

$$P_F = \int E_F n_D n_T \langle \sigma v \rangle d\mathbf{r} \quad (2.17)$$

575

$$E_F = 17.6 \text{ MeV} \quad (2.18)$$

576 The E_F quantity is the energy created from a deuterium-tritium fusion reaction. The
 577 n_D and n_T in this equation then represent the density of the deuterium and tritium
 578 ions, respectively. Assuming a 50-50 mix of the two, they can be related to the
 579 electron density – i.e. the one used in this model – through the dilution factor (f_D).

580 This dilution factor represents the decrease in available fuel from part of the plasma
 581 actually being composed of non-hydrogen gasses:

$$n_D = n_T = f_D \cdot \left(\frac{n}{2}\right) \quad (2.19)$$

582 The fusion reactivity, $\langle\sigma v\rangle$, is then a nonlinear function of the temperature, T , which
 583 the model approximates using the Bosch-Hale tabulation (described in Appendix C).
 584 As this tabulated value appears inside an integral, it seems important to point out
 585 that the temperature is now the most difficult dynamic variable to handle – over R_0 ,
 586 B_0 , \bar{n} , and I_P . This will come into play when the model is formalized next chapter.

587 The next step in the derivation of fusion power is transforming the three-dimensional
 588 volume integral (see Eq. 2.17) into a zero-dimension averaged value. First, the volume
 589 analogue of the previously given surface-area integral is:

$$Q_V = 4\pi^2 R_0 a^2 \kappa g \int_0^1 Q(\rho) \rho d\rho \quad (E.24)$$

590 Where Q is an arbitrary function of ρ and g is a geometric factor approximately equal
 591 to one – both described in Appendix E. The fusion power can now be rewritten as:

$$P_F = \pi^2 E_F f_D^2 R_0 a^2 \kappa g \int_0^1 n^2 \langle\sigma v\rangle \rho d\rho \quad (2.20)$$

592 In standardized units, this becomes:

$$P_F = K_F \cdot \bar{n}^2 \cdot R_0^3 \cdot (\sigma v) \quad (2.21)$$

593

$$K_F = 278.3 \cdot f_D^2 \cdot (\epsilon^2 \kappa g) \quad (2.22)$$

594 Where the standardized fusion reactivity is now,

$$(\sigma v) = 10^{21} (1 + \nu_n)^2 \int_0^1 (1 - \rho^2)^{2\nu_n} \langle\sigma v\rangle \rho d\rho \quad (2.23)$$

595 At this point, the current drive needed for steady-state can now be defined.

596 2.2.4 Using Current Drive

597 As may have been lost along the way, this chapter's mission is to define a formula for
598 steady current – from the current balance equation for steady-state tokamaks:

$$I_P = I_{BS} + I_{CD} \quad (2.7)$$

599 In standardized units, the equation for current drive is often given in the literature
600 as:²⁶

$$I_{CD} = \eta_{CD} \cdot \left(\frac{P_H}{\bar{n}R_0} \right) \quad (2.24)$$

601 Here, η_{CD} is the current drive efficiency with units $\left(\frac{\text{MA}}{\text{MW-m}^2} \right)$ and P_H is the heating
602 power in megawatts driven by LHCD (and absorbed by the plasma).*

603 Let it be known, though, that driving current in a plasma is hard! In fact, pulsed
604 reactor designers (i.e. European fusion researchers) think it is so difficult, they may
605 choose to forego it completely – focusing only on inductive sources that necessitate
606 reactor fatigue and downtime.

607 For LHCD, a common current drive efficiency (η_{CD}) seen in many designs is 0.3 ± 0.1
608 in the standard units.^{3,6,26} It is however inherently a function of all the plasma
609 parameters – with subtlety put off until the discussion of self-consistency. For now it
610 assumed to have some constant/static value.

611 The remaining step in deriving an equation for driven current (I_{CD}) is a formula for
612 the heating power (P_H). The way fusion systems models – like this one – handle the
613 heating power is through the physics gain factor, Q. Sometimes referred to as big Q,
614 this value represents how many times over the heating power (P_H) is amplified as it

*A more formal introduction to LHCD, as well as the reasoning behind selecting it over neutral beam (NBCD) and electron cyclotron current drive (ECCD), are given in Appendix G.

615 is transformed into fusion power (P_F):

$$P_H = \frac{P_F}{Q} \quad (2.25)$$

616 Now, utilizing the previously defined Greenwald density and fusion power:

$$\bar{n} = K_n \cdot \left(\frac{I_P}{R_0^2} \right) \quad (2.10)$$

617

$$P_F = K_F \cdot \bar{n}^2 \cdot R_0^3 \cdot (\sigma v) \quad (2.21)$$

618 The current from LHCD can be written as:

$$I_{CD} = K_{CD} \cdot I_P \cdot (\sigma v) \quad (2.26)$$

619

$$K_{CD} = (K_F K_n) \cdot \frac{\eta_{CD}}{Q} \quad (2.27)$$

620 As η_{CD} and Q appear within a static coefficient, it is implied that both remain con-
 621 stant throughout a solve. This subtlety is lifted when handling η_{CD} self-consistently,
 622 which will be discussed shortly. However, even in that context, it proves beneficial to
 623 still think of η_{CD} as a sequence of static variables – set by the model rather than the
 624 user.

625 2.2.5 Completing the Steady Current

626 The goal of this chapter has been to derive a simple formula for steady current (I_P).

627 The problem started with current balance in a steady-state reactor:

$$I_P = I_{BS} + I_{CD} \quad (2.7)$$

Two equations were then found for the bootstrap (I_{BS}) and driven (I_{CD}) current:

$$I_{BS} = K_{BS} \cdot \bar{T} \quad (2.14)$$

$$I_{CD} = K_{CD} \cdot I_P \cdot (\sigma v) \quad (2.26)$$

Combining these three equations and solving for the total plasma current (I_P) – in mega-amps – yields:

$$I_P = \frac{K_{BS} \bar{T}}{1 - K_{CD}(\sigma v)} \quad (2.28)$$

This is the answer we have been seeking!

As mentioned before, this simple formula appears to only depend on temperature!*

Apparently, the plasma should have the same current at some temperature (i.e. $\bar{T} = 15$ keV), regardless of the size of the machine or the strength of its magnets. This has the important corollary that each temperature maps to only one current value. Further, each temperature would then map to a single magnet strength, capital cost, etc. (as shown next chapter).

As has become a mantra, though, the subtlety of this behavior lies in the self-consistency of the current-drive efficiency – η_{CD} .

2.3 Handling Current Drive Self-Consistently

Although a thorough description of the wave theory behind lower-hybrid current drive (LHCD) is well outside the scope of this text, it does motivate the solving of a tokamak's major radius (R_0) and field strength (B_0). It also shows how what was once a simple problem has now transformed into a rather complex one – a common

* This dependence only on temperature refers to dynamic variables. The plasma current can still be highly volatile to many of the static variables, such as: ϵ , κ , N_G , f_D , ν_n , l_i , etc.

647 occurrence with plasmas.

648 The logic behind finding a self-consistent current-drive efficiency is starting at some
649 plausible value (i.e. $\eta_{CD} = 0.3$), solving for the steady current – i.e. $I_P = f(\overline{T})$ – and
650 then somehow iteratively creeping towards a value deemed self-consistent. What this
651 means is that in addition to the solver described in the last section, there needs to
652 be a black-box function that solutions are sent through to get better guesses at η_{CD} .
653 The black-box function we use is a variation of the Ehst-Karney model.²⁷ A thorough
654 description of this algorithm is given in Appendix G.

655 As mentioned, though, a self-consistent η_{CD} is found once a trip through the Ehst-
656 Karney black-box results in the same η_{CD} as was sent in – to some tolerable level of
657 error. This consistency incorporates an explicit dependence on the tokamak configu-
658 ration. Mathematically,

$$\tilde{\eta}_{CD} = f(R_0, B_0, \bar{n}, \overline{T}, I_P) \quad (2.29)$$

659 As such, to recalculate it after every solution of the steady current requires a value
660 for both B_0 and R_0 – the targets of this model’s primary and limiting constraints.
661 These will be the highlight of the next chapter.

Chapter 3

Formalizing the Systems Model

The goal of this chapter is to take a step back from the steady current derivation and see the larger picture behind reactor design. As such, a more in-depth description of static and dynamic variables is given. This discussion of dynamic variables will then lend itself to a description of the framework underpinning the fusion systems model. As such, we will now need formulas for the radius and magnet strength of the tokamak. Moving forward, the current will remain a connecting piece as we redirect focus to pulsed tokamaks and compare the underlying solvers of the two schemes.

The end result of this analysis will then be equations that allow the density (\bar{n}), current (I_P), major radius (R_0), and magnet strength (B_0) to be written as functions of the temperature (\bar{T}) and static variables (e.g. ν_n , N_G , f_D). These formulas are the product of applying constraints required for all tokamak reactors with several other limiting constraints. The constraints relevant to all tokamak reactors are: the Greenwald limit, current balance, and power balance. Limit constraints then include: the Troyon beta limit, the kink safety factor, the wall loading limit, the maximum power constraint, and the heat loading limit.

Actual methodologies for solving for the five dynamic variables simultaneously – i.e. \bar{T} , \bar{n} , I_P , R_0 , B_0 – are put off until Chapter 5.

3.1 Explaining Static Variables

In this model, static variables are ones that remain constant while solving for a reactor. These include geometric scalings (i.e. ϵ , δ , κ), profile parameters (i.e. ν_n , ν_T , l_i), and a couple dozen of physics constants related to pulsed and steady-state design (e.g. Q , N_G , f_D). For a complete list of static variables, consult Appendix A.1. The point to make now is that this model treats static variables as immutable objects. As such they often reside in static coefficients – K_\square – which are treated as constants.

3.2 Connecting Dynamic Variables

Dynamic variables – \bar{T} , \bar{n} , I_P , R_0 , B_0 – are the first-class variables of this fusion systems model. They represent the fundamental properties of a plasma and tokamak (which constitute a fusion reactor). As such, they will be reintroduced one at a time, explaining how they fit into the model – and which equations are capable of representing them.

Table 3.1: Dynamic Variables

Symbol	Name	Units
I_P	Plasma Current	MA
\bar{T}	Plasma Temperature	keV
\bar{n}	Electron Density	10^{20} m^{-3}
R_0	Major Radius	m
B_0	Magnet Strength	T

Bluntly, this fusion systems model is a simple algebra problem: solve five equations with five unknowns (i.e. \bar{T} , \bar{n} , I_P , R_0 , B_0). Although this naive approach would work, we can do a little better by collapsing these five equations down to just one. This was already done while deriving the steady current. It just happened that the current was not directly dependent on the tokamak size (R_0) or magnet strength (B_0).

*Note that the magnet strength (B_0) used throughout this text refers particularly to the strength of the toroidal magnetic field on axis – i.e. at $\rho = 0$.

699 This will prove more challenging for the generalized current needed for pulsed op-
700 eration. Even so, this equation will still be reduced to one equation with a single
701 unknown – I_P . A solution to which can be solved much faster than the naive 5
702 equation approach. This is one reason the model is so fast.

703 **The Plasma Temperature – \bar{T}**

704 The plasma temperature, measured in keV (kilo-electron-volts), is one of the most
705 nonlinear variables in the fusion systems framework. It first proved troublesome
706 when it was shown that a pedestal profile – not a parabolic one used here – would
707 be needed for an accurate calculation of bootstrap current. The black-box tabulation
708 for reactivity – (σv) – which appeared in fusion power only further exposed this
709 nonlinearity.

710 Acknowledging that temperature is the most difficult to handle parameter prompts
711 its use as the scanned variable. What this means practically is scanning temperatures
712 is the most straightforward method to produce curves of reactors. By example, a scan
713 may be run over the average temperatures (\bar{T}): 10, 15, 20, 25, and 30 keV – where
714 each corresponds to its own reactor with its own toroidal field strength (B_0), plasma
715 current (I_P), etc. In equation form, this becomes:

$$\boxed{\bar{T} = const.} \tag{3.1}$$

716 The constant value, here, happens to be 10 keV in one run, 15 keV for the next, and
717 30 keV in the fifth.

718 **The Plasma Density – \bar{n}**

719 The Greenwald density limit is a constraint with a simple form that applies to all
720 tokamak reactors. It is for this reason – as well as being a good approximation –
721 that a parabolic profile was rationalized over a pedestal (H-Mode) one. Repeated,

722 the Greenwald density limit is:

$$\bar{n} = K_n \cdot \frac{I_P}{R_0^2} \quad (2.10)$$

723 Where K_n is given by Eq. (2.11). This is an exceptionally simple relationship and
724 why it guided the model. Unlike the next three variables, it is actually used in their
725 derivations.

726 The Plasma Current – I_P

727 The plasma current is what separates steady-state from pulsed operation. From
728 before, the steady current was found to be:

$$I_P = \frac{K_{BS}\bar{T}}{1 - K_{CD}(\sigma v)} \quad (2.28)$$

729 This was derived by setting the total current equal to the two sources of current:
730 bootstrap and current drive. Or in fractional form,

$$I_P = I_{BS} + I_{CD} \rightarrow 1 = f_{BS} + f_{CD} \quad (3.2)$$

731 This says that the current fractions of bootstrap and current drive must sum to one.
732 As shown next chapter, inductive sources can be included into this current balance:

$$1 = f_{BS} + f_{CD} + f_{ID} \quad (3.3)$$

733 This equation shows how steady-state and pulsed operation can coexist (see Fig. 3-1).
734 The final point to make is reducing the model to being purely pulsed – i.e. neglecting
735 the current drive:

$$1 = f_{BS} + f_{ID} \quad (3.4)$$

736 Therefore, the next chapter will generalize the steady current to allow pulsed oper-
737 ation, and then simplify it to the purely pulsed case. Just as steady current faced

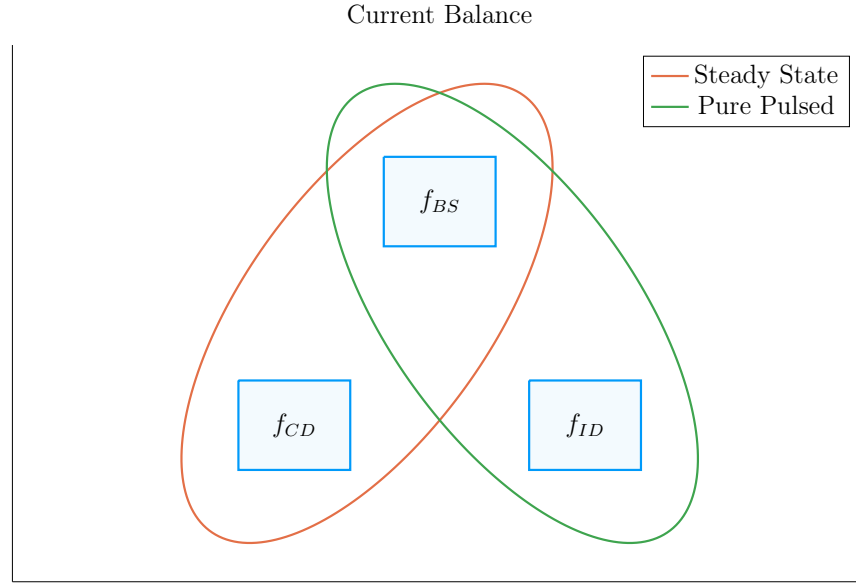


Figure 3-1: Current Balance in a Tokamak

In a tokamak, there needs to be a certain amount of current – and that current has to come from somewhere. All good reactors have an adequate bootstrap current. What provides the remaining current is what distinguishes steady state from pulsed operation.

self-consistency issues with η_{CD} , this current will also involve its own root solving
conundrum – the description of which will be given in the following two chapters.

The Tokamak Magnet Strength – B_0

The tokamak magnet strength has no unique equation to eliminate it. With foresight, the one this model uses is the power balance inherent to every reactor. Similar to current balance, power balance is what separates a reactor from a device incapable of producing net electricity. As such, it is referred throughout this document as: the primary constraint. It will be derived later this chapter.

The Tokamak Major Radius – R_0

Much like the magnet strength, the major radius has no unique relation to express it. The model therefore uses this equation to handle a reactor’s various physical and engineering-based constraints. This list of requirements further restricts reactor

space to the curves shown in the results section. Collectively, these are referred to as the limiting constraints – discussed later this chapter. These constraints all just happen to depend on the size of the reactor – the reason they are chosen to represent the radius.

3.3 Enforcing Power Balance

What separates a reactor from a device incapable of producing net electricity is power balance. Within a tokamak, it accounts for how the power going into a plasma’s core exactly matches the power coming out of it. To approximate this conservation equation, two sets of power will be introduced: the sources and the sinks.

The sources have mainly been introduced at this point – they include the alpha power (P_α) from fusion reactions and the heating power (P_H), as well as a new ohmic power term (P_Ω). The remaining two powers – the sinks – then appear through the radiation and heat conduction losses, which will be given shortly. In equation form, power balance becomes:

$$\sum_{sources} P = \sum_{sinks} P \quad (3.5)$$

or expanded to fit this model:

$$P_\alpha + P_H + P_\Omega = P_{BR} + P_\kappa \quad (3.6)$$

For clarity, the left-hand side of this equality are the sources. Whereas the remaining two are sinks, i.e. Bremsstrahlung radiation (P_{BR}) and heat conduction losses (P_κ).

3.3.1 Collecting Power Sources

As suggested, the two dominant sources of power in a tokamak are: alpha power (P_α) and auxiliary heating (P_H). From Appendix C, it was determined that alpha particles (i.e. helium nuclei) carry around 20% of the total fusion power; or as we put

771 it mathematically:

$$P_\alpha = \frac{P_F}{5} \quad (\text{C.4})$$

772 Additionally, it was determined that the heating power is what was eventually am-
773 plified into fusion power – or through equation:

$$P_H = \frac{P_F}{Q} \quad (2.25)$$

774 The final source term then is the ohmic power (P_Ω). This is identical to how copper
775 wires in a home heat up as current runs through them. From a simple circuits
776 picture, the power across the plasma is related to its current and resistance – in our
777 standardized units – through:⁷

$$P_\Omega = 10^6 \cdot I_P^2 \cdot R_P \quad (3.7)$$

778 This fusion systems model handles the plasma resistance (R_P) with the neoclassical
779 Spitzer resistivity. Through equation,⁵

$$R_P = \frac{K_{RP}}{R_0 \bar{T}^{3/2}} \quad (3.8)$$

780

$$K_{RP} = 5.6e-8 \cdot \left(\frac{Z_{eff}}{\epsilon^2 \kappa} \right) \cdot \left(\frac{1}{1 - 1.31\sqrt{\epsilon} + 0.46\epsilon} \right) \quad (3.9)$$

781 Combined with the Greenwald limit, ohmic power can be written more compactly as,

782

$$P_\Omega = K_\Omega \cdot \left(\frac{\bar{n}^2 R_0^3}{\bar{T}^{3/2}} \right) \quad (3.10)$$

783

$$K_\Omega = 10^6 \cdot \frac{K_{RP}}{K_n^2} \quad (3.11)$$

784 With the sources defined, we are now in a position to discuss the two sink terms used
785 in this model's power balance.

3.3.2 Approximating Radiation Losses

All nuclear reactors emit radiation. From a power balance perspective, this means some power has to always be reserved to recoup from its losses – measured in megawatts. In a fusion reactor, the three most important types of radiation are: Bremsstrahlung radiation, line radiation, and synchrotron radiation.

This model chooses to only model Bremsstrahlung radiation – as it usually dominates within the plasma’s core. Within most designs, Bremsstrahlung radiation outweighs the other two’s contribution, to core power balance, two-to-one.^{3,8} However, adding the effects of line-radiation and synchrotron radiation would drive results closer to real-world experiments. For example, line-radiation would better account for the effects of heavy impurities that are emitted from the divertor plate and first wall

For clarity, Bremsstrahlung – or braking – radiation is what occurs when a charged particle (e.g. an electron) is accelerated by some means. In a tokamak, this happens all the time as electrons collide with the ion species.²⁸ This term can be described by the volume integral:⁵

$$P_{BR} = \int S_{BR} d\mathbf{r} \quad (3.12)$$

Where the radiation power density (S_{BR}) is given by:

$$S_{BR} = \left(\frac{\sqrt{2}}{3\sqrt{\pi^5}} \cdot \frac{e^6}{\epsilon_0^2 c^3 h m_e^{3/2}} \right) \cdot (Z_{eff} n^2 T^{1/2}) \quad (3.13)$$

The constants in the left set of parentheses all have their usual physics meanings (i.e. c is the speed of light and m_e is the mass of an electron). What is new is the effective charge: Z_{eff} .⁵

$$Z_{eff} = \frac{1}{n_e} \sum_j n_j Z_j^2 \quad (3.14)$$

The effective charge is a scheme for reducing the charge each ion has to a single representative value. Fundamental charge, here, is what: neutrons lack, electrons and hydrogen have one of, and helium has two. As such, a plasma with a purely deuterium and tritium fuel would have an effective charge of one. This value would

809 then quickly rise if a Tungsten tile – with 74 units of charge – were to fall into the
 810 plasma core from the walls of the tokamak.*

811 Using the volume integral – seen in the derivation of fusion power – allows the
 812 Bremsstrahlung power to be written in standardized units as:

$$P_{BR} = K_{BR} \bar{n}^2 \bar{T}^{1/2} R_0^3 \quad (3.15)$$

813

$$K_{BR} = 0.1056 \frac{(1 + \nu_n)^2 (1 + \nu_T)^{1/2}}{1 + 2\nu_n + 0.5\nu_T} Z_{eff} \epsilon^2 \kappa g \quad (3.16)$$

814 This power term represents the radiation power losses involved in power balance. All
 815 that is needed now is a formula for heat conduction losses – one of the most difficult
 816 plasma behaviors to model to date.

817 3.3.3 Estimating Heat Conduction Losses

818 Heat is energy that moves about randomly on a microscopic level. Macroscopically,
 819 it generally moves from hotter areas to colder ones. As hinted by the plasma profile
 820 for temperature, heat emanates from the center of a plasma and migrates towards the
 821 walls of its tokamak enclosure. It therefore is a critical quantity to calculate when
 822 balancing power in a plasma's core.

823 The difficulty of estimating heat conduction, though, lies in the nonlinear behaviors
 824 of plasmas – no quick-running computation today can properly model it. As such, re-
 825 actor designers have turned towards experimentalists for empirical scaling laws based
 826 on the dozen or so strongest tokamaks in the world. These are collectively referred
 827 to as confinement time scalings, i.e. the ELMy H-Mode Scaling Law.

828 The derivation of this heat conduction loss term (P_κ) starts in a manner similar to
 829 the previous powers. To begin, an equation for P_κ can be found using the following

*Typical effective charges (Z_{eff}) for a reactor are expected to be between 1 and 3.^{3,6,8}

830 volume integral:⁵

$$P_{\kappa} = \frac{1}{\tau_E} \int U d\mathbf{r} \quad (3.17)$$

831 This volume integral includes two new terms: the confinement time (τ_E) and the
832 internal energy (U). Before explaining these terms, a qualitative description is in
833 order. As mentioned previously, the heat – or microscopically random – energy is
834 captured by the internal energy (U). Then the confinement time (τ_E) is how long it
835 would take for the heat to undergo an e-folding if the device were suddenly turned
836 off.

837 A formula for confinement time will be delayed till the end of this section, when it is
838 needed to solve for the magnetic field (B_0). The internal energy (U), however, can be
839 given now as it has its typical physics meaning. This assumes that all three plasma
840 species are held nearly at the same temperature (T) as the electrons:

$$U = \frac{3}{2} (n + n_D + n_T) T \quad (3.18)$$

841 Here again, n_D and n_T – the density of deuterium and tritium, respectively – are
842 related to the electron density (used in this model) through the dilution factor, which
843 assumes a 50-50 mix of D-T fuel:

$$n_D = n_T = f_D \cdot \left(\frac{n}{2} \right) \quad (3.19)$$

844 After several substitutions, the equations here can be combined to form an equation
845 for P_{κ} – the heat conduction losses – in standardized units:

$$P_{\kappa} = K_{\kappa} \frac{R_0^3 \bar{n} \bar{T}}{\tau_E} \quad (3.20)$$

846

$$K_{\kappa} = 0.4744 (1 + f_D) \frac{(1 + \nu_n)(1 + \nu_T)}{1 + \nu_n + \nu_T} (\epsilon^2 \kappa g) \quad (3.21)$$

847 Now that all five terms have been defined in power balance, the next step is expanding

848 it and solving for the tokamak's toroidal magnetic field strength: B_0 .

849 3.3.4 Writing the Lawson Parameter

850 Before arriving at a formula for the magnet strength (B_0) using power balance, – it
851 seems appropriate to take a detour and explain an intermediate solution: the Lawson
852 Parameter.²⁵ Within the fusion community, the Lawson Parameter is the cornerstone
853 in any argument on the possibility of a tokamak ever being used as a reactor.

854 An equation for the Lawson Parameter – sometimes referred to as the *triple product*
855 – is easily found in the literature as:⁵

$$n \cdot T \cdot \tau_E = \frac{60}{E_F} \cdot \frac{T^2}{\langle \sigma v \rangle} \quad (3.22)$$

856 Similar to the steady current derived earlier, the right-hand side is only dependent
857 on temperature. Further, as the left-hand side is a measure of difficult to achieve
858 parameters, the goal is to minimize both sides. As shown in Fig. 3-2, this occurs
859 when the plasma temperature is around 15 keV – a fact well known to many fusion
860 engineers. As will be seen, this is a simplified result of our model. This is why $\bar{T} = 15$
861 keV is not always the optimum temperature – but usually is in the right neighborhood
862 for reasonable reactor designs.

As all the terms in power balance have already been defined, the starting point will

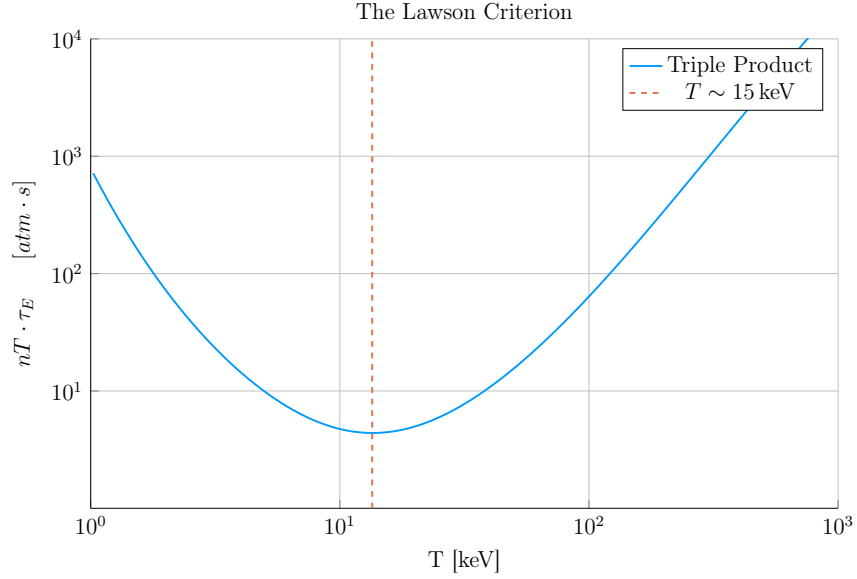


Figure 3-2: Power Balance in a Reactor

Power balance is what differentiates a reactor from a net power loss experiment. When cast as the Lawson Parameter for fusion, it explains why D-T plasmas often have a temperature around 15 keV.

be simply repeating the standardized equations for all five included powers.

$$P_{\alpha} = \frac{P_F}{5} \quad (\text{C.4})$$

$$P_H = \frac{P_F}{Q} \quad (2.25)$$

$$P_{\Omega} = K_{\Omega} \cdot \left(\frac{\bar{n}^2 R_0^3}{\bar{T}^{3/2}} \right) \quad (3.10)$$

$$P_{BR} = K_{BR} \bar{n}^2 \bar{T}^{1/2} R_0^3 \quad (3.15)$$

$$P_{\kappa} = K_{\kappa} \frac{R_0^3 \bar{n} \bar{T}}{\tau_E} \quad (3.20)$$

863 With the fusion power again being,

$$P_F = K_F \cdot \bar{n}^2 \cdot R_0^3 \cdot (\sigma v) \quad (2.21)$$

864 These can then be substituted into power balance:

$$P_\alpha + P_H + P_\Omega = P_{BR} + P_\kappa \quad (3.6)$$

865 After a couple lines of algebra, power balance can be rewritten in a form analogous
866 to the triple product:

$$\bar{n} \cdot \bar{T} \cdot \tau_E = \frac{K_\kappa \bar{T}^2}{\left(K_P (\sigma v) + K_{OH} \bar{T}^{-3/2}\right) - K_{BR} \bar{T}^{1/2}} \quad (3.23)$$

867

$$K_P = K_F \cdot \left(\frac{5 + Q}{5 \times Q}\right) \quad (3.24)$$

868 As expected, this shares a form similar to the simple Lawson Parameter:

$$n \cdot T \cdot \tau_E = \frac{60}{E_F} \cdot \frac{T^2}{\langle \sigma v \rangle} \quad (3.22)$$

869 The main difference is this model does not ignore ohmic power and radiation losses
870 completely. The inclusion of radiation for example sometimes bars a range of temper-
871 atures from being physically realizable.* With this intermediate relation in place, the
872 goal is now to give a formula for the confinement time and solve it for the magnetic
873 field strength (B_0) – thus giving the Primary Constraint.

874 3.3.5 Finalizing the Primary Constraint

875 The goal now is to transform the Lawson Parameter into an equation for magnet
876 strength (B_0). This choice to solve the equation for B_0 was motivated by the goals
877 of analysis and how it will fit into the fusion systems model. To solve the primary
878 constraint, the confinement time scaling law will need to be introduced. At the end,

* The denominator of Eq 3.23 has discontinuities when the $K_{BR} \bar{T}^{1/2}$ term exactly equals the parenthesised one. Therefore, valid reactors only exist outside the discontinuities, when the entire triple product is finite and positive.

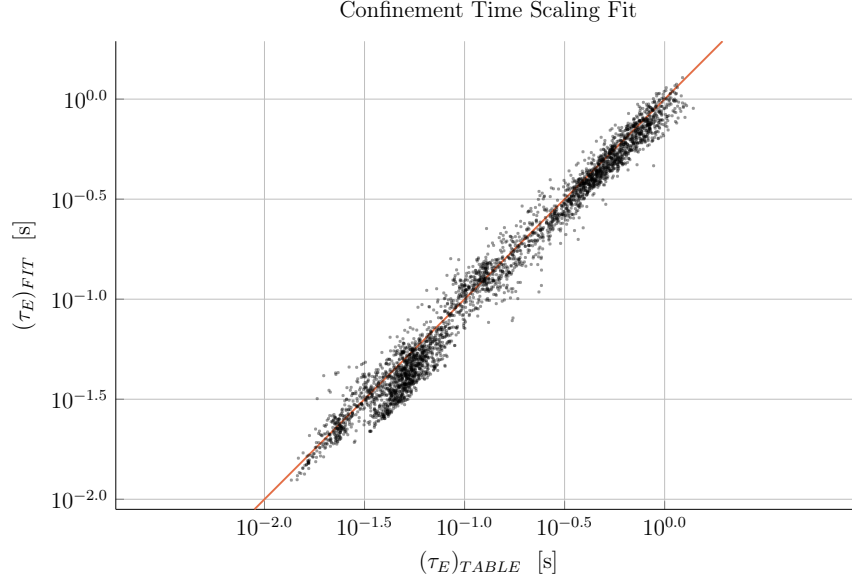


Figure 3-3: H-Mode Confinement Time Scaling

This plot shows how well the ELMy H-Mode Scaling Law does for fitting τ_E to the ITER98 database of global tokamaks. For most values, the fit is at least 80% accurate with the measured value.²⁹

879 a convoluted – albeit highly useful – relation will be the reward.

880 The energy confinement time – τ_E – is one of the most difficult to obtain terms in all
 881 of fusion energy. It is an attempt to reduce all the nonlinear behaviors of plasmas into
 882 a simple measure of how fast its internal energy would be ejected from the tokamak
 883 if the device was instantaneously shut down. As such, reactor designers have turned
 884 toward experimentalists for empirical scalings based on the world’s tokamaks (see
 885 Fig. 3-3). These all share a form similar to:

$$\tau_E = K_\tau H \frac{I_P^{\alpha_I} R_0^{\alpha_R} a^{\alpha_a} \kappa^{\alpha_\kappa} \bar{n}^{\alpha_n} B_0^{\alpha_B} A^{\alpha_A}}{P_{src}^{\alpha_P}} \quad (3.25)$$

886 This regressional fit is how the field actually designs machines (i.e. ITER). Let it be
 887 known, though, that fits of this kind often do remarkable well, having relative errors
 888 less than 20% on interpolated data. The new terms in this equation are: P_{src} , K_τ , H ,
 889 A , and the α_\square factors.

890 First, the loss power is a metric used in the engineering community to quantify the
 891 power being transported out of the “core” of the plasma by charged particles (i.e. not
 892 the neutrons).⁷ To optimize fits, experimentalists have defined this as a combination
 893 of the source power terms:

$$P_{src} = P_{\alpha} + P_H + P_{\Omega} \quad (3.26)$$

894 Moving on, K_{τ} is simply a constant fit-makers use in their scalings. Whereas H is
 895 the enhancement factor over the empirical fit. Next, A is the average mass number of
 896 the fuel source, in atomic mass units. For a 50-50 D-T fuel, this is 2.5, as deuterium
 897 weighs two amus and tritium weighs three. Lastly, the alpha factors (e.g. α_n , α_a ,
 898 α_P) are fitting parameters that represent each variable’s relative importance in the
 899 scaling.

900 For ELMy H-Mode, this confinement scaling law can be written as:

$$\tau_E^H = 0.145 H \frac{I_P^{0.93} R_0^{1.39} a^{0.58} \kappa^{0.78} \bar{n}^{0.41} B_0^{0.15} A^{0.19}}{P_{src}^{0.69}} \quad (3.27)$$

901 However, similar scaling laws can be written for L-Mode, I-Mode, etc. One final
 902 remark to make before moving on is that even these fits have subtleties. The value
 903 of κ , for example, may have a slightly different geometric meaning from tokamak to
 904 tokamak. And the exact definition of loss power – P_{src} – introduces an even larger
 905 area of discrepancy.

906 Returning to the problem at hand, though, this model’s Lawson Parameter (eq. 3.23)
 907 can be simplified after expanding the left-hand side using the Greenwald density and
 908 substituting in a confinement time scaling law. After a few lines of algebra, this can
 909 be transformed into a formula for B_0 !

$$B_0 = \left(\frac{G_{PB}}{K_{PB}} \cdot \left(I_P^{\alpha_I^*} R_0^{\alpha_R^*} \right)^{-1} \right)^{\frac{1}{\alpha_B}} \quad (3.28)$$

910

$$G_{PB} = \frac{\bar{T} \cdot \left(K_P(\sigma v) + K_\Omega \bar{T}^{-3/2} \right)^{\alpha_P}}{\left(K_P(\sigma v) + K_\Omega \bar{T}^{-3/2} - K_{BR} \bar{T}^{1/2} \right)} \quad (3.29)$$

911

$$K_{PB} = H \cdot \left(\frac{K_\tau K_n^{\alpha_n^*}}{K_\kappa} \right) \cdot (\epsilon^{\alpha_a} \kappa^{\alpha_\kappa} A^{\alpha_A}) \quad (3.30)$$

Where we have added new starred alpha values for the density, current, and radius:

$$\alpha_n^* = 1 + \alpha_n - 2\alpha_P \quad (3.31)$$

$$\alpha_I^* = \alpha_I + \alpha_n^* \quad (3.32)$$

$$\alpha_R^* = \alpha_R + \alpha_a - 2\alpha_n^* - 3\alpha_p \quad (3.33)$$

912 This equation for B_0 – derived from power balance – is thus the primary constraint
 913 for reactor designs. It is the first step in connecting the plasma (i.e. \bar{n} , \bar{T} , and I_P) to
 914 its tokamak enclosure (i.e. B_0 and R_0). The remaining step is finding an equation –
 915 or in this case, equations – for the major radius of the device. These radius equations
 916 will collectively be referred to as: the limiting constraints.

917 3.4 Collecting Limiting Constraints

918 As of now, the only missing equation within our list of static variables – i.e. R_0 , B_0 ,
 919 \bar{T} , \bar{n} , and I_P – is for the major radius of the tokamak. This equation will come from
 920 around five potential limits, each either physical or engineering-based. These limits
 921 will then correspond to different curves through reactor space. As will be shown,
 922 many of these reactors will be invalid (as they violate at least one of the other limits).
 923 Our analysis is always based on selecting the most stringent criterion.

924 Before tackling the subject of finding reactors that exist on the fine line of satisfying
 925 every limiting constraints, though, it is essential to collect them one-by-one. These
 926 are: the Troyon Beta Limit, the Kink Safety Factor, the Wall Loading Limit, the

927 Power Cap Constraint, and the Heat Loading Limit.

928 The goal of this section is to solve for each of these constraints on the major radius.
929 As with the primary constraint, this choice of solving for R_0 was not completely
930 unique, just motivated by physics and engineering concerns. It just so happens that
931 each limit described here depends on the size of a reactor – which is not true for the
932 magnetic field strength.

933 3.4.1 Introducing the Beta Limit

934 The Beta Limit is the most important limiting constraint – especially for steady-
935 state reactors. It sets a maximum on the amount of pressure a plasma is willing
936 to tolerate. As with future limiting constraints, literature-based equations will be
937 transformed into formulas for R_0 . Each will then contain some limiting quantity that
938 can be handled by a static variable – as β_N will be used shortly.

939 The starting point for the beta limit is to define the important plasma physics quan-
940 tity: β – the plasma beta. This value is a ratio between a plasma’s internal pressure
941 and the pressure exerted on it by the tokamak’s magnetic configuration. Mathemat-
942 ically,⁵

$$\beta = \frac{\text{plasma pressure}}{\text{magnetic pressure}} = \frac{\bar{p}}{\left(\frac{B_0^2}{2\mu_0}\right)} \quad (3.34)$$

943 Using this model’s temperature and density profiles, the volume-averaged pressure
944 (\bar{p}) can be written in units of atmospheres (i.e. atm) as:

$$\bar{p} = 0.1581 (1 + f_D) \frac{(1 + \nu_n)(1 + \nu_T)}{1 + \nu_n + \nu_T} \bar{n} \bar{T} \quad (3.35)$$

945 Moving forward, the final step is plugging this definition for plasma beta into the
946 Troyon Beta Limit derived using standard MHD stability analysis. This equation can
947 be written in the following form, where β_N is the normalized plasma beta – i.e. a

948 static variable usually set between 2% and 4%.¹²

$$\beta = \beta_N \frac{I_P}{aB_0} \quad (3.36)$$

949 Substituting the plasma β from eq. 3.34, into this relation results in the model's first
950 equation for tokamak radius:

$$R_0 = \frac{K_{TB} \bar{T}}{B_0} \quad (3.37)$$

951

$$K_{TB} = 4.027 \times 10^{-2} \cdot \left(\frac{K_n \epsilon}{\beta_N} \right) \cdot (1 + f_D) \cdot \frac{(1 + \nu_n)(1 + \nu_T)}{1 + \nu_n + \nu_T} \quad (3.38)$$

952 As mentioned, this is often the dominating constraint in a steady-state reactor. The
953 often dominating constraint for pulsed designs – the kink safety factor – will be the
954 focus of the next subsection.

955 3.4.2 Giving the Kink Safety Factor

956 Just like how the Troyon Beta Limit set a fluids-based maximum on plasma pressure,
957 the Kink Safety Factor sets one on the plasma's current. This constraint usually
958 only appears in pulsed designs, as it is assumed that getting to this high a current in
959 steady-state (with only LHCD) would prove extremely unpractical.

960 The starting point, again, is an equation from the literature for the kink condition:^{7,30}

961

$$q_* = 5\epsilon^2 \cdot \frac{R_0 B_0}{I_P} \cdot \left(\frac{1 + \kappa^2 \cdot (1 + 2\delta^2 - 1.2\delta^3)}{2} \right) \quad (3.39)$$

962 Here the safety factor – q_* – typically has values around 3.

963 Combined, the kink safety factor can now be written in standardized units as:

$$R_0 = \frac{K_{SF} I_P}{B_0} \quad (3.40)$$

964

$$K_{SF} = \frac{q_*}{5\epsilon^2} \cdot \left(\frac{2}{1 + \kappa^2 \cdot (1 + 2\delta^2 - 1.2\delta^3)} \right) \quad (3.41)$$

965 This relation is the limiting constraint important for most pulsed reactor designs. As
 966 with the Beta Limit, the two are derived through plasma physics alone. The remaining
 967 limiting constraints, however, are engineering-based in origin – these include: the Wall
 968 Loading Limit, the Power Cap Constraint, and the Heat Loading Limit. Each will be
 969 defined shortly.

970 3.4.3 Working under the Wall Loading Limit

971 The first engineering-based limiting constraint – the wall loading limit – will prove
 972 to be an important quantity when determining the magnet strength at which reactor
 973 costs begin to increase. As hinted, its definition originates from nuclear engineering
 974 concerns: it is a measure of the maximum neutron damage a tokamak’s walls can
 975 take over the lifetime of the machine.*

976 The first step in deriving a limiting constraint for wall loading is a description of the
 977 problem it models. In a reactor, fusion reactions typically make high-energy neutrons
 978 – with around 14.1 MeV of kinetic energy – that collide with the tokamak enclosure.
 979 Therefore a simple metric would be limiting the amount of neutron power that can
 980 be unloaded on the surface area of a tokamak. This can be written as:¹³

$$P_W = \frac{P_n}{S_P} \quad (3.42)$$

981

$$S_P = 4\pi^2 a R_0 \cdot \frac{\left(1 + \frac{2}{\pi} (\kappa^2 - 1)\right)}{\kappa} \quad (3.43)$$

982 Here, S_P is the surface area of the tokamak’s inner wall and P_n is the neutron power
 983 derived in the subsection on fusion power. The quantity, P_W , then serves a role

*For clarity, the wall loading limit should actually be a energy fluence limit. It is converted to an instantaneous power limit for ease of design purposes.

analogous to β_N for the beta limit and q_* for the kink safety factor – it is a static variable representing the maximum allowed wall loading. For fusion reactors, P_W is assumed to be around 2-4 $\frac{\text{MW}}{\text{m}^2}$. It will be shown that the wall loading limit is important in any tokamak – regardless of operating mode (i.e. steady-state or pulsed).

Finishing this limiting constraint, the Wall Loading limit can be written in standardized units as:

$$R_0 = K_{WL} \cdot I_P^{\frac{2}{3}} \cdot (\sigma v)^{\frac{1}{3}} \quad (3.44)$$

$$K_{WL} = \left(\frac{K_F K_n^2}{5\pi^2 P_W} \cdot \frac{\kappa}{\epsilon} \cdot \frac{1}{1 + \frac{2}{\pi} \cdot (\kappa^2 - 1)} \right)^{\frac{1}{3}} \quad (3.45)$$

3.4.4 Setting a Maximum Power Cap

As opposed to the previous three limiting constraints, the maximum power cap is more of a constraint set by economic competitiveness. Because no reactor – coal, solar, or otherwise – has a 4000 MW reactor, neither should fusion.* It makes sense from a practical position after realizing the long history of tokamaks being delayed, underfunded, or completely canceled. Mathematically, this has the simple form:

$$P_E \leq P_{CAP} \quad (3.46)$$

Here, P_{CAP} is the maximum allowed power output of the reactor. Similar to the other limiting quantities, P_{CAP} is treated as a static variable (i.e. set to 4000 MW). The electrical power output of the reactor (P_E) is then related to the fusion power through:⁵

$$P_E = 1.273 \eta_T \cdot P_F \quad (3.47)$$

*Note that this 4000 MW (electric) is a maximum. A 1000 MW reactor would obviously not violate this constraint. Instead it would likely be pressing on either the kink or beta limit.

1003 The variable η_T is the thermal efficiency of the reactor – which is usually found to
 1004 be around 40%. And the constant in front (i.e. 1.273) represents some extra power
 1005 the reactor makes as fuel is bred by the fusion neutrons passing through a tokamak’s
 1006 lithium-filled blanket. Explicitly this results from including the energy released by
 1007 lithium-6 as it undergoes neutron capture (E_{Li}).

$$1.273 = \frac{E_F + E_{Li}}{E_F} \quad (3.48)$$

$$E_{Li} = 4.8 \text{ MeV} \quad (3.49)$$

1008 Substituting in fusion power and solving for the major radius results in:

$$R_0 = K_{PC} \cdot I_P^2 \cdot (\sigma v) \quad (3.50)$$

1009

$$K_{PC} = K_F K_n^2 \cdot \left(\frac{1.273 \eta_T}{P_{max}} \right) \quad (3.51)$$

1010 This limiting constraint can be used to create curves of reactors, although it is mainly
 1011 used as a stopping point for designs – i.e. if you get to the power-cap regime, you
 1012 have gone too far. This is different than the next constraint, which is fundamentally
 1013 an unsolved problem within the modern tokamak design paradigm.³¹

1014 3.4.5 Listing the Heat Loading Limit

1015 Fusion plasmas are hot. The commonly given relation is one electron volt is around
 1016 20,000 °F – which makes 15 keV around a quarter-billion Fahrenheit. Although this
 1017 connotation of temperature is slightly deceptive, heat damage to a tokamak is an
 1018 all too real concern. The problem is there is currently no solution to the problem.
 1019 Although researchers have explored various types of heat divertors, none have been
 1020 shown to withstand the gigawatts-per-square-meter of heat emitted from a reactor-

1021 size tokamak.³¹

1022 As such, this model takes an approach similar to the research community, calculating
1023 it at the end as a manual check on the difficulty of building such a device – but not
1024 using it to explicitly guide design. For completeness though, a limiting constraint will
1025 still be derived. The first step is giving the heat load limit commonly found in the
1026 literature:¹³

$$q_{DV} = \frac{K_{DV}}{K_F} \cdot \frac{P_F I_P^{1.2}}{R_0^{2.2}} \quad (3.52)$$

1027

$$K_{DV} = \frac{18.31 \times 10^{-3}}{\epsilon^{1.2}} \cdot K_P \cdot \left(\frac{2}{1 + \kappa^2} \right)^{0.6} \quad (3.53)$$

1028 This is the heat load that impinges on an extended leg, double null divertor – primarily
1029 from the outer midplane of the plasma core. After a simple rearrangement and
1030 substitution for fusion power, this becomes:

$$R_0 = K_{DH} \cdot I_P \cdot (\sigma v)^{\frac{1}{3.2}} \quad (3.54)$$

1031

$$K_{DH} = \left(\frac{K_{DV} K_n^2}{q_{DV}} \right)^{\frac{1}{3.2}} \quad (3.55)$$

1032 At this point all the limiting constraints have been defined. The next step is taking
1033 a step back and motivating the derivation of a current equation suitable for pulsed
1034 tokamaks.

1035 3.5 Summarizing the Fusion Systems Model

1036 Stepping back, this chapter focused on the bigger picture behind designing a zero-
1037 dimension fusion systems model. It started with a description of various design pa-
1038 rameters and then moved onto explaining the five relations needed to close the model
1039 – i.e. for \overline{T} , \overline{n} , I_P , B_0 , and R_0 .

Before generalizing the steady current to allow modeling pulsed reactors, though, a quick recap of the equations will prove beneficial. The first variable described was temperature – i.e. scan five evenly-spaced \bar{T} values between 10 and 30 keV. This was then quickly followed by the Greenwald density limit – the a simple relation assumed to apply to all fusion reactors. Through equations, these two were written as:

$$\bar{T} = \text{const.} \quad (3.1)$$

$$\bar{n} = K_n \cdot \frac{I_P}{R_0^2} \quad (2.10)$$

1040 The next variable handled was the steady current:

$$I_P = \frac{K_{BS}\bar{T}}{1 - K_{CD}(\sigma v)} \quad (2.28)$$

1041 As was mentioned then, this only directly depends on temperature, but is strongly af-
 1042 fected by a tokamak's configuration – R_0 and B_0 - through the current drive efficiency
 1043 (η_{CD}). For pulsed reactors, this equation proves too simple as it ignores inductive
 1044 current. To remedy the situation, current balance will be revisited next chapter. The
 1045 main point to make now, though, is that the R_0 and B_0 dependence will be made
 1046 explicit.

1047 Moving on, the remaining equations were the primary and limiting constraints for B_0
 1048 and R_0 , respectively. It was through these relations that a tokamak's configuration
 1049 was brought back into the fold. The choice of solving the two constraints for their
 1050 respective variables was not completely unique – motivated only by the foresight of
 1051 how they fit into the model. Repeated below, they served as the proper vehicles for
 1052 closing the system of equations.

$$B_0 = \left(\frac{G_{PB}}{K_{PB}} \cdot \left(I_P^{\alpha_I^*} R_0^{\alpha_R^*} \right)^{-1} \right)^{\frac{1}{\alpha_B}} \quad (3.28)$$

$$R_0 = \frac{K_{TB}\overline{T}}{B_0} \quad (3.37)$$

$$R_0 = \frac{K_{SF}I_P}{B_0} \quad (3.40)$$

$$R_0 = K_{WL} \cdot I_P^{\frac{2}{3}} \cdot (\sigma v)^{\frac{1}{3}} \quad (3.44)$$

$$R_0 = K_{PC} \cdot I_P^2 \cdot (\sigma v) \quad (3.50)$$

$$R_0 = K_{DH} \cdot I_P \cdot (\sigma v)^{\frac{1}{3.2}} \quad (3.54)$$

1053 The next step now is to learn how to generalize the current formula and design a
 1054 pulsed tokamak reactor (see Chapter 4). After this is done, Chapter 5 will pick up
 1055 where this chapter leaves off – transforming this fusion systems model into a simple
 1056 reactor solver.

1057 Chapter 4

1058 Designing a Pulsed Tokamak

1059 Pulsed tokamaks are the flagship of the European fusion reactor design effort. As such,
1060 this paper's model will now be generalized to accommodate this mode of operation.
1061 Fundamentally, this involves transforming current balance into flux balance – adding
1062 inductive (pulsed) sources to stand alongside the LHCD (steady-state) ones.

1063 The first step in generalizing current balance will be understanding the problem from
1064 a basic electrical engineering perspective – i.e. with circuit analysis. The resulting
1065 equation will then be transformed into the flux balance seen in other models from
1066 the literature. All that will need to be done then is solving the problem for plasma
1067 current (I_P) and simplifying it for various situations – e.g. steady-state operation.

1068 This generalized plasma current will then be found to be a function of the other
1069 dynamic variables (i.e. R_0 , B_0 , and \bar{T}). This, of course, is more difficult to handle
1070 computationally than the steady current, which only directly depended on tempera-
1071 ture (\bar{T}). Discussion about solving this new root solving problem will be the topic of
1072 the next chapter.

1073 4.1 Modeling Plasmas as Circuits

1074 Although it may have been lost along the way, what makes plasmas so interesting and
1075 versatile – in comparison to gases – is their ability to respond to electric and magnetic
1076 fields. It seems natural then to model plasma current from a circuits perspective (i.e.
1077 with resistors, voltage sources, and inductors). By name, this circuit is referred to as
1078 a transformer where: the plasma is the secondary and the yet-to-be discussed central
1079 solenoid (of the tokamak) is the primary.

1080 The first step in deriving a current equation is to determine the circuit equations
1081 that govern pulsed operation in a tokamak. This will be done in two steps. First, we
1082 will draw a circuit diagram and write the equations that describe it. Next, we will
1083 use a simple schematic for how current evolves in a transformer to boil the resulting
1084 differential equations into simple algebraic ones – as is the hallmark of our model.

1085 4.1.1 Drawing the Circuit Diagram

1086 Understanding a circuit always starts with drawing a simple diagram, see Fig. 4-1.
1087 This figure depicts the transformer governing pulsed reactor. The left sub-circuit
1088 is the transformer’s primary – the central solenoid component of the tokamak that
1089 provides most of the inductive current. Whereas, the right sub-circuit is the plasma
1090 acting as the transformer’s secondary. The central solenoid, here, is then a coiled
1091 metal structure that fits within the inner ring of the doughnut. For now, every other
1092 flux source (besides this central solenoid) is neglected.

1093 This is described by the standard circuits involving voltage sources, resistors, and
1094 inductors:

$$V_i = \sum_j^n \frac{d}{dt} (M_{ij} I_j) + I_i R_i , \quad \forall i = 1, 2, \dots, n \quad (4.1)$$

1095 Without going into the inductances (M) and resistances (R), the variable n is the
1096 number of sub-circuits, here being 2. Whereas, the variables i and j are the indices
1097 of sub-circuits (i.e. 1 for the primary, 2 for the secondary). For illustrative purposes,

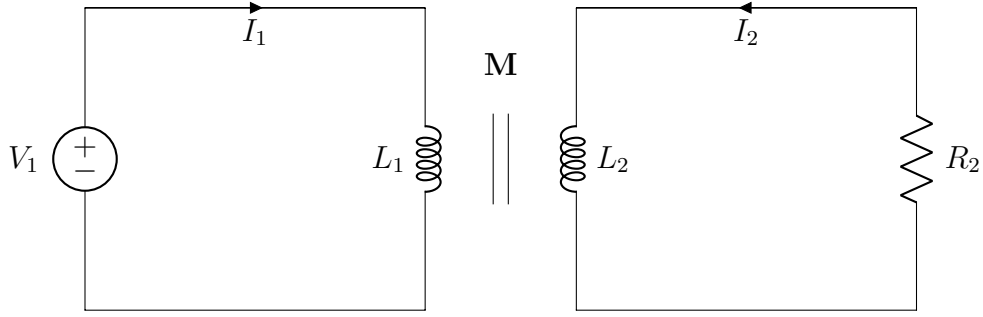


Figure 4-1: A Simple Plasma Transformer Description

A plasma transformer consists of a solenoid primary (left) and a plasma secondary (right). They are connected by their mutual inductance, M . Note that the two currents – I_1 and I_2 – travel in opposite directions.

1098 this would boil down to the following relation for a battery attached to a lightbulb:

$$V = IR \quad (4.2)$$

Back to the transformer diagram, the equations for the two subcircuits can be expanded and greatly simplified. Besides ignoring every inductive source other than the central solenoid, the next powerful assumption is treating the solenoid as a superconductor (i.e. with negligible resistance). Lastly, the inductances between components and themselves are held constant – independent of time. This allows the coupled transformer equations to be written as:

$$V_1 = L_1 \dot{I}_1 - M \dot{I}_2 \quad (4.3)$$

$$-I_2 R_P = L_2 \dot{I}_2 - M \dot{I}_1 \quad (4.4)$$

1099 With I_1 and I_2 going in opposite directions. Note, here, that the subscript on M
 1100 has been dropped, as there are only two components. This was done in conjunction
 1101 to adding internal (self-)inductance terms. Mathematically, the mapping between
 1102 variables is:

$$M = M_{12} = M_{21} \quad (4.5)$$

$$L_1 = M_{11} \tag{4.6}$$

$$L_2 = M_{22} \tag{4.7}$$

1103 Repeated, the one subscript represents the primary – the central solenoid – and the
 1104 two stands for the plasma as the transformer’s secondary. Exact definitions for the
 1105 inductances will be put off till the end of the next subsection.

1106 4.1.2 Plotting Pulse Profiles

1107 Up until now, little has been discussed that has a time dependence. For steady-state
 1108 tokamaks, this did not occur because it is an extreme case where pulses could last
 1109 weeks or months. By definition, though, a pulsed machine has pulses – with around
 1110 ten scheduled per day.³² For this reason, a fusion pulse is now investigated in detail.

1111 Transformer pulses between the central solenoid and the plasma occur on the timescale
 1112 of hours. During this time, a plasma is brought up to some quasi-steady-state current
 1113 (I_P^*) for several hour and then ramped back down using the available flux in the
 1114 solenoid (measured in volt-seconds). For clarity, each pulse is subdivided into four
 1115 phases: ramp-up, flat-top, ramp-down, and dwell. Pictorially represented in Fig. 4-2,
 1116 these divisions allow a simple scheme for transforming the coupled circuit differential
 1117 equations – from Eqs. (4.3) and (4.4) – into simple algebraic formulas.

1118 Along the way, we will approximate derivatives with linear piecewise functions. Using
 1119 t_i to represent the initial time and t_f as the final one, these can be written as:

$$\dot{I} = \frac{I(t_f) - I(t_i)}{t_f - t_i} \tag{4.8}$$

1120 In tabular form, the data from Fig. 4-2 can be written in this piecewise fashion as:

Table 4.1: Piecewise Linear Scheme for Pulsed Operation

(a) Currents			(b) Voltage			
Time	I_1	I_2	Phase	t_i	t_f	V_1
0	$-I_{max}$	0	Ramp-Up	0	t_1	$+V_{max}$
t_1	$-\tilde{I}$	I_P^*	Flattop	t_1	t_2	$+\tilde{V}$
t_2	$+I_{max}$	I_P^*	Ramp-Down	t_2	t_3	$-V_{max}$
t_3	$+\tilde{I}$	0	Dwell	t_3	t_4	$-V_{max}$
t_4	$-I_{max}$	0				

1121 The exact definitions for the plasma's inductive current (I_P^*) and the maximum volt-
 1122 age in the central solenoid (V_{max}) will be put off until the end of the section.

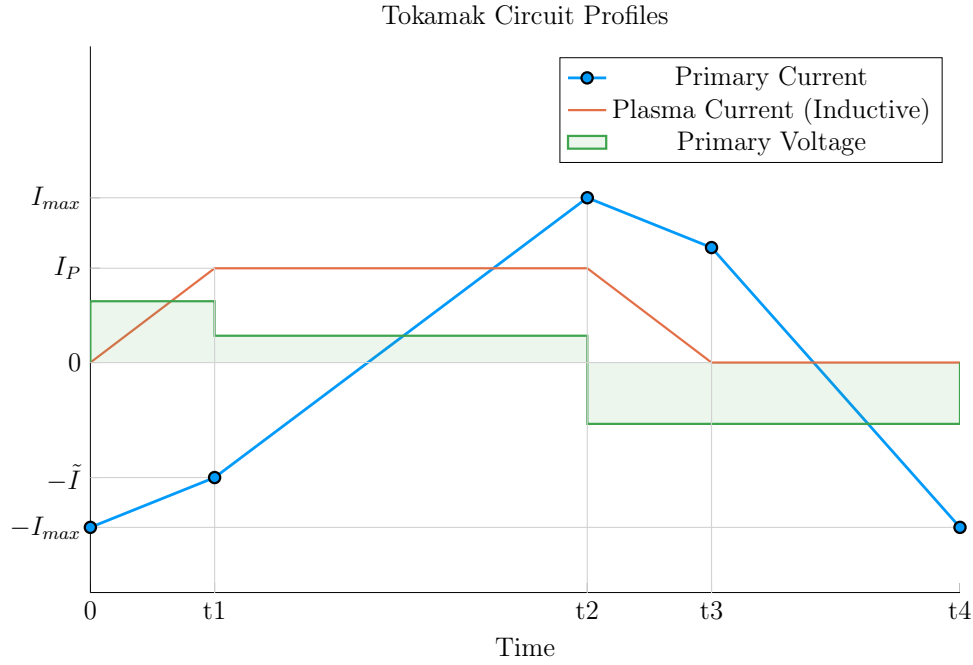


Figure 4-2: Time Evolution of Circuit Profiles

A circuit pulse involves four phases: (1) Ramp-Up, (2) Flattop, (3) Ramp-Down, and (4) Dwell. In reality, flattop can last more than 90% of the pulse.⁸ This makes the slope of the primary current during this phase much shallower than shown.

The first phase in every plasma pulse is the ramp-up. During ramp-up, the central solenoid starts discharging from its fully charged values, as the plasma is brought to its quasi-steady-state current. As this occurs on the timescale of minutes – not hours – resistive effects of the plasma can safely be ignored. This results in the ramp-up equations becoming:

$$V_{max} = \frac{1}{\tau_{RU}} \cdot \left(L_1 \cdot (I_{max} - \tilde{I}) - M \cdot I_{ID} \right) \quad (4.9)$$

$$0 = \frac{1}{\tau_{RU}} \cdot \left(M \cdot (I_{max} - \tilde{I}) - L_2 \cdot I_{ID} \right) \quad (4.10)$$

1124 Simplifying these equations will be done shortly, for now the new terms are what
 1125 is important. The maximum voltage of the solenoid is V_{max} – usually measured in
 1126 kilovolts. Next, I_{max} is the solenoid’s current at the beginning of ramp-up. Whereas
 1127 \tilde{I} is the magnitude of the current once the plasma is at its flattop inductive-drive
 1128 current – I_{ID} . The τ_{RU} quantity, then, is the duration of time it takes to ramp-
 1129 up (i.e. RU). Again, L_1 and L_2 are the microhenry-scale internal inductances of the
 1130 solenoid and plasma, respectively, and M is the mutual inductance between them.

1131 The last step in discussing ramp-up is giving the two important formulas that come
 1132 from it:

$$\tilde{I} = I_{max} - I_{ID} \cdot \left(\frac{L_2}{M} \right) \quad (4.11)$$

1133

$$\tau_{RU} = \frac{I_{ID}}{V_{max}} \cdot \left(\frac{L_1 L_2 - M^2}{M} \right) \quad (4.12)$$

1134

1135 The Flattop Phase – FT

1136 The most important phase in any reactor’s pulse is flattop – the quasi-steady-state
 1137 time when the tokamak is making electricity. Flattops are assumed to last a couple
 1138 of hours for a profitable machine, during which the central solenoid completely dis-
 1139 charges to overcome a plasma’s resistive losses – keeping it in a quasi-steady-state
 1140 mode of operation. In a steady-state reactor, this phases constitutes the entirety of
 1141 the pulse.

Although the resistance cannot be safely neglected for flattop – as it was for ramp-up –
 the plasma’s inductive current (I_{ID}) is assumed constant. This leads to its derivative
 in equations cancelling out! Mathematically,

$$\tilde{V} = \frac{L_1}{\tau_{FT}} \cdot (I_{max} + \tilde{I}) \quad (4.13)$$

$$I_{ID}R_P = \frac{M}{\tau_{FT}} \cdot (I_{max} + \tilde{I}) \quad (4.14)$$

1142 As with ramp-up, the simplifications will be given shortly. The new terms here,
 1143 however, are an intermediate voltage for the central solenoid (\tilde{V}), and the duration
 1144 of the flattop (τ_{FT}). The resistance term was given in Eq. (3.8). Solutions can then
 1145 be found by substituting \tilde{I} – from Eq. (4.11) – into the flattop equations:

$$\tilde{V} = I_{ID}R_P \cdot \left(\frac{L_1}{M} \right) \quad (4.15)$$

1146

$$\tau_{FT} = \frac{I_{max} \cdot 2M - I_{ID} \cdot L_2}{I_{ID}R_P} \quad (4.16)$$

1147

1148 The Ramp-Down Phase – RD

1149 Due to the simplicity – and symmetry – of this model’s reactor pulse, ramp-down is
1150 the exact mirror of ramp-up. It takes the same amount of time and results in the
1151 same algebraic equations. For brevity, this will just be represented as:

$$\tau_{RD} = \tau_{RU} \quad (4.17)$$

1152 For clarity, this is the time when a plasma’s current is brought down from its flattop
1153 value to zero.

1154 The Dwell Phase – DW

1155 Where the first three phases had little ambiguity, the dwell phase changes definition
1156 from model to model. For now, it is assumed to be the time it takes the central
1157 solenoid to reset after a plasma has been completely ramped-down to an off-mode.
1158 To get a more realistic duty factor for cost estimates, it could include an evacuation
1159 time, set to last around thirty minutes. During this evacuation, a plasma is vacuumed
1160 out of a device as it undergoes some inter-pulse maintenance.

1161 Ignoring evacuation for now, the dwell phase involves resetting the central solenoid
1162 when the plasma’s current is negligible. This means the secondary of the transformer
1163 is an open circuit – fundamentally the central solenoid is the only component. In
1164 equation form,

$$V_{max} = \frac{L_1}{\tau_{DW}} \cdot (I_{max} + \tilde{I}) \quad (4.18)$$

1165 Or substituting in \tilde{I} and solving for τ_{DW} ,

$$\tau_{DW} = \frac{L_1}{M} \cdot \frac{(I_{max} \cdot 2M - I_{ID} \cdot L_2)}{V_{max}} \quad (4.19)$$

1166

1167 4.1.3 Specifying Circuit Variables

1168 The goal now is to collect the results from the four phases and introduce the induc-
 1169 tance, resistance, voltage, and current terms relevant to our model. This will motivate
 1170 recasting the problem as flux balance in a reactor – the form commonly used in the
 1171 literature (and discussed next section).

First, collecting the phase durations in one place:

$$\tau_{RU} = \frac{I_{ID}}{V_{max}} \cdot \left(\frac{L_1 L_2 - M^2}{M} \right) \quad (4.12)$$

$$\tau_{FT} = \frac{I_{max} \cdot 2M - I_{ID} \cdot L_2}{I_{ID} R_P} \quad (4.16)$$

$$\tau_{RD} = \tau_{RU} \quad (4.17)$$

$$\tau_{DW} = \frac{L_1}{M} \cdot \frac{(I_{max} \cdot 2M - I_{ID} \cdot L_2)}{V_{max}} \quad (4.19)$$

1172 These can be used in the definition of the duty-factor: the fraction of time a reactor
 1173 is putting electricity on the grid. Formulaically,

$$f_{duty} = \frac{\tau_{FT}}{\tau_{pulse}} \quad (4.20)$$

1174

$$\tau_{pulse} = \tau_{RU} + \tau_{FT} + \tau_{RD} + \tau_{DW} \quad (4.21)$$

1175 As will turn out, the solving of pulsed current actually only involves Eq. (4.16).
 1176 What is interesting about this, is that there is no explicit dependence on ramp-down
 1177 or dwell! Whereas ramp-up passes \tilde{I} to the flattop phase, the other two are just
 1178 involved in calculating the duty factor.

1179 The remainder of this subsection will then be defining the following circuit variables:

1180 I_{ID} , I_{max} , V_{max} , L_1 , L_2 , and M . Again, the resistance was defined last chapter as:

$$R_P = \frac{K_{RP}}{R_0 \bar{T}^{3/2}} \quad (3.8)$$

1181 **The Inductive Current – I_{ID}**

1182 The inductive current is the source of current that separates pulsed from steady-state
1183 operation. Quickly fitting it into the previous definitions of current balance – see
1184 Eq. (3.3):

$$I_{ID} = I_P - (I_{BS} + I_{CD}) \quad (4.22)$$

1185 As before, I_P is the total plasma current in mega-amperes, I_{BS} is the bootstrap current,
1186 and I_{CD} is the current from LHCD (i.e. lower hybrid current drive). For this model,
1187 the relation can be rewritten as:

$$I_{ID} = I_P \cdot \left(1 - K_{CD}(\sigma v)\right) - K_{BS} \bar{T} \quad (4.23)$$

1188

1189 **The Central Solenoid Maximums – V_{max} and I_{max}**

1190 For this simple model, the central solenoid has two maximum values: the voltage and
1191 current. The voltage is the easier to give value. Literature values have this around:⁶

$$V_{max} \approx 5 \text{ kV} \quad (4.24)$$

1192 The maximum current, on the other hand, can be defined through Ampere's Law on
1193 a helically-shaped central solenoid:¹¹

$$I_{max} = \frac{B_{CS} h_{CS}}{N \mu_0} \quad (4.25)$$

Here, B_{CS} is a magnetic field strength the central solenoid is assumed to operate at (i.e. 12 T), h_{CS} is the height of the solenoid, N is the number of loops, and μ_0 has its usual physics meaning (i.e. $40\pi \frac{\mu H}{m}$). As will be seen, the value of N does not directly affect the model, as it cancels out in the final flux balance. The height of the central solenoid will be the focus of an upcoming section on improving tokamak geometry.

The Central Solenoid Inductance – L_1

For a central solenoid with circular cross-sections of finite thickness (d), the inductance can be written as:¹²

$$L_1 = G_{LT} \cdot \left(\frac{\mu_0 \pi N^2}{h_{CS}} \right) \quad (4.26)$$

1203

$$G_{LT} = \frac{R_{CS}^2 + R_{CS} \cdot (R_{CS} + d) + (R_{CS} + d)^2}{3} \quad (4.27)$$

Note that R_{CS} is the inner radius of the central solenoid and $(R_{CS} + d)$ is the outer one. In the limit where d is negligible, this says that the inductance is quadratically dependent on the radius of the central solenoid:

$$\lim_{d \rightarrow 0} G_{LT} = G_{LT}^\dagger = R_{CS}^2 \quad (4.28)$$

The formulas for both R_{CS} and d will be defined in a few sections.

The Plasma Inductance – L_2

The plasma inductance is a composite of several different terms, but overall scales with radius. Through equation,

$$L_2 = K_{LP} R_0 \quad (4.29)$$

1211 This static coefficient – K_{LP} – then combines three inductive behaviors of the plasma.
 1212 The first is its own self inductance (through l_i).⁵ The next is a resistive component
 1213 through the Ejima coefficient, C_{ejima} , which is usually set to $\sim \frac{1}{3}$.⁷ And lastly, a
 1214 geometric component – involving ϵ and κ – is given by the Hirshman-Neilson model.³³
 1215 Mathematically,

$$K_{LP} = \mu_0 \cdot \left(\frac{l_i}{2} + C_{ejima} + \frac{(b_{HN} - a_{HN})(1 - \epsilon)}{(1 - \epsilon) + \kappa d_{HN}} \right) \quad (4.30)$$

Here the HN values come from the 1985 Hirshman-Neilson paper:

$$a_{HN}(\epsilon) = 2.0 + 9.25\sqrt{\epsilon} - 1.21 \epsilon \quad (4.31)$$

$$b_{HN}(\epsilon) = \ln(8/\epsilon) \cdot (1 + 1.81\sqrt{\epsilon} + 2.05 \epsilon) \quad (4.32)$$

$$d_{HN}(\epsilon) = 0.73\sqrt{\epsilon} \cdot (1 + 2\epsilon^4 - 6\epsilon^5 + 3.7\epsilon^6) \quad (4.33)$$

1216 The Mutual Inductance – M

1217 The mutual inductance – M – represents the coupling between the solenoid primary
 1218 and the plasma secondary. A common method for treating this mutual inductance is
 1219 through a coupling coefficient, k, that links the two self-inductances. Formulaically,

$$M = k\sqrt{L_1 L_2} \quad (4.34)$$

1220 The value of the coupling coefficient, k, is always less than (or equal to) 1, but usually
 1221 has a value around one-third. With all the equations defined, we are now at a position
 1222 to explain one of the larger nuances of this fusion systems framework: declaring the
 1223 pulse length of a tokamak.

1224 4.1.4 Constructing the Pulse Length

1225 This subsection focuses on a quantitative estimate for how to select a pulse length.
1226 As no fusion reactor exists in the world today, the writers believe this is an acceptable
1227 calculation. Further, the resulting length of two hours matches the durations of other
1228 studies in the literature.

1229 Starting at the end, our goal is to find the pulse length of a tokamak reactor in
1230 seconds – as dictated by cyclical stress concerns. The first piece of information is
1231 the expected lifetime of the central solenoid, $N \approx 10$ years. The next is the desired
1232 number of pulses the central solenoid will have to last: $M \approx 50,000$ pulses.* This
1233 gives the rough estimate of around 10 pulses a day – or a flattop pulse length of two
1234 hours.

With the pulse length defined, we are now in a position to justify neglecting the duty factor for pulsed reactors in this model. Using expected reactor values – while assuming the central solenoid has around 4000 turns – leads to the following scalings:

$$\tau_{FT} \sim \tau_{pulse} \sim \text{O}(\text{hours}) \quad (4.35)$$

$$\tau_{RU} \sim \tau_{RD} \sim \tau_{DW} \sim \text{O}(\text{mins}) \quad (4.36)$$

1235 As such, even pulsed tokamak reactors should have a duty factor of around unity:

$$f_{duty} \approx 1 \quad (4.37)$$

1236 This analysis of course would change if the central solenoid became an inexpensive
1237 component to replace. For example, if a tokamak had a new one installed annually,
1238 the pulse length could shorten to be on the order of minutes.

1239 Now that all the terms in a pulsed circuit have been explored, we will move on to
1240 rearranging the flattop equation to reproduce flux balance. This will then naturally
1241 lead to a generalized current equation – which is the main result of the chapter.

*This 50,000 pulses is based on the values from the ITER design specifications.³⁴

1242 4.2 Producing Flux Balance

1243 The goal of this section is to arrive at a conservation equation for flux balance that
 1244 mirrors the ones in the literature. The fusion systems model this one attempts to
 1245 follow most is the PROCESS code.⁷ In a manner similar to power balance, flux
 1246 balance can be written as:

$$\sum_{sources} \Phi = \sum_{sinks} \Phi \quad (4.38)$$

1247 4.2.1 Rearranging the Circuit Equation

1248 The way to arrive at flux balance from the circuit equation is to rearrange the flattop
 1249 phase's duration equation:

$$\tau_{FT} = \frac{I_{max} \cdot 2M - I_{ID} \cdot L_2}{I_{ID} R_P} \quad (4.16)$$

1250 Multiplying by the right-hand side's denominator and moving the negative term over
 1251 yields:

$$2MI_{max} = I_{ID} \cdot (L_2 + R_P \tau_{FT}) \quad (4.39)$$

1252 This equation is flux balance, where the left-hand side are the sources (e.g. the central
 1253 solenoid), and the other terms are the sinks (i.e. ramp-up and flattop). The source
 1254 term can currently be encapsulated in:

$\Phi_{CS} = 2MI_{max}$

(4.40)

1255 The sinks, namely the ramp-up inductive losses (Φ_{RU}) and the flattop resistive losses
 1256 (Φ_{FT}), are what drain up the flux. Again, ramp-down and dwell are not included as
 1257 sinks because flux balance only tracks till the end of flattop. They come into play
 1258 when measuring the cost of electricity – through the duty factor from Eq. (4.20).

1259 Relabeling terms, flux balance can now be rewritten as:

$$\Phi_{CS} = \Phi_{RU} + \Phi_{FT} \quad (4.41)$$

1260 With the ramp-up and flattop flux given respectively by:

$$\Phi_{RU} = L_2 \cdot I_{ID} \quad (4.42)$$

1261

$$\Phi_{FT} = (R_P \tau_{FT}) \cdot I_{ID} \quad (4.43)$$

1262

1263 On comparing these quantities to the ones from the PROCESS paper,⁷ Φ_{RU} and Φ_{FT}
 1264 are exactly the same. The source terms, on the other hand, are off for two reasons
 1265 – both related to the central solenoid being the only source term in flux balance.
 1266 This can partially be remedied by adding the second most dominant source of flux
 1267 a posteriori – i.e. the PF coils. The second, and inherently limiting factor, is the
 1268 simplicity of the current model. All that can be shown to this regard is that the Φ_{CS}
 1269 terms does reasonably predict the values from the PROCESS code.⁸

1270 4.2.2 Adding Poloidal Field Coils

1271 Adding the effect of PF coils – belts of current driving plates on the outer edges of
 1272 the tokamak – leads to as much as a 50% improvement^{7,8} over relying solely on the
 1273 central solenoid for flux generation. From the literature, this can be modeled as:¹²

$$\Phi_{PF} = \pi B_V \cdot (R_0^2 - (R_{CS} + d)^2) \quad (4.44)$$

1274 Where again R_{CS} and d are the inner radius and thickness of the central solenoid,
 1275 respectively. These will be the topic of the next section.

1276 Moving forward, the vertical field – B_V – is a magnetic field oriented up-and-down

1277 with the ground. It is needed to prevent a tokamak plasma from drifting radially out
 1278 of the machine. From the literature, the magnitude of this vertical field (valid for a
 1279 circular plasma) is given by:⁷

$$|B_V| = \frac{\mu_0 I_P}{4\pi R_0} \cdot \left(\ln \left(\frac{8}{\epsilon} \right) + \beta_p + \frac{l_i}{2} - \frac{3}{2} \right) \quad (4.45)$$

1280 Analogous to the previously covered plasma beta, the poloidal beta can be represented
 1281 by:³⁵

$$\beta_p = \frac{\bar{p}}{\left(\frac{\bar{B}_p}{2\mu_0} \right)} \quad (4.46)$$

1282 Where the average poloidal magnetic field comes from a simple application of Am-
 1283 pere's law:

$$\bar{B}_p = \frac{\mu_0 I_P}{l_p} \quad (4.47)$$

1284 The variable l_p is then the perimeter of the tokamak's cross-sectional halves:

$$l_p = 2\pi a \cdot \sqrt{g_p} \quad (4.48)$$

1285 Here, g_p is another geometric scaling factor,

$$g_p = \frac{1 + \kappa^2(1 + 2\delta^2 - 1.2\delta^3)}{2} \quad (4.49)$$

1286 After a few lines of algebra, this relation for the magnitude of the vertical magnetic
 1287 field can be written in standardized units as:

$$|B_V| = \left(\frac{1}{10 \cdot R_0} \right) \cdot (K_{VI} I_P + K_{VT} \bar{T}) \quad (4.50)$$

1288

$$K_{VT} = K_n \cdot (\epsilon^2 g_p) \cdot (1 + f_D) \frac{(1 + \nu_n)(1 + \nu_T)}{1 + \nu_n + \nu_T} \quad (4.51)$$

1289

$$K_{VI} = \ln \left(\frac{8}{\epsilon} \right) + \frac{l_i}{2} - \frac{3}{2} \quad (4.52)$$

1290 For clarity, this will be plugged into the new PF coil flux contribution (Φ_{PF}):

$$\Phi_{PF} = \pi B_V \cdot (R_0^2 - (R_{CS} + d)^2) \quad (4.44)$$

1291 Which then gets plugged into a more complete flux balance:

$$\Phi_{CS} + \Phi_{PF} = \Phi_{RU} + \Phi_{FT} \quad (4.53)$$

1292 The R_{CS} and d terms found in Φ_{PF} will now be discussed as they are needed for this
1293 more sophisticated tokamak geometry.

1294 4.3 Improving Tokamak Geometry

1295 From before, this fusion systems model has been said to depend on the major and
1296 minor radius – R_0 and a , respectively – and along the way, various geometric param-
1297 eters have been defined (e.g. ϵ , κ , δ) to describe the geometry further. Now three
1298 more thicknesses will be added: b , c , and d . Additionally, two fundamental dimension
1299 corresponding to the solenoid will be given: the radius (R_{CS}) and height (h_{CS}). These
1300 are the topics of this section.

1301 4.3.1 Defining Central Solenoid Dimensions

1302 The best way to conceptualize tokamak geometry is through cartoon – see Fig. E-2.
1303 What this says is there is a gap at the very center of a tokamak. This gap extends
1304 radially outwards to R_{CS} meters where the coiled central solenoid – of thickness d
1305 – begins. Between the outer edge of the solenoid and the wall of the torus (i.e. the
1306 doughnut) are the blanket and toroidal field (TF) coils.

The blanket and TF coils have thicknesses of b and c , respectively. Before defining b , c , and d , though, it proves fruitful to relate all the quantities in equations for the

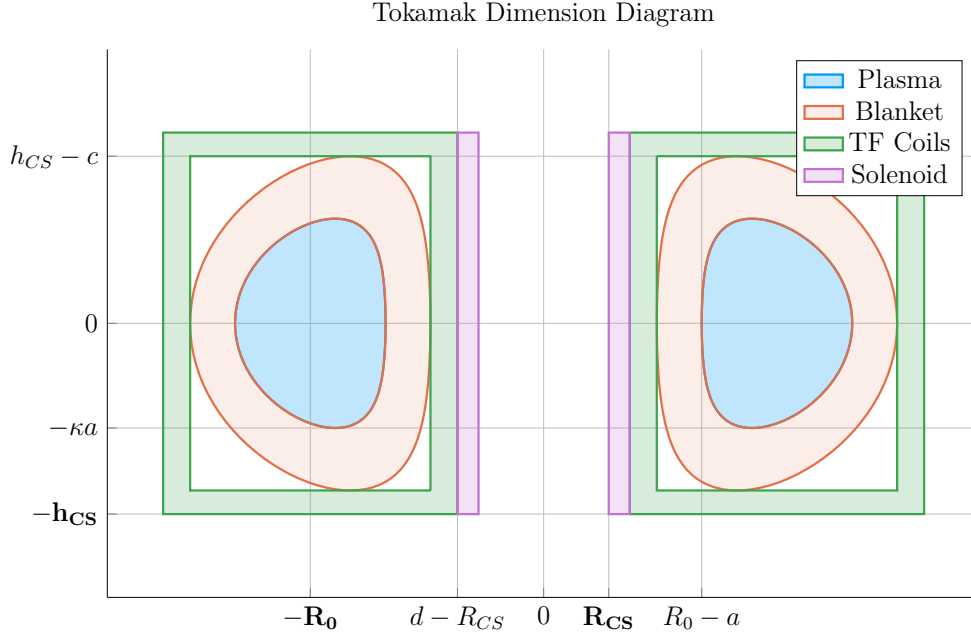


Figure 4-3: Dimensions of Tokamak Cross-Section

Geometrically, a tokamak consists mainly of four components: the plasma, its metallic blanket, the toroidal field magnets surrounding them, and the central solenoid. These have thicknesses of a , b , c and d , respectively. R_{CS} is where the solenoid starts.

inner radius (R_{CS}) and height (h_{CS}) of the central solenoid.

$$R_{CS} = R_0 - (a + b + c + d) \quad (4.54)$$

$$h_{CS} = 2 \cdot (\kappa a + b + c) \quad (4.55)$$

1307 Again, this relation is pictorially represented in Fig. E-2. The next step is defining:
1308 b , c , and d – to close the variable loop.

1309 4.3.2 Calculating Component Thicknesses

1310 In between the inner surface of the central solenoid and the major radius of the
1311 tokamak are four thicknesses: a , b , c , and d . This subsection will go over them
1312 one-by-one.

1313 The Minor Radius – a

1314 The minor radius was the first of these thicknesses we encountered. To calculate it,
1315 we introduced the inverse aspect ratio (ϵ) to relate it to the major radius (R_0):

$$a = \epsilon \cdot R_0 \quad (2.1)$$

1316 The Blanket Thickness – b

1317 The blanket is an area between the TF coils and the torus that is composed mainly of
1318 lithium and steel. It serves to both: protect the superconducting magnet structures
1319 from neutron damage, as well as breed more tritium fuel from stray fusion neutrons.³⁶
1320 In equation form, the blanket thickness is given by:¹³

$$b = 1.23 + 0.074 \ln P_W \quad (4.56)$$

1321 Here, P_W is a correction to account for extra wall loading (as discussed in Sec-
1322 tion 3.4.3).

1323 Moving forward, the remaining two thicknesses – c and d – are handled differently,
1324 estimating structural steel portions as well as magnetic current-carrying ones.

1325 The Toroidal Field Coil Thickness – c

1326 The thickness of the TF coils – c – is a little beyond the scope of this paper. It does,
1327 however, have a form that combines a structural steel component with a magnetic
1328 portion. From a previous model, this can be given as:¹³

$$c = G_{CI}R_0 + G_{CO} \quad (4.57)$$

$$G_{CI} = \frac{B_0^2}{4\mu_0\sigma_{TF}} \cdot \frac{1}{(1 - \epsilon_b)} \cdot \left(\frac{4\epsilon_b}{1 + \epsilon_b} + \ln \left(\frac{1 + \epsilon_b}{1 - \epsilon_b} \right) \right) \quad (4.58)$$

$$G_{CO} = \frac{B_0}{\mu_0 J_{TF}} \cdot \frac{1}{(1 - \epsilon_b)} \quad (4.59)$$

1329 The critical stress – σ_{TF} in G_{CI} implies it depends on the structural component,
 1330 whereas the maximum current density – J_{TF} – implies a magnetic predisposition
 1331 in G_{CO} . The use of G_{\square} in these quantities, instead of K_{\square} is because they include
 1332 the toroidal magnetic field strength – B_0 . For this reason, they are referred to as
 1333 dynamic coefficients. Lastly, the term ϵ_b represents the blanket inverse aspect ratio
 1334 that combines the minor radius with the blanket thickness:

$$\epsilon_b = \frac{a + b}{R_0} \quad (4.60)$$

1335 The Central Solenoid Thickness – d

1336 Finishing this discussion where we started, the central solenoid's thickness – d – has
 1337 a form similar to the TF coil's (i.e. c). In mathematical form, this can be represented
 1338 as:¹³

$$d = K_{DR}R_{CS} + K_{DO} \quad (4.61)$$

1339

$$K_{DR} = \frac{3B_{CS}^2}{6\mu_0\sigma_{CS} - B_{CS}^2} \quad (4.62)$$

1340

$$K_{DO} = \frac{6B_{CS}\sigma_{CS}}{6\mu_0\sigma_{CS} - B_{CS}^2} \cdot \left(\frac{1}{J_{OH}} \right) \quad (4.63)$$

1341 Here, the use of K_{\square} for the coefficients signifies their use as static coefficients. There-
 1342 fore, B_{CS} must be treated as a static variable representing the magnetic field strength
 1343 in the central solenoid. For prospective solenoids using high temperature supercon-
 1344 ducting (HTS) tape, B_{CS} may be around 20 T. The values of σ_{CS} and J_{CS} have similar

meanings to the ones for TF coils. These are collected in a table below with example values representative of our model.

Table 4.2: Example TF Coils and Central Solenoid Critical Values

(a) Stresses [MPa]			(b) Current Densities [MA/m ²]		
Item	Symbol	Limit	Item	Symbol	Limit
Solenoid	σ_{CS}	600	Solenoid	J_{CS}	100
TF Coils	σ_{TF}	600	TF Coils	J_{TF}	200

Before moving on, it seems important to say that although K_{DI} and K_{DO} do not depend on dynamic variables, R_{CS} most definitely does. This is what makes the central solenoid's thickness difficult.

4.3.3 Revisiting Central Solenoid Dimensions

Now that the various thicknesses have been defined (i.e. a , b , c , and d), the equations for the solenoid's dimensions (i.e. R_{CS} and h_{CS}), can now be revisited and simplified. From before,

$$R_{CS} = R_0 - (a + b + c + d) \quad (4.54)$$

$$h_{CS} = 2 \cdot (\kappa a + b + c) \quad (4.55)$$

Utilizing the four thicknesses from before, these can now be expanded to simple formulas. Repeating the thicknesses:

$$a = \epsilon \cdot R_0 \quad (2.1)$$

$$b = 1.23 + 0.074 \ln P_W \quad (4.56)$$

$$c = G_{CI}R_0 + G_{CO} \quad (4.57)$$

$$d = K_{DR}R_{CS} + K_{DO} \quad (4.61)$$

1351 Plugging these into the central solenoid's dimensions results in:

$$h_{CS} = 2 \cdot (R_0 \cdot (\epsilon\kappa + G_{CI}) + (b + G_{CO})) \quad (4.64)$$

1352

$$R_{CS} = \frac{1}{1 + K_{DR}} \cdot (R_0 \cdot (1 - \epsilon - G_{CI}) - (K_{DO} + b + G_{CO})) \quad (4.65)$$

1353

1354 These are the complete central solenoid dimension formulas. To make them more
 1355 tractable to the reader, they will now be simplified one step at a time. (The same
 1356 simplification exercise will be done again after the generalized current is derived later
 1357 this chapter.)

1358 The first simplification to make while estimating central solenoid dimensions is to
 1359 neglect the magnetic current-carrying portions of the central solenoid and TF coils.
 1360 This results in:

$$\lim_{\substack{G_{CO} \rightarrow 0 \\ K_{DO} \rightarrow 0}} h_{CS} = h_{CS}^{\dagger} = 2R_0 \cdot (K_{EK} + \epsilon_b + G_{CI}) \quad (4.66)$$

1361

$$\lim_{\substack{G_{CO} \rightarrow 0 \\ K_{DO} \rightarrow 0}} R_{CS} = R_{CS}^{\dagger} = \frac{R_0}{1 + K_{DR}} \cdot (1 - \epsilon_b - G_{CI}) \quad (4.67)$$

1362 The new static coefficient, here, is:

$$K_{EK} = \epsilon \cdot (\kappa - 1) \quad (4.68)$$

1363 The next simplification is ignoring the TF coil thickness – and thus magnetic field
 1364 dependence – altogether:

$$\lim_{G_{CI} \rightarrow 0} h_{CS}^{\dagger} = h_{CS}^{\ddagger} = 2R_0 \cdot (K_{EK} + \epsilon_b) \quad (4.69)$$

1365

$$\lim_{G_{CI} \rightarrow 0} R_{CS}^{\dagger} = R_{CS}^{\ddagger} = \frac{R_0}{1 + K_{DR}} \cdot (1 - \epsilon_b) \quad (4.70)$$

1366 These oversimplifications will be used later this chapter while simplifying the gener-
 1367 alized current equation to something more tractable. For now, they highlight how the
 1368 dimensions change as different components are neglected. The next step is bringing
 1369 plasma physics back into the flux balance equation and solving for the generalized
 1370 current.

1371 4.4 Piecing Together the Generalized Current

The goal of this section is to quickly expand flux balance using all the defined quantities and then massage it into an equation for plasma current – which is suitable for root solving. This starts with a restatement of flux balance in a reactor:

$$\Phi_{CS} + \Phi_{PF} = \Phi_{RU} + \Phi_{FT} \quad (4.53)$$

$$\Phi_{CS} = 2MI_{max} \quad (4.40)$$

$$\Phi_{PF} = \pi B_V \cdot (R_0^2 - (R_{CS} + d)^2) \quad (4.44)$$

$$\Phi_{RU} = L_2 \cdot I_{ID} \quad (4.42)$$

$$\Phi_{FT} = (R_P \tau_{FT}) \cdot I_{ID} \quad (4.43)$$

The first step is realizing that the central solenoid flux can now be rewritten using the new geometry in a standardized form:

$$\Phi_{CS} = K_{CS} \cdot \sqrt{R_0 G_{LT} h_{CS}} \quad (4.71)$$

$$K_{CS} = 2k B_{CS} \cdot \sqrt{\frac{\pi K_{LP}}{\mu_0}} \quad (4.72)$$

Next, we will slightly simplify the PF coil flux using a dynamic variable coefficient:

$$\Phi_{PF} = G_V \cdot \frac{K_{VI} I_P + K_{VT} \bar{T}}{R_0} \quad (4.73)$$

$$G_V = \frac{\pi}{10} \cdot (R_0^2 - (R_{CS} + d)^2) \quad (4.74)$$

1372 This allows us to rewrite the generalized current as:

$$I_P = \frac{(K_{BS} + G_{IV}/G_{IP}) \cdot \bar{T}}{1 - K_{CD}(\sigma v) - G_{ID}/G_{IP}} \quad (4.75)$$

$$G_{IV} = K_{VT} G_V + K_{CS} R_0^{3/2} \cdot \frac{\sqrt{h_{CS} G_{LT}}}{\bar{T}} \quad (4.76)$$

$$G_{ID} = K_{VI} G_V \quad (4.77)$$

$$G_{IP} = K_{LP} R_0^2 + \frac{K_{RP} \tau_{FT}}{\bar{T}^{3/2}} \quad (4.78)$$

1373 As we will show in the next section, this form not only has a form remarkably similar
1374 to the steady current – it reduces to it in the limit of infinitely long pulses!

1375 4.5 Simplifying the Generalized Current

1376 This section focuses on making various simplifications to the generalized current:

$$I_P = \frac{(K_{BS} + G_{IV}/G_{IP}) \cdot \bar{T}}{1 - K_{CD}(\sigma v) - G_{ID}/G_{IP}} \quad (4.75)$$

1377 As promised, this will start with the trivial simplification of the generalized current
1378 into steady state. Next it will move on to a basic simplification for the purely pulsed
1379 case. These two activities should shed some light on how to interpret the equation in
1380 the more complicated hybrid case.

1381 4.5.1 Recovering the Steady Current

1382 The place to start with the steady current is the dynamic coefficient, G_{IP} :

$$G_{IP} = K_{LP}R_0^2 + \frac{K_{RP}\tau_{FT}}{\bar{T}^{3/2}} \quad (4.78)$$

1383 As can be seen, as $\tau_{FT} \rightarrow \infty$, so does the coefficient,

$$\lim_{\tau_{FT} \rightarrow \infty} G_{IP} = \infty \quad (4.79)$$

1384 Because G_{IU} and G_{ID} remain constant, their contribution to plasma current becomes
1385 insignificant in this limit. Concretely,

$$\lim_{\tau_{FT} \rightarrow \infty} I_P = \frac{K_{BS}\bar{T}}{1 - K_{CD}(\sigma v)} \quad (4.80)$$

1386 This is precisely the steady current given by Eq. (2.28)! The generalized current
1387 automatically works when modeling steady-state tokamaks.*

1388 4.5.2 Extracting the Pulsed Current

1389 For pulsed reactors, we have to resolve a similar problem – except now τ_{FT} is expected
1390 to be a reasonably sized number (i.e. 2 hours).

1391 With an aim at intuition, the reactor is first treated as purely pulsed – having no
1392 current drive assistance:

$$\lim_{\eta_{CD} \rightarrow 0} I_P = \frac{(K_{BS} + G_{IU}/G_{IP}) \cdot \bar{T}}{1 - (G_{ID}/G_{IP})} \quad (4.81)$$

1393 Next, for simplicity-sake, the PF coil contribution to flux balance is assumed negli-

* It should be noted that this is much harder when setting τ_{FT} to a large, but finite number – as η_{CD} still needs to be solved self-consistently.

1394 ble, as it was always just a correction term:

$$\lim_{\Phi_{PF} \ll \Phi_{CS}} G_{IU} = K_{CS} R_0^{3/2} \cdot \frac{\sqrt{h_{CS} G_{LT}}}{\bar{T}} \quad (4.82)$$

1395

$$\lim_{\Phi_{PF} \ll \Phi_{CS}} G_{ID} = 0 \quad (4.83)$$

1396 Piecing this altogether, we can write a new current for this highly simplified case,

$$I_P^\dagger = K_{BS} \bar{T} + \frac{K_{CS} R_0^{3/2} \cdot \sqrt{h_{CS} G_{LT}}}{K_{LP} R_0^2 + K_{RP} \tau_{FT} \bar{T}^{-3/2}} \quad (4.84)$$

1397 As this is not quite simple enough, these previous simplifications will be incorporated:

1398

$$G_{LT}^\dagger = R_{CS}^2 \quad (4.28)$$

1399

$$h_{CS}^\dagger = 2R_0 \cdot (K_{EK} + \epsilon_b) \quad (4.69)$$

1400

$$R_{CS}^\dagger = \frac{R_0}{1 + K_{DR}} \cdot (1 - \epsilon_b) \quad (4.70)$$

1401 Taking these into consideration results in the following current formula:

$$I_P^\dagger = K_{BS} \bar{T} + \left(\frac{K_{CS} R_0^3}{K_{LP} R_0^2 + K_{RP} \tau_{FT} \bar{T}^{-3/2}} \cdot \frac{(1 - \epsilon_b) \cdot \sqrt{2(K_{EK} + \epsilon_b)}}{1 + K_{DR}} \right) \quad (4.85)$$

1402 In the limit that the pulse length drops to zero (and bootstrap current is negligible),

$$\lim_{\tau_{FT} \rightarrow 0} I_P^\dagger = R_0 \cdot \left(\frac{K_{CS}}{K_{LP}} \cdot \frac{(1 - \epsilon_b) \cdot \sqrt{2(K_{EK} + \epsilon_b)}}{1 + K_{DR}} \right) \quad (4.86)$$

1403 This implies that a purely pulsed current scales with major radius to leading order.

1404 4.5.3 Rationalizing the Generalized Current

1405 From the previous two subsections, we arrived at equations for infinitely large and
 1406 infinitely small pulse lengths:

$$\lim_{\tau_{FT} \rightarrow \infty} I_P = \frac{K_{BS} \bar{T}}{1 - K_{CD}(\sigma v)} \quad (4.80)$$

1407

$$\lim_{\tau_{FT} \rightarrow 0} I_P^\dagger = R_0 \cdot \left(\frac{K_{CS}}{K_{LP}} \cdot \frac{(1 - \epsilon_b) \cdot \sqrt{2(K_{EK} + \epsilon_b)}}{1 + K_{DR}} \right) \quad (4.86)$$

1408 What these imply at an intuitive level is that at small pulses, current scales with the
 1409 major radius. While for long pulses, current scales with plasma temperature. In the
 1410 general case, of course, the problem becomes much harder to predict. – as shown by
 1411 the code’s results using Eq. (4.75).

1412 Chapter 5

1413 Completing the Systems Model

1414 As opposed to previous chapters, this one will focus on the numerics behind the
1415 fusion systems model. A simple algebra will lead to a generalized solver for exploring
1416 reactor space for low cost and interesting machines. This will then naturally segue
1417 into a discussion of how plots are made and should be interpreted. The remaining
1418 chapters will then decouple the presentation of results from their analytic conclusions.

1419 5.1 Describing a Simple Algebra

1420 In essence, the systems model used here is a simple algebra problem – given five
1421 equations, solve for five unknowns. The goal is then to pick the five equations that
1422 best represent modern fusion reactor design (as shown in Fig. 5-1). This selection
1423 should also be done in such a way that actually reduces the system of equations to a
1424 simple univariate root solving equation (i.e. one equation with one unknown). As will
1425 be shown in the results, this model does reasonably well: matching other modeling
1426 campaigns in seconds.

1427 The logical place to start in a discussion of this algebra problem is with the three equa-
1428 tions fundamental to all reactor-grade tokamaks – both in steady-state and pulsed
1429 operation. These are: the Greenwald density limit, power balance, and current bal-

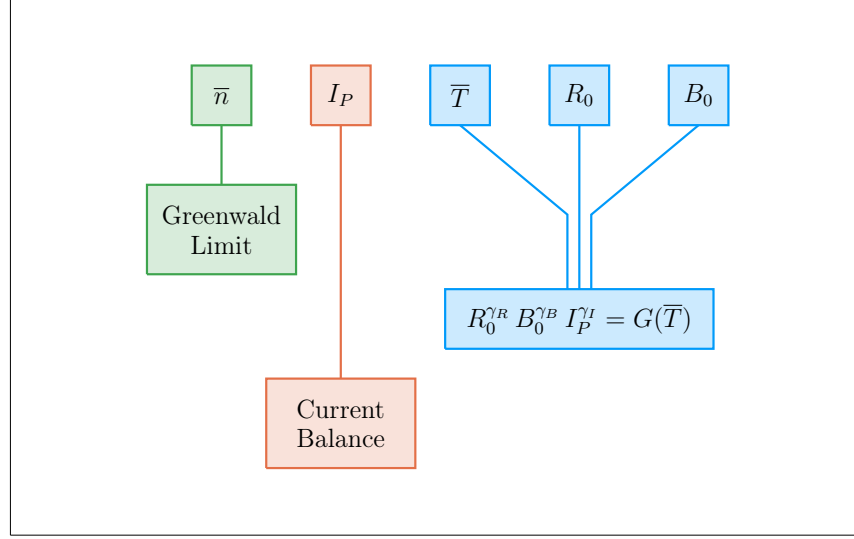


Figure 5-1: Equation Selection for Fusion System

This systems model selects five variables to solve for all the dynamic variables. These are the Greenwald limit for density, current balance for the plasma current, and three generalized formulas for the temperature, major radius, and toroidal field strength.

1430 ance. The Greenwald density's importance was hinted early on when it was used to
1431 simplify every equation derived thereafter.

$$\bar{n} = K_n \cdot \frac{I_P}{R_0^2} \quad (2.10)$$

1432 The two balance equations proved to be slightly more complicated. As was shown,
1433 current balance was the more difficult of the two – bringing forth the notion of self-
1434 consistency for steady-state machines and a highly-coupled multi-root equation for
1435 pulsed ones. As such, current balance stands as the equation everything is substituted
1436 into to do a final univariate root solve.

$$I_P = \frac{(K_{BS} + G_{IV}/G_{IP}) \cdot \bar{T}}{1 - K_{CD}(\sigma v) - G_{ID}/G_{IP}} \quad (4.75)$$

1437 Although slightly buried in Eq. (4.75), the right-hand side actually depends on all the
1438 quantities (including I_P through the wall loading term in blanket thickness). Through
1439 equation,

$$I_P = f(I_P, \bar{T}, R_0, B_0) \quad (5.1)$$

1440 The remaining equation common to all reactor-grade tokamaks is power balance –
 1441 the relation that quantifies its net electricity production capabilities. Due to the use
 1442 of the ELMy H-Mode scaling law for modeling the diffusion coefficient, this had the
 1443 complicated form of:

$$R_0^{\alpha_R} \cdot B_0^{\alpha_B} \cdot I_P^{\alpha_I} = \frac{G_{PB}}{K_{PB}} \quad (5.2)$$

1444 Although being rather cumbersome, this equation actually remains relatively simple
 1445 in that all three quantities on the left-hand side are separable. To close the system,
 1446 two more equations of this form are needed. These have the following form and will
 1447 be described next.

$$R_0^{\gamma_R} \cdot B_0^{\gamma_B} \cdot I_P^{\gamma_I} = G(\overline{T}) \quad (5.3)$$

1448

1449 5.2 Generalizing Previous Equations

1450 Where the equations defined up to this point in the chapter are shared among all
 1451 fusion reactors, the remaining two equations – needed to close the system – must
 1452 be partially chosen by the user. These equations come in three varieties: limits,
 1453 intermediate quantities, and dynamic variables. By convention, we enforce that at
 1454 least one limit must be used. The other constraint can then come from any of the
 1455 three defined collections, which we will refer to as the closure equation.

1456 5.2.1 Including Limiting Constraints

1457 The limits category is composed of the limiting constraints given in Chapter 3. These
 1458 include the physics derived limits from MHD theory – i.e. the beta limit (β_N) and
 1459 the kink safety factor (q_*) – which for clarity, set maximums on the allowed plasma
 1460 pressure and current, respectively. Additionally, there were several engineering limits
 1461 also described: wall loading, heat loading, and maximum power capacity. For this
 1462 paper, wall loading from neutrons (P_W) is assumed to be important, whereas the

1463 other two engineering limits are not allowed to explicitly guide designs.

1464 Combined all these limits, as well as the yet to be defined dynamic and intermediate
1465 equations, are given in Table 5.1. These share a remarkably similar form to power
1466 balance when put into a generalized, separable state. This hints at why the major
1467 radius (R_0), the toroidal field strength (B_0), and the plasma current (I_P) can easily
1468 be separated and substituted out of the current balance equation.

1469 Before moving on, it proves useful to explain the two limits not used to explicitly guide
1470 reactor design – divertor heat loading and the maximum power capacity. The simpler

Table 5.1: Main Equation Bank

To close the system of equations for potential reactors, different equations can be used to lock down tokamak designs. These include physics and engineering limits (L), as well as ways to set dynamic (D) or intermediate (I) variables to constant values.

Variable	Category	$G(\bar{T})$	γ_R	γ_B	γ_I
Power Balance	-	G_{PB}/K_{PB}	α_R^*	α_B	α_I^*
Beta (β_N)	L	$K_{TB}\bar{T}$	1	1	0
Kink (q_*)	L	K_{KF}	1	1	-1
Wall Loading (P_W)	L	$K_{WL}(\sigma v)^{1/3}$	1	0	$-2/3$
Power Cap (P_E)	L	$K_{PC}(\sigma v)$	1	0	-2
Heat Loading (q_{DV})	L	$K_{DV}(\sigma v)^{1/3.2}$	1	0	-1
Major Radius (R_0)	D	$(R_0)_{const}$	1	0	0
Magnet Strength (B_0)	D	$(B_0)_{const}$	0	1	0
Plasma Current (I_P)	D	$(I_P)_{const}$	0	0	1
Plasma Temperature (\bar{T})	D	$(\bar{T})_{const}/\bar{T}$	0	0	0
Electron Density (\bar{n})	D	$(\bar{n})_{const}/K_n$	-2	0	1
Plasma Pressure (\bar{p})	I	$(\bar{p})_{const}/K_n K_{nT} \bar{T}$	-2	0	1
Bootstrap Current (f_{BS})	I	$(f_{BS})_{const}/K_{BS} \bar{T}$	0	0	-1
Fusion Power (P_F)	I	$(P_F)_{const}/K_F K_n^2(\sigma v)$	-1	0	2
Magnetic Energy (W_M)	I	$(W_M)_{const}/K_{WM}$	3	2	0
Cost-per-Watt (C_W)	I	$(C_W)_{const} \cdot (K_F K_n^2(\sigma v)/K_{WM})$	4	2	-2

1471 of the two to reason is the heat loading limit. Although removing the gigawatts-per-
 1472 square-meter of heat is extremely difficult, it remains an unsolved problem worthy of
 1473 its own research machine.³¹ As such, it is only kept to provide a human-interpreted
 1474 measure of difficulty. The power cap, on the other hand, is just handled informally.
 1475 If a reactor surpasses it (i.e. $P_E > 4000MW$), it is considered invalid.

1476 While the maximum power cap informally sets a maximum major radius for a ma-
 1477 chine, there also exists an implicit minimum major radius. This minimum occurs due
 1478 to the hole-size constraint – i.e. at some point there is no longer enough room on the
 1479 inside of the machine to store the central solenoid, blanket, and TF coils.

1480 At this point, we can now explain how various quantities in the systems model can
 1481 be set to user-given constant values. This basically allows users to treat one dynamic
 1482 variable as a static one (e.g. the temperature and bootstrap fraction).

1483 5.2.2 Minimizing Intermediate Quantities

1484 Whereas the limits from the previous section represented constraints with real physics
 1485 and engineering repercussions, the intermediate quantities here are just used to find
 1486 when reactors reach certain user-supplied values. Most notable are the capital cost
 1487 (through the magnetic energy – W_M) and the cost-per-watt (C_W). The model also,
 1488 however, allows easily setting values for the bootstrap fraction, plasma pressure, and
 1489 fusion power. As mentioned previously, they are given in Table 5.1 through a gener-
 1490 alized representation of the form:

$$R_0^{\gamma_R} \cdot B_0^{\gamma_B} \cdot I_P^{\gamma_I} = G(\bar{T}) \quad (5.3)$$

1491 What this collection of variables is really useful for, though, is finding minimum cost
 1492 reactors – both in a capital context as well as a cost-per-watt one. This is done in
 1493 a three stage process. The first of which is to find a valid reactor – i.e. one that
 1494 satisfies every limiting constraint. Practically, this is done by searching over a range
 1495 of scanned temperatures.

1496 After a valid reactor is found, its cost is recorded leading to a drill-down stage. In
 1497 this step, the cost is continuously halved until a valid reactor cannot be found. Once
 1498 this invalid reactor is reached, it sets a bound on the minimum cost reactor. As such,
 1499 the final stage is a simple bisection step where the minimum cost is honed down to
 1500 some acceptable margin of error – see Fig. 5-2.

1501 5.2.3 Pinning Dynamic Variables

1502 The remaining collection of closure equations is for the five dynamic variables in the
 1503 systems model: R_0 , B_0 , \bar{n} , \bar{T} , and I_P . As we are making equations of the following
 1504 form, the formulas for R_0 , B_0 , and I_P are trivial.

$$R_0^{\gamma_R} \cdot B_0^{\gamma_B} \cdot I_P^{\gamma_I} = G(\bar{T}) \quad (5.3)$$

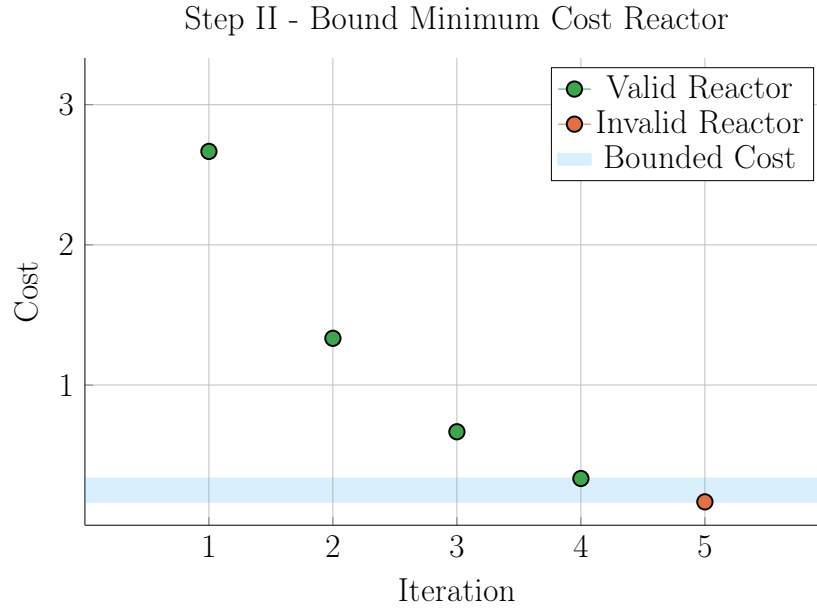
1505 Next, the equation for \bar{n} – shown in Table 5.1 – is just a simple undoing of the Green-
 1506 wald density limit. The remaining equation is then from the original temperature
 1507 equation:

$$\bar{T} = \text{const.} \quad (3.1)$$

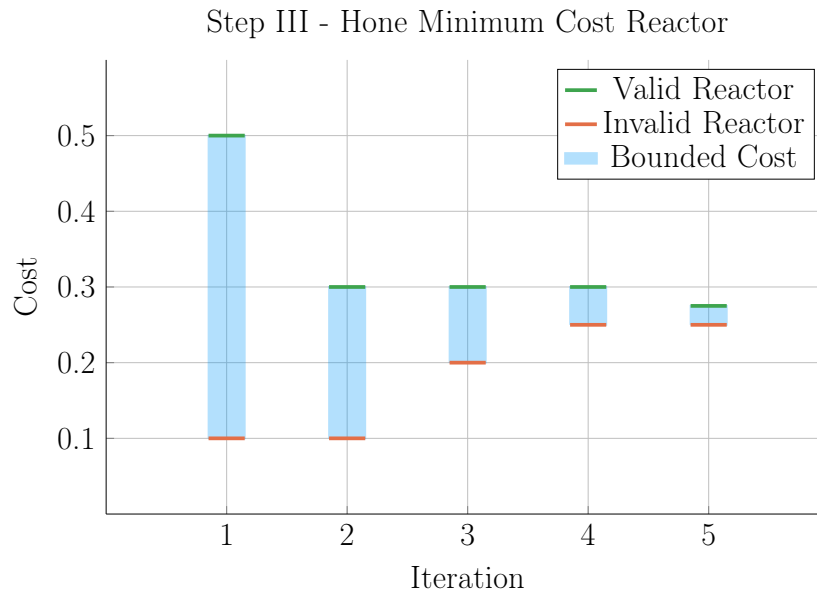
1508 As was assumed earlier, this is sort of a default equation for the systems model. By
 1509 this, we mean reactor curves can be created by scanning over temperatures, i.e. set
 1510 $\bar{T} = 5$ keV in one run, 10 in the next, etc. This temperature equation also brings
 1511 up a difficulty for the algebraic solver, as it does not depend on: current, radius, or
 1512 magnet strength. Overcoming this difficulty is discussed next subsection.

1513 5.2.4 Detailing the Equation Solver

1514 The algorithm that motivated this generalized equation approach most notably bi-
 1515 furcates in the situation where the closure equation does not depend on R_0 , B_0 , or I_P
 1516 (i.e. for the temperature equation). The two scenarios are given in Eqs. (5.4) to (5.10)
 1517 – where at least R_0 and B_0 are substituted out of the system. In the temperature



(a) Minimize Step II



(b) Minimize Step III

Figure 5-2: Minimize Cost Step II/III – Optimize Reactor

After a valid reactor has been found, it is a simple process to find the minimum cost reactor. This involves first continually searching for reactors that are half the cost until a valid one can no longer be found. After the costing interval has been bounded by a valid and invalid reactor, the interval is bisected until there is negligible error.

1518 case, I_P is not needed to be explicitly removed.

1519 Concretely, the root solve for the temperature scenario is for the current, whereas it
 1520 is for the temperature in all other cases. The nomenclature in the code is a *match*
 1521 for Scenario I (i.e. root solving for plasma temperature), and a *solve* for Scenario II
 1522 (i.e. root solving for plasma current).

1523 Scenario I – Match for \bar{T}

$$R_0(\bar{T}) = \left(G_1^{(\gamma_{B,2} \gamma_{I,3} - \gamma_{B,3} \gamma_{I,2})} \cdot G_2^{(\gamma_{B,3} \gamma_{I,1} - \gamma_{B,1} \gamma_{I,3})} \cdot G_3^{(\gamma_{B,1} \gamma_{I,2} - \gamma_{B,2} \gamma_{I,1})} \right)^{\frac{1}{\gamma_{RBI}}} \quad (5.4)$$

$$B_0(\bar{T}) = \left(G_1^{(\gamma_{I,2} \gamma_{R,3} - \gamma_{I,3} \gamma_{R,2})} \cdot G_2^{(\gamma_{I,3} \gamma_{R,1} - \gamma_{I,1} \gamma_{R,3})} \cdot G_3^{(\gamma_{I,1} \gamma_{R,2} - \gamma_{I,2} \gamma_{R,1})} \right)^{\frac{1}{\gamma_{RBI}}} \quad (5.5)$$

$$I_P(\bar{T}) = \left(G_1^{(\gamma_{R,2} \gamma_{B,3} - \gamma_{R,3} \gamma_{B,2})} \cdot G_2^{(\gamma_{R,3} \gamma_{B,1} - \gamma_{R,1} \gamma_{B,3})} \cdot G_3^{(\gamma_{R,1} \gamma_{B,2} - \gamma_{R,2} \gamma_{B,1})} \right)^{\frac{1}{\gamma_{RBI}}} \quad (5.6)$$

$$\gamma_{RBI} = (\gamma_{R,1} \gamma_{B,2} \gamma_{I,3} + \gamma_{R,2} \gamma_{B,3} \gamma_{I,1} + \gamma_{R,3} \gamma_{B,1} \gamma_{I,2}) - \quad (5.7)$$

$$(\gamma_{R,1} \gamma_{B,3} \gamma_{I,2} + \gamma_{R,2} \gamma_{B,1} \gamma_{I,3} + \gamma_{R,3} \gamma_{B,2} \gamma_{I,1})$$

1524 Scenario II – Solve for I_P

$$R_0(\bar{T}) = \left(G_1^{\gamma_{B,2}} \cdot G_2^{-\gamma_{B,1}} \cdot I_P^{(\gamma_{B,1} \gamma_{I,2} - \gamma_{B,2} \gamma_{I,1})} \right)^{\frac{1}{\gamma_{RBT}}} \quad (5.8)$$

$$B_0(\bar{T}) = \left(G_1^{-\gamma_{R,2}} \cdot G_2^{\gamma_{R,1}} \cdot I_P^{(\gamma_{I,1} \gamma_{R,2} - \gamma_{I,2} \gamma_{R,1})} \right)^{\frac{1}{\gamma_{RBT}}} \quad (5.9)$$

1525

$$\gamma_{RBT} = \gamma_{R,1} \gamma_{B,2} - \gamma_{R,2} \gamma_{B,1} \quad (5.10)$$

1526

1527 5.3 Wrapping up the Logic

1528 As stated at the beginning of the chapter, this systems model basically reduces to a
1529 simple 5 equation/5 unknown algebra problem. The Greenwald density was implicitly
1530 used in the initial derive to simplify the logic. The current balance was then delegated
1531 to be the root solve equation. Lastly, three equations were needed to remove the major
1532 radius and magnet strength, as well as either the current or temperature. These 16
1533 equations were given in Table 5.1 with the generalized solution given in Eqs. (5.4)
1534 to (5.10).

1535 This now sets the stage for the most interesting part of the document – the results.
1536 These will come in several forms. The first result type will be temperature scans
1537 that allow us to validate the model against other designs from the literature. These
1538 are created using the Scenario II solver.

1539 The Scenario I matcher will then be used to create sensitivity studies and Monte
1540 Carlo samplings. The simple one variable sensitivities will reveal local trends from
1541 sweeping various static (i.e. input) variables – namely H , κ , B_{CS} , etc. – one at a time.
1542 Whereas the samplings will highlight global trends as many static/input variables are
1543 allowed to vary simultaneously.

1544 These Scenario I matchers are further subdivided in regards to the nature of their
1545 closure equation. The first type comes from finding so called two limit solutions,
1546 which live at the point where the beta and kink (or wall) limits are just marginally
1547 satisfied. The second main type is then minimum cost reactors – measured in either
1548 a capital cost or cost-per-watt context. These will be used in depth next chapter.

1549 Chapter 6

1550 Presenting the Code Results

1551 Now that our fusion systems model has been formulated and completed, the next
1552 logical step is to build a codebase and explore reactor space. To this, the code
1553 encompassing this document’s model – Fussy.jl – is available at git.io/tokamak (with
1554 a short guide given in Appendix B). The results from this chapter will be divided into
1555 three sections. The first is an attempt to test how accurate the model is by comparing
1556 it with other codes in the field.^{1,6,7} The next will be two prototypes developed to
1557 fairly compare pulsed and steady state reactors, the initial motivation for this project.

1558 This chapter will then conclude with a discussion on how best to lower reactor costs.
1559 In line with the MIT mission, this will highlight how using stronger magnets leads
1560 to more compact, economic machines. The new piece of insight, then, is how to
1561 optimally incorporate high-temperature superconducting (HTS) tape technology –
1562 the assumed technological advancement found in the ARC design family.

1563 Succinctly, we will show that HTS tape should be used in the TF coils for steady-state
1564 tokamaks (i.e. B_0), whereas it should only be appear in the central solenoid (i.e. B_{CS})
1565 for pulsed ones. This is a fundamentally new result!

1566 6.1 Testing the Code against other Models

1567 After developing a new model, the first next step is to make sure its results are sensical.
1568 The goal, however, is to not go too far, i.e. by: comparing it with too many models
1569 or requiring perfect matches with their results. To this, we will compare Fussy.jl with
1570 five designs from the literature – hopefully casting a wide enough net through reactor-
1571 space to prove sufficient. It should be noted that for how simple this model is, it does
1572 a remarkable job matching the other group’s more sophisticated frameworks. It also
1573 highlights how discrepancies arise in this highly non-linear computational problem.

1574 The first reactor design that will provide a basis for comparison is the ARC reactor.⁶
1575 As it was also designed by MIT researchers, the fit is shown to be almost exact. This
1576 of course probably involves a fair amount of inherent biases stemming from shared
1577 scientific philosophies and knowledge base.

1578 The next set of reactor designs come from the ARIES four-act study.³ This ARIES
1579 team is a United States effort to reevaluate the problem of designing a fusion reactor
1580 around once a decade. The most recent study focused on how tokamaks would look as
1581 you assume optimistic and conservative values for physics and engineering parameters.
1582 Although our model recovers their results, it does highlight one peculiarity of their
1583 algorithm – reliance on the minimum achievable value of H .

1584 The final series of reactors comes from the major codebase used among European
1585 fusion systems experts: PROCESS.⁷ As such, this group actually gives an example for
1586 pulsed vs. steady-state tokamaks. Although these designs have the most discrepancies
1587 with our model, discussion will be given that remedy some of the shortcomings. These
1588 basically amount to: alternative definitions for heat loss appearing in the ELMy H-
1589 Mode Scaling, as well as the simplified nature of our flux balance equation – which
1590 only accounts for central solenoid and PF coil source terms.

1591 The most important detail to take from the comparisons done in Tables 6.1 to 6.4,
1592 however, is that each steady state design from the literature has H factors and Green-
1593 wald densities (N_G) that violate standard values (i.e. 1.0). What this means, prac-

1594 tically, is steady-state reactors are not possible in the current tokamak paradigm –
1595 some technological advancement is needed.

1596 6.1.1 Comparing with the PSFC ARC Reactor

1597 As mentioned, this model matches the results from the ARC design almost perfectly –
1598 see Table 6.1 and Fig. 6-2. This probably stems from how both models were developed
1599 within the MIT community. Two notable discrepancies between the models, however,
1600 are in the fusion power (P_F) and bootstrap current fraction (f_{BS}). These discrepancies
1601 likely arise from the use of simple parabolic profiles for temperature and, thus, can
1602 be seen in the subsequent model comparisons.

1603 Before moving on, though, it is important to explain how the plots and table used
1604 for this comparison are made. First, a list of temperatures between 1 and 40 keV is
1605 scanned to produce a set of reactors – each with their own size (R_0), magnet strength
1606 (B_0), etc. These reactors are then turned into the two curves shown in Fig. 6-2 by
1607 mapping to their respective values. Note that R_0 vs. B_0 is then a measure of the
1608 accuracy in the tokamak’s engineering, while I_P vs \bar{T} is a measure on its plasma’s
1609 physics.

1610 Once these curves are created, a design point is chosen on them that has the least
1611 distance to the marked point (from the original model’s paper). These two points – or
1612 reactors – are then compared in detail in Table 6.1. Note that the input variables are
1613 shared between the original model and this model’s input file. The output between
1614 the two is what is different. For clarity, V is the volume of a tokamak in cubic
1615 meters, and the dash on the inductive current fraction f_{ID} implies it makes up 0% of
1616 the current.

1617 The use of a dash for β_N brings up the final piece of information needed to understand
1618 the plots and table creation process – limiting constraints. Note that in Fig. 6-2, the
1619 solid curve has two portions: **beta** and **wall**. These are the portions where the beta
1620 limit and the wall loading limit are the driving constraints, respectively. For example

1621 at $B_0 = 5\text{T}$, the wall loading (P_W) will be much less than the maximum allowed
1622 2.5 MW/m^2 . This is why the dash is next to β_N in Table 6.1, as it is held at the
1623 maximum allowed value (i.e. $\beta_N = 0.026$.)

1624 Finally, the reason there is a dashed **pulsed** curve and a solid **steady** one is because
1625 this reactor was run in both modes of operation. The pulsed label is actually a
1626 slight misnomer as it implies the generalized current balance formula is used (over
1627 the simple steady current from Eq. (2.28)). Because pulses are set to 50 years, they
1628 are functionally steady-state regardless. The real reason the two curves diverge is
1629 because the steady current has a self-consistent current drive efficiency (η_{CD}).

1630 **6.1.2 Contrasting with the ARIES ACT Studies**

1631 Moving on, the ARIES ACT study focuses on how steady-state reactors would look
1632 under both a conservative and optimistic perspective. This is highlighted in Fig. 6-1,
1633 which shows how costs decreases as the H factor is allowed to increase. Notice that
1634 for every value of H, the ACT I study (i.e. the optimistic act) has a lower cost than
1635 the design from ACT II (i.e. the conservative one).

1636 This figure also highlights another peculiarity of the ARIES study – a reliance on the
1637 minimum possible value of H. Note that just left of the reactor point on both plots
1638 is a highly erratic portion of the curve. As such, if even a slightly smaller value of H
1639 were used in either case, a quite distinct reactor would occur. This is not a robust
1640 way to design machines. A better approach would be to build with some safety factor
1641 – i.e at a slightly more optimistic value of H. This can be seen in ARC’s H-Sweep.

1642 **ACT I – Advanced Physics and Engineering**

1643 ACT 1 is the ARIES study that assumes advanced physics and engineering design
1644 parameters. Although this paper’s model does a fair job recovering the results from
1645 their paper – see Table 6.2 and Fig. 6-3 – it does show what optimistic design really
1646 means. As can be seen, this design actually only surpasses the minimum possible

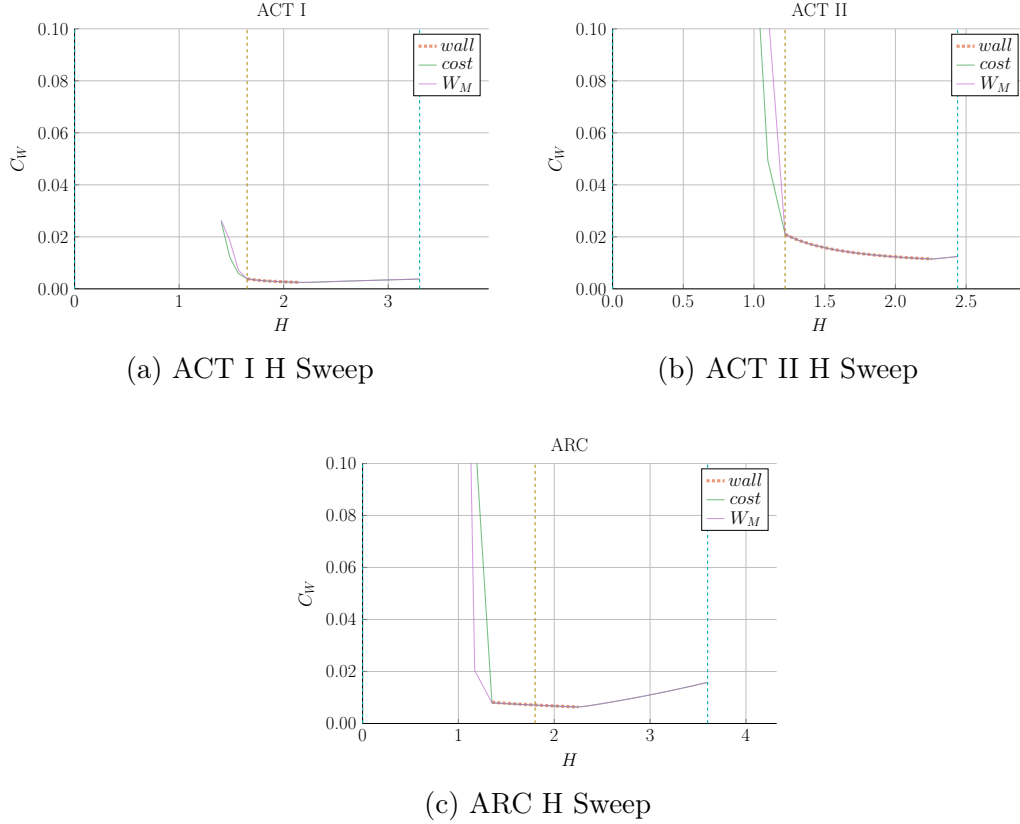


Figure 6-1: ARC and ACT Studies Cost Dependence on the H Factor

The cost of steady-state reactors can usually be reduced by increasing the enhancement factor. As shown, though, none of these reactors are possible at the standard $H = 1$ value!

1647 toroidal field strength by as less than a Tesla! Practically, this means their reactor
 1648 is barely realizable. Trying to build a 5T device would not be possible using their
 1649 stated reactor input parameters.

1650 ACT II – Conservative Physics and Engineering

1651 ARIES more conservative design – ACT II – is much more like ARC in nature. From
 1652 Fig. 6-4, it is obvious the paper’s model is basically right on top of the reactor curve
 1653 made using Fussy.jl. Much like ARC, too, it shows how the model overestimates fusion
 1654 power and underestimates bootstrap fraction due to their selection of a pedestal profile
 1655 for plasma temperature. This can be seen in Table 6.3.

1656 6.1.3 Benchmarking with the Process DEMO Designs

1657 The PROCESS team’s prospective designs for successors to ITER constitute the final
1658 set of model comparisons: the steady-state and pulsed DEMO reactors. As this paper
1659 is designed to compare these modes of operation, this study proves most informative.
1660 It also highlights how common model decisions can dramatically alter what reactors
1661 come out of the solvers.

1662 The first discrepancy is how the PROCESS team defines the loss term in the ELMy H-
1663 Mode scaling law. As shown in their paper, they actually subtract out a Bremsstrahlung
1664 component, while leaving the fitting coefficients the same.⁷ After modifying Fussy.jl
1665 to incorporate this definition, the steady-state reactor is easily reproducible in $R_0 -$
1666 B_0 slice of reactor space.

$$P_L^{DEMO} = P_{src} - P_{BR} \quad (6.1)$$

1667 Unlike the steady-state case, however, the modified power loss term does not fix the
1668 pulsed case, as it actually draws the reactor curves further from the design in their
1669 paper. As such, it is flux balance that is now the main culprit for discrepancies
1670 between the two models. This makes sense, as this model uses highly simplified
1671 source terms – namely neglecting anything but the central solenoid and PF coils (as
1672 well as ignoring crucial physics for these two components). Even acknowledging the
1673 differences between the two models, Fussy.jl still does reasonably well at reproducing
1674 their much more sophisticated coding framework.

1675 The final point to make is about selecting optimum points to build as the dynamic
1676 variables are allowed to make curves through reactor space. Up to this point, only
1677 steady-state tokamak designs have been explored. In every single one of these, though,
1678 the paper values have been very close to the point where the beta curves and wall
1679 loading curves cross. This is because they all result in the minimum cost-per-watt.

1680 For pulsed designs, on the other hand, kink curves start to appear for low magnetic
1681 field strengths. Just as beta-wall intersections were optimum places to design for low
1682 cost-per-watt (C_W) reactors, these beta-kink intersections will prove to be the place

1683 where minimum capital cost (W_M) reactors usually occur. This is discussed in more
1684 detail in Section 6.3.1.

1685 DEMO Steady – A Steady-State ITER Successor

1686 As shown in Fig. 6-5 and Table 6.4, the DEMO steady reactor is the design captured
1687 worst by the Fussy.jl model. Some discrepancy, however can be removed by using
1688 the PROCESS team’s modified version of heat loss, as given by Eq. (6.1).⁷ Although
1689 not supported by the official ITER database fit,³⁷ the PROCESS team reduces the
1690 absorbed power by the Bremsstrahlung power³⁸ – which can lengthen τ_E by more
1691 than 25%.⁸

1692 With this correction, the $R_0 - B_0$ curve is drawn to be right on top of their model’s
1693 design. The same cannot be said for the $I_P - \bar{T}$ curve as steady current was shown to
1694 have little dependence on tokamak configuration (R_0 and B_0) and, correspondingly,
1695 the limiting constraint (e.g. `beta` and `wall`).

1696 Note that the labels of `modified` and `pulsed` are slightly obscure in this context.
1697 Pulsed, for starters, is actually the generalized solver that does not rely on self-
1698 consistent current drive (i.e. in η_{CD}). The modified label is then when the pulsed
1699 solver uses the P_L^{DEMO} value in approximating heat conductive losses.

1700 DEMO Pulsed – A Pulsed ITER Successor

1701 This pulsed version of DEMO is the only reactor in our collection that is not run in
1702 steady-state. As such, it may be the most important one (i.e. it is the only pulsed
1703 reactor). The first observation from Fig. 6-6 is that this design actually has no valid
1704 wall loading portion – only a kink and beta curve exist! Even so, the results match
1705 pretty well (see Table 6.5). It should be noted, though, that this current drive is
1706 treated as an input and not solved self-consistently.

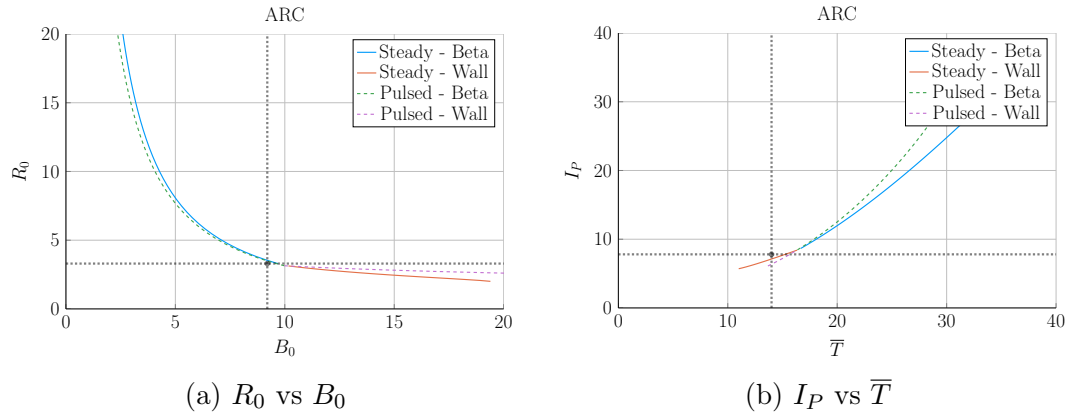


Figure 6-2: ARC Model Comparison

Table 6.1: ARC Variables

(a) Input Variables

Input	Value
H	1.8
Q	13.6
N_G	0.67
ϵ	0.333
κ_{95}	1.84
δ_{95}	0.333
ν_n	0.385
ν_T	0.929
l_i	0.670
A	2.5
Z_{eff}	1.2
f_D	0.9
τ_{FT}	1.6e9
B_{CS}	12.77

(b) Output Variables

Output	Original	Fussy.jl
R_0	3.3	3.4
B_0	9.2	9.5
I_P	7.8	8.8
\bar{n}	1.3	1.3
\bar{T}	14.0	16.8
β_N	0.026	-
q_{95}	7.2	6.1
P_W	2.5	2.2
f_{BS}	0.63	0.56
f_{CD}	0.37	0.44
f_{ID}	-	-
V	141	157
P_F	525	726
η_{CD}	0.321	0.316

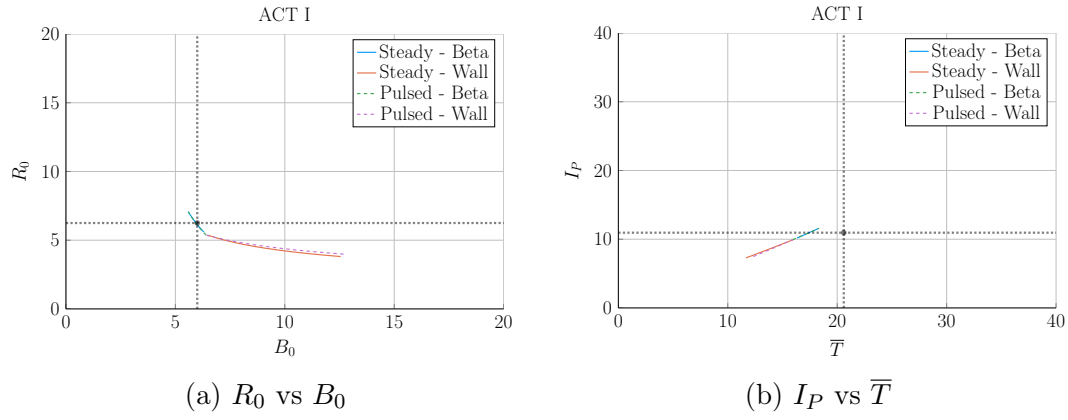


Figure 6-3: ARIES ACT I Model Comparison

Table 6.2: ACT I Variables

(a) Input Variables

Input	Value
H	1.65
Q	42.5
N_G	1.0
ϵ	0.25
κ_{95}	2.1
δ_{95}	0.4
ν_n	0.27
ν_T	1.15
l_i	0.359
A	2.5
Z_{eff}	2.11
f_D	0.75
τ_{FT}	1.6e9
B_{CS}	12.77

(b) Output Variables

Output	Original	Fussy.jl
R_0	6.25	6.23
B_0	6.0	6.0
I_P	10.95	10.78
\bar{n}	1.3	1.3
\bar{T}	20.6	17.2
β_N	0.0427	-
q_{95}	4.5	4.0
P_W	2.45	2.00
f_{BS}	0.91	0.91
f_{CD}	0.09	0.09
f_{ID}	-	-
V	582.0	621.4
P_F	1813	1865
η_{CD}	0.188	0.185

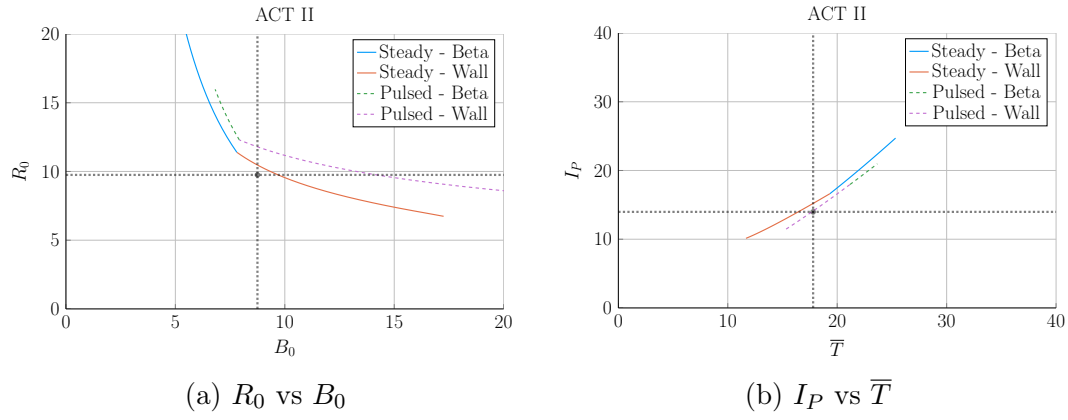


Figure 6-4: ARIES ACT II Model Comparison

Table 6.3: ACT II Variables

(a) Input Variables

Input	Value
H	1.22
Q	25.0
N_G	1.3
ϵ	0.25
κ_{95}	1.964
δ_{95}	0.42
ν_n	0.41
ν_T	1.15
l_i	0.603
A	2.5
Z_{eff}	2.12
f_D	0.74
τ_{FT}	1.6e9
B_{CS}	12.77

(b) Output Variables

Output	Original	Fussy.jl
R_0	9.75	10.22
B_0	8.75	9.05
I_P	13.98	14.84
\bar{n}	0.86	0.82
\bar{T}	17.8	17.4
β_N	0.026	0.023
q_{95}	8.0	6.6
P_W	1.46	-
f_{BS}	0.77	0.66
f_{CD}	0.23	0.34
f_{ID}	-	-
V	2209	2559
P_F	2637	3460
η_{CD}	0.256	0.307

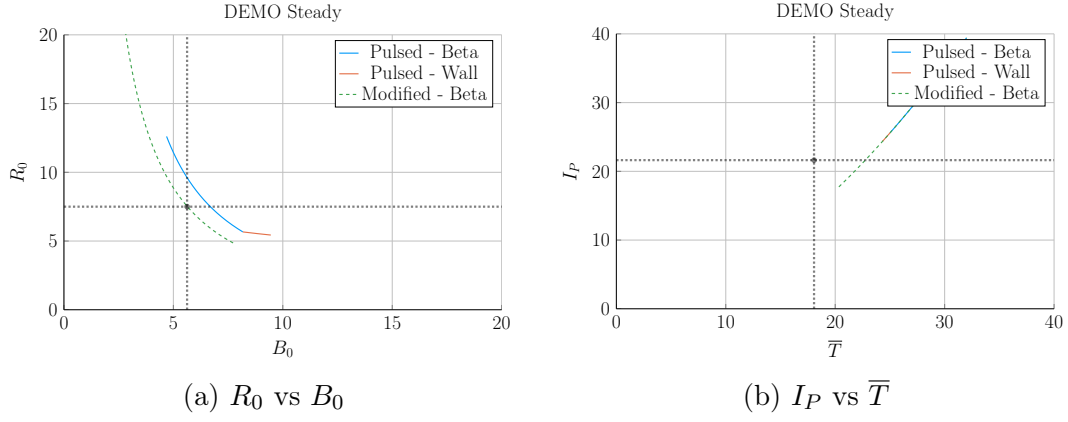


Figure 6-5: DEMO Steady Model Comparison

Table 6.4: DEMO Steady Variables

(a) Input Variables

Input	Value
H	1.4
Q	24.46
N_G	1.2
ϵ	0.385
κ_{95}	1.8
δ_{95}	0.333
ν_n	0.3972
ν_T	0.9187
l_i	0.900
A	2.856
Z_{eff}	4.708
f_D	0.7366
τ_{FT}	1.6e9
B_{CS}	12.85

(b) Output Variables

Output	Original	Fussy.jl	Modified
R_0	7.5	8.2	7.6
B_0	5.627	6.307	5.577
I_P	21.63	30.93	22.05
\bar{n}	0.875	1.048	0.855
\bar{T}	18.07	27.83	23.00
β_N	0.038	-	-
q_{95}	4.405	3.761	4.360
P_W	1.911	4.151	2.281
f_{BS}	0.611	0.424	0.492
f_{CD}	0.389	0.576	0.508
f_{ID}	-	-	-
V	2217	2879	2351
P_F	3255	8971	4306
η_{CD}	0.4152	-	-

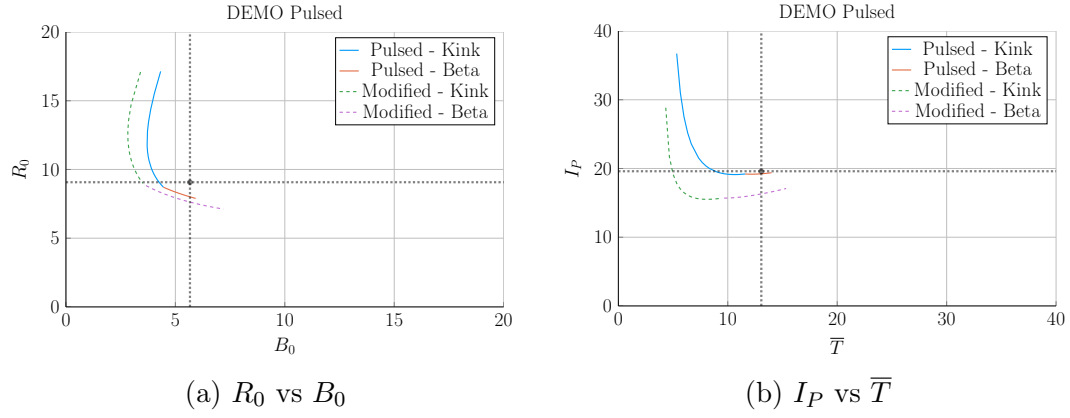


Figure 6-6: DEMO Pulsed Model Comparison

Table 6.5: DEMO Pulsed Variables

(a) Input Variables

Input	Value
H	1.1
Q	39.86
N_G	1.2
ϵ	0.3226
κ_{95}	1.59
δ_{95}	0.333
ν_n	0.27
ν_T	1.094
l_i	1.155
A	2.735
Z_{eff}	2.584
f_D	0.7753
τ_{FT}	7273
B_{CS}	12.77

(b) Output Variables

Output	Original	Fussy.jl	Modified
R_0	9.07	8.10	7.61
B_0	5.67	5.48	5.71
I_P	19.6	19.3	16.3
\bar{n}	0.7983	0.9795	0.9384
\bar{T}	13.06	13.28	13.00
β_N	0.0259	-	-
q_{95}	3.247	2.853	3.303
P_W	1.05	1.47	1.23
f_{BS}	0.348	0.164	0.190
f_{CD}	0.096	0.106	0.103
f_{ID}	0.557	0.730	0.707
V	2502	1751	1452
P_F	2037	2376	1756
η_{CD}	0.2721	-	-

1707 6.2 Developing Prototype Reactors

1708 Now that the model used in Fussy.jl has been tested against other fusion systems codes
1709 in the field, we will develop our own prototype reactors. Because this paper is about
1710 making a levelized comparison of pulsed and steady-state tokamaks, we will develop
1711 middle-of-the-road reactors that only differ by operating mode. The parameters for
1712 these two designs are captured in Tables 6.6 and 6.7.

1713 To compare the two modes of operation, the steady-state prototype, Charybdis, is
1714 the obvious choice to start with – as the model was tested against four of these typed
1715 reactors. It was also pointed out that the model did remarkably well when recreating
1716 ARC. As the authors share many of the ARC team’s philosophies, Charybdis uses
1717 static parameters very similar to them.⁶

1718 Next, although led to believe Charybdis’ pulsed twin reactor – Proteus – would be
1719 created by a simple flip of the switch, it was a slight oversimplification. The first
1720 difference is that the pulsed twin, Proteus, is assumed to be purely pulsed: $\eta_{CD} = 0$.
1721 Further, the bootstrap current is much less important than it was for steady-state
1722 tokamaks. This corresponds to a current profile peaked at the origin – i.e. a parabola.
1723 Numerically, this is done by raising l_i from around 0.55 to 0.6.

1724 The final difference creates the largest change in the twin reactors: the choice of
1725 necessary technological advancement. As mentioned several times before, the H fac-
1726 tor is a common way designers artificially boost the confinement of their machines.
1727 This H value will thus be the technological advancement needed for Charybdis, the
1728 steady-state prototype. Next, as the main conclusion of this paper is to state the ad-
1729 vantages of high magnetic field, an inexpensive way to strengthen the central solenoid
1730 of Proteus – through B_{CS} – will be employed using HTS coils.

1731 The goal now is to impose a constraint on a reactor’s economic competitiveness by
1732 setting the fusion power to a relatively low value for both designs – i.e. 1250 MW.
1733 As Fig. 6-7 shows, this results in Charybdis having an H factor of 1.7 and Proteus
1734 having a B_{CS} of around 20T. As shown in the Proteus cost curve, this was at a point

1735 where the ratio between the minimum capital cost and the minimum cost-per-watt
 1736 leveled off.

1737 Note that these technological advancements (in H and B_{CS}) are necessary to get
 1738 economic – or even physically realizable – reactors. This is the same reason why all
 1739 the literature reactors used values for H and N_G that violate standard values.

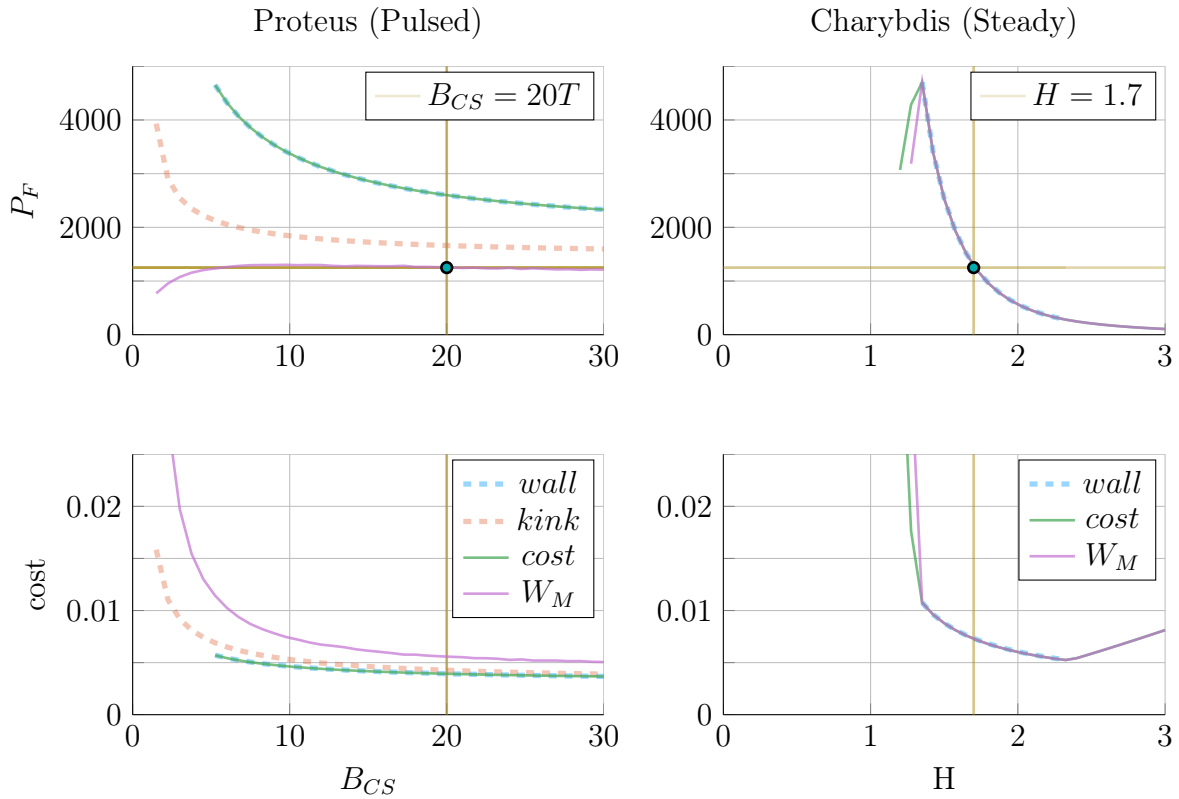


Figure 6-7: Designing Reactor Prototypes

As is convention in fusion engineering, designs are built using one assumed technological advancement. For steady-state reactors, we assume a method for improving confinement – by increasing H . While in the pulsed case, the advancement is inexpensive magnet technology for stronger fields in the central solenoid – B_{CS} .

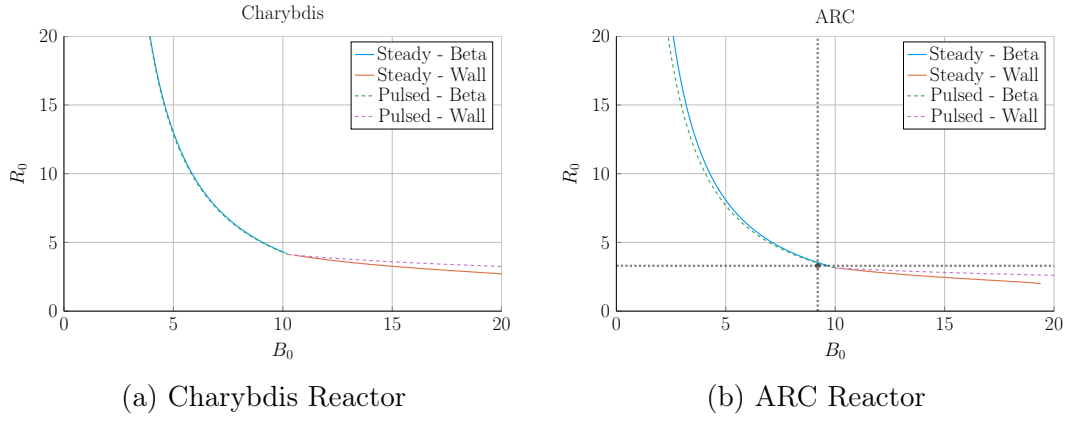


Figure 6-8: Steady State Prototype Comparison

Table 6.6: Charybdis Variables

(a) Input Variables

Input	Value
H	1.7
Q	25.0
N_G	0.9
ϵ	0.3
κ_{95}	1.8
δ_{95}	0.35
ν_n	0.4
ν_T	1.1
l_i	0.558
A	2.5
Z_{eff}	1.75
f_D	0.9
τ_{FT}	1.6e9
B_{CS}	12.0

(b) Output Variables

Output	Value
R_0	4.13
B_0	10.28
I_P	8.98
\bar{n}	1.47
\bar{T}	15.81
β_N	0.028
q_{95}	6.089
P_W	3.003
f_{BS}	0.723
f_{CD}	0.277
f_{ID}	0.0
V	225.5
P_F	1294
η_{CD}	0.291

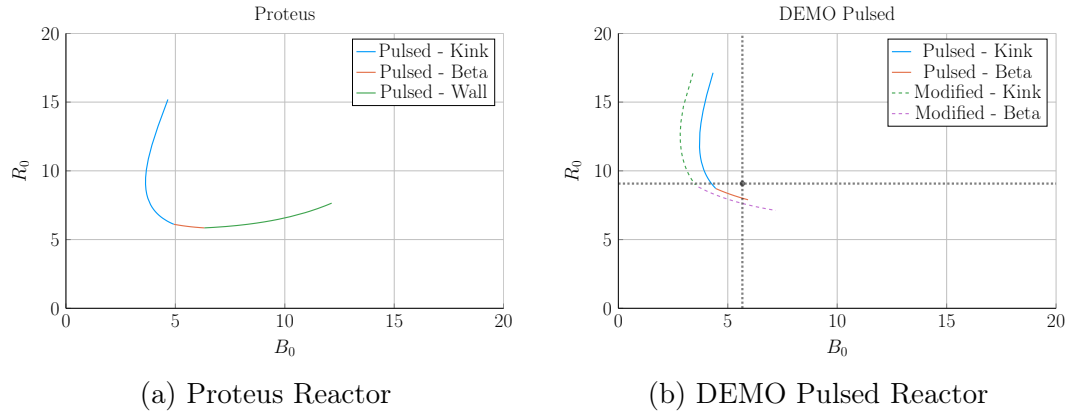


Figure 6-9: Pulsed Prototype Comparison

Table 6.7: Proteus Variables

(a) Input Variables

Input	Value
H	1.0
Q	25.0
N_G	0.9
ϵ	0.3
κ_{95}	1.8
δ_{95}	0.35
ν_n	0.4
ν_T	1.1
l_i	0.633
A	2.5
Z_{eff}	1.75
f_D	0.9
τ_{FT}	7200
B_{CS}	20.0

(b) Output Variables

Output	Value
R_0	6.11
B_0	4.93
I_P	15.54
\bar{n}	1.16
\bar{T}	11.25
β_N	0.028
q_{95}	2.5
P_W	1.763
f_{BS}	0.2675
f_{CD}	0.0
f_{ID}	0.7325
V	732.6
P_F	1667
η_{CD}	0.0

1740 6.2.1 Navigating around Charybdis

1741 The Charybdis reactor is the steady-state twin developed for this paper. As men-
 1742 tioned, its parameters are similar to the ARC design. This is shown in Fig. 6-8, where
 1743 the two $R_0 - B_0$ curves are almost interchangeable. Before moving on, it proves useful
 1744 to note that the optimum place to build on these curves is where the two portions
 1745 intersect – as it minimizes costs. These cost curves are shown in Fig. 6-11.

1746 6.2.2 Pinning down Proteus

1747 The pulsed twin reactor, Proteus, highlights the effects of a high field central solenoid.
 1748 When compared to the Pulsed DEMO design, the $R_0 - B_0$ curve looks far more favor-
 1749 able – i.e. each machine built at a certain magnet strength would be more compact
 1750 (and cheaper). An interesting facet of Proteus is that it exhibits all three used limits:
 1751 kink safety factor, Troyon beta, and wall loading. Cost curves are shown in Fig. 6-12.

Table 6.8: Proteus and Charybdis Comparison

The twin pulsed and steady-state prototypes show general trends in terms of what value values the dynamic variables will have. As can be seen, the radius (R_0) of the pulsed prototype (Proteus) is two meters larger than its steady-state twin (Charybdis).

(a) Charybdis		(b) Proteus	
Output	Value	Output	Value
R_0	4.13	R_0	6.11
B_0	10.28	B_0	4.93
I_P	8.98	I_P	15.54
\bar{n}	1.47	\bar{n}	1.16
\bar{T}	15.81	\bar{T}	11.25
f_{BS}	0.72	f_{BS}	0.27
f_{CD}	0.28	f_{ID}	0.73
P_F	1300	P_F	1650
W_M	9.48	W_M	7.09
C_W	0.007	C_W	0.004

1752 6.2.3 Highlighting Operation Differences

1753 Before moving onto general conclusions taken from the data, a quick investigation
1754 into the pulsed vs steady-state twin results is in order. A comparison between the
1755 two is best abridged in Table 6.8.

1756 Most apparently, pulsed reactors are typically larger than steady-state ones and are
1757 meant to be run at higher plasma currents. The former behavior was seen with the
1758 DEMO designs,^{7,8} – as the larger size was needed for long pulse lengths.³⁹ The latter
1759 was then already mentioned in discussing how steady-state reactors never saw a kink
1760 (current limiting) regime. Additionally pulsed machines can be run at much lower
1761 temperatures because their higher current improves confinement.

1762 These combined effects lead to the minimum cost reactors for steady-state operation
1763 having much higher toroidal field strengths than their pulsed counterparts. This is
1764 discussed in Section 6.3.2 when explaining optimum use of HTS tape.

1765 6.3 Learning from the Data

1766 Now that the model has been properly vetted and prototypes designed, we can ex-
1767 plore how pulsed and steady-state tokamaks scale. This will lead to three mostly
1768 independent results. The first result will explore how to minimize costs for a reactor
1769 by choosing optimum design points. The next will be an argument for how to prop-
1770 erly utilize the HTS magnet technology in component design. Lastly, we will take a
1771 cursory look at the other parameters capable of lowering machine costs.

1772 6.3.1 Picking a Design Point

1773 With more than twenty design parameters, finding the most economic reactor is com-
1774 putationally intractable. Intuition building aside, finding optimum reactors becomes
1775 much more feasible when only focusing on dynamic variables – i.e. when keeping static

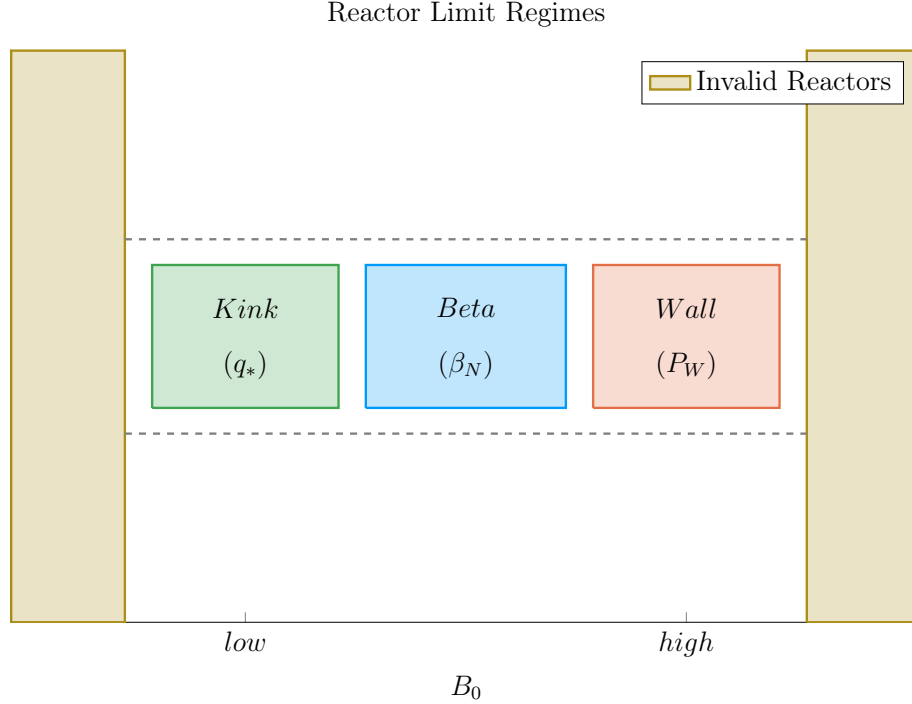


Figure 6-10: Limiting Constraint Regimes

At a simple level, a reactor has around three regimes of design limiting constraints. At low fields, the kink safety factor – through q_* and Eq. (3.40) – drives design. Then at high fields, wall loading – through P_W and Eq. (3.44) – guide reactors. And between the two, the beta limit – through β_N and Eq. (3.37) – are the limiting constraint.

1776 variables constant. This method, for example, is how all the $R_0 - B_0$ curves have
 1777 been produced this chapter. Once these curves are produced, it is up to the user to
 1778 choose which reactor on them to build. However, the guiding metric usually involves
 1779 lowering some cost, either: capital cost or cost-per-watt.

1780 Regardless of reactor type, most economic tokamaks operate near the beta limit –
 1781 where plasma pressure is greatest. Besides being a regime highly sensitive to magnetic
 1782 field strength, the beta limit is a constraint that occurs on every reactor (seen by the
 1783 authors). This beta limit (β_N) is usually nested between the kink limit (q_*) to lower
 1784 B_0 values and wall loading (P_W) to higher ones. Understanding these regimes is the
 1785 first step towards building an intuition favoring economic machines – see Fig. 6-10.

1786 Now that the beta limit curve has been designated as the most economic regime to
 1787 operate in (usually), the goal is to select which reactor on it is the best one to build.

1788 Starting with the easier of the two, the optimum design point for steady-state reactors
1789 is the point where wall loading first starts to dominate the design. Due to the wall
1790 loading relation (see Eq. (3.44)), this causes the reactor to start increasing in size and
1791 cost – which is bad. This conclusion is justified by the cost curves for all five reactors
1792 in Fig. 6-11. As these show, it is also where these reactor designers pinned down their
1793 tokamaks.*

1794 The problem of selecting an optimum design is more difficult for the pulsed case.
1795 This is mainly due to there being a regime where the kink safety factor can actually
1796 be a guiding limiting constraint. Following the conclusion from steady-state reactors
1797 would be an oversimplification because there are actually two costs relevant to a
1798 reactor: capital cost and cost-per-watt. These beta-wall reactors are actually the
1799 points often best for minimizing cost-per-watt (i.e. your rate of return). The new
1800 beta-kink reactors, then, lead to cheap to build machines – as they minimize capital
1801 cost. These conclusions are shown in Fig. 6-12.

1802 Summarizing the conclusions of this subsection, the beta limit is usually the best
1803 constraint to operate at. For lowering the cost-per-watt, a reactor should always be
1804 run at the highest magnetic field strength (B_0) that has the beta limit at its maximum
1805 allowed value. This most often occurs when wall loading takes over (for steady-state
1806 reactors) or reactors start being physically unrealizable (for pulsed ones). Building
1807 cheap to build reactors – i.e. minimizing capital cost – then actually proved to make
1808 pulsed design one of trade-offs. This is because the beta-kink curve intersection
1809 produces a low capital cost reactor, but at the price of operating at a subpar cost-
1810 per-watt. Designers should therefore balance the two cost metrics when pinning down
1811 a pulsed reactor.

* Simply stated, the optimum reactor for steady-state tokamaks is one that just barely satisfies the beta and wall loading limit simultaneously – i.e. where the two curves intersect.

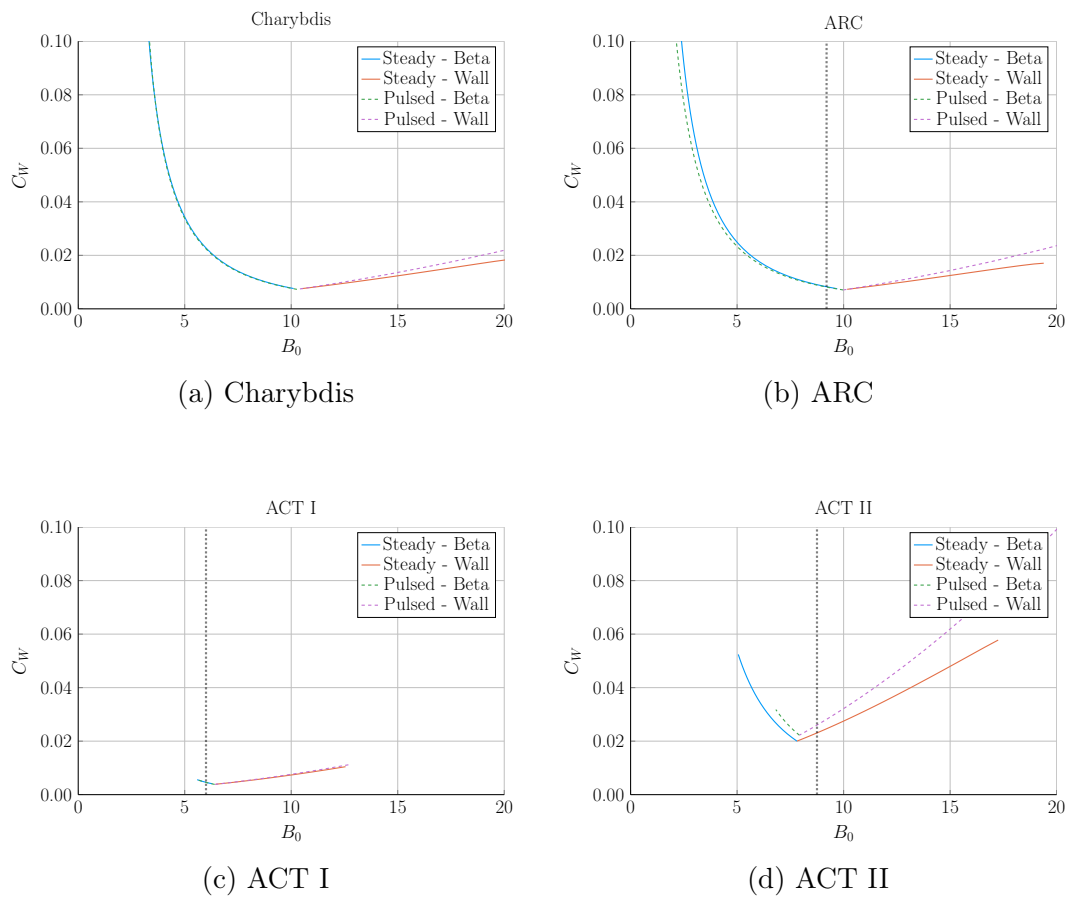
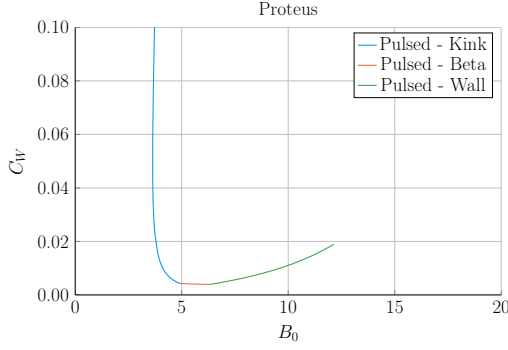
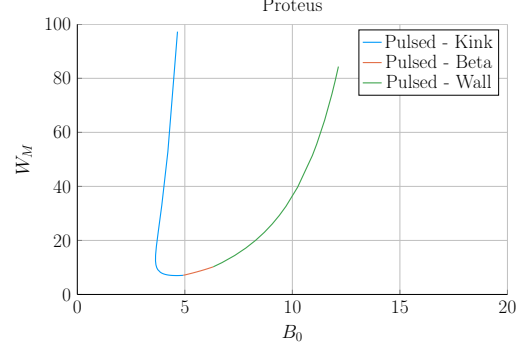


Figure 6-11: Steady State Cost Curves

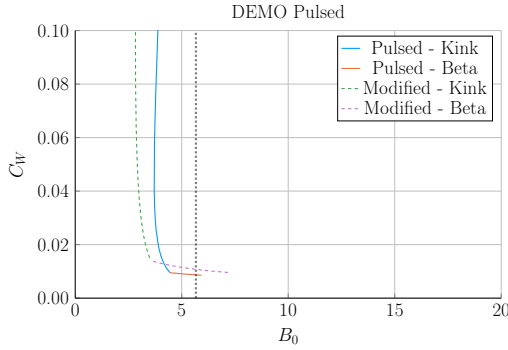
Steady state reactors typically have two regimes – a lower magnet strength **beta** limiting one and a high field **wall** loading one. As shown, each steady state scan produces a minimum cost reactor at the point where the two regimes meet.



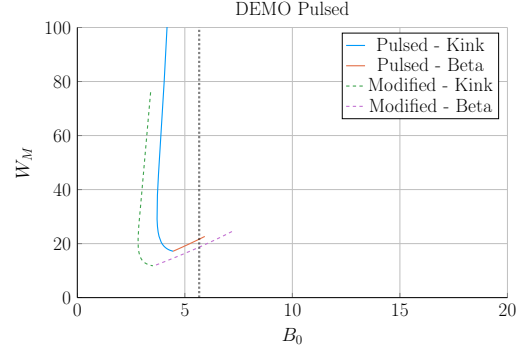
(a) Proteus Cost-per-Watt



(b) Proteus Capital Cost



(c) DEMO Pulsed Cost-per-Watt



(d) DEMO Pulsed Capital Cost

Figure 6-12: Pulsed Cost Curves

Pulsed reactor design is slightly more ambiguous than steady-state in terms of selecting an operating point. These plots show that the cost-per-watt is reduced at the highest field strength available to **beta** regime reactors. The minimum capital cost then occurs when the **beta** and **kink** limit are both just marginally satisfied.

1812 6.3.2 Utilizing High Field Magnets

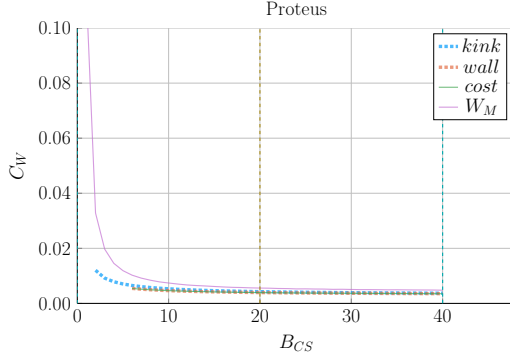
1813 The main conclusion for this paper is that high field magnets are the way to go to
1814 build an economic, compact fusion reactor. In line with the MIT ARC effort, these
1815 high fields will be built with high-temperature superconducting (HTS) tape. This
1816 innovation is set to nearly double the strength of conventional magnets. The real
1817 question is how best to use this technology.

1818 At a very simple level, there are two main places strong magnets can be employed:
1819 the toroidal fields (B_0) and the central solenoid (B_{CS}). The easier mode of operation
1820 to start with is steady-state. This is because steady-state tokamaks do not rely on
1821 a central solenoid to run their functionally infinite length pulses. Further, the cost
1822 curves in Fig. 6-11 show that all these designs would benefit from toroidal fields (B_0)
1823 not achievable with conventional magnets – which can only reach around 13 T.¹²

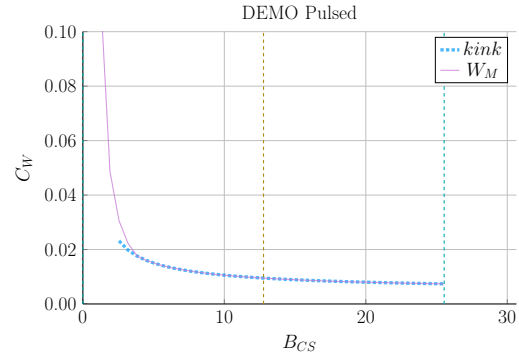
1824 The more interesting result is that pulsed reactors gain no real benefit from using
1825 HTS toroidal field magnets – as mentioned previously in Section 6.2.3. Within the
1826 modern paradigm (i.e. D-T fuel, H-Mode, etc), pulsed reactors never have to exceed
1827 the limits of less expensive LTS magnets. The place HTS can really help is with the
1828 central solenoid, which governs how long a pulse can last. Further, improvements
1829 to the central solenoid have diminishing returns past the range accessible to HTS
1830 tape. Again, HTS would be more than adequate for the modern paradigm. These
1831 conclusions are shown in Figs. 6-13 and 6-14.

1832 Summarizing this subsection, HTS tape is one of the best ways to lower the cost of
1833 fusion reactors at a commercial scale. For steady-state reactors, HTS works best in
1834 the toroidal field coils (B_0), while the tape would fare better in the central solenoid
1835 (B_{CS}) of pulsed reactors. Further, both effects saturate within the range of this HTS
1836 tape, rendering more sophisticated magnetic technology unnecessary. HTS is thus
1837 one technological advancement that could help usher in an era of affordable fusion
1838 energy.*

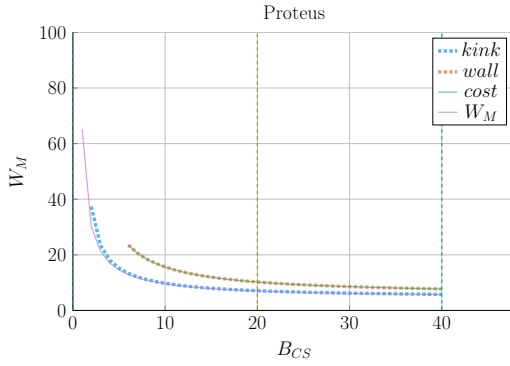
*This notion of HTS technology leading the way to affordable fusion energy is in line with the 2018 FESAC TEC⁴⁰ and NAS burning plasma⁴¹ reports.



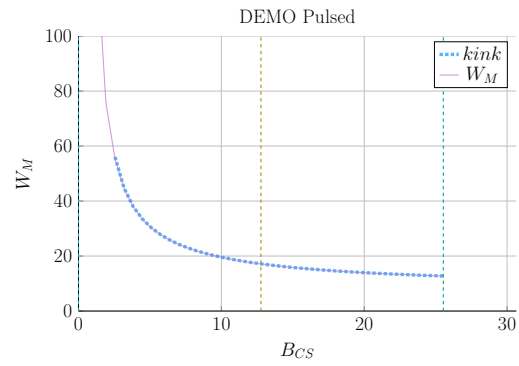
(a) Proteus Cost-per-Watt



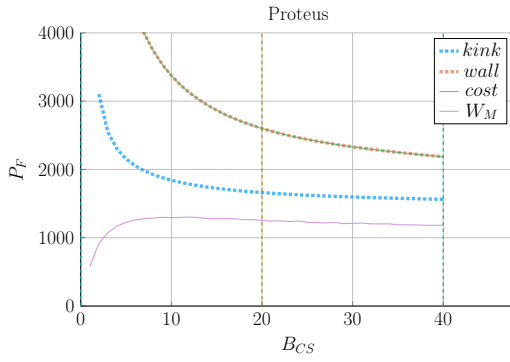
(b) DEMO Pulsed Cost-per-Watt



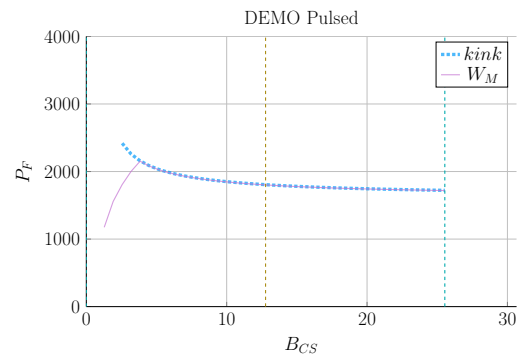
(c) Proteus Capital Cost



(d) DEMO Pulsed Capital Cost



(e) Proteus Fusion Power



(f) DEMO Pulsed Fusion Power

Figure 6-13: Pulsed B_{CS} Sensitivities

Pulsed machines become more economically attractive as their central solenoid is strengthened. However as these plots show, the positive benefits of this have rapidly diminishing returns. HTS tape's magnet range happens to be inside regime.

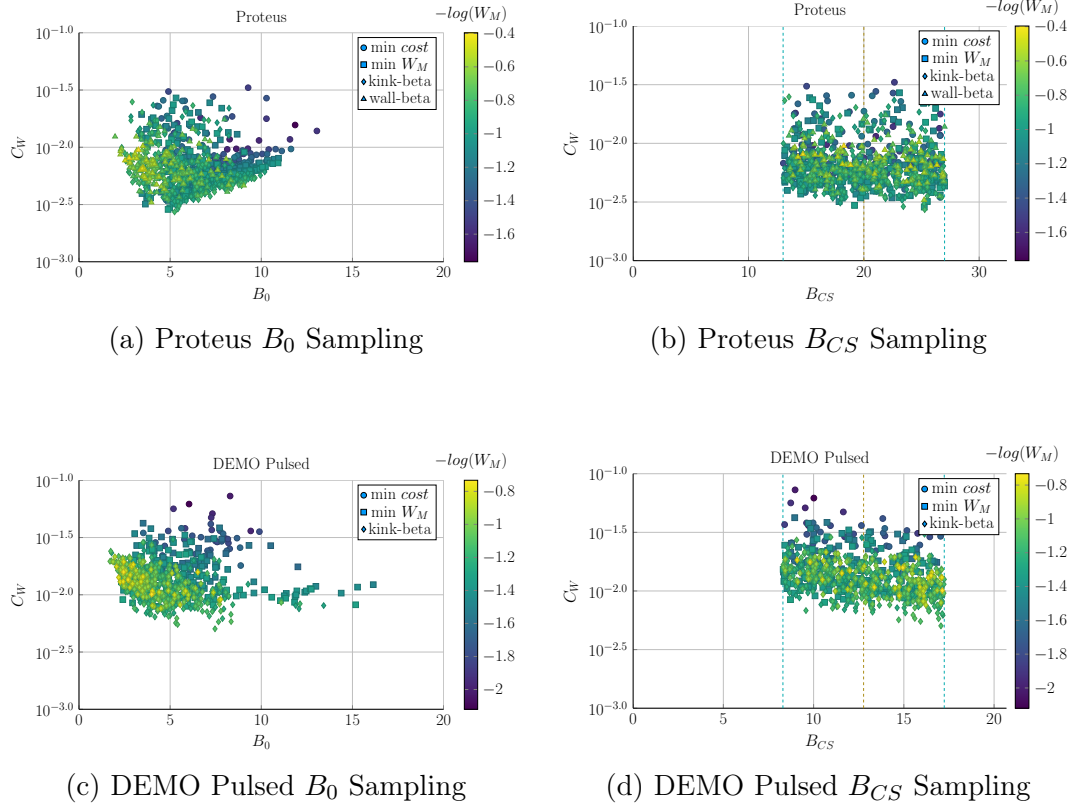


Figure 6-14: Pulsed Monte Carlo Sampling

As shown, pulsed machines have a preference towards small toroidal field strengths (B_0) – as they minimize both capital costs and costs-per-watt. Further, increasing central solenoid strength (B_{CS}) can lead to dramatically more competitive reactors. This effect saturates at higher field strengths, however, as is shown in subfigure (b).

1839 6.3.3 Looking at Design Alternatives

1840 Even in this relatively simple fusion model, there are more than twenty static/in-
1841 put variable knobs a designer can tune to improve reactor feasibility. Many have
1842 practical limits, such as being physically realizable or fitting within the ELMY H-
1843 Mode database. Thus, the goal of this subsection is to investigate some of the more
1844 interesting results. Although many more plots are available in Appendix H.

1845 Capitalizing the Bootstrap Current

1846 Besides artificially enhancing a plasmas confinement with the H-factor, steady-state
1847 reactor designers may also heavily rely on high bootstrap currents. This is because
1848 bootstrap current is the portion of current you do not have to pay for. The research
1849 groups most focused on this technological advancement are General Atomic's DIII-
1850 D²⁴ in San Diego and PPPL's NSTX-U in New Jersey.⁴² This advancement relies on
1851 tailoring current profiles to be much more hollow.

1852 Quickly reasoning this thought process are two sets of plots. The first plot (Fig. 6-
1853 15) highlights how the cheapest possible steady-state designs have bootstrap fractions
1854 approaching unity – they use almost no current drive. This makes sense as current
1855 drive is extremely cost prohibitive (i.e. why people consider pulsed tokamaks).

1856 The next plot (Fig. 6-16) is the parameter that determines a current profile's peak
1857 radius: l_i . As can be seen, the current peak approaches the outer edge of the plasma
1858 as l_i decreases. This in turn boosts the bootstrap fraction closer to one – leading to
1859 inexpensive reactors.

1860 Contextualizing the H-Factor

1861 From before, increasing the H-factor always led to more cost effective steady-state
1862 reactors. This is because the enhanced confinement allows for smaller machines.
1863 This was already heavily explored in Fig. 6-1. These plots also show that steady

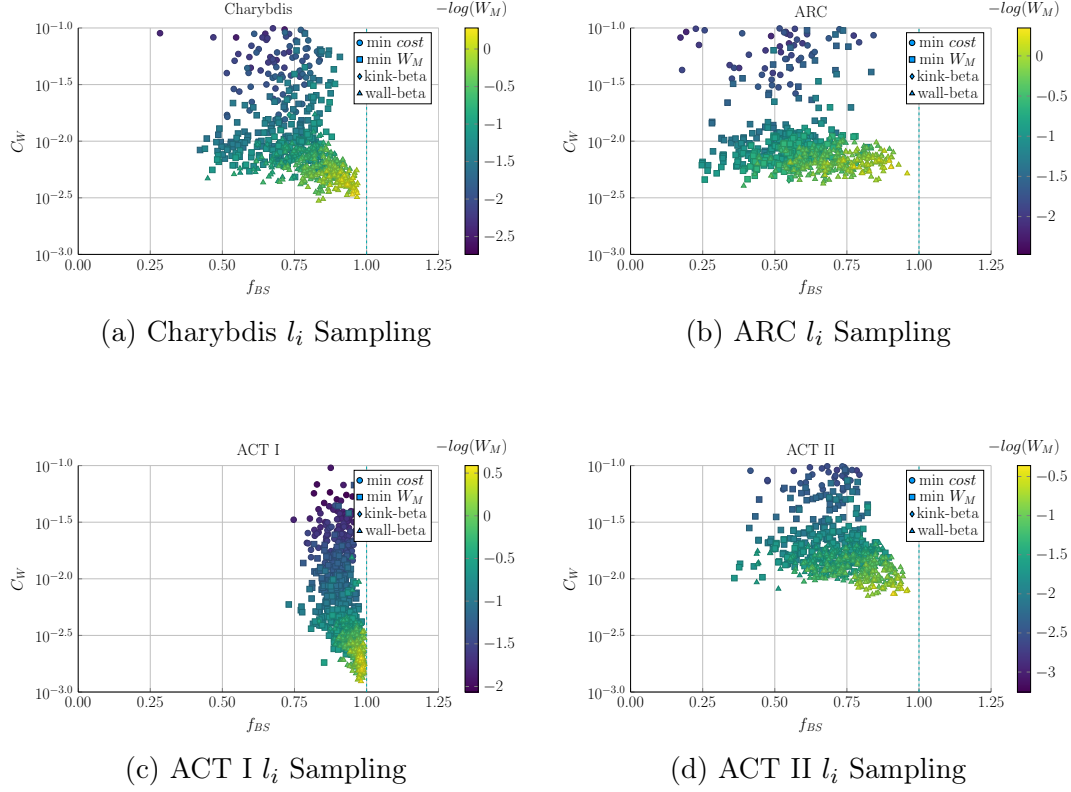
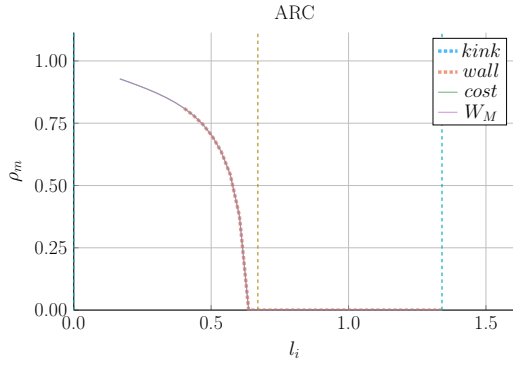
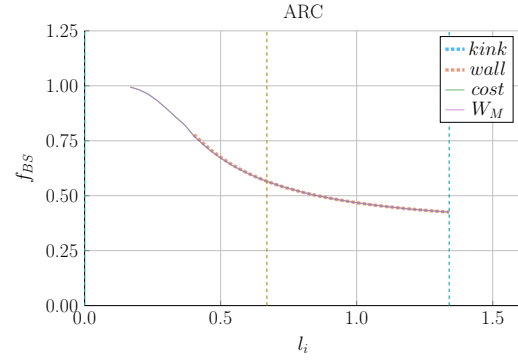


Figure 6-15: Bootstrap Current Monte Carlo Sampling

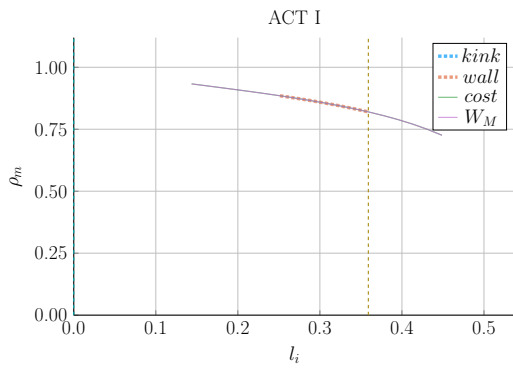
The purpose of these plots is to show that a high bootstrap current always reduces the cost of a steady state reactor – highly independent of actual input quantities (i.e. ϵ , l_i , etc.)



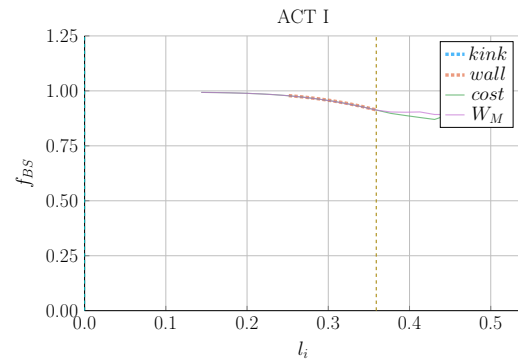
(a) ARC Peak Radius



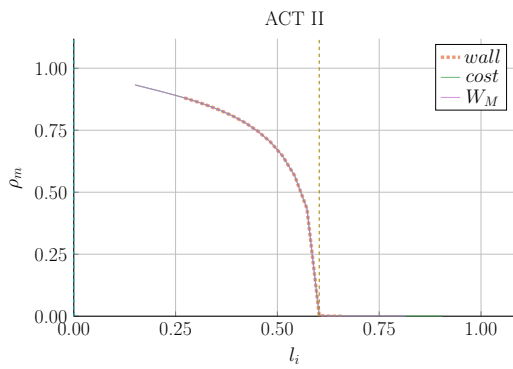
(b) ARC Bootstrap Fraction



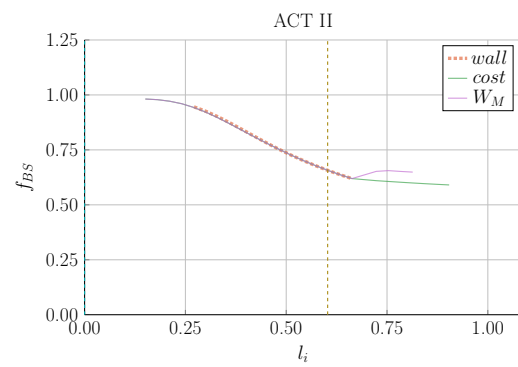
(c) ACT I Peak Radius



(d) ACT I Bootstrap Fraction



(e) ACT II Peak Radius



(f) ACT II Bootstrap Fraction

Figure 6-16: Internal Inductance Sensitivities

The internal inductance has a strong influence on the peaking radius (ρ_m) of the hollow profile and the bootstrap current fraction (f_{BS}). Lowering the internal inductance thus makes a profile more hollow, which in turn increases the bootstrap fraction.

1864 state reactors would not be physically possible using a default H factor of one! In
1865 other words, steady-state tokamaks require some technical advancement before they
1866 can ever be used as fusion reactors. The same cannot be said for pulsed machines.

1867 For pulsed reactors, increasing H always reduces capital cost, but may actually in-
1868 crease the cost-per-watt. This is because the fusion power can decrease at a faster
1869 rate than the capital cost in a pulsed tokamak – both of which appear in Eq. (1.3)
1870 defining the cost-per-watt. This interesting result demonstrates the unusual behaviors
1871 of highly non-linear systems: masterclass intuition may not match model results.

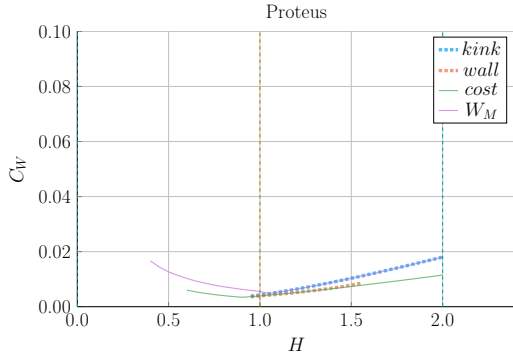
1872 **Showcasing the Current Drive Efficiency**

1873 The last exploration is less about building an economic machine and more about
1874 understanding the self-consistent current drive efficiency in steady-state tokamaks.
1875 Using the Ehst-Karney model²⁷ coupled with standard analysis⁵ leads to a remarkably
1876 simple and accurate solver. As shown in Fig. 6-18, the model captures the physics
1877 almost exactly for the different designs.*

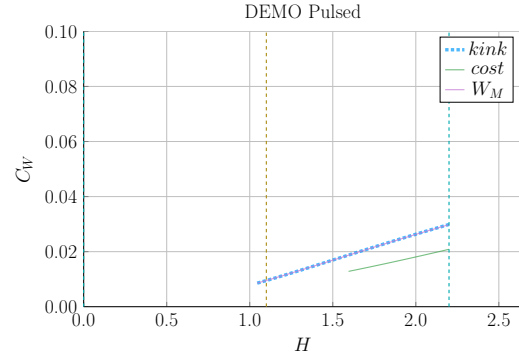
1878 In a similar fashion as the bootstrap fraction results, the variable that most captures
1879 how to directly maximize η_{CD} is the LHCD wave launch angle, θ_{wave} . When below
1880 90° it is considered outside launch, whereas up to 135° it is considered inside launch.
1881 Notably, these curves are not monotonic, there is an optimum launching angle – as
1882 shown in Fig. 6-19.

1883 It should be noted that the launch angle was not found to have a major impact. This
1884 may be a due to an oversimplification of the model, as sources suggest inside launch
1885 is preferable for multiple reasons./citeadx

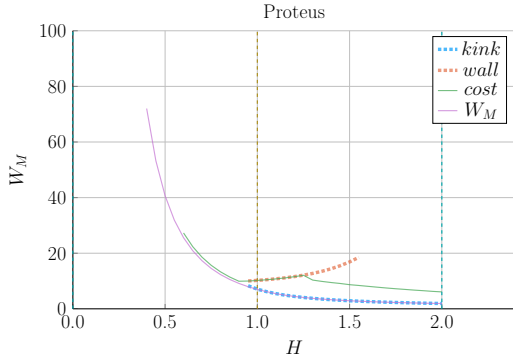
* It did, however, not converge for the DEMO steady reactor. This is probably due to lack of self-consistency for η_{CD} in their systems framework.



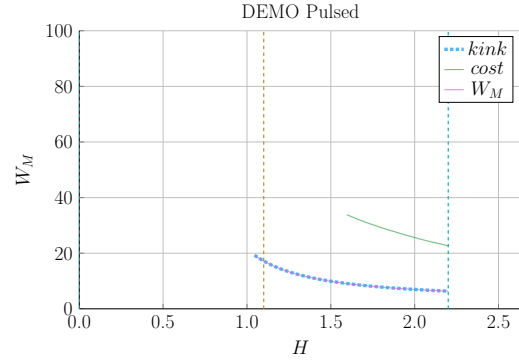
(a) Proteus Cost-per-Watt



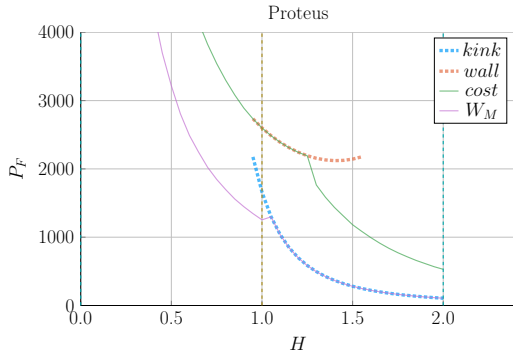
(b) DEMO Pulsed Cost-per-Watt



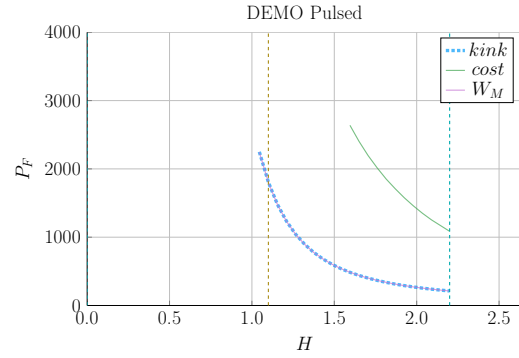
(c) Proteus Capital Cost



(d) DEMO Pulsed Capital Cost



(e) Proteus Fusion Power



(f) DEMO Pulsed Fusion Power

Figure 6-17: Pulsed H Sensitivities

One curious result from the model is that the enhancement factor (H) can actually increase the cost-per-watt (C_W) of a tokamak reactor. This is because C_W depends on both the capital cost (W_M) and the fusion power (P_F). Although the two do both generally decrease, the fusion power decreases at a faster rate for realistic values of H .

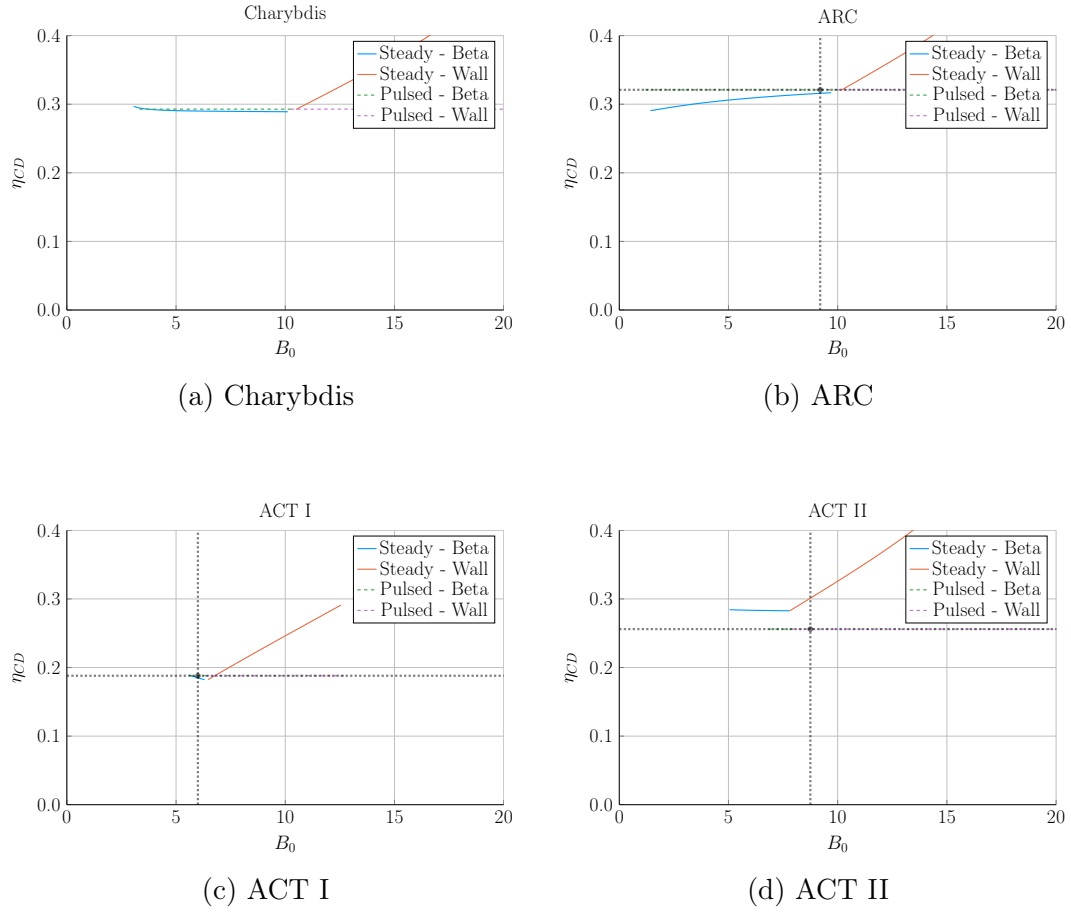
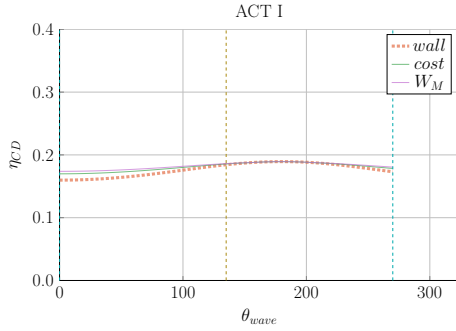
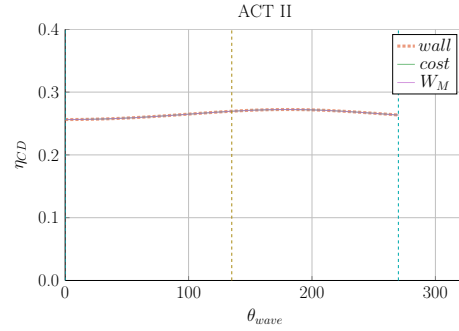


Figure 6-18: Steady State Current Drive Efficiency

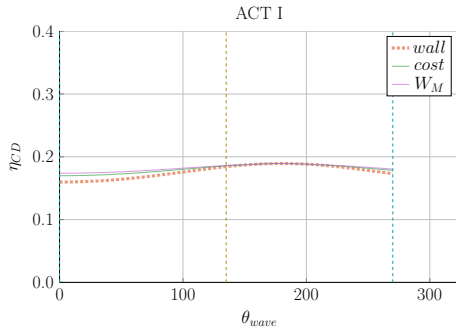
These plots shows that the Ehst-Karney current drive efficiency model²⁷ used by this model recovers values from other research studies with decent accuracy.



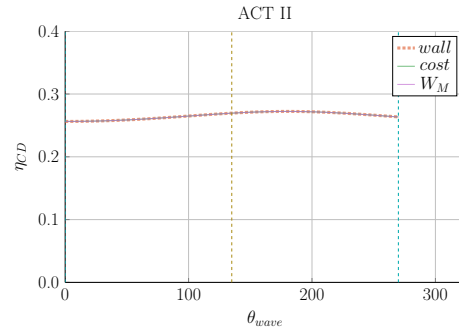
(a) Charybdis



(b) ARC



(c) ACT I



(d) ACT II

Figure 6-19: Current Drive Efficiency vs Launch Angle

These plots show that the Ehst-Karney model does have an optimum angle, but most likely understates its importance – sources suggest inside launch is preferable for multiple reasons./citeadx

1886 Chapter 7

1887 Planning Future Work for the Model

1888 This model may run and produce interesting results, but there is always more to
1889 be done. This chapter explores three potential fusion reactors that could help guide
1890 real world designs. These are: a stellarator (Ladon), a steady-state/pulsed composite
1891 (Janus), and a tokamak capable of reaching H, L, and I modes (Daedalus). The
1892 chapter then concludes by describing several possible model improvements, including:
1893 adding radiation sources, using pedestal profiles, and improving flux balance.

1894 7.1 Incorporating Stellarator Technology – Ladon

1895 A stellarator is, at a basic level, a tokamak helically twisted along the length of its
1896 major circle (see Fig. 7-1). For a long time they were dismissed because of their poor
1897 transport properties. Recent technological improvements, though, have eased this
1898 situation – as seen with the Wendelstein 7-X device in Germany. The problem now is
1899 engrained in the underdeveloped scaling laws stemming from a lack of machines and,
1900 more fundamentally, data points.⁴³

1901 To model Ladon, this paper’s proposed stellarator, one would need to replace at
1902 least: the Greenwald density limit and the confinement time scaling law. In place of
1903 the Greenwald density will likely be some other density or current limit, possibly the

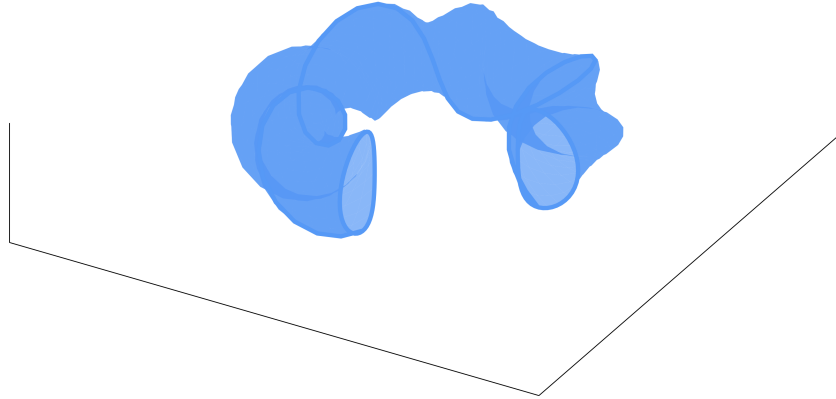


Figure 7-1: Cut-Away of Stellarator Reactor

A stellarator has a geometry similar to a tokamak, except it twists around its major axis. This eliminates the need for net current to keep the device in equilibrium.

1904 Bremsstrahlung density limit.⁴⁴ This may require the density to be carried throughout
1905 analysis – thus appearing explicitly in one column of Table 5.1.

1906 7.2 Making a Composite Reactor – Janus

1907 The next interesting reactor would be a composite tokamak incorporating pulsed and
1908 steady-state operation: Janus. Fundamentally, this would involve current coming
1909 from both LHCD (steady-state), as well as inductive (pulsed) sources. How the two
1910 can coexist is shown in Fig. 7-2. This was actually used in DEMO Pulsed, but the
1911 current drive was not handled self-consistently. Coupling these two current sources
1912 could reduce reliance on bootstrap current and lead to much more compact machines.

1913 The arguments against this are mainly technical: why build two difficult auxiliary
1914 systems when one is needed – especially when they probably work against each other.
1915 Although rational, it may turn out that the larger current achievable with two sources
1916 leads to a smaller, more economic machine.

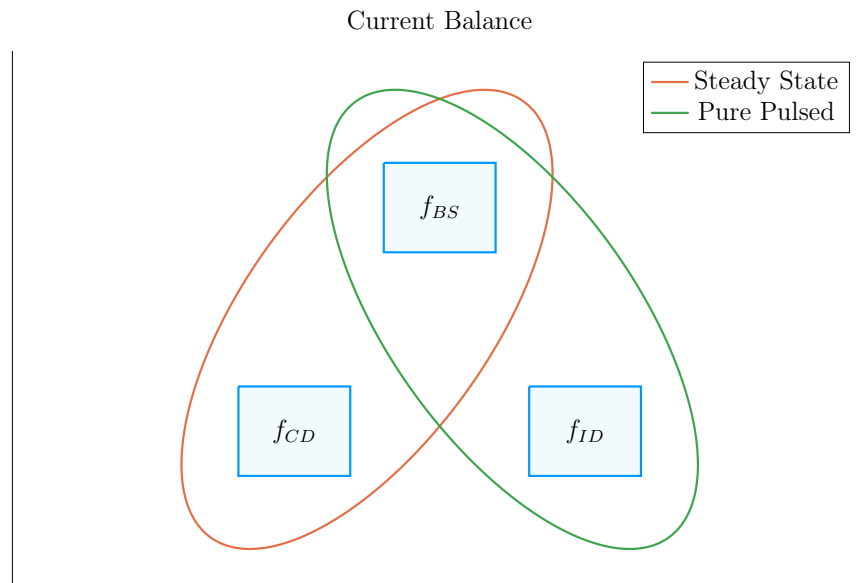


Figure 7-2: Current Balance in a Tokamak

In a tokamak, there needs to be a certain amount of current – and that current has to come from somewhere. All good reactors have an adequate bootstrap current. What provides the remaining current is what distinguishes steady state from pulsed operation.

1917 7.3 Bridging Confinement Scalings – Daedalus

1918 The final potential reactor – Daedalus – is designed so that it can be run in H-
 1919 Mode, L-Mode, and I-Mode. Up until now, only H-Mode (high confinement) has
 1920 been discussed due to its use in conventional reactor design. However, L-Mode (low)
 1921 and I-Mode⁴⁵ (intermediate) may prove to produce more favorable scalings – in terms
 1922 of cost – as more of reactor space is explored.

1923 Because L-Mode is available on any machine, the first step is actually building under
 1924 H-Mode. The goal then is to find reactors that can also reach I-Mode – simultaneously
 1925 improving the scaling law’s fit and possibly making the actual reactor more economic.

1926 Presented below are the three confinement scaling laws, as well as the generalized
 1927 formula. As should be noted, the I-Mode scaling currently lacks a true radial depen-
 1928 dence – as it has only been found on two machines.⁴⁵ This is one reason Daedalus

1929 would be so valuable.*

$$\tau_E = K_\tau H \frac{I_P^{\alpha_I} R_0^{\alpha_R} a^{\alpha_a} \kappa^{\alpha_\kappa} \bar{n}^{\alpha_n} B_0^{\alpha_B} A^{\alpha_A}}{P_{src}^{\alpha_P}} \quad (3.25)$$

$$\tau_E^H = 0.145 H \frac{I_P^{0.93} R_0^{1.39} a^{0.58} \kappa^{0.78} \bar{n}^{0.41} B_0^{0.15} A^{0.19}}{P_{src}^{0.69}} \quad (3.27)$$

1930

$$\tau_E^L = 0.048 H \frac{I_P^{0.85} R_0^{1.2} a^{0.3} \kappa^{0.5} \bar{n}^{0.1} B_0^{0.2} A^{0.5}}{P_{src}^{0.5}} \quad (7.1)$$

1931

$$\tau_E^I = \frac{0.014 H}{0.68^{\lambda_R} \cdot 0.22^{\lambda_a}} \cdot \frac{I_P^{0.69} R_0^{\lambda_R} a^{\lambda_a} \kappa^{0.0} \bar{n}^{0.17} B_0^{0.77} A^{0.0}}{P_{src}^{0.29}} \quad (7.2)$$

1932

$$\lambda_R + \lambda_a = 2.2 \quad (7.3)$$

1933 A final point to make is reemphasizing that the I-Mode scaling law – developed by
 1934 the authors – is significantly underdeveloped. It is the target of ongoing research at
 1935 the MIT PSFC.⁴⁵

1936 7.4 Addressing Model Shortcomings

1937 Before moving on to the final conclusions, we will give a quick recap of several of the
 1938 more overly simplified phenomena in this fusion systems framework. These include:
 1939 approximating temperature profiles as simple parabolas, neglecting all radiation ex-
 1940 cept Bremsstrahlung, and handling flux sources at too basic a level. This list is
 1941 non-comprehensive, as more sophisticated analysis would also help: the divertor heat
 1942 load, the neutron wall loading, etc.

* In H-Mode and L-Mode's favor, they have been found on every machine that should see them.

1943 **7.4.1 Integrating Pedestal Temperature Profiles**

1944 One of the biggest shortcomings of this model is not handling plasma profiles self-
1945 consistently – instead replacing them with simple parabolas. Although these parabo-
1946 las work for densities and L-Mode plasma temperatures, the same cannot be said
1947 about H-Mode temperatures. This is because they have a distinct pedestal region on
1948 the outer edge of the plasma.

1949 The usage of pedestal temperatures – discussed in Appendix D – improves two aspects
1950 of the model: the fusion power and the bootstrap current. These were shown in the
1951 results to be over-calculated and underestimated, respectively. First, pedestals have
1952 a lower core temperature than parabolic profiles with the same average value. This
1953 would cause a decrease in the total fusion power. Additionally, the pedestal’s quick
1954 drop near the plasma’s edge would boost the bootstrap current, due to the steep
1955 derivative there.

1956 These improvements could easily be added to the code, because temperature was
1957 addressed as a difficult parameter to handle from the beginning.

1958 **7.4.2 Expanding the Radiation Loss Term**

1959 The next area that would be improved by more sophisticated theory would be the
1960 radiation loss term. From before, it was pointed out that the Bremsstrahlung ra-
1961 diation was the dominant term within the plasma core and, therefore, provided a
1962 first-order approximation. Drawing the radiation losses closer to real world values
1963 would involve adding line radiation and synchrotron radiation. The former of which
1964 would be needed as high-Z impurities become more important.

1965 **7.4.3 Taking Flux Sources Seriously**

1966 The final oversimplification in the model deals with the flux sources involved in a
1967 pulsed reactor – existing at multiple level. First, the derivation of flux balance started

1968 with a simple transformer between a solenoid primary and a plasma secondary.

1969 After we developed an equation for flux balance, we compared it to ones in the
1970 literature (i.e. PROCESS) to build confidence in the model. To draw this equation
1971 closer to theirs, we then added a PF coil contribution a posteriori. This implicitly
1972 ignored coupling between most of the components. Thus leading to another source
1973 of error for the model. Moreover, this formula for PF coil contribution was much
1974 simpler than ones found in other fusion systems codes.

1975 Even though this model may be extremely simple, it does remarkably well at matching
1976 more sophisticated codes – and does so at a much faster pace. These suggestions were
1977 just ways to account for more realistic physics.

1978 Chapter 8

1979 Concluding Reactor Discussion

1980 The goal of this document was to fairly compare pulsed and steady-state tokamaks
1981 – using a single, comprehensive model. The main conclusion is that both modes of
1982 operation can produce economic reactors, assuming some technological advancement.
1983 The advancement most supported by the results was in magnet technology, as MIT is
1984 currently exploring with high-temperature superconducting (HTS) tape. Succinctly,
1985 pulsed operation can be economically competitive and the United States should put
1986 a larger research effort behind it.

1987 Although some skepticism should be allotted to these conclusions, it was shown that
1988 this simple algebraic solver was capable of matching more sophisticated frameworks
1989 with speed and ease. This model may not provide an engineer’s level of rigor for cost
1990 measurements, but does produce empirically-drawn trends applicable to a physics au-
1991 dience. Ultimately, it serves to complement higher dimension codes when researchers
1992 want to investigate new areas of reactor space.

1993 What the results truly show, though, is no economic reactor can be built using existing
1994 technology – regardless of whether it runs as pulsed or steady-state. This is why every
1995 design from the literature exceeds standard values for H and N_G . Some technological
1996 advancement is needed. These may then come from research and development into:

- 1997 • building stronger magnets using HTS tape

- 1998 • discovering reliable regimes of enhanced confinement
- 1999 • producing higher bootstrap fractions with tailored profiles
- 2000 • optimizing aspect ratio and elongation geometric parameters

2001 As mentioned, using HTS tape to nearly double achievable magnet strengths is one
2002 such advancement capable of making reactors economically viable. To best utilize
2003 this resource, though, HTS tape should only appear in the TF coils for steady-state
2004 machines and in the central solenoid for pulsed ones. This was because the opti-
2005 mum toroidal field strength for pulsed machines was found to be achievable with
2006 conventional low-temperature superconducting (LTS) magnets.

2007 Further, it was shown that past the regime of magnet strengths relevant to HTS, cost
2008 curves undergo considerably diminished returns. As such, HTS technology would be
2009 the final major magnet advancement in the current H-Mode, D-T plasma paradigm.

Appendix A

Cataloging Model Variables

A.1 Static Variables

Table A.1: List of Static Variables

Name	Value
is_pulsed	is reactor pulsed or steady-state
H	Enhancement factor for ELMy H-mode scaling
Q	Physics Gain (P_F/P_H)
ϵ	Inverse aspect ratio
κ_{95}	Elongation at 95 flux surface
δ_{95}	Triangularity at 95 flux surface
ν_n	Parabolic density peaking factor
ν_T	Parabolic temperature peaking factor
Z_{eff}	Effective charge
f_D	Dilution factor
A	Average mass number (in amus)
l_i	Internal inductance (interchangeable with ρ_m)
ρ_m	Normalized radius of current peak (interchangeable with l_i)
N_G	Greenwald density fraction
η_T	Thermal efficiency of the reactor
η_{RF}	Efficiency of the RF antenna
τ_{FT}	Time of flattop of reactor pulse
B_{CS}	Strength of magnetic field in central solenoid
$(\beta_N)_{max}$	Max allowed normalized beta normal
$(q_*)_{max}$	Minimum allowed safety factor
$(P_W)_{max}$	Maximum allowed wall loading power per surface area

A.2 Dynamic Variables

Table A.2: List of Dynamic Variables

Symbol	Name	Units
I_P	Plasma Current	MA
\overline{T}	Plasma Temperature	keV
\bar{n}	Electron Density	10^{20} m^{-3}
R_0	Major Radius	m
B_0	Magnet Strength	T

A.3 Intermediate Variables

Table A.3: List of Intermediate Variables (Noncomprehensive)

Name	Value
C_W	Cost-per-watt
W_M	Magnetic energy
P_F	Fusion power
P_Ω	Resistive power
P_{BR}	Bremsstrahlung power
P_κ	Conductive heat losses
P_W	Wall loading
β_N	Plasma beta normal
q_*	Kink safety factor
V	Tokamak volume in cubic meters
f_{BS}	Bootstrap current fraction
f_{CD}	Current drive fraction
f_{ID}	Indirect drive current fraction
\bar{p}	Volume-averaged plasma pressure
$\langle \sigma v \rangle$	Bosch-Hale fusion reactivity
R_P	Plasma resistance
τ_E	Confinement time
a	Tokamak minor radius
b	Blanket thickness
c	TF coil thickness
d	Central solenoid thickness
R_{CS}	Central solenoid inner radius

2015 Appendix B

2016 Simulating with Fussy.jl

2017 Fussy.jl is a 0-D fusion systems code written using the Julia language. The reason for
2018 choosing Julia over say Matlab and Python was due to metaprogramming concerns
2019 and its tight-knit computational community, respectively. Incorporating the model
2020 used throughout this paper, the code is quick to run and matches more sophisticated
2021 frameworks with high fidelity.

2022 This chapter will be broken down into three steps. The first is getting a user up
2023 and running with the code. Once the user gets to this point, hopefully they will
2024 wonder how the code is structured. This will be the second step. The final step
2025 will be explaining the various functions callable on reactor objects – the atomic data
2026 structure for Fussy.jl.

2027 B.1 Getting the Code to Work

2028 The hardest step of any codebase is getting it up and running. These instructions
2029 should get a user to a point where they are a few internet searches away from a
2030 working copy of Fussy.jl. As an aide, you can view an interactive collection of Fussy.jl
2031 Jupyter notebooks at the following website:

2032 www.fusion.codes

2033 Although `fusion.codes` is a nice tool for viewing this document's results, it is a little
2034 slow for producing new data – and it also lacks a method for storing it. Therefore,
2035 an advanced user should first download a copy of Julia from:

2036 julialang.org/downloads

2037 Currently the `Fussy.jl` codebase is written using `v0.6`, but should be `v1.0` compatible
2038 by 2019. Using Julia nomenclature, `Fussy.jl` is a Julia package. It can be cloned using
2039 Julia conventions from the following Github repository:

2040 <https://github.com/djseagal/Fussy.jl.git>

2041 Once the `Fussy.jl` package has been cloned into your Julia package library, you should
2042 be able to access it through the Julia REPL or a Jupyter notebook. You can now
2043 reproduce every plot in this text. A quick test to see if your code works is:

```
2044     using Fussy
2045     cur_reactor = Reactor(15)
2046     @assert cur_reactor.T_bar == 15
2047     println("It works!")
```

2048 If the code works, you should get a "It works!" message as output.

2049 B.2 Sorting out the Codebase

2050 Assuming the user got to this section, the code works and now you want to know
2051 what you can do with it. The place to start is in the `src` folder, again viewable online
2052 at:

2053 git.io/tokamak

2054 Within the `src` folder are several subfolders as well as a few files (e.g. `Fussy.jl` and
2055 `defaults.jl`). In an attempt to not bore the reader, we will be painting with thick
2056 brushstrokes. Further, the `methods` subfolder will be the topic of the next section –
2057 as most involve calls on a reactor object.

2058 **B.2.1 Typing out Structures**

2059 The place to start in any modeling framework is its data structures. These type
2060 definitions allow the building of nested hierarchies of constructed objects. The most
2061 atomic of these is the Reactor struct, but several other ones allow for solving broader
2062 scoped questions (i.e. Scans, Sensitivities, and Samplings.)

2063 **The Reactor Structure**

2064 Reactors are the most atomic data structure in this fusion systems model. They
2065 store all the fields needed to represent a reactor as it exists in reactor space. This
2066 obviously includes its temperature, current, and radius, but also includes derived
2067 quantities, such as the cost-per-watt and bootstrap fraction. They can be initialized,
2068 solved, updated, and honed. Most other data structures are just wrappers to hold
2069 these reactors – they are described next.

2070 **The Scan Structure**

2071 A Scan object is a collection of reactors made from scanning a list of temperatures.
2072 For example, a scan of five temperatures from 5 keV to 25 keV would result in several
2073 arrays of five reactors. Most often, one of these lists would correspond to beta reactors,
2074 one to kink reactors, and one to wall loading reactors. There may then be fewer than
2075 five reactors in a list if some of the reactors are invalid or fundamentally unsolvable.
2076 This is the data structure that produces the various comparison plots in the results.

2077 **The Sensitivity Structure**

2078 Sensitivity studies are how computationalists test the effect of changing a variable
2079 over multiple values – i.e. do a 20% sensitivity around the H factor. Like Scans,
2080 Sensitivities store various lists of reactors, each corresponding to an interesting data
2081 point. These include limit reactors where the beta limit and kink limit are just

2082 satisfied or when the beta limit and wall loading are just satisfied. Additionally, they
2083 include the minimum capital cost reactors and the minimum cost-per-watt ones.

2084 **The Sampling Structure**

2085 The Sampling struct was created to do simple Monte Carlo runs over a reactor's static
2086 values. While sensitivities only allow one variable to change at a time, samplings
2087 randomly assign a list of variables to some neighborhood of possible values. These
2088 are how the scatter plots are made. Succinctly, where sensitivity studies show local
2089 changes to variables, Monte Carlo samplings show global trends in reactor design.

2090 **The Equation Structure**

2091 In order to store the various equations from Table 5.1 is the Equation Struct. It stores
2092 the γ exponents for: R_0 , B_0 , and I_P . – as well as the function representing $G(\bar{T})$.
2093 Repeated these are the unknowns in:

$$R_0^{\gamma_R} \cdot B_0^{\gamma_B} \cdot I_P^{\gamma_I} = G(\bar{T}) \quad (5.3)$$

2094 Concretely, there are 16 objects that use this struct – one for each equation (e.g. for
2095 fusion power, the beta limit, and temperature assignment).

2096 **The Equation Set Structure**

2097 The step up from the Equation struct are the Equation Sets. These collections of
2098 three equations allow R_0 , B_0 , and maybe I_P to be substituted out of the current
2099 balance root-solving equation. This is where Eqs. (5.4) to (5.10) come into play.

2100 B.2.2 Referencing Input Decks and Solutions

2101 With more than twenty static variables in the model, the range of tokamak reactors
2102 is basically infinite. To help users build a net of designs to explore reactor space are
2103 seven input decks. These are the ones given in the results: ARC, ACT I /II, DEMO
2104 Steady/Pulsed, Proteus and Charybdis. Coupled with the non-prototype reactors are
2105 solution reactors that store various quantities from the original papers (e.g. P_F , f_{BS} ,
2106 R_0). These are how the comparison tables were constructed.

2107 B.2.3 Acknowledging Utility Functions

2108 For the uninitiated, utility functions are grab bag functions that do not really belong
2109 in a codebase – but do anyway. This sentiment does not mean they are worthless,
2110 just not fusion related at all. In Fussy.jl, the most notable are a normalized integral
2111 calculator, a filter that includes numeric tolerances, and a robust root solver.

2112 Although since incorporated into the official Roots.jl package, `find_roots` allows
2113 finding an arbitrary number of roots within a bounded range. This was needed
2114 because many roots can be found at various levels of the reactor solving problem –
2115 i.e. for I_P , \bar{T} , η_{CD} , etc.

2116 B.2.4 Mentioning Base Level Files

2117 In addition to subdirectories within the `src` folder are three files: Fussy.jl, abstracts.jl,
2118 and defaults.jl. Fussy.jl is the package’s main file that actually stores the Fussy
2119 module. While, abstracts.jl stores various abstract structures that help clean up
2120 other files.

2121 Finally, defaults.jl stores various default values that are important to the codebase.
2122 For example, this is where the various scaling law exponents are stored. It is also
2123 where the bounding values for the different root solving problems live. These include
2124 minimum and maximum values for: I_P , \bar{T} , η_{CD} .

2125 Now that a majority of the files have been discussed, we can turn to the reactor
2126 methods. These constitute most of the interesting functionality within the codebase.

2127 **B.3 Delving into Reactor Methods**

2128 The reactor is the most atomic data structure in this model. It therefore makes
2129 sense that it has many instance methods. These include all the coefficients, fluxes,
2130 powers, etc. It also includes methods that solve a reactor, perform a match on some
2131 field's value, or converge η_{CD} to self-consistency. The various subdirectories within
2132 the `src/methods/reactors` folder will now be discussed.

2133 **Calculations**

2134 The calculation subdirectory of reactor methods are used to set various important
2135 values in the solver. For dynamic variables, these include: \bar{n} , R_0 , B_0 , and I_P . This
2136 folder also includes the calculation of the Bosch-Hale reactivity and the Ehst-Karney
2137 current drive efficiency.

2138 **Coefficients and Composites**

2139 The coefficients and composites directories correspond to the model's static and dy-
2140 namic coefficients, respectively. For clarity, static coefficients, including K_n and K_{CD} ,
2141 were labeled with a K. Whereas, dynamic coefficients then started with G's – i.e. G_{PB}
2142 and G_V .

2143 **Fluxes and Powers**

2144 Within flux balance and power balance were around a dozen terms or sub-terms.
2145 Although not directly used in the conservation equations, sub-terms are used to com-
2146 pare the model to ones from the literature. For clarity, fluxes include: Φ_{CS} , Φ_{PF} ,
2147 Φ_{RU} , Φ_{FT} , Φ_{res} , and Φ_{ind} . The powers, then, include: P_F , P_{BR} , P_κ , P_{src} , P_W , etc.

2148 Profiles

2149 The next collection of reactor methods are the various profiles. Most obviously, these
2150 include radial plasma profiles for density, temperature, and current. However, this
2151 folder also includes the magnetic field strength as a function of radius – as was used
2152 within current drive efficiency calculations.

2153 Geometries

2154 Additionally, there are many geometric relations. These include the various tokamak
2155 thicknesses: a, b, c, d – as well as the radius and height of the central solenoid. This
2156 group also includes the volume, perimeter, surface area, and cross-sectional area.
2157 It also includes the many subscripted fields. For example, the elongation (i.e. κ_{95})
2158 includes the following alternative definitions: κ_X , κ_P , and κ_T

2159 Formulas

2160 The final set of reactor methods are formulas that do not really fit anywhere else.
2161 If a method is not related to geometry, power, calculations, etc, it ends up here.
2162 For example, this group includes: β_N , f_{BS} , C_W , and τ_E . Total, there are around 25
2163 formulas – as of the writing of this document.

2164 B.4 Demonstrating Code Usage

2165 Now that the Fussy.jl package has been described in detail, the final step is showing a
2166 simple example that can recreate a figure from the results chapter. This will closely
2167 match the Jupyter notebook available at:

2168 www.git.io/fussy_sensitivity

2169 Our goal will be to make a cost curve for the ARC reactor as a function of H – a so
2170 called sensitivity study plot.

2171 B.4.1 Initializing the Workspace

2172 The first step for any Fussy.jl Jupyter notebook is loading the required packages – i.e.
2173 the Fussy.jl and Plots.jl packages. This can be done using the following commands:*

```
2174     addprocs(6)
2175     @everywhere using Fussy
2176     using Plots
```

2177 The Plots.jl package may take a minute to load – similar to Matlab’s initial boot
2178 time. If the kernel raises an error about Plots.jl not being installed, use the following
2179 lines:

```
2180     import Pkg
2181     Pkg.add("Plots")
```

2182 B.4.2 Running a Study

2183 Now that the necessary packages have been loaded, we can move on to actually
2184 running the sensitivity study. We will split this command into two steps to make it
2185 more explicit.

2186 The first step will be making several variables that store: boolean flags, numbers, and
2187 symbols – which are like strings, but prefaced with a colon (:) instead of surrounded
2188 by double quotes (").

```
2189     cur_param = :H
2190     cur_deck = :arc
2191     is_pulsed = false
2192     is_consistent = true
2193     cur_sensitivity = 1.0
2194     cur_num_points = 41
```

*The `addprocs` and `@everywhere` commands are to parallelize the code. This is because `addprocs(6)` activates 6 worker processes and `@everywhere Fussy.jl` adds Fussy.jl to the main kernel and worker processes.

2195 These six variables almost completely describe a sensitivity study. The first two
 2196 saw we are using the ARC reactor deck and running a sensitivity over the H-factor
 2197 parameter. Next, the two boolean values refer to the reactor (1) being treated as
 2198 pulsed or steady-state and (2) whether to handle η_{CD} self-consistently.* Ergo, what
 2199 these two flags do is make sure ARC is being handled as a steady-state reactor with
 2200 a self-consistent η_{CD} . The last two variables are then ways to change the sensitivity
 2201 of the study (with 1.0 \rightarrow 100%) and the number of reactors it will produce (i.e. 41).
 2202 Now all six of these variables can be piped into a call to the `Study` struct to start
 2203 running the sensitivity study:

```
2204     cur_study = Study(  

  2205         cur_param,  

  2206         deck = cur_deck,  

  2207         is_pulsed = is_pulsed,  

  2208         is_consistent = is_consistent,  

  2209         sensitivity = cur_sensitivity,  

  2210         num_points = cur_num_points  

  2211     )
```

2212 Note here that the equal signs inside the parentheses are called keyword arguments,
 2213 which are common to most modern programming languages. After executing the
 2214 command, the code will need to run for a few minutes.

2215 B.4.3 Extracting Results

2216 At this point, a user should have a completed sensitivity study they wish to plot.
 2217 To make the plot useful, the study data structure first has to be unpacked and its
 2218 contents cleaned. This is the goal of this subsection.

2219 First and foremost, a study has four families of reactors within it: beta-wall (i.e.
 2220 "wall"), beta-kink (i.e. "kink"), minimum capital cost (i.e. "W_M"), and minimum

*Note that, currently, a pulsed reactor cannot be self-consistent in η_{CD} – it therefore causes an error.

2221 cost-per-watt (i.e. "cost"). Therefore, we will extract these reactor lists into a new
2222 dictionary data structure:

```
2223     cur_dict = Dict()  
2224  
2225     cur_dict["Beta-Wall"] = cur_study.wall_reactors  
2226     cur_dict["Beta-Kink"] = cur_study.kink_reactors  
2227  
2228     cur_dict["Min Cost-per-Watt"] = cur_study.cost_reactors  
2229     cur_dict["Min Capital Cost"] = cur_study.W_M_reactors
```

2230 Next, we will want to filter out all the invalid reactors that constitute non-physically
2231 realizable ones. These would likely be reactors that could fit in your hand or take up
2232 a whole city block.

```
2233     for (cur_key, cur_value) in cur_dict  
2234         cur_dict[cur_key] = filter(  
2235             cur_reactor -> cur_reactor.is_valid,  
2236             deepcopy(cur_value)  
2237         )  
2238     end
```

2239 B.4.4 Plotting Curves

2240 Our goal is now to turn our unpacked, clean reactor lists into plots – i.e. measuring
2241 costs-per-watt as a function of H. For simplicity, this will lack a lot of the features
2242 shown in the Jupyter notebook from the beginning of the section. Additionally, we
2243 will be doing it in an iterative process made possible by the Plots.jl framework.

2244 The first step is simply making a plot object

```
2245     cur_plot = plot()
```

2246 After execution, this should produce the plank 2-D plot shown in Fig. B-1.

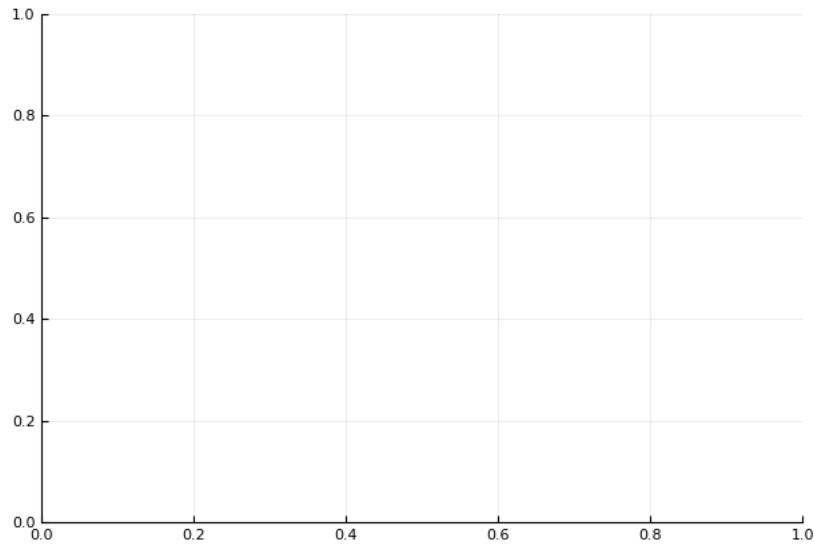


Figure B-1: A Blank Plot

A simple 2-D plot with no labels or data.

2247 Next we will add a simple title and labels for the axes:

```
2248     title!("ARC")
```

```
2249
```

```
2250     xlabel!("H")
```

```
2251     ylabel!("Cost")
```

2252 The exclamation marks ensure this title and the labels are added to the `cur_plot`.

2253 Upon execution, you should see a plot with this information (Fig. B-2).

2254 Now we will loop over the dictionary of reactors and add them one at a time.

```
2255     for (cur_key, cur_value) in cur_dict
```

```
2256         cur_x = map(cur_reactor -> cur_reactor.H, cur_value)
```

```
2257         cur_y = map(cur_reactor -> cur_reactor.cost, cur_value)
```

```
2258         plot!(cur_x, cur_y, label=cur_key)
```

```
2259     end
```

```
2260     plot!()
```

2261 This results in the not very useful plot shown in Fig. B-3. Note that each label is

2262 exactly the key assigned to it in `cur_dict`.

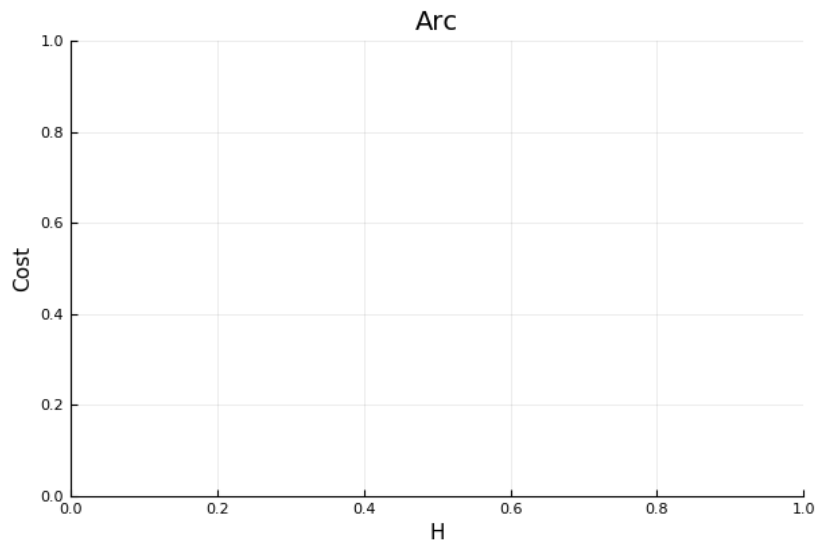


Figure B-2: An Empty Plot

A simple 2-D plot with labels, but no data.

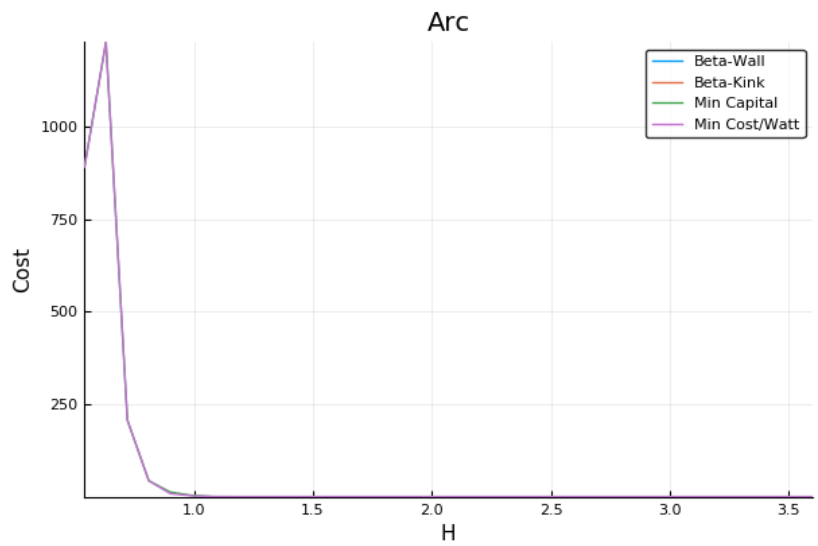


Figure B-3: An Unscaled Plot

A simple 2-D plot with Bad Limits.

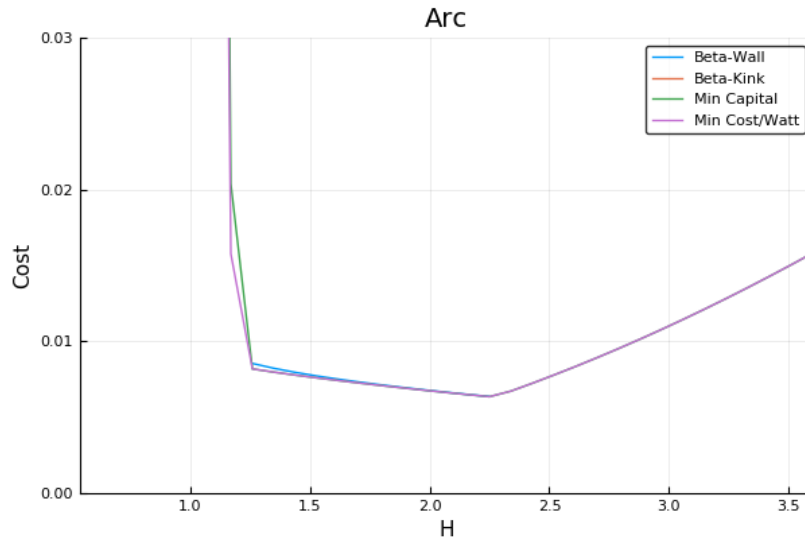


Figure B-4: A Scaled Plot

An example plot showing cost as a function of the H factor.

2263 The final step is adding proper limits to make what is going on obvious to the reader:

2264 `ylims!(0, 0.03)`

2265 The addition of which can be seen in Fig. B-4.

2266 This completes the example. At this point, you should now be able to use every

2267 feature of Fussy.jl. Good luck!

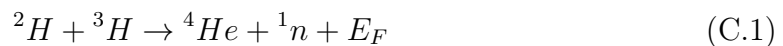
2268 Appendix C

2269 Discussing Fusion Power

2270 In a tokamak reactor, the main source of output power is fusion. Therefore, this
2271 chapter goes over a quick background of fusion power and describes a method for
2272 how to calculate the reactivity term that appears inside it. The particular method
2273 used for this reactivity approximation was done by Bosch and Hale in 1992.⁴⁶

2274 C.1 Theoretical Background

2275 The natural place to start when introducing fusion energy is the binding energy per
2276 nucleon curve shown in Fig. C-1. As can be seen, this function reaches a maximum
2277 value around the element Iron (A=56). What this means at a basic level is: elements
2278 lighter than iron can *fuse* into a heavier one (i.e. hydrogens into helium), whereas
2279 heavier elements can *fission* into lighter ones (e.g. uranium into krypton and barium).
2280 This is what differentiates fission (uranium-fueled) reactors from fusion (hydrogen-
2281 fueled) ones. For fusion reactors, the most common reaction in a first-generation
2282 tokamak will be:



2283

$$E_F = 17.6 \text{ MeV} \quad (\text{C.2})$$

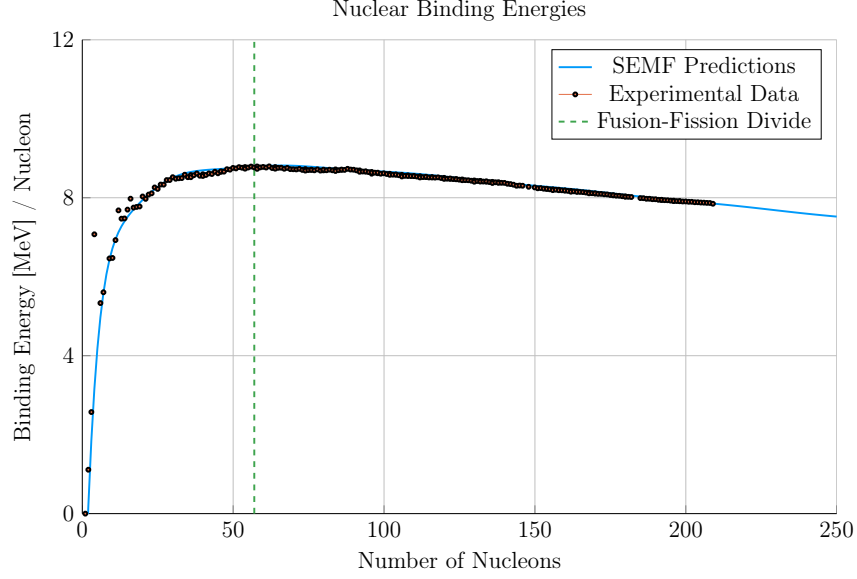


Figure C-1: Comparing Nuclear Fusion and Fission

The binding energy per nucleon is what differentiates nuclear fusion from fission. Nuclei heavier than Iron fission (e.g. Uranium), while light ones – such as Hydrogen – fuse.

2284

2285 What this reaction (shown in Fig. C-2) describes is two isotopes of hydrogen – i.e.
 2286 deuterium and tritium – fusing into a heavier element, helium, while simultaneously
 2287 ejecting a neutron. The entire energy of the fusion reaction (E_F) is then divvied
 2288 up 80-20 between the neutron and helium, respectively. Quantitatively, the helium
 2289 (often referred to as an alpha particle) receives 3.5 MeV.

$$P_n = 0.8 \cdot P_F \quad (\text{C.3})$$

2290

$$P_\alpha = 0.2 \cdot P_F \quad (\text{C.4})$$

2291 The final point to make is the main difference between the two fusion products:
 2292 helium (i.e. the alpha particle) and the neutron. First, neutrons lack a charge – they
 2293 are neutral. This means they cannot be confined with magnetic fields. As such, they
 2294 simply move in straight lines until they collide with other particles. As the structure

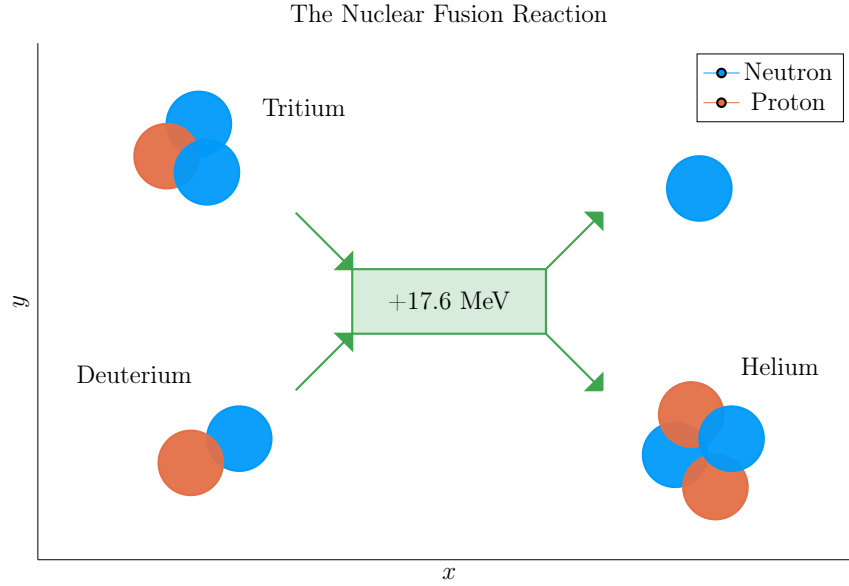


Figure C-2: The D-T Fusion Reaction

In a first generation tokamak reactor, the main source of energy will come from two hydrogen isotopes fusing into a helium particle – and ejecting a 14.1 MeV neutron.

of a tokamak is mainly metal, the neutron is much more likely to collide there than the gaseous plasma, which is orders of magnitude less dense. Conversely, alpha particles are charged – when stripped of their electrons – and can therefore be kept within the plasma using magnets. What this means practically is that of the 17.6 MeV that comes from every fusion reaction, only 3.5 MeV remains inside the plasma (within the helium particle species).

C.2 Bosch-Hale Reactivity

The formula for fusion power used in this model makes use of a reactivity term – (σv) .⁵

$$P_F = \int E_F n_D n_T \langle \sigma v \rangle d\mathbf{r} \quad (\text{C.5})$$

Summarizing the work of Section 2.2.3, this fusion power volume integral can be reduced to a 0-D form – assuming the geometry prescribed by this model:

$$P_F = K_F \cdot (\bar{n}^2 R_0^3) \cdot (\sigma v) \quad [MW] \quad (C.6)$$

$$(\sigma v) = 10^{21} (1 + \nu_n)^2 \int_0^1 (1 - \rho^2)^{2\nu_n} \langle \sigma v \rangle \rho d\rho \quad (C.7)$$

$$K_F = 278.3 (f_D^2 \epsilon^2 \kappa g) \quad (C.8)$$

2304 This reactivity term (or volumetric fusion reaction rate) can then be approximated
2305 by the Bosch-Hale parameterization, with coefficients given in Table C.1.^{46,47}

$$\langle \sigma v \rangle = C_1 \cdot \theta \cdot \exp(-3\xi) \cdot \sqrt{\frac{\xi}{m_\mu c^2 T^3}} \quad [\text{m}^3/\text{s}] \quad (C.9)$$

$$\theta = T \cdot \left(1 - \frac{T(C_2 + T(C_4 + TC_6))}{1 + T(C_3 + T(C_5 + TC_7))} \right)^{-1} \quad (C.10)$$

$$\xi = \left(\frac{B_G^2}{4\theta} \right)^{1/3} \quad (C.11)$$

2308 For D-T (Deuterium-Tritium) fuel within a standard fusion temperature regime (i.e.
2309 $T \in [10, 20]$ keV), this can be simplified to:⁴⁷

$$\langle \sigma v \rangle_{\text{DT}} = 1.1 \times 10^{-24} \cdot T^2 \quad [\text{m}^3/\text{s}] \quad (C.12)$$

2310 In our model, each appearance of T is set to the radial profile defined earlier – as it
2311 appears inside an integral.

2312 Example tabulations for this reactivity are given in Table C.2.^{46–48}

Table C.1: Bosch-Hale Parametrization Coefficients

	${}^2\text{H}(\text{d,n}){}^3\text{He}$	${}^2\text{H}(\text{d,p}){}^3\text{H}$	${}^3\text{H}(\text{d,n}){}^4\text{He}$	${}^3\text{He}(\text{d,p}){}^4\text{He}$
B_G [keV $^{1/2}$]	31.3970	31.3970	34.3827	68.7508
$m_\mu c^2$ [keV]	937 814	937 814	1 124 656	1 124 572
C_1	5.43360×10^{-12}	5.65718×10^{-12}	1.17302×10^{-9}	5.51036×10^{-10}
C_2	5.85778×10^{-3}	3.41267×10^{-3}	1.51361×10^{-2}	6.41918×10^{-3}
C_3	7.68222×10^{-3}	1.99167×10^{-3}	7.51886×10^{-2}	-2.02896×10^{-3}
C_4	0.0	0.0	4.60643×10^{-3}	-1.91080×10^{-5}
C_5	-2.96400×10^{-6}	1.05060×10^{-5}	1.35000×10^{-2}	1.35776×10^{-4}
C_6	0.0	0.0	-1.06750×10^{-4}	0.0
C_7	0.0	0.0	1.36600×10^{-5}	0.0
Valid range (keV)	$0.2 < T_i < 100$	$0.2 < T_i < 100$	$0.2 < T_i < 100$	$0.5 < T_i < 190$

Table C.2: Tabulated Bosch-Hale Reactivities

T (keV)	${}^2\text{H}(\text{d,n}){}^3\text{He}$	${}^2\text{H}(\text{d,p}){}^3\text{H}$	${}^3\text{H}(\text{d,n}){}^4\text{He}$	${}^3\text{He}(\text{d,p}){}^4\text{He}$
1.0	9.933×10^{-29}	1.017×10^{-28}	6.857×10^{-27}	3.057×10^{-32}
1.5	8.284×10^{-28}	8.431×10^{-28}	6.923×10^{-26}	1.317×10^{-30}
2.0	3.110×10^{-27}	3.150×10^{-27}	2.977×10^{-25}	1.399×10^{-29}
3.0	1.602×10^{-26}	1.608×10^{-26}	1.867×10^{-24}	2.676×10^{-28}
4.0	4.447×10^{-26}	4.428×10^{-26}	5.974×10^{-24}	1.710×10^{-27}
5.0	9.128×10^{-26}	9.024×10^{-26}	1.366×10^{-23}	6.377×10^{-27}
8.0	3.457×10^{-25}	3.354×10^{-25}	6.222×10^{-23}	7.504×10^{-26}
10.0	6.023×10^{-25}	5.781×10^{-25}	1.136×10^{-22}	2.126×10^{-25}
12.0	9.175×10^{-25}	8.723×10^{-25}	1.747×10^{-22}	4.715×10^{-25}
15.0	1.481×10^{-24}	1.390×10^{-24}	2.740×10^{-22}	1.175×10^{-24}
20.0	2.603×10^{-24}	2.399×10^{-24}	4.330×10^{-22}	3.482×10^{-24}

Appendix D

Selecting Plasma Profiles

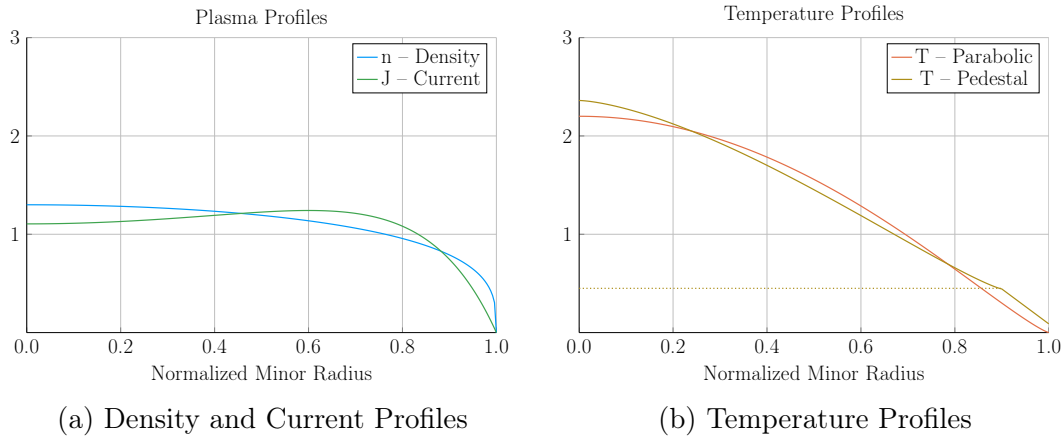


Figure D-1: Radial Plasma Profiles

The three most fundamental properties of a fusion plasma are its temperature, density, and current. These profiles allow the model to reduce from three dimensions to half of one.

D.1 Density — n

The Density is important to us. We use it in the Greenwald density limit, so it should be clean in both line-averaged and volume-averaged forms. Because of its flat profile,

2318 a parabola is a good approximation for H-mode pulses:

$$n(\rho) = \bar{n} \cdot (1 + \nu_n) \cdot (1 - \rho^2)^{\nu_n} \quad (\text{D.1})$$

2319 The line average density is related to \bar{n} through:

$$\hat{n} = \bar{n} \cdot \left(\frac{\pi^{1/2}}{2} \right) \cdot \frac{\Gamma(\nu_n + 2)}{\Gamma(\nu_n + 3/2)} \quad (\text{D.2})$$

2320 The convenience of this function comes from how the volumetric average comes out.

2321 To relate this to the volume integral, we use:

$$\bar{x} = \frac{1}{V} \int x(\rho) dV \quad (\text{D.3})$$

2322 For a normalized radial profile that does not depend on angle,

$$V = \int_0^1 \rho d\rho = 1/2 \quad (\text{D.4})$$

2323 Then, when $x = n$,

$$\bar{n} = 2 \int_0^1 n(\rho) \rho d\rho = \bar{n} \quad (\text{D.5})$$

2324 Additionally, the Greenwald Density limit that we will use throughout,

$$\hat{n} = N_G \cdot \left(\frac{I_M}{\pi a^2} \right) \quad (\text{D.6})$$

can now be written in the following form:

$$\bar{n} = K_n \cdot \left(\frac{I_M}{R_0^2} \right) \quad (\text{D.7})$$

$$K_n = \frac{2 N_G}{\epsilon^2 \pi^{3/2}} \cdot \left(\frac{\Gamma(\nu_n + 3/2)}{\Gamma(\nu_n + 2)} \right) \quad (\text{D.8})$$

2325 D.2 Temperature – T

2326 The Temperature is the swept variable in our model framework. Therefore, it's the
 2327 one we can allow people to be the most cavalier with. Additionally, as temperature
 2328 profiles are highly peaked, their pedestal region is sometimes wrongfully neglected
 2329 with a parabola.

$$T(\rho) = \bar{T} \cdot (1 + \nu_T) \cdot (1 - \rho^2)^{\nu_T} \quad (\text{D.9})$$

2330 Therefore, our model sometimes treats the system as if it had a pedestal region. This
 2331 is mainly for the bootstrap current and fusion power, which were previously known
 2332 to misalign and overshoot, respectively.

$$T(\rho) = \begin{cases} T_{para} , & x \in [0, \rho_{ped}] \\ T_{line} , & x \in (\rho_{ped}, 1] \end{cases} \quad (\text{D.10})$$

Where the piecewise functions are given by,

$$T_{para} = T_{ped} + (T_0 - T_{ped}) \cdot \left(1 - \left(\frac{\rho}{\rho_{ped}} \right)^{\lambda_T} \right)^{\nu_T} \quad (\text{D.11})$$

$$T_{line} = T_{sep} + (T_{ped} - T_{sep}) \cdot \left(\frac{1 - \rho}{1 - \rho_{ped}} \right) \quad (\text{D.12})$$

2333 This temperature profile is related to the volume-averaged temperature through,

$$\bar{T} \cdot V = \int_0^{\rho_{ped}} T_{para}(\rho) \rho d\rho + \int_{\rho_{ped}}^1 T_{line}(\rho) \rho d\rho \quad (\text{D.13})$$

2334 Starting with the second integral,

$$\int_{\rho_{ped}}^1 T_{line}(\rho) \rho d\rho = \frac{1}{3} \cdot (1 - \rho_{ped}) \cdot ((T_{sep} + T_{ped}/2) + \rho_{ped} \cdot (T_{ped} + T_{sep}/2)) \quad (\text{D.14})$$

The first integral can be handled by breaking it into to,

$$\int_0^{\rho_{ped}} T_{para}(\rho) \rho d\rho = T_{ped} \cdot \int_0^{\rho_{ped}} \rho d\rho + (T_0 - T_{ped}) \cdot \int_0^{\rho_{ped}} \left(1 - \left(\frac{\rho}{\rho_{ped}}\right)^{\lambda_T}\right)^{\nu_T} \cdot \rho d\rho \quad (D.15)$$

2335 The first sub-integral is then,

$$T_{ped} \cdot \int_0^{\rho_{ped}} \rho d\rho = \frac{T_{ped} \rho_{ped}^2}{2} \quad (D.16)$$

Utilizing the following transformation,

$$u = \frac{\rho}{\rho_{ped}} \quad (D.17)$$

$$d\rho = \rho_{ped} du \quad (D.18)$$

$$u(\rho = \rho_{ped}) = 1 \quad (D.19)$$

2336 The second sub-integral becomes (assuming independence from T_0 and T_{ped}),

$$(T_0 - T_{ped}) \cdot \rho_{ped}^2 \cdot \int_0^1 (1 - u^{\lambda_T})^{\nu_T} \cdot u du \quad (D.20)$$

2337 Where:

$$\int_0^1 (1 - u^{\lambda_T})^{\nu_T} \cdot u du = \frac{\Gamma(1 + \nu_T) \Gamma\left(\frac{2}{\lambda_T}\right)}{\lambda_T \cdot \Gamma\left(1 + \nu_T + \frac{2}{\lambda_T}\right)} \quad (D.21)$$

2338 We are now in a position to solve for T_0 in terms of \bar{T} :

$$T_0 = T_{ped} + \frac{\bar{T} - K_{TU}}{K_{TD}} \quad (D.22)$$

2339

$$K_{TU} = T_{ped} \rho_{ped}^2 + \frac{(1 - \rho_{ped})}{3} \cdot ((2T_{sep} + T_{ped}) + \rho_{ped} \cdot (2T_{ped} + T_{sep})) \quad (D.23)$$

2340

$$K_{TD} = \rho_{ped}^2 \cdot \left(\frac{2}{\lambda_T} \right) \cdot \frac{\Gamma(1 + \nu_T) \Gamma\left(\frac{2}{\lambda_T}\right)}{\Gamma\left(1 + \nu_T + \frac{2}{\lambda_T}\right)} \quad (D.24)$$

2341 Which although not pretty, can be plugged into the original equation.

2342 D.3 Pressure – p

2343 The first point to make is that we are not using the same temperature profile for
 2344 the pressure as for the temperature. This is because it would lead to hypergeometric
 2345 functions that are not worth the headache.

2346 As most of the pressure is at the center, we use simple parabolic profile. This leads
 2347 to:

$$\bar{p} = 0.1581 (1 + f_D) \frac{(1 + \nu_n)(1 + \nu_T)}{1 + \nu_n + \nu_T} \bar{n} \bar{T} \quad [atm] \quad (D.25)$$

2348 D.4 Bootstrap Current – f_{BS}

2349 We start with,

$$f_{BS} = \frac{I_{BS}}{I_P} = \frac{2\pi a^2 \kappa}{I_P} \int_0^1 J_B \rho d\rho \quad (D.26)$$

2350 Expanding the previous equation using the following relations,

$$J_B = -4.85 \cdot R_0 \epsilon^{1/2} \cdot \left(\frac{\rho^{1/2} n T}{d\psi/d\rho} \right) \cdot \left(\frac{dn/d\rho}{n} + 0.54 \cdot \frac{dT/d\rho}{T} \right) \quad (D.27)$$

2351

$$\frac{d\psi}{d\rho} = \frac{\mu_0 R_0 I_P}{\pi} \cdot \left(\frac{\kappa}{1 + \kappa^2} \right) \cdot b_p(\rho) \quad (D.28)$$

2352 Yields:

$$f_{BS} = -K_{BS} \int_0^1 (1 - \rho^2)^{\nu_n} \cdot \left(\frac{\rho^{3/2}}{b_p(\rho)} \right) \cdot \left(\frac{T}{n} \cdot \frac{dn}{d\rho} + 0.54 \cdot \frac{dT}{d\rho} \right) d\rho \quad (D.29)$$

2353

$$K_{BS} = K_n \cdot \left(\frac{2\pi^2 \cdot 4.85 \cdot \epsilon^{5/2}}{\mu_0} \right) \cdot (1 + \nu_n) \cdot (1 + \kappa^2) \quad (D.30)$$

2354 Here, b_p comes from:

$$b_p(\rho) = \frac{-e^{\gamma\rho^2}(\gamma\rho^2 - 1 - \gamma) - 1 - \gamma}{\rho(e^\gamma - 1 - \gamma)} \quad (D.31)$$

2355 And the value of γ comes from the the normalized internal inductance:

$$l_i = \frac{4\kappa}{1 + \kappa^2} \int_0^1 b_p^2 \frac{d\rho}{\rho} \quad (D.32)$$

2356 With our profiles,

$$-\left(\frac{T}{n} \cdot \frac{dn}{d\rho}\right) = 2\nu_n \cdot \left(\frac{T \cdot \rho}{1 - \rho^2}\right) \quad (D.33)$$

2357 While treating temperature differently results in,

$$-\left(\frac{dT}{d\rho}\right)_{para} = \left(\frac{T_0 - T_{ped}}{\rho_{ped}^{\lambda_T}}\right) \cdot (\nu_T \lambda_T) \cdot \rho^{\lambda_T-1} \cdot \left(1 - \left(\frac{\rho}{\rho_{ped}}\right)^{\lambda_T}\right)^{\nu_T-1} \quad (D.34)$$

2358

$$-\left(\frac{dT}{d\rho}\right)_{line} = \left(\frac{T_{ped} - T_{sep}}{1 - \rho_{ped}}\right) \quad (D.35)$$

2359 Where we will be using the new symbol definition,

$$\partial T = -\left(\frac{dT}{d\rho}\right) \quad (D.36)$$

Which ultimately allows us to write,

$$f_{BS} = K_{BS} \int_0^1 H_{BS} d\rho \quad (D.37)$$

$$H_{BS} = (1 - \rho^2)^{\nu_n-1} \cdot \left(\frac{\rho^{3/2}}{b_p(\rho)}\right) \cdot \left(2\nu_n \cdot \rho \cdot T + 0.54 \cdot (1 - \rho^2) \cdot \partial T\right) \quad (D.38)$$

Where the values of T are determined through,

$$T_{para} = T_{ped} + (T_0 - T_{ped}) \cdot \left(1 - \left(\frac{\rho}{\rho_{ped}} \right)^{\lambda_T} \right)^{\nu_T} \quad (D.39)$$

$$T_{line} = T_{sep} + (T_{ped} - T_{sep}) \cdot \left(\frac{1 - \rho}{1 - \rho_{ped}} \right) \quad (D.40)$$

And the values of ∂T are:

$$\partial T_{para} = \left(\frac{T_0 - T_{ped}}{\rho_{ped}^{\lambda_T}} \right) \cdot (\nu_T \lambda_T) \cdot \rho^{\lambda_T - 1} \cdot \left(1 - \left(\frac{\rho}{\rho_{ped}} \right)^{\lambda_T} \right)^{\nu_T - 1} \quad (D.41)$$

$$\partial T_{line} = \left(\frac{T_{ped} - T_{sep}}{1 - \rho_{ped}} \right) \quad (D.42)$$

2360 D.5 Volume Averaged Powers

2361 The first thing to consider in a fusion reactor is power balance. It is what separates
2362 a net power producing reactor from a power-consuming research device.

$$P_\alpha + P_H = P_\kappa + P_B \quad (D.43)$$

$$P_\alpha = \frac{P_F}{5} \quad (D.44)$$

$$P_H = \frac{P_F}{Q} \quad (D.45)$$

$$P_\kappa = \frac{3}{2\tau_E} \int p \, d\mathbf{r} \quad [3D] \quad (D.46)$$

$$P_B = 5.35e3 Z_{eff} \int n_{\bar{n}}^2 \sqrt{T} \, d\mathbf{r} \quad [3D] \quad (D.47)$$

2363 As mentioned before, P_F is handled by (σv) and therefore the lefthand-side uses the
2364 pedestal temperature profiles. However, for the same reasons as discussed earlier, the
2365 righthand-side (P_κ and P_B) need to use the parabolic temperature profiles.

Using the parabolic profiles (for n and T) gives for the Bremsstrahlung radiation,

$$P_B = K_B \cdot \left(R_0^3 \bar{n}^2 \sqrt{\bar{T}} \right) \quad [MW] \quad (D.48)$$

$$K_B = 0.1056 \cdot Z_{eff} \cdot (\epsilon^2 \kappa g) \cdot \frac{(1 + \nu_n)^2 (1 + \nu_T)^{1/2}}{1 + 2 \nu_n + 0.5 \nu_T} \quad (D.49)$$

And a similar exercise for the thermal conduction losses results in:

$$P_\kappa = K_\kappa \cdot \left(\frac{R_0^3 \bar{n} \bar{T}}{\tau_E} \right) \quad [MW] \quad (D.50)$$

$$K_\kappa = 0.4744 \cdot (1 + f_D) \cdot (\epsilon^2 \kappa g) \cdot \frac{(1 + \nu_n) (1 + \nu_T)}{1 + \nu_n + \nu_T} \quad (D.51)$$

Appendix E

Determining Plasma Flux Surfaces

This chapter goes over the flux surface coordinates that define the tokamak geometry. These are then used to approximate the surface area and volume, as well as create surface and volume integrals.

A Magnetic Fusion Reactor

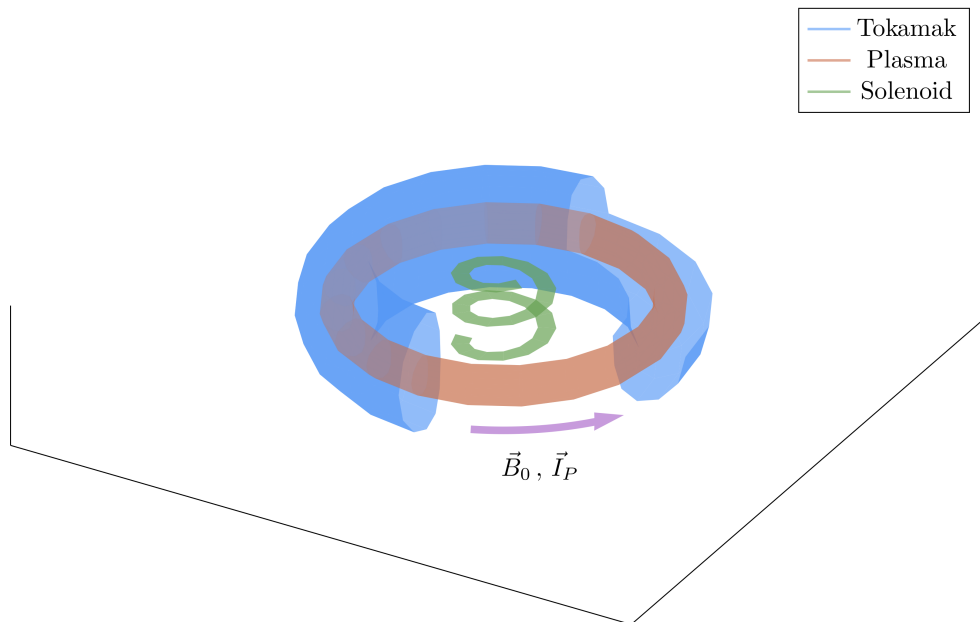


Figure E-1: Cut-Away of Tokamak Reactor

The three main components of a magnetic fusion reactor are: the tokamak structure, the plasma fuel, and the spring-like solenoid at the center.

E.1 Flux Surface Coordinates

We begin with the shape of the outer plasma surface (i.e. the 95% flux surface) written in terms of normalized coordinates x and y as follows – with α being an angle-like coordinate:

$$R = R_0 + ax(\alpha) \quad (\text{E.1})$$

$$Z = ay(\alpha) \quad (\text{E.2})$$

$$0 \leq \alpha \leq 2\pi \quad (\text{E.3})$$

The surface representation can now be written as:

$$x(\alpha) = c_0 + c_1 \cos(\alpha) + c_2 \cos(2\alpha) + c_3 \cos(3\alpha) \quad (\text{E.4})$$

$$y(\alpha) = \kappa \sin(\alpha) \quad (\text{E.5})$$

The constraints determining c_j – for $j = 1, 2, 3$ – are chosen as:

$$x(0) = 1 \quad (\text{E.6})$$

$$x(\pi) = -1 \quad (\text{E.7})$$

$$x\left(\frac{\pi}{2}\right) = -\delta \quad (\text{E.8})$$

$$x_{\alpha\alpha}(\pi) = 0.3 \cdot (1 - \delta^2) \quad (\text{E.9})$$

The last constraint, which is related to the surface curvature at $\alpha = \pi$, is chosen to make sure that the surface is always convex. A trial and error empirical fit resulted in the choice $x_{\alpha\alpha}(\pi) = 0.3 \cdot (1 - \delta^2)$. The constraint relations are easily evaluated and

then solved, leading to values for the c_j ,

$$c_0 = -\frac{\delta}{2} \quad (\text{E.10})$$

$$c_1 = g \quad (\text{E.11})$$

$$c_2 = \frac{\delta}{2} \quad (\text{E.12})$$

$$c_3 = 1 - g \quad (\text{E.13})$$

2372 Here, g is a shaping parameter approximately equal to one:

$$g = \frac{9 - 2\delta - 0.3 \cdot (1 - \delta^2)}{8} \quad (\text{E.14})$$

2373

2374 E.2 Cross-sectional Area and Volume

The plasma cross-sectional area and volume can be evaluated by straightforward calculations,

$$\begin{aligned} A &= \int \int dR dZ = a^2 \int \int dx dy = a^2 \int_0^{2\pi} x \frac{dy}{d\alpha} d\alpha \\ &= \pi a^2 \kappa g \end{aligned} \quad (\text{E.15})$$

$$\begin{aligned} V &= \int \int \int R dR dZ d\Phi = 2\pi a^2 \int \int R dx dy \\ &= 2\pi a^2 R_0 \int_0^{2\pi} \left(x + \epsilon \frac{x^2}{2} \right) \frac{dy}{d\alpha} d\alpha \approx 2\pi a^2 R_0 \int_0^{2\pi} x \frac{dy}{d\alpha} d\alpha \\ &= 2\pi^2 R_0 a^2 \kappa g \end{aligned} \quad (\text{E.16})$$

2375 The second form of the volume integral makes use of the small inverse aspect ratio
2376 expansion, $\epsilon \ll 1$, which is a good approximation and used throughout the analysis.

E.3 Surface and Volume Integrals

Eqs. (E.4) and (E.5) are simple formulas describing the shape of the outer plasma surface. We next modify the model so that it gives a plausible description of the interior flux surfaces as well. The idea is to introduce a normalized flux label, which is radial-like in behavior. This label is denoted by ρ and $\rho \in [0, 1]$ with $\rho = 1$ being the outer plasma surface (i.e. the 95% surface) and $\rho = 0$ being the magnetic axis. Additional trial and error results in the following representation for the flux surfaces,

$$x(\rho, \alpha) = \sigma(1 - \rho^2) + c_0\rho^4 + c_1\rho \cos(\alpha) + c_2\rho^2 \cos(2\alpha) + c_3\rho^3 \cos(3\alpha) \quad (\text{E.17})$$

$$y(\rho, \alpha) = \kappa\rho \sin(\alpha) \quad (\text{E.18})$$

with σ being the shift of the magnetic axis. Usually, $\sigma \sim 0.1$ for a high field tokamak.

Lastly, we note that in the course of the work it will be necessary to integrate functions of ρ over the volume and cross-sectional area of the plasma. Specifically we will need to evaluate:

$$Q_V = \int \int \int Q(\rho) R dR dZ d\Phi \approx 2\pi R_0 a^2 \int \int Q(\rho) dx dy \quad (\text{E.19})$$

$$Q_A = \int \int Q(\rho) dR dZ = a^2 \int \int Q(\rho) dx dy \quad (\text{E.20})$$

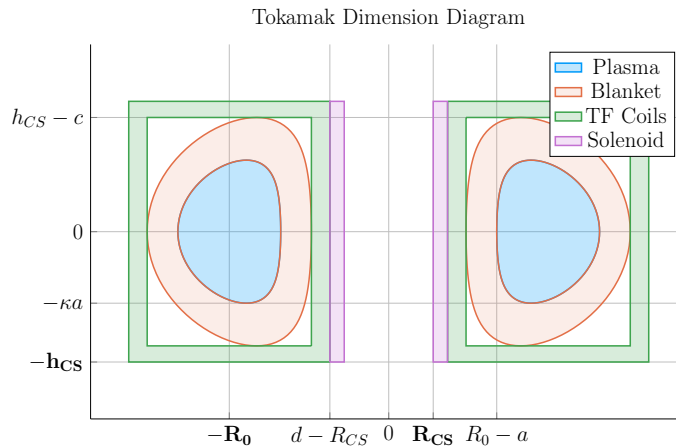


Figure E-2: Dimensions of Tokamak Cross-Section

2379 Here, $Q(\rho)$ is an arbitrary function of ρ such as pressure or temperature. In the large
 2380 aspect ratio limit, both integrals require the evaluation of the same quantity:

$$K = \int \int Q(\rho) dx dy \quad (\text{E.21})$$

2381 To evaluate this integral, we need to convert from x, y coordinates to ρ, α coordinates.
 2382 Using the Jacobian of the transformation leads to

$$K = \int \int Q(\rho) (x_\rho y_\alpha - x_\alpha y_\rho) d\rho d\alpha \quad (\text{E.22})$$

2383 Here,

$$\begin{aligned} x_\rho y_\alpha - x_\alpha y_\rho = & \kappa \sin(\alpha) \cdot (c_1 \rho \sin(\alpha) + 2c_2 \rho^2 \sin(2\alpha) + 3c_3 \rho^3 \sin(3\alpha)) \\ & + \kappa \rho \cos(\alpha) \cdot \left[\right. \\ & - 2\rho\sigma + 4\rho^3 c_0 + c_1 \cos(\alpha) \\ & + 2c_2 \rho \cos(2\alpha) + 3c_3 \rho^2 \cos(3\alpha) \\ & \left. \right] \end{aligned} \quad (\text{E.23})$$

2384 Since Q is only a function of ρ , the α integral can be carried out analytically. The
 2385 only term that survives the averaging are the ones containing c_1 . A simple integration
 2386 over α then yields the desired results:

$$Q_V = 4\pi^2 R_0 a^2 \kappa g \int_0^1 Q(\rho) \rho d\rho \quad (\text{E.24})$$

2387

$$Q_S = 2\pi a^2 \kappa g \int_0^1 Q(\rho) \rho d\rho \quad (\text{E.25})$$

2388

2389 Appendix F

2390 Expanding on the Bootstrap Current

2391 The bootstrap current fraction – f_{BS} – is an important parameter that enters in
2392 the design of tokamak reactors. It must be calculated with reasonable accuracy to
2393 determine how much external current drive is required. The value of f_{BS} thus has
2394 a strong impact on the overall fusion energy gain. Obtaining reasonable accuracy
2395 requires a moderate amount of analysis, which is presented in a following section.
2396 The results are summarized below.

2397 F.1 Summarized Results

2398 The analysis is based on an expression for the bootstrap current valid for arbitrary
2399 cross section assuming (1) equal temperature electrons and ions $T_e = T_i = T$, (2) large
2400 aspect ratio $\epsilon \ll 1$, and (3) negligible collisionality $\nu_* \rightarrow 0$. Under these assumptions
2401 the bootstrap current $\mathbf{J}_{BS} \approx J_{BS} \mathbf{e}_\phi$ has the form

$$J_{BS} = -3.32 f_T R_0 n T \left(\frac{1}{n} \frac{dn}{d\psi} + 0.054 \frac{1}{T} \frac{dT}{d\psi} \right) \quad (\text{F.1})$$

2402 Here, $f_T \approx 1.46(r/R_0)^{1/2}$ is an approximate expression for the trapped particle frac-
2403 tion and ψ is the poloidal flux.

The analysis next section shows that Eq. (F.1) leads to an expression for the bootstrap fraction, assuming for simplicity elliptical flux surfaces, that can be written as:

$$f_{BS} = \frac{I_{BS}}{I} = \frac{2\pi a^2 \kappa}{I} \int_0^1 J_{BS} \rho d\rho = \frac{K_{BS}}{K_n} \frac{\bar{n} \bar{T} R_0^2}{I_P^2} \quad (\text{F.2})$$

$$K_{BS} = 4.879 \cdot K_n \cdot \left(\frac{1 + \kappa^2}{2} \right) \cdot \epsilon^{5/2} \cdot H_{BS} \quad (\text{F.3})$$

$$H_{BS} = (1 + \nu_n)(1 + \nu_T)(\nu_n + 0.054\nu_T) \int_0^1 \frac{\rho^{5/2} (1 - \rho^2)^{\nu_n + \nu_T - 1}}{b_p} d\rho \quad (\text{F.4})$$

$$b_p(\rho) = \frac{-e^{\gamma \rho^2} (\gamma \rho^2 - 1 - \gamma) - 1 - \gamma}{\rho (e^\gamma - 1 - \gamma)} \quad (\text{F.5})$$

$$\bar{J}_\phi(\rho) = -\frac{I}{\pi a^2 \kappa} \left[\frac{\gamma^2 (1 - \rho^2) e^{\gamma \rho^2}}{e^\gamma - 1 - \gamma} \right] \quad (\text{F.6})$$

2404 In this expression b_p is a normalized form of the poloidal magnetic field derived from
 2405 a prescribed model for the *total* flux surface averaged current density profile $\bar{J}_\phi(\rho)$.
 2406 The $\bar{J}_\phi(\rho)$ profile, in analogy with the density and temperature profiles, is not self-
 2407 consistent but is chosen to have a plausible experimental shape characterized by the
 2408 parameter γ . The profile can have either an on-axis ($\gamma < 1$) or off-axis peak ($\gamma > 1$).
 2409 The normalized internal inductance l_i and radial location of the current peak ρ_m are
 2410 related to the value of γ by:

$$l_i = \frac{4\kappa}{1 + \kappa^2} \int_0^1 b_p^2 \rho d\rho$$

(F.7)

2411

$$\rho_m = \begin{cases} \left(\frac{\gamma}{\gamma - 1} \right)^{1/2}, & \gamma > 1 \\ 0, & \gamma < 1 \end{cases} \quad (\text{F.8})$$

2412 F.2 Detailed Analysis

2413 The starting point for the analysis is the general expression for the bootstrap current
 2414 in a tokamak with arbitrary cross section.⁴⁹ This expression can be simplified by
 2415 assuming (1) equal temperature electrons and ions $T_e = T_i = T$, (2) large aspect ratio
 2416 $\epsilon \ll 1$, and (3) negligible collisionality $\nu_* \rightarrow 0$. The bootstrap current $\mathbf{J}_{BS} \approx J_{BS} \mathbf{e}_\phi$
 2417 reduces to

$$J_{BS} = -3.32 f_T R_0 n T \left(\frac{1}{n} \frac{dn}{d\psi} + 0.054 \frac{1}{T} \frac{dT}{d\psi} \right) \quad (\text{F.9})$$

2418 Several values of the trapped particle fraction f_T have been given in the literature.⁵⁰
 2419 For simplicity we use a form valid for large aspect ratio. This is a slightly optimistic
 2420 value but saves a large amount of detailed calculation. It can be written as,

$$f_T \approx 1.46 (r/R_0)^{1/2} = 1.46 \epsilon^{1/2} \rho^{1/2} \quad (\text{F.10})$$

2421 Here, as in the main text, ρ is a radial-like flux surface label that varies between
 2422 $0 \leq \rho \leq 1$. In other words $\psi = \psi(\rho)$. Under these assumptions the bootstrap current
 2423 reduces to:

$$J_{BS} = -4.85 R_0 \epsilon^{1/2} \left(\frac{\rho^{1/2} n T}{d\psi/d\rho} \right) \left(\frac{1}{n} \frac{dn}{d\rho} + 0.054 \frac{1}{T} \frac{dT}{d\rho} \right) \quad (\text{F.11})$$

2424 Since we have specified profiles for $n(\rho)$ and $T(\rho)$ all that remains in order to be able
 2425 to evaluate $J_{BS}(\rho)$ is to determine $\psi' = d\psi/d\rho$. Keep in mind that at this point, in
 2426 spite of the approximations that have been made, the expression for $J_{BS}(\rho)$ is still
 2427 valid for arbitrary cross section.

2428 The analysis that follows shows how to calculate ψ' for an arbitrary cross section
 2429 including finite aspect ratio. As an example an explicit expression for large aspect
 2430 ratio, finite elongation ellipse is obtained. Consider the Grad-Shafranov equation for
 2431 the flux: $\Delta^* \psi = -\mu_0 R J_\psi$. We integrate this equation over the volume of an arbitrary

2432 flux surface making use of Gauss' theorem, which leads to:

$$\int_S \frac{\mathbf{n} \cdot \nabla \psi}{R^2} dS = -\mu_0 \int_V \frac{J_\phi}{R} d\mathbf{r} \quad (\text{F.12})$$

Next, assume that the coordinates of the flux surface can be expressed in terms of ρ and an angular-like parameter α with $0 \leq \alpha \leq 2\pi$. In other words, the flux surface coordinates can be written as $R = R(\rho, \alpha) = R_0 + ax(\rho, \alpha)$ and $Z = Z(\rho, \alpha) = ay(\rho, \alpha)$. The functions $R(\rho, \alpha)$ and $Z(\rho, \alpha)$ are assumed to be known. The term on the left hand side can be evaluated by noting that

$$d\mathbf{l} = dl \mathbf{t} \quad (\text{F.13})$$

$$dl = (R_\alpha^2 + Z_\alpha^2)^{1/2} d\alpha \quad (\text{F.14})$$

$$\mathbf{t} = \frac{R_\alpha \mathbf{e}_R + Z_\alpha \mathbf{e}_Z}{(R_\alpha^2 + Z_\alpha^2)^{1/2}} \quad (\text{F.15})$$

$$\mathbf{n} = \mathbf{e}_\phi \times \mathbf{t} = \frac{Z_\alpha \mathbf{e}_R - R_\alpha \mathbf{e}_Z}{(R_\alpha^2 + Z_\alpha^2)^{1/2}} \quad (\text{F.16})$$

$$dS = R d\phi dl = 2\pi R (R_\alpha^2 + Z_\alpha^2)^{1/2} d\alpha \quad (\text{F.17})$$

2433 It then follows that

$$\mathbf{n} \cdot \nabla \psi = \frac{1}{(R_\alpha^2 + Z_\alpha^2)^{1/2}} \left(Z_\alpha \frac{\partial \psi}{\partial R} - R_\alpha \frac{\partial \psi}{\partial Z} \right) = \frac{1}{(R_\alpha^2 + Z_\alpha^2)^{1/2}} \frac{d\psi}{d\rho} Z_\alpha \rho_R - R_\alpha \rho_Z \quad (\text{F.18})$$

2434 We can rewrite the last term by noting that

$$\begin{aligned} dR = R_\rho d\rho + R_\alpha d\alpha &\rightarrow d\rho = (Z_\alpha dR - R_\alpha dZ) / (R_\rho Z_\alpha - R_\alpha Z_\rho) \\ dZ = Z_\rho d\rho + Z_\alpha d\alpha &\rightarrow d\alpha = (-Z_\rho dR + R_\rho dZ) / (R_\rho Z_\alpha - R_\alpha Z_\rho) \end{aligned} \quad (\text{F.19})$$

2435 from which follows

$$\begin{aligned}\rho_R &= \frac{Z_\alpha}{(R_\rho Z_\alpha - R_\alpha Z_\rho)} \\ \rho_Z &= -\frac{R_\alpha}{(R_\rho Z_\alpha - R_\alpha Z_\rho)}\end{aligned}\tag{F.20}$$

2436 the normal gradient reduces to

$$\mathbf{n} \cdot \nabla \psi = \frac{R_\alpha^2 + Z_\alpha^2}{(R_\rho Z_\alpha - R_\alpha Z_\rho)} \frac{d\psi}{d\rho}\tag{F.21}$$

2437 Using this relation we see that the left hand side of Eq. (F.12) can now be written

2438 as:

$$\int_S \frac{\mathbf{n} \cdot \nabla \psi}{R^2} dS = 2\pi \frac{d\psi}{d\rho} \int_0^{2\pi} \frac{R_\alpha^2 + Z_\alpha^2}{(R_\rho Z_\alpha - R_\alpha Z_\rho)} \frac{d\alpha}{R}\tag{F.22}$$

2439 Consider now the right hand side of Eq. (F.12). The critical assumption is that the

2440 current density is approximated by its flux surface averaged value, $J_\phi(\rho, \alpha) \approx \bar{J}_\phi(\rho)$.

2441 This is obviously not self-consistent with the Grad-Shafranov equation. Even so, it

2442 should suffice for present purposes where we only need to evaluate global volume

2443 integrals. Also, in the same spirit as prescribing $n(\rho)$ and $T(\rho)$ we assume that $\bar{J}_\phi(\rho)$

2444 is also prescribed. Under these assumptions the right hand side of Eq. (F.12) simplifies

2445 to:

$$\begin{aligned}-\mu_0 \int_V \frac{J_\phi}{R} d\mathbf{r} &= -2\pi\mu_0 \int_A J_\phi dA \\ &= -2\pi\mu_0 \int_0^\rho d\rho \int_0^{2\pi} J_\phi (R_\rho Z_\alpha - R_\alpha Z_\rho) d\alpha \\ &\approx -2\pi\mu_0 \int_0^\rho d\rho \left[\bar{J}_\phi \int_0^{2\pi} (R_\rho Z_\alpha - R_\alpha Z_\rho) d\alpha \right]\end{aligned}\tag{F.23}$$

2446 Combining the results in Eqs. (F.22) and (F.23) leads to the required general expres-

2447 sion for $d\psi/d\rho$,

$$\frac{d\psi}{d\rho} \int_0^{2\pi} \frac{R_\alpha^2 + Z_\alpha^2}{(R_\rho Z_\alpha - R_\alpha Z_\rho)} \frac{d\alpha}{R} = -\mu_0 \int_0^\rho d\rho \left[\bar{J}_\omega \int_0^{2\pi} (R_\rho Z_\alpha - R_\alpha Z_\rho) d\alpha \right]\tag{F.24}$$

2448 Next, to help specify a plausible choice for \bar{J}_ϕ it is useful to define the kink safety

2449 factor and the actual local safety factor. The kink safety factor is defined by

$$q_* = \frac{2\pi a^2 B_0}{\mu_0 R_0 I} \left(\frac{1 + \kappa^2}{2} \right) \quad (\text{F.25})$$

2450 where

$$I = \int J_o dA = \int_0^1 d\rho \left[\bar{J}_o \int_0^{2\pi} (R_\rho Z_\alpha - R_\alpha Z_\rho) d\alpha \right] \quad (\text{F.26})$$

2451 This leads to

$$\frac{1}{q_*} = \frac{\mu_0 R_0}{2\pi a^2 B_0} \left(\frac{2}{1 + \kappa^2} \right) \int_0^1 d\rho \left[\bar{J}_\phi \int_0^{2\pi} (R_\rho Z_\alpha - R_\alpha Z_\rho) d\alpha \right] \quad (\text{F.27})$$

2452 Similarly, the local safety factor can be expressed as

$$q(\rho) = \frac{F(\rho)}{2\pi} \int \frac{dl}{RB_p} \quad (\text{F.28})$$

2453 Here, $F(\rho) = RB_o$. Substituting $RB_p = \mathbf{n} \cdot \nabla \psi$ then yields

$$q(\rho) = \frac{F(\rho)}{2\pi \psi'} \int_0^{2\pi} \frac{1}{R} (R_\rho Z_\alpha - R_\alpha Z_\rho) d\alpha \quad (\text{F.29})$$

2454 with $\psi' = d\psi/d\rho$.

2455 For present purposes we can obtain relatively simple analytic expressions for all the
 2456 quantities of interest by assuming the flux surfaces are concentric ellipses, character-
 2457 ized by $R = R_0 + a\rho \cos \alpha$ and $Z = \kappa a\rho \sin \alpha$. We assume low β so that $F(\rho) \approx R_0 B_0$.
 2458 This model accounts for elongation but neglects the effects of triangularity and finite
 2459 aspect ratio. The derivatives in Eqs. (F.24), (F.27) and (F.29) can now be easily
 2460 evaluated. Also, after some trial and error we chose $\bar{J}_\phi(\rho)$ to be a plausible profile
 2461 which is peaked off-axis at $\rho = \rho_m$.

$$\bar{J}_\phi(\rho) = -\frac{I}{\pi a^2 \kappa} \left[\frac{\gamma^2 (1 - \rho^2) e^{\gamma \rho^2}}{e^\gamma - 1 - \gamma} \right] \quad (\text{F.30})$$

2462 Here, $\gamma = 1/(1 - \rho_m^2)$.

2463 These profiles are substituted into Eq. (F.24) after which each of the integrals can be
 2464 evaluated analytically. A straightforward calculation yields:

$$\begin{aligned}\rho \frac{d\psi}{d\rho} &= -2\mu_0 R_0 a^2 \left(\frac{\kappa^2}{1 + \kappa^2} \right) \int_0^\rho \bar{J}_\phi \rho d\rho \\ &= \frac{\mu_0 R_0 I}{\pi} \left(\frac{\kappa}{1 + \kappa^2} \right) \frac{(1 + \gamma - \gamma \rho^2) e^{\gamma \rho^2} - 1 - \gamma}{e^\gamma - 1 - \gamma}\end{aligned}\tag{F.31}$$

2465 The safety factors are given by

$$\begin{aligned}\frac{1}{q_*} &= \frac{\psi'(1)}{\kappa a^2 B_0} \\ \frac{q(\rho)}{q_*} &= \frac{\rho \psi'(1)}{\psi'(\rho)}\end{aligned}\tag{F.32}$$

Eq. (F.31) is now substituted into the expression for the bootstrap current given by Eq. (F.11). The resulting expression can then be integrated over the plasma cross section to yield the bootstrap fraction. A straightforward calculation leads to:

$$f_{BS} = \frac{I_{BS}}{I} = \frac{2\pi a^2 \kappa}{I} \int_0^1 J_{BS} \rho d\rho = \frac{K_{BS}}{K_n} \frac{\bar{n} \bar{T} R_0^2}{I_P^2}\tag{F.33}$$

$$K_{BS} = 4.879 \cdot K_n \cdot \left(\frac{1 + \kappa^2}{2} \right) \cdot \epsilon^{5/2} \cdot H_{BS}\tag{F.34}$$

$$H_{BS} = (1 + \nu_n)(1 + \nu_T)(\nu_n + 0.054\nu_T) \int_0^1 \frac{\rho^{5/2} (1 - \rho^2)^{\nu_n + \nu_T - 1}}{b_p} d\rho\tag{F.35}$$

$$b_p(\rho) = \frac{-e^{\gamma \rho^2} (\gamma \rho^2 - 1 - \gamma) - 1 - \gamma}{\rho (e^\gamma - 1 - \gamma)}\tag{F.36}$$

2466 This is the desired result.

2467 Appendix G

2468 Elaborating on the Current Drive

2469 The driven current fraction – f_{CD} – is an important parameter that enters in the
2470 design of steady-state tokamak reactors. It must be calculated with reasonable ac-
2471 curacy to determine how much bootstrap current is required. The value of f_{CD} thus
2472 has a strong impact on the overall fusion energy gain. Obtaining reasonable accuracy
2473 requires a moderate amount of analysis, which is presented in a following section.
2474 The results are summarized below.

2475 G.1 Summarized Results

2476 We assume that current drive is provided by lower hybrid waves because of the cor-
2477 responding relatively high efficiency and naturally occurring off-axis peaking which
2478 aligns with the bootstrap current. The externally driven lower hybrid current (I_{CD})
2479 is given in terms of the current drive efficiency, η_{CD} , defined as follows:²⁶

$$I_{CD} = \eta_{CD} \frac{P_H}{\bar{n}_{20} R_0} = \frac{\eta_{CD}}{Q} \frac{P_F}{\bar{n}_{20} R_0} \quad (\text{G.1})$$

2480 Here, for simplicity and slightly optimistically, we assume that 100% of the klystron
2481 RF power, P_H , is absorbed in the plasma.

2482 The current drive fraction – $f_{CD} = I_{CD}/I_P$ – can then be written as,

$$\begin{aligned} f_{CD} &= K_{CD} \frac{\eta_{CD} \bar{n}_{20} R_0^2 (\hat{\sigma} v)}{I_M} \\ K_{CD} &= 278 \frac{f_D^2 \varepsilon^2 \kappa}{Q} = 0.634 \end{aligned} \quad (\text{G.2})$$

2483 Typical values for η_{CD} are around 0.3.²⁶ However, this current drive efficiency is
 2484 actually a function of: \bar{n} , \bar{T} , and B_0 . This dependence must be included in the
 2485 design to obtain reliable results. A self consistent calculation of $\eta_{CD} = \eta_{CD}(\bar{n}, \bar{T}, B_0)$
 2486 requires considerable analysis, the details of which are presented next section.

2487 G.2 Detailed Analysis

2488 To design a steady state fusion reactor, it is necessary to calculate η_{CD} for lower
 2489 hybrid current drive (LHCD). Recall that the driven lower hybrid current I_{CD} is
 2490 related to the lower hybrid RF klystron power absorbed by the plasma P_H by the
 2491 relation:

$$I_{CD} = \eta_{CD} \frac{P_H}{n_{20} R} \quad (\text{G.3})$$

2492 Here, $P_H = \eta_{RF} P_{RF}$, with P_{RF} equal to the total wall power used for current drive
 2493 (plus heating) and $\eta_{RF} \approx 0.5$ is the conversion efficiency from wall power to RF
 2494 absorbed power. Also, $n_{20} = n_{20}(\rho_j)$ and $R = R(\rho_j, \theta)$ are the density and major
 2495 radius evaluated at the minor radius $\rho = \rho_j$ and launch angle θ with ρ_j corresponding
 2496 to the location of the peak driven current density: $J_{max} = J_{CD}(\rho_j, \theta)$. The angle
 2497 θ is a known quantity set by the experimental configuration while ρ_j is yet to be
 2498 determined.

2499 The value of η_{CD} is related to a normalized quantity $\tilde{\eta}$, the efficiency usually calculated
 2500 in the literature, by a series of connecting formulas. The inter-relations start with

$$\eta_I = \frac{\int_A J_{CD} dA}{\int_V S_H dV} \approx \frac{1}{2\pi} \left[\frac{J_{CD}}{R S_H} \right]_{\rho_j, \theta} = \frac{\eta_{LH}}{2\pi R} \left[\frac{J_{CD}}{R S_{LH}} \right]_{\rho_j, \theta} \quad (\text{G.4})$$

2501 where $\eta_I = I_{CD} = P_H A/W$ is the overall current drive efficiency measuring how many

2502 delivered watts of klystron RF power are required to drive one ampere of current. For
 2503 simplicity and slightly optimistically all delivered power is assumed to be absorbed
 2504 by the plasma. Also, $S_H(\rho, \theta)$ is the klystron power density delivered to the plasma,
 2505 whose absorption is localized around $\rho = \rho_j$.

2506 Due to various losses, only a fraction of the absorbed klystron power, $\eta_{LH} \approx 0.75$,
 2507 actually drives current. These losses have to do with the fact that the power spectrum
 2508 arising from a realistic waveguide array has both positive and negative lobes – it
 2509 is not an ideal positive delta function. The combination of finite spectral width
 2510 plus oppositely driven current from the negative lobe implies that only a portion of
 2511 the total absorbed power actually drives a net positive current. The result of this
 2512 discussion is that the power density, S_{LH} , driving lower hybrid current is related to
 2513 the delivered klystron power density by $S_{LH} = \eta_{LH} S_H$.

Now, the efficiency, $\tilde{\eta}$ usually calculated in the literature is defined by:

$$\tilde{\eta}(\rho_J, \theta) = \left[\frac{J_{CD}/en v_{Te}}{S_{LH}/m_e n \nu_0 v_{Te}^2} \right]_{\rho_j, \theta} \quad (\text{G.5})$$

$$v_{Te}(\rho_J) = \left[\frac{2T_e}{m_e} \right]_{\rho_J}^{1/2} \quad (\text{G.6})$$

$$\nu_0(\rho_J) = \left[\frac{\omega_{pe}^4 \ln \Lambda}{2\pi n_e v_{Te}^3} \right]_{\rho_J} \quad (\text{G.7})$$

2514 It then follows that

$$\eta_I = \frac{\eta_{LH}}{2\pi} \left[\frac{e}{R m_e \nu_0 v_{Te}} \right]_{\rho_j, \theta} \tilde{\eta}(\rho_J, \theta) \quad (\text{G.8})$$

2515 From Eq. (G.3), we see that $\eta_{CD} = \eta_I [n_{20} R]_{\rho_j, \theta}$, which leads to the desired conversion
 2516 relation:

$$\eta_{CD} = \frac{\eta_{LH}}{2\pi} \left[\frac{e n_{20}}{m_e \nu_0 v_{Te}} \right]_{\rho_j} \tilde{\eta}(\rho_J, \theta) = 0.06108 \frac{\eta_{LH}}{\ln \Lambda} T_k \tilde{\eta} \quad (\text{G.9})$$

2517 **An expression for $\tilde{\eta}$**

2518 Needed for the design code is an expression for $\tilde{\eta}(\rho_j, \theta)$. Such an expression, valid for
 2519 arbitrary ρ , has been determined by Ehst and Karney²⁷ – based on a sophisticated
 2520 theoretical analysis combined with extensive numerical results. Once ρ_j is determined
 2521 we set $\rho = \rho_j$ in the expression for $\tilde{\eta}(\rho, \theta)$. Ehst and Karney find that a good fit for
 2522 $\tilde{\eta}(\rho, \theta)$ can be written as:

$$\tilde{\eta} = CMR\eta_0 \quad (\text{G.10})$$

For LHCD, the parameters appearing in Eq. (G.10) have the form:

$$M = 1 \quad (\text{G.11})$$

$$R(\rho, \theta) = 1 - \frac{\varepsilon^n \rho^n (x_r^2 + w^2)^{1/2}}{\varepsilon^n \rho^n x_r + w} \quad n = 0.77 \quad x_r = 2.47 \quad (\text{G.12})$$

$$C(\rho, \theta) = 1 - \exp(-c^m x_t^{2m}) \quad m = 1.38 \quad c = 0.778 \quad (\text{G.13})$$

$$\eta_0(\rho, \theta) = \frac{K}{w} + D + \frac{8w^2}{5 + Z_{eff}} \quad K = \frac{2.12}{Z_{eff}} \quad D = \frac{3.83}{Z_{eff}^{0.707}} \quad (\text{G.14})$$

2523 All quantities have been defined except for $x_t^2(\rho, \theta)$ and $w(\rho, \theta)$. The quantity w is a
 2524 normalized form of the resonant particle velocity which absorbs energy and momen-
 2525 tum from the lower hybrid wave,

$$w(\rho, \theta) = \frac{\omega}{k_{\parallel} v_{Te}} = \frac{c}{v_{Te}} \frac{1}{n_{\parallel}} \quad (\text{G.15})$$

2526 with n_{\parallel} the parallel index of refraction. The value of $n_{\parallel}(\rho, \theta)$ will be discussed shortly.

2527 The quantity x_t^2 is a toroidal correction associated with the fact that trapped particles
 2528 cannot contribute to toroidal current flow. It can be expressed in terms of the local
 2529 mirror ratio by

$$x_t^2(\rho, \theta) = w^2 \left(\frac{B}{B_M - B} \right) \quad (\text{G.16})$$

where from simple guiding center theory assuming that $B \approx B_\phi$

$$B_M = \frac{B_0}{1 - \varepsilon \rho} \quad (\text{G.17})$$

$$B = \frac{B_0}{1 + \varepsilon \rho \cos \theta} \quad (\text{G.18})$$

2530 Calculation of $n_\parallel^2(\rho, \theta)$

2531 The next step in the evaluation of η_{CD} is the calculation of $n_\parallel^2(\rho, \theta)$. Its value is deter-
 2532 mined by the requirements for accessibility from the plasma edge into the absorption
 2533 layer. The relevant physics follows from an analysis of the cold plasma dispersion
 2534 relation given by

$$n_\perp^2(\rho, \theta) = -\frac{K_\parallel}{2K_\perp} \left\{ n_\parallel^2 - K_\perp + \frac{K_A^2}{K_\parallel} \pm \left[\left(n_\parallel^2 - K_\perp + \frac{K_A^2}{K_\parallel} \right)^2 + \frac{4K_\perp K_A^2}{K_\parallel} \right]^{1/2} \right\} \quad (\text{G.19})$$

2535 The plus sign corresponds to the desired root and is often referred to as the slow
 2536 wave.

2537 In the lower hybrid regime the relevant ordering of parameters is

$$\begin{aligned} \omega_{pe}/\Omega_e &\sim \omega_{pi}/\omega \sim n_\parallel \sim 1 \\ \omega_{pi}/\Omega_i &\sim \omega/\Omega_i \sim \Omega_e/\omega \sim n_\perp \sim m_i/m_e^{1/2} \gg 1 \end{aligned} \quad (\text{G.20})$$

2538 leading to the following simple forms for the elements of the dielectric tensor

$$\begin{aligned} K_\perp(\rho, \theta) &= 1 + \frac{\omega_{pe}^2}{\Omega_e^2} - \frac{\omega_{pi}^2}{\omega^2} \sim 1 \\ K_A(\rho, \theta) &= \frac{\omega_{pe}^2}{\omega \Omega_e} \sim m_i/m_e^{1/2} \\ K_\parallel(\rho) &= -\frac{\omega_{pe}^2}{\omega^2} \sim m_i/m_e \end{aligned} \quad (\text{G.21})$$

2539 The first requirement for accessibility is that the function under the square root
 2540 be positive. When this function passes through zero there is a double root for n_\perp^2
 2541 causing a mode conversion from the slow wave to the fast wave. The fast wave does

not propagate into the plasma. It is reflected back out through the plasma surface, obviously an undesirable result. Avoiding mode conversion requires a sufficiently large value of n_{\parallel}^2 to keep the function under the square root positive. This value must satisfy

$$n_{\parallel}^2(\rho, \theta) \geq \left[K_{\perp}^{1/2} + \left(-\frac{K_A^2}{K_{\parallel}} \right)^{1/2} \right]^2 \quad (\text{G.22})$$

Since $\eta_{CD} \propto 1/n_{\parallel}^2$ we see that current drive efficiency is maximized when $n_{\parallel}^2(\rho, \theta)$ is minimized – the inequality in Eq. (G.22) must be set to equality.

At this point there is an important subtlety that must be taken into account. The issue is that the wavelength spectrum of the applied klystron source is not a delta function – it has a finite half width, $\Delta n_{\parallel} \approx 0.2$ and a negative lobe. For simplicity, we have modeled the spectrum as rectangular and ignore the negative lobe. The negative lobe is accounted for through the value of η_{LH} , since this power obviously does not drive current in the desired direction. Now, Eq. (G.22) is an inequality and we want to minimize $n_{\parallel}^2(\rho, \theta)$ over all ρ for the given θ where the power is absorbed. Therefore, we must use the equality sign in Eq. (G.22) for the strictest case – that $n_{\parallel}(\hat{\rho}_J, \theta) = n_{\parallel}(\rho_J, \theta) - \Delta n_{\parallel}$ – where $\hat{\rho}_J$ and ρ_J (both as yet undetermined) are the corresponding strictest and average radii where power is absorbed.

With this in mind, after substituting the simplified expressions for the elements of the dielectric tensor we obtain

$$\begin{aligned} n_{\parallel}^2(\hat{\rho}_J, \theta) &= \left[\left(1 - \frac{1-\hat{\omega}^2}{\hat{\omega}^2} X \right)^{1/2} + X^{1/2} \right]^2 \\ X(\hat{\rho}_J, \theta) &= \omega_{pe}^2(\hat{\rho}_J) / \Omega_e^2(\hat{\rho}_J, \theta) \\ \hat{\omega}^2(\hat{\rho}_J, \theta) &= \omega^2 / \Omega_e(\hat{\rho}_J, \theta) \Omega_i(\hat{\rho}_J, \theta) \end{aligned} \quad (\text{G.23})$$

The question now is how do we choose the frequency: $\hat{\omega}$? There are actually three constraints on the frequency and we must choose the strictest one to determine $\hat{\omega}^2$.

2562 The constraints are as follows:

$$\begin{aligned}
\omega^2 &> \omega_{LH}^2(\hat{\rho}_J, \theta) && \text{Avoid mode conversion before reaching } \hat{\rho}_J, \theta \\
\omega^2 &> 4\omega_{LH}^2(\hat{\rho}_J, \theta) && \text{Avoid the PDI before reaching } \hat{\rho}_J, \theta \\
\omega^2 &> k_\perp^2(\hat{\rho}_J, \theta) v_\alpha^2 && \text{Avoid coupling to } \alpha \text{ particles before reaching } \hat{\rho}_J, \theta
\end{aligned} \tag{G.24}$$

2563 Here, $\omega_{LH}^2(\hat{\rho}_J, \theta) = \omega_{pi}^2 / (1 + \omega_{pe}^2 / \Omega_e^2)$ is the square of the lower hybrid frequency and
2564 $v_\alpha = (2E_\alpha / m_\alpha)^{1/2}$ is the alpha particle speed. Also, PDI denotes parametric decay
2565 instability. The second and third constraints are approximate values, used here for
2566 simplicity.

2567 Each of these constraints is substituted into the expression for n_\parallel^2 . We find that in
2568 the regime of interest the α particle coupling requirement is the strictest. We thus
2569 choose the frequency to satisfy $\omega / k_\perp = v_\alpha$, or in normalized units:

$$n_\perp^2(\hat{\rho}_J, \theta) = \frac{c^2}{v_\alpha^2} \tag{G.25}$$

2570 This expression is simplified by evaluating n_\perp^2 using Eq. (G.19) coupled with n_\parallel^2 given
2571 by Eq. (G.22)

$$n_\perp^2(\hat{\rho}_J, \theta) = -\frac{K_\parallel}{K_\perp^{1/2}} \left(-\frac{K_A^2}{K_\parallel} \right)^{1/2} = \frac{m_i}{m_e \hat{\omega}} \frac{X^{3/2}}{[\hat{\omega}^2(1+X) - X]^{1/2}} \tag{G.26}$$

2572 Eq. (G.26) is a quadratic equation for $\hat{\omega}^2$, which can be easily solved, yielding:

$$\begin{aligned}
\hat{\omega}^2(\hat{\rho}_J, \theta) &= \frac{1}{2} \frac{X}{1+X} + \frac{1}{2} \left[\frac{X^2}{(1+X)^2} + 4\gamma^2 \frac{X^3}{1+X} \right]^{1/2} \\
\gamma &= \frac{m_i}{m_e} \frac{1}{n_\perp^2} = \frac{2m_i E_\alpha}{m_e m_\alpha c^2} = 8.562
\end{aligned} \tag{G.27}$$

2573 This value of $\hat{\omega}^2$ is substituted into Eq. (G.23) to obtain the desired expression for
2574 $n_\parallel^2 = n_\parallel^2(X)$.

2575 Calculation of $\hat{\rho}_j$

2576 The calculation of $\hat{\rho}_j$ requires a very lengthy analysis of Landau damping. We can
 2577 bypass this complication by making use of a simple rule of thumb that is reasonably
 2578 accurate. This rule states that lower hybrid power is absorbed and driven current
 2579 produced in a somewhat narrow layer of the plasma profile whose location is deter-
 2580 mined by the requirement that the parallel phase velocity be approximately equal to
 2581 three times the electron thermal speed,

$$\frac{\omega}{k_{\parallel}} \approx 3v_T \quad (\text{G.28})$$

2582 The equation can be rewritten in terms of \hat{n}_{\parallel} leading to a transcendental algebraic
 2583 equation for $\hat{\rho}_j$,

$$(1 + \nu_T) (1 - \hat{\rho}_J^2)^{\nu_T} n_{\parallel}^2(\hat{\rho}_J, \theta) = \frac{m_e c^2}{18\bar{T}} = \frac{28.39}{\bar{T}_k} \quad (\text{G.29})$$

2584 This is a simple equation to solve numerically.

2585 Calculation of ρ_j

2586 The last step in the analysis is to map the results at the strictest absorption location –
 2587 (ρ, θ) – to the center of the absorption layer (ρ_J, θ) where the current drive efficiency
 2588 is defined. This is easily done by noting that power is always absorbed in at the local
 2589 radius where $\omega/k_{\parallel} = 3v_{Te}$. Consequently, the relations at ρ_J are related to those at
 2590 $\hat{\rho}_J$ by:

$$\begin{aligned} (1 + \nu_T) (1 - \hat{\rho}_J^2)^{\nu_T} n_{\parallel}^2(\hat{\rho}_J, \theta) &= \frac{28.39}{\bar{T}_k} \\ (1 + \nu_T) (1 - \rho_J^2)^{\nu_T} n_{\parallel}^2(\rho_J, \theta) &= \frac{28.39}{\bar{T}_k} \end{aligned} \quad (\text{G.30})$$

2591 Since $n_{\parallel}(\hat{\rho}_J, \theta) = n_{\parallel}(\rho_J, \theta) - \Delta n_{\parallel}$, it follows that $\hat{\rho}_J$ and ρ_J are related by:

$$\frac{(1 - \rho_J^2)^{\nu_T}}{(1 - \hat{\rho}_J^2)^{\nu_T}} = \left[1 - \frac{\Delta n_{\parallel}}{n_{\parallel}(\rho_J, \theta)} \right]^2 \rightarrow \rho_J^2 = 1 - (1 - \hat{\rho}_J^2) \left[1 - \frac{\Delta n_{\parallel}}{n_{\parallel}(\rho_J, \theta)} \right]^{2/\nu_T} \quad (\text{G.31})$$

2592 Note that in general: $\rho_J > \hat{\rho}_J$. The strictest location determining $n_{\parallel}(\hat{\rho}_J, \theta)$ is the
 2593 innermost radial point on the temperature profile where power is absorbed.

2594 Abridged Modus Operandi

2595 Assume the following quantities are given as inputs: $B_0, \theta, \bar{n}_{20}, \bar{T}_k, \varepsilon, \Delta n_{\parallel}, \eta_{LH}$. Carry
 2596 out the following steps:

- 2597 1. Solve the equations below simultaneously to determine $n_{\parallel}^2(\hat{\rho}_J, \theta), \hat{\omega}^2(\hat{\rho}_J, \theta)$, and $\hat{\rho}_J$

2598

$$\begin{aligned} n_{\parallel}^2(\hat{\rho}_J, \theta) &= \left[\left(1 - \frac{1 - \hat{\omega}^2}{\hat{\omega}^2} X \right)^{1/2} + X^{1/2} \right]^2 \\ \hat{\omega}^2(\hat{\rho}_J, \theta) &= \frac{1}{2} \frac{X}{1+X} + \frac{1}{2} \left[\frac{X^2}{(1+X)^2} + 4\gamma^2 \frac{X^3}{1+X} \right]^{1/2} \\ (1 + \nu_T)(1 - \hat{\rho}_J^2)^{\nu_T} n_{\parallel}^2(\hat{\rho}_J, \theta) &= \frac{m_e c^2}{2\bar{T}} = \frac{28.39}{\bar{T}_k} \end{aligned} \quad (\text{G.32})$$

- 2599 2. Solve for $\tilde{\eta}(\hat{\rho}_J, \theta)$

$$\tilde{\eta}(\hat{\rho}_J, \theta) = CM R \eta_0 \quad (\text{G.33})$$

- 2600 3. Solve for $n_{\parallel}(\rho_J, \theta)$

$$n_{\parallel}(\rho_J, \theta) = n_{\parallel}(\hat{\rho}_J, \theta) + \Delta n_{\parallel} \quad (\text{G.34})$$

- 2601 4. Solve for ρ_J

$$\rho_J^2 = 1 - (1 - \hat{\rho}_J^2) \left[1 - \frac{\Delta n_{\parallel}}{n_{\parallel}(\rho_J, \theta)} \right]^{2/\nu_T} \quad (\text{G.35})$$

- 2602 5. Re-evaluate $\tilde{\eta}(\rho_J, \theta)$ by substituting the values of $\rho_J, n_{\parallel}(\rho_J, \theta)$ into Eq. (G.33).

- 2603 6. Solve for η_{CD}

$$\eta_{CD} = \frac{1}{2\pi} \left(\frac{en_{20}}{m_e \nu_0 v_{Te}} \right) \tilde{\eta} = 0.06108 \frac{\eta_{LH}}{\ln \Lambda} (1 + \nu_T) \bar{T}_k (1 - \rho_J^2)^{\nu_r} \tilde{\eta}(\rho_J, \theta) \quad (\text{G.36})$$

2604 In the end there will have to be some iteration with the rest of the analysis to make
 2605 sure the values of \bar{n}_{20} and \bar{T}_k are self-consistent.

2606 Appendix H

2607 Compending Code Plots

2608 This chapter gives a brief overview of the plots that come from using this model on
2609 several reactor prototypes: Charybdis, Proteus, ARC, DEMO Pulsed, the two ARIES
2610 ACT studies. The two types of results this information comes in are: magnet strength
2611 scans and cost sensitivity studies.

2612 In the former, all static variables are kept constant and only the magnet strength is
2613 allowed to change. The latter then focuses on changing one static variable at a time
2614 and finding several magnet strengths that satisfy certain constraints – i.e. minimum
2615 cost or when two limits are both just marginally satisfied.

2616 You can recreate all the plots shown here at the following website. Note that this
2617 interactive plotting tool also allows you to view the Monte Carlo samplings, which
2618 produced the scatter plots used in this document.

2619 www.fusion.codes

2620 H.1 Magnet Strength Scans

2621 This section includes the following magnet strength scans:

- 2622 1. Plasma Temperature – \overline{T}
- 2623 2. Plasma Density – \overline{n}
- 2624 3. Plasma Current – I_P
- 2625 4. Major Radius – R_0
- 2626 5. Plasma Pressure – \overline{p}
- 2627 6. Confinement Time – τ_E
- 2628 7. Current Drive Efficiency – η_{CD}
- 2629 8. Bootstrap Fraction – f_{BS}
- 2630 9. Magnetic Energy – W_M
- 2631 10. Cost-per-Watt – C_W
- 2632 11. Divertor Head Load – q_{DV}
- 2633 12. Normalized Beta Normal – $(\beta_N)_{norm}$
- 2634 13. Normalized Kink Safety Factor – $(q_{95})_{norm}$
- 2635 14. Normalized Wall Loading – $(P_W)_{norm}$
- 2636 15. Fusion Power – P_F
- 2637 16. Blanket Thickness – b
- 2638 17. TF Coil Thickness – c
- 2639 18. Central Solenoid Thickness – d
- 2640 19. Central Solenoid Height – h_{CS}
- 2641 20. Central Solenoid Inner Radius – R_{CS}

8.1.1 Plasma Temperature – \bar{T}

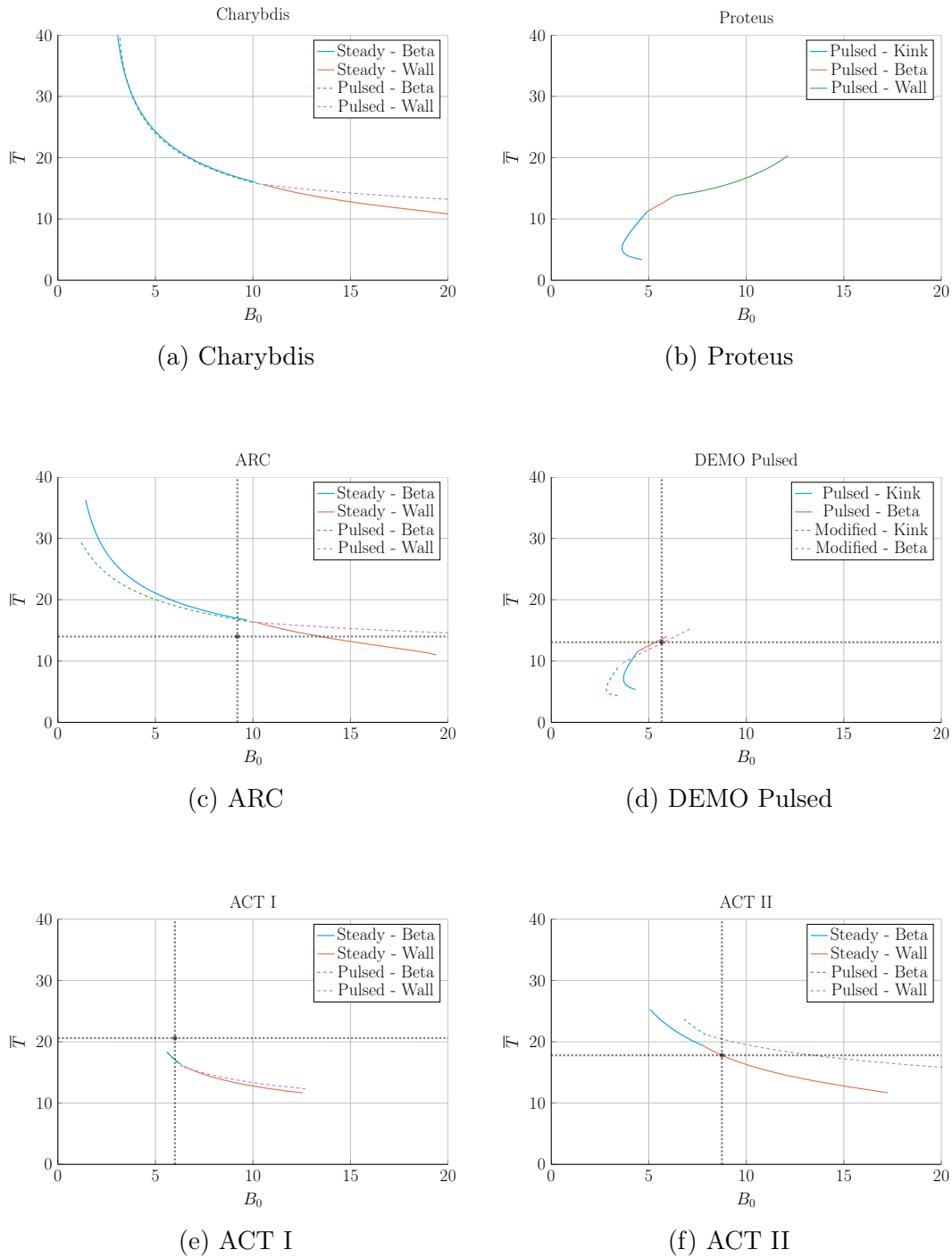
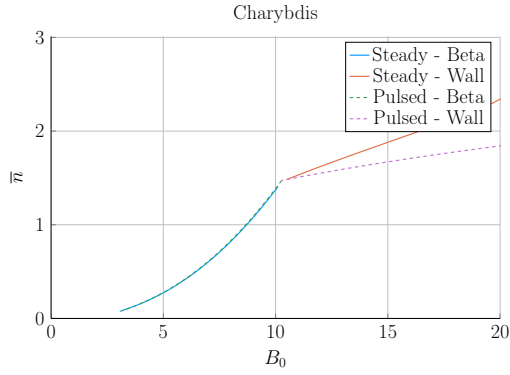
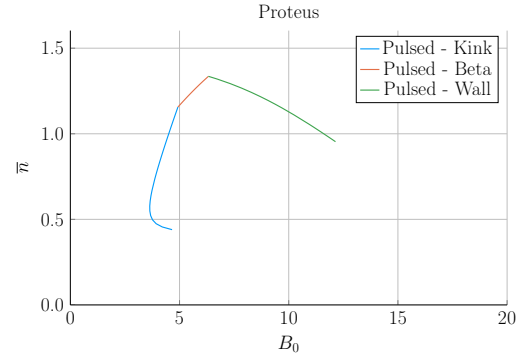


Figure H-1: Magnet Scan: \bar{T} vs B_0

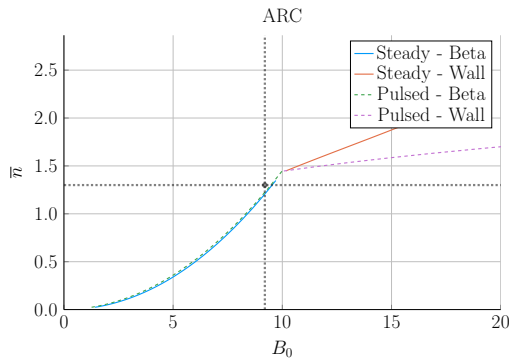
8.1.2 Plasma Density – \bar{n}



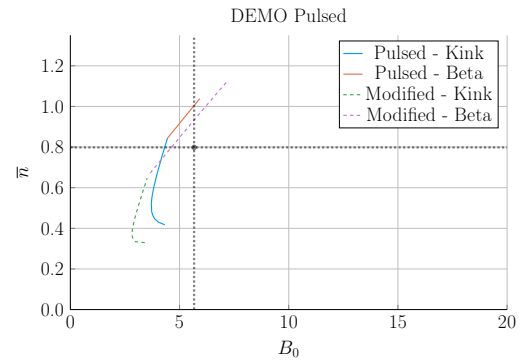
(a) Charybdis



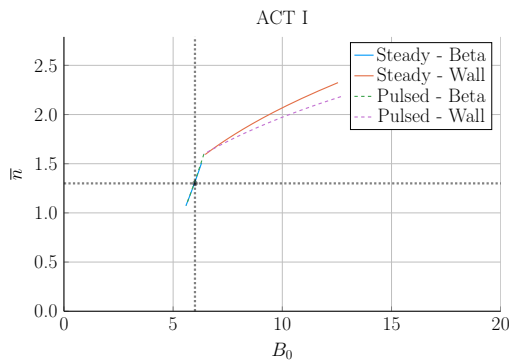
(b) Proteus



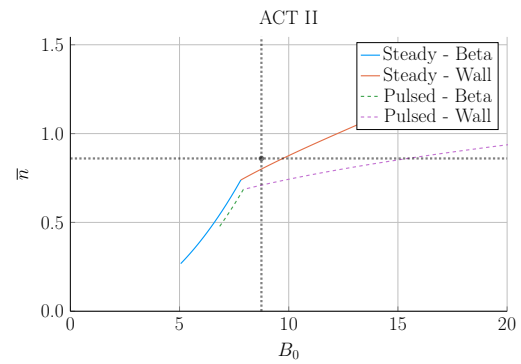
(c) ARC



(d) DEMO Pulsed



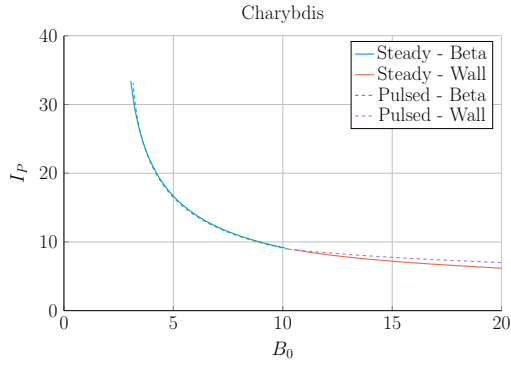
(e) ACT I



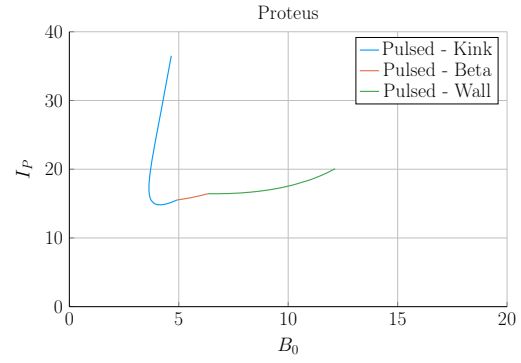
(f) ACT II

Figure H-2: Magnet Scan: \bar{n} vs B_0

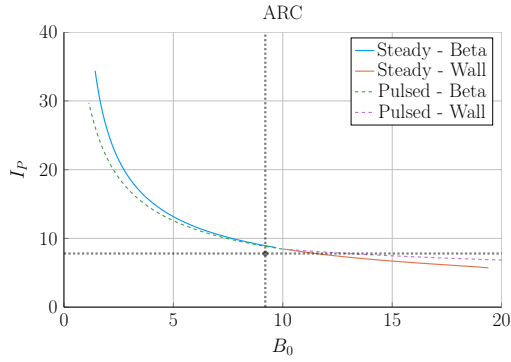
8.1.3 Plasma Current – I_P



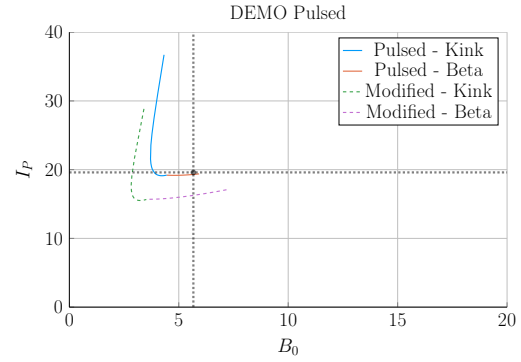
(a) Charybdis



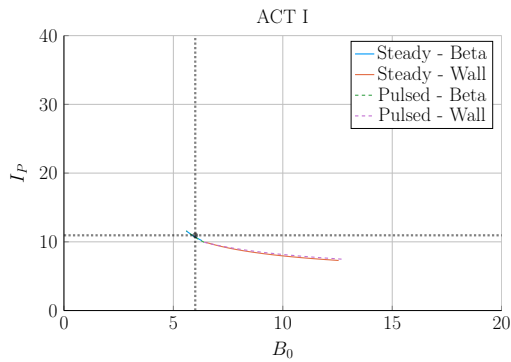
(b) Proteus



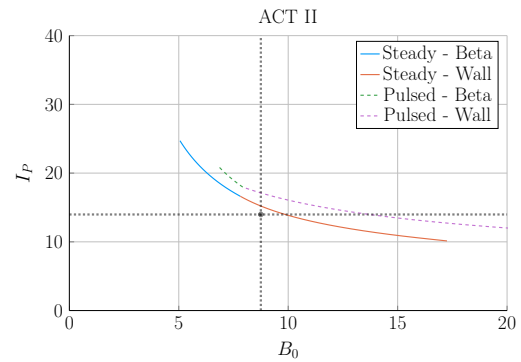
(c) ARC



(d) DEMO Pulsed



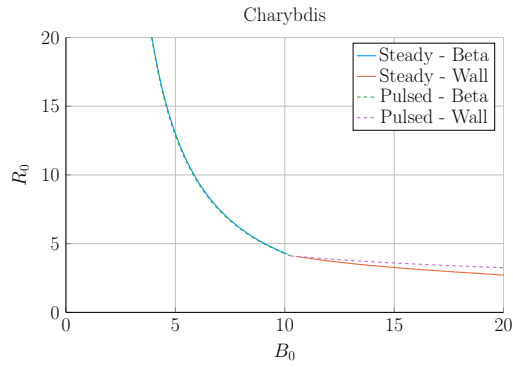
(e) ACT I



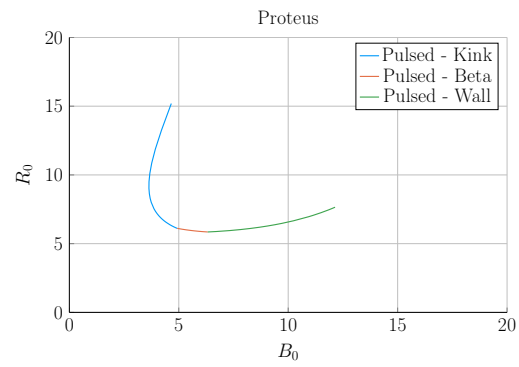
(f) ACT II

Figure H-3: Magnet Scan: I_P vs B_0

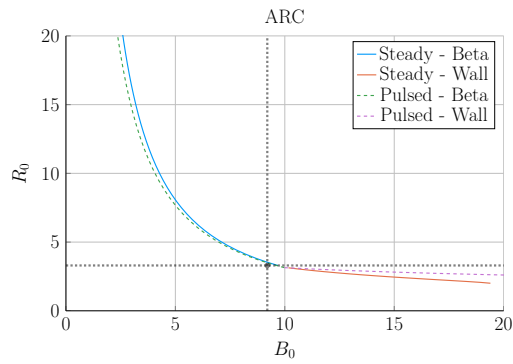
8.1.4 Major Radius – R_0



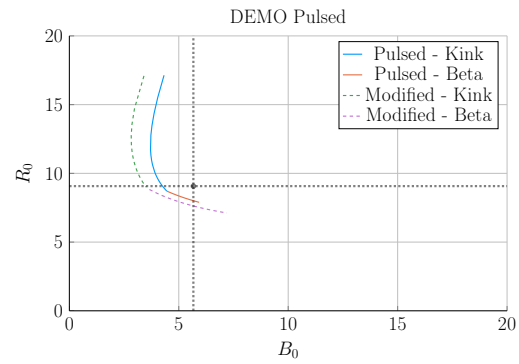
(a) Charybdis



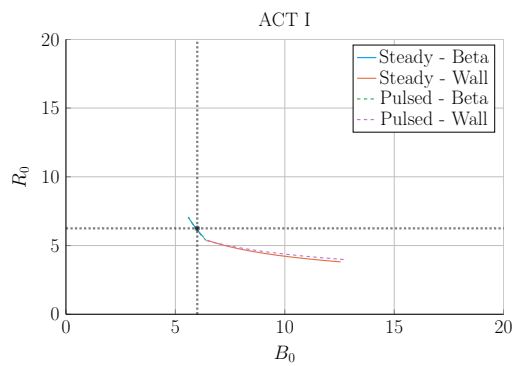
(b) Proteus



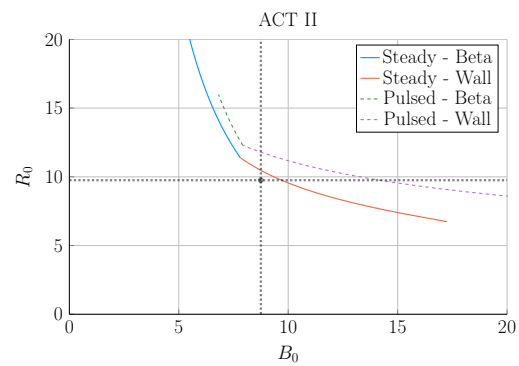
(c) ARC



(d) DEMO Pulsed



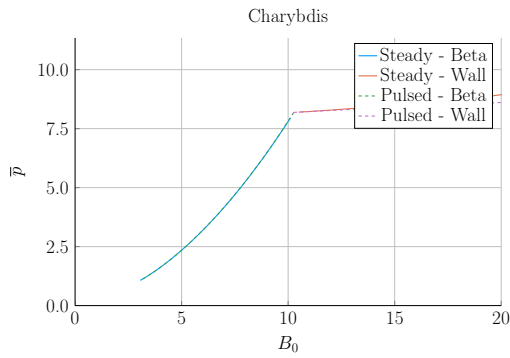
(e) ACT I



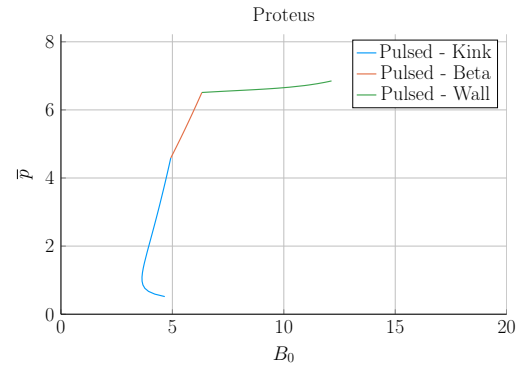
(f) ACT II

Figure H-4: Magnet Scan: R_0 vs B_0

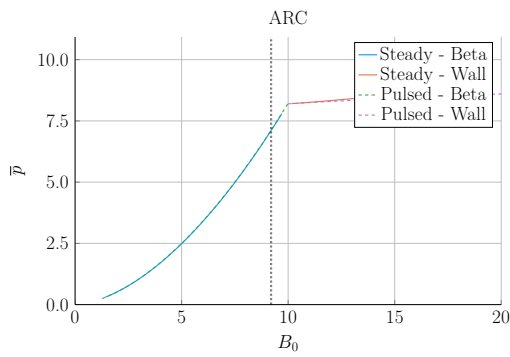
8.1.5 Plasma Pressure – \bar{p}



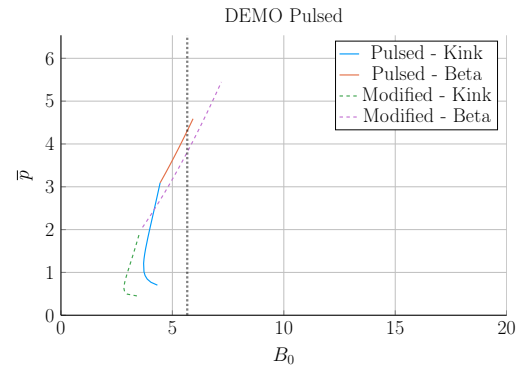
(a) Charybdis



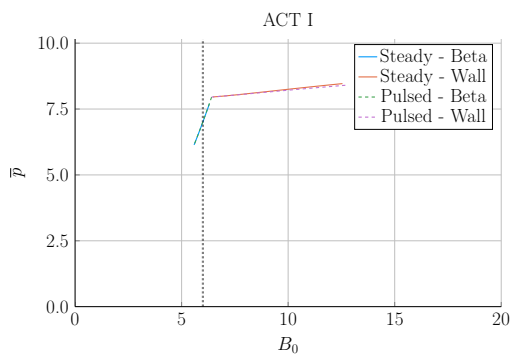
(b) Proteus



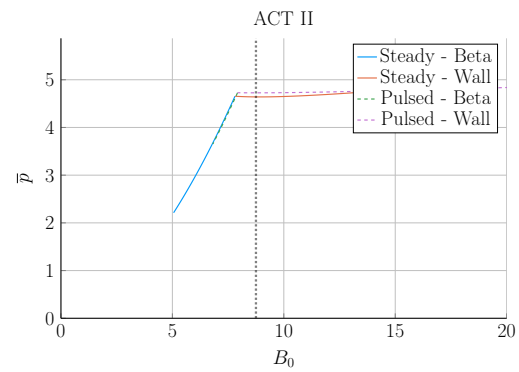
(c) ARC



(d) DEMO Pulsed



(e) ACT I



(f) ACT II

Figure H-5: Magnet Scan: \bar{p} vs B_0

8.1.6 Confinement Time – τ_E

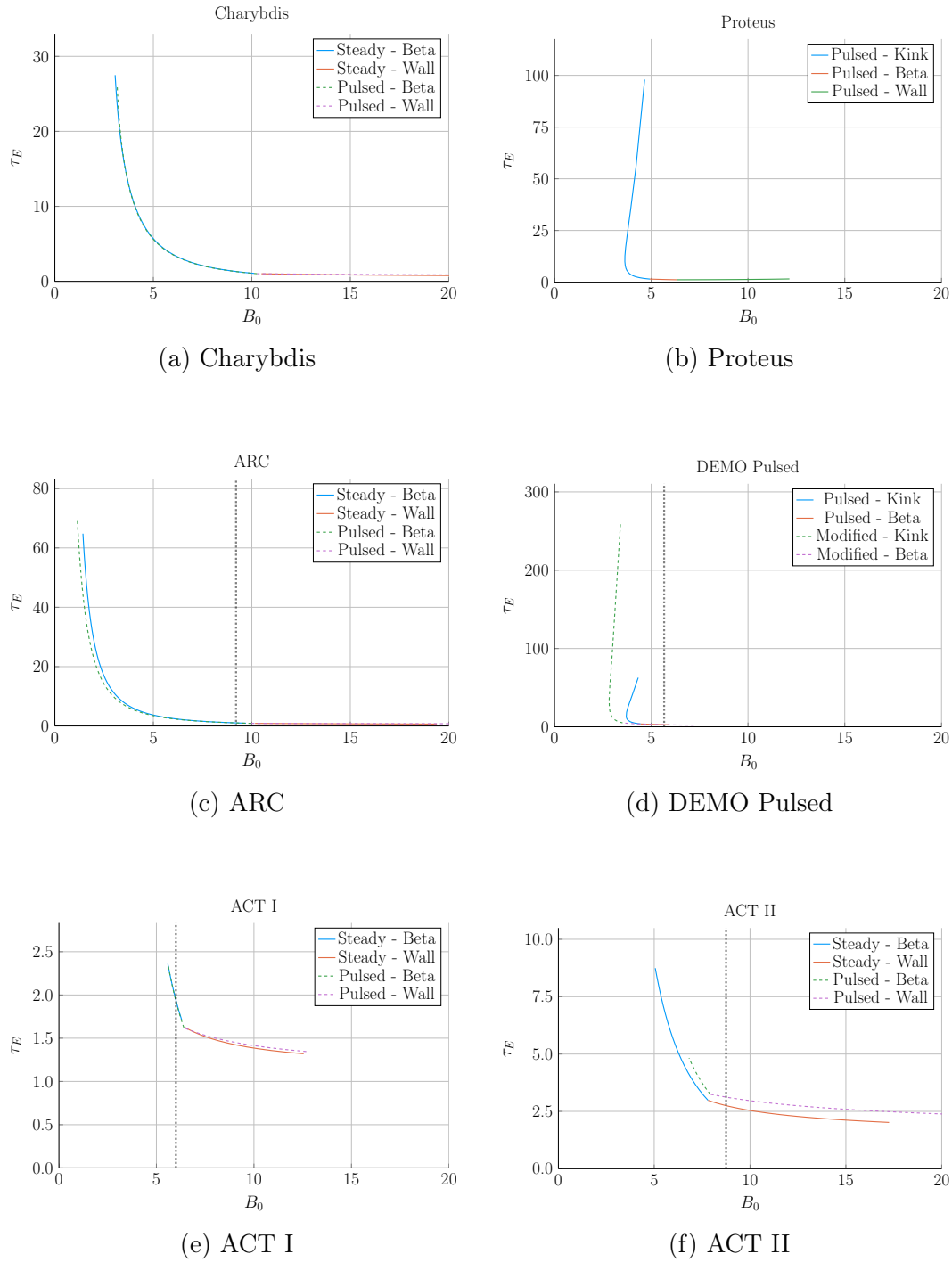
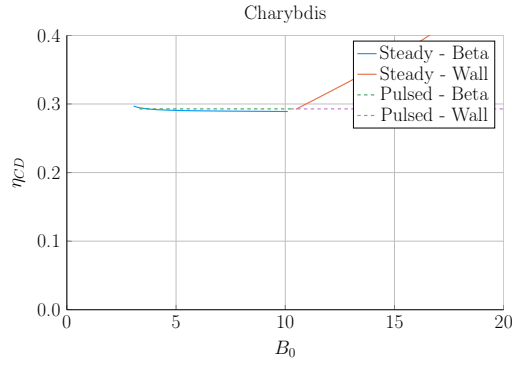
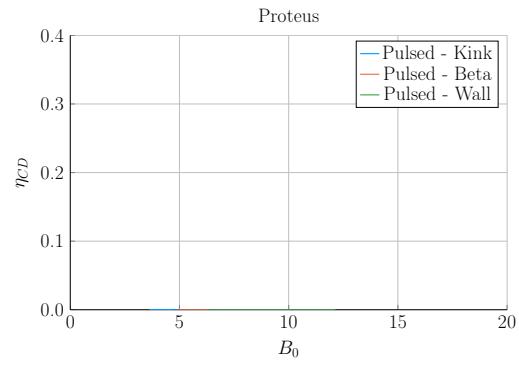


Figure H-6: Magnet Scan: τ_E vs B_0

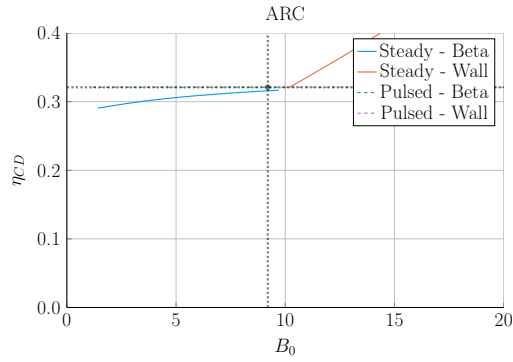
8.1.7 Current Drive Efficiency – η_{CD}



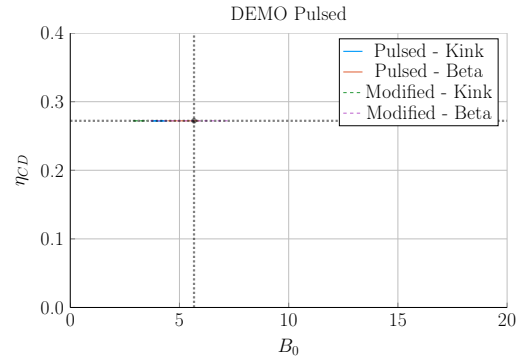
(a) Charybdis



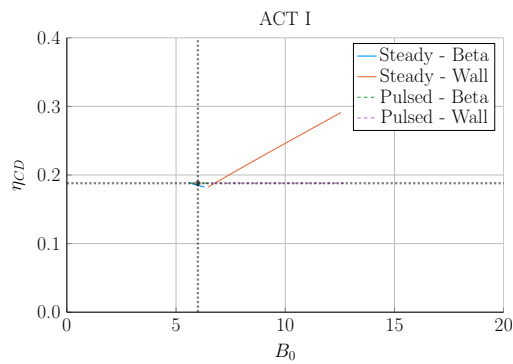
(b) Proteus



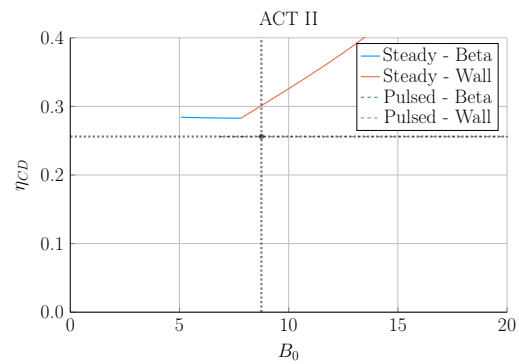
(c) ARC



(d) DEMO Pulsed



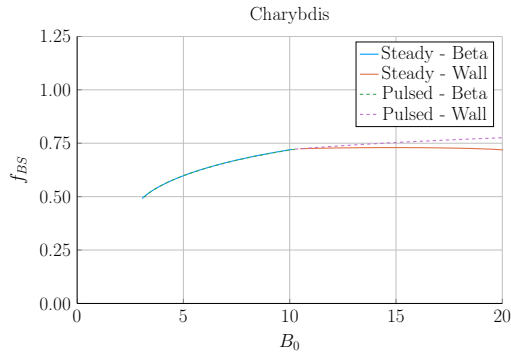
(e) ACT I



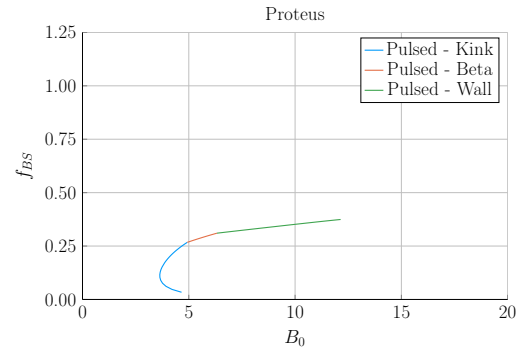
(f) ACT II

Figure H-7: Magnet Scan: η_{CD} vs B_0

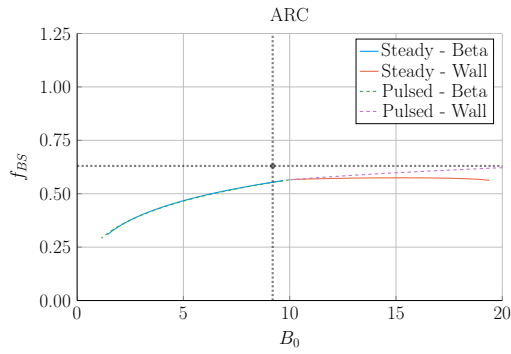
8.1.8 Bootstrap Fraction – f_{BS}



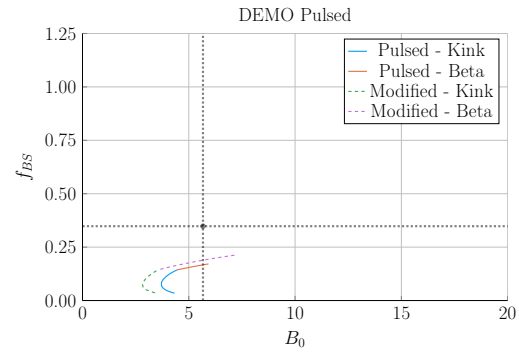
(a) Charybdis



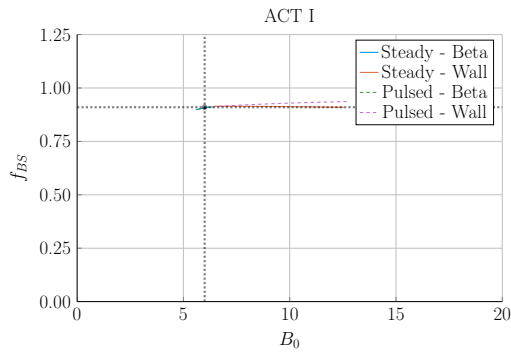
(b) Proteus



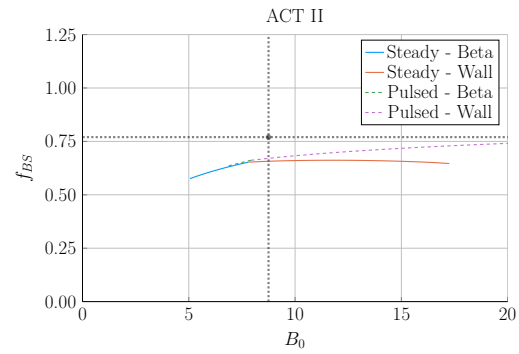
(c) ARC



(d) DEMO Pulsed



(e) ACT I



(f) ACT II

Figure H-8: Magnet Scan: f_{BS} vs B_0

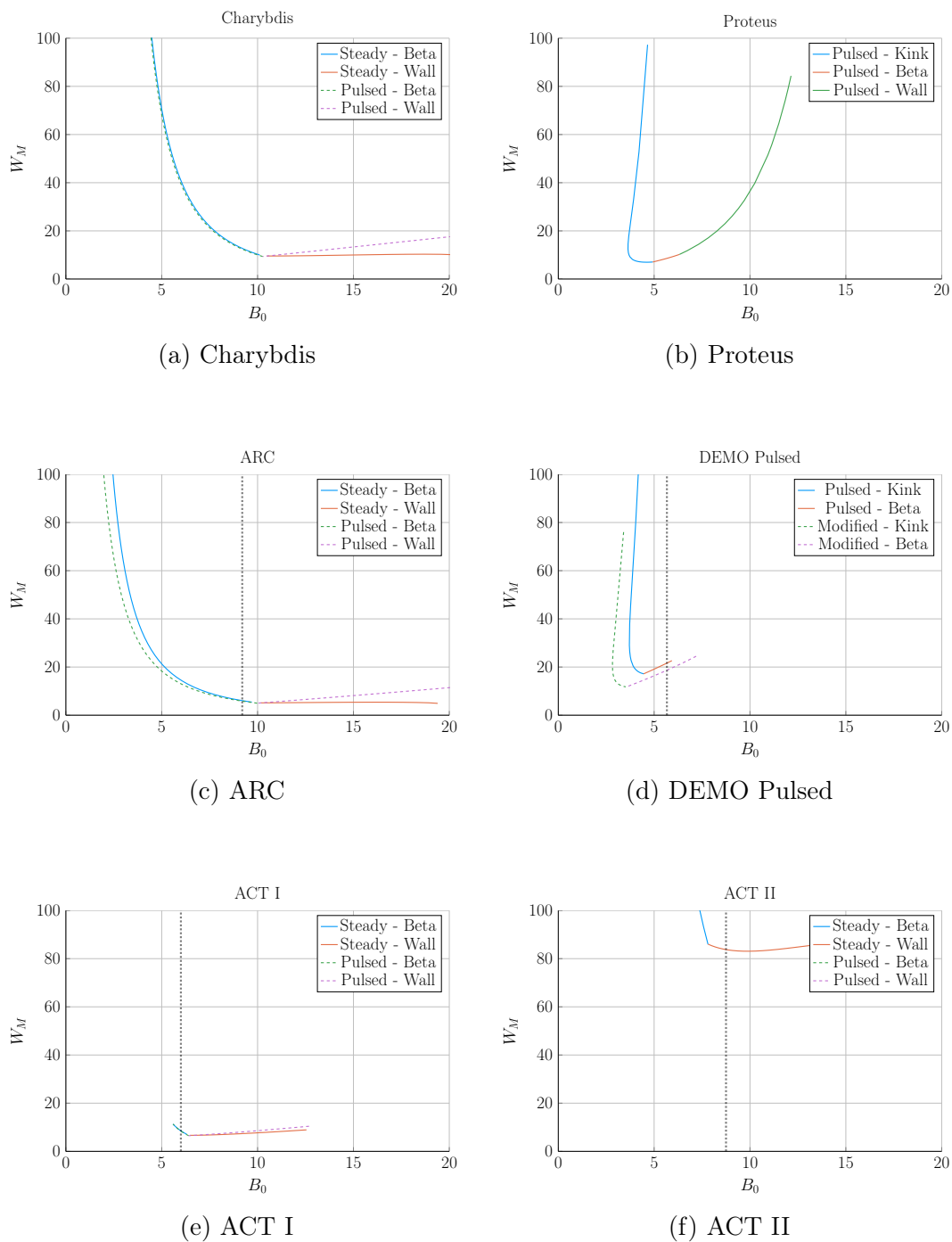
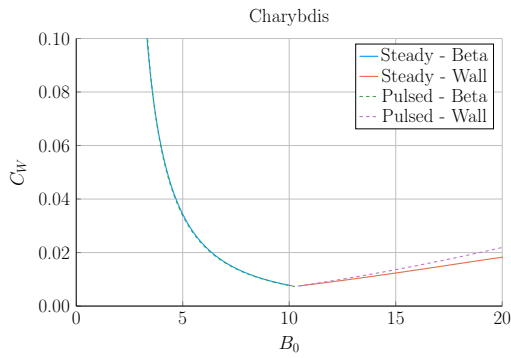
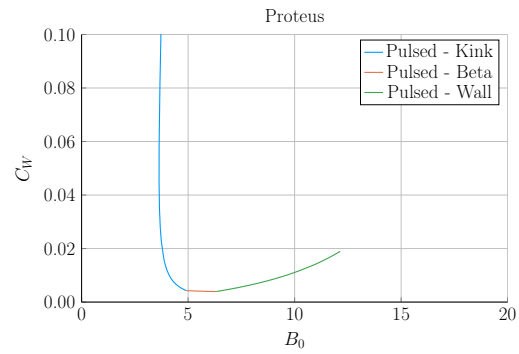


Figure H-9: Magnet Scan: W_M vs B_0

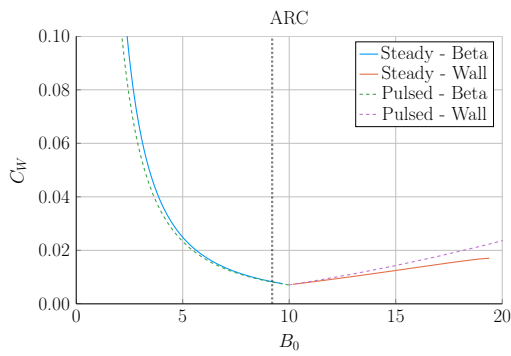
8.1.10 Cost-per-Watt – C_W



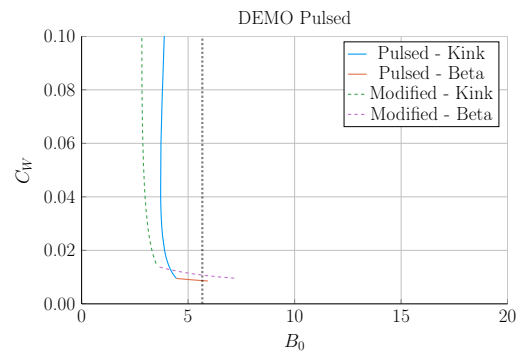
(a) Charybdis



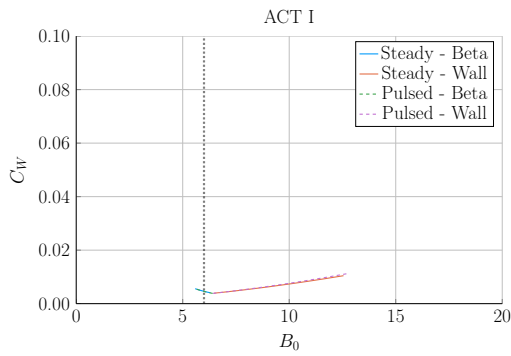
(b) Proteus



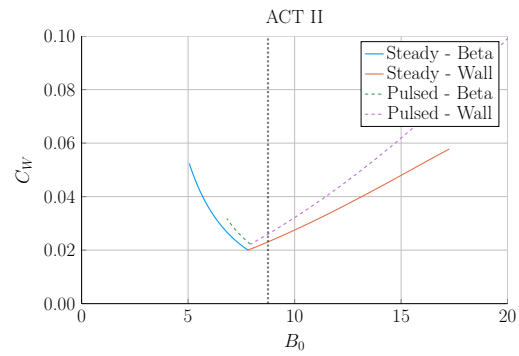
(c) ARC



(d) DEMO Pulsed



(e) ACT I



(f) ACT II

Figure H-10: Magnet Scan: C_W vs B_0

8.1.11 Divertor Head Load – q_{DV}

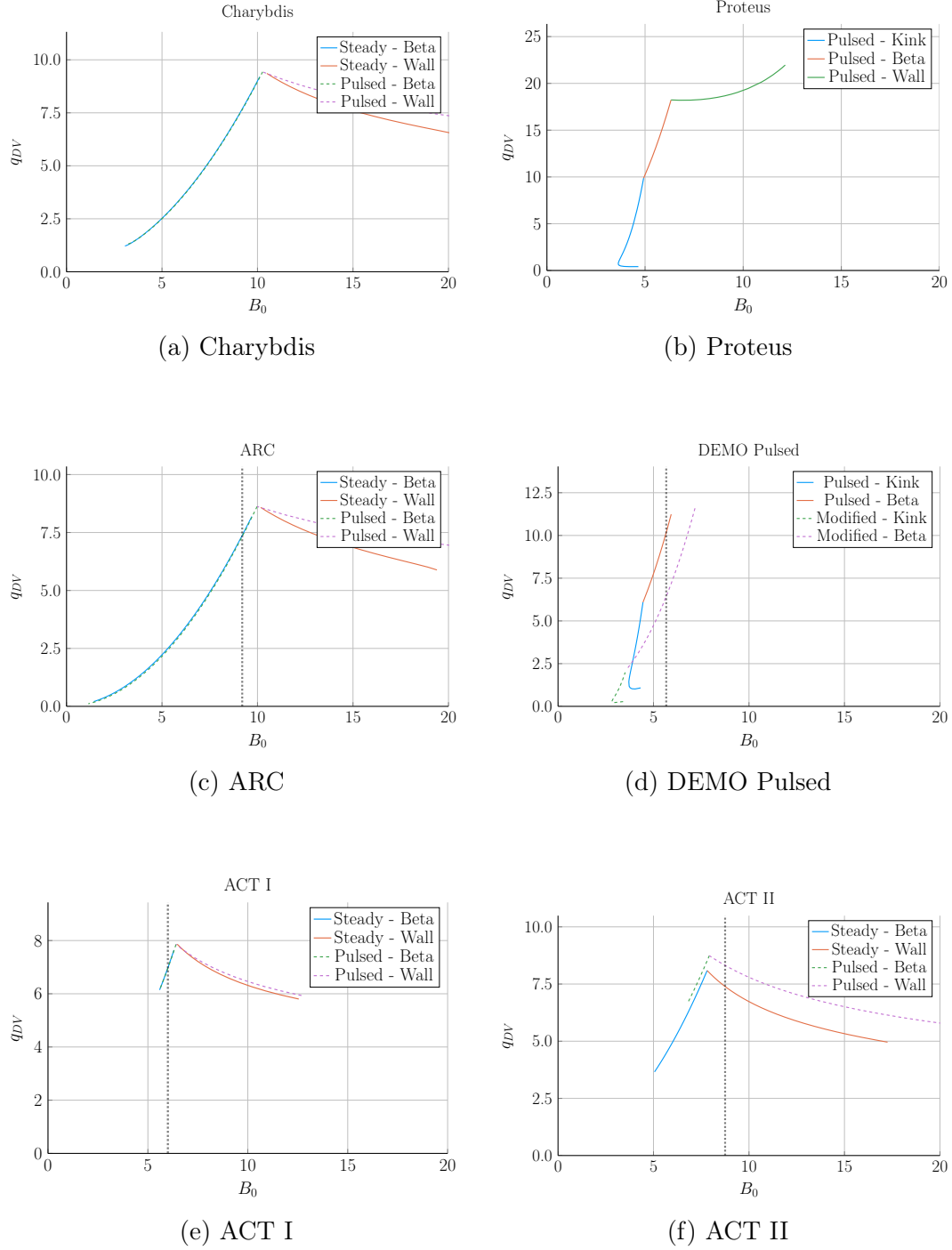


Figure H-11: Magnet Scan: q_{DV} vs B_0

8.1.12 Normalized Beta Normal – $(\beta_N)_{norm}$

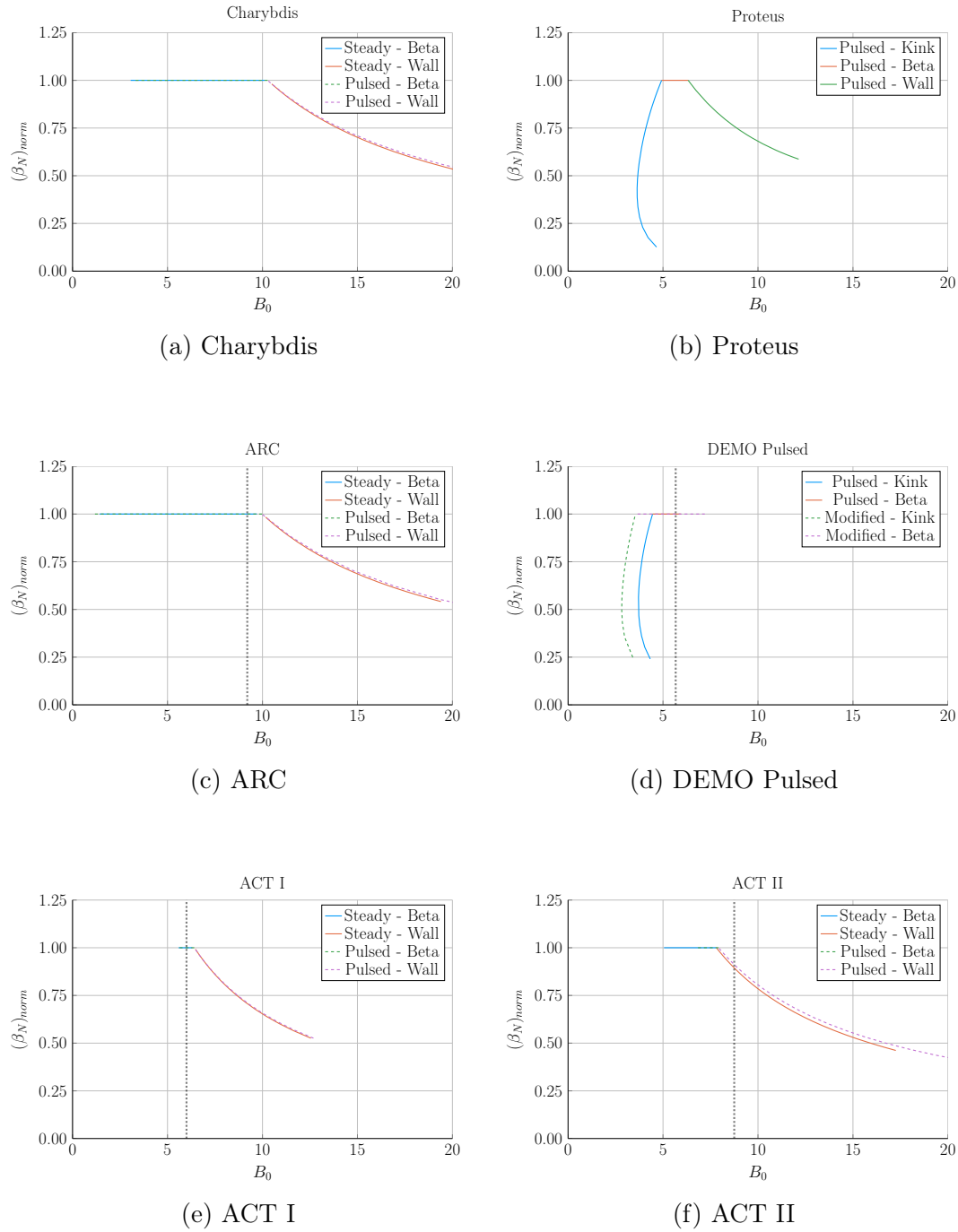


Figure H-12: Magnet Scan: $(\beta_N)_{norm}$ vs B_0

8.1.13 Normalized Kink Safety Factor – $(q_{95})_{norm}$

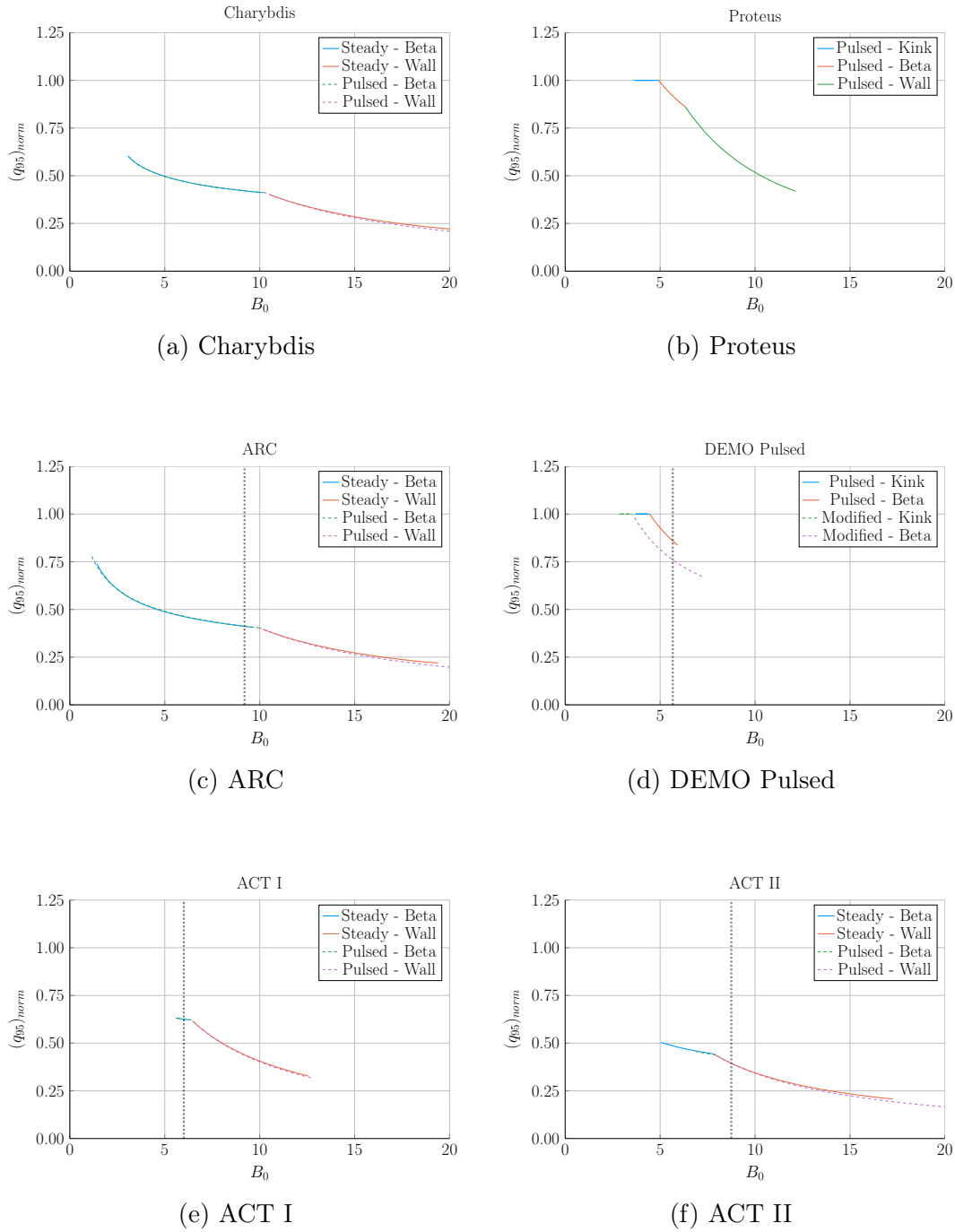


Figure H-13: Magnet Scan: $(q_{95})_{norm}$ vs B_0

8.1.14 Normalized Wall Loading – $(P_W)_{norm}$

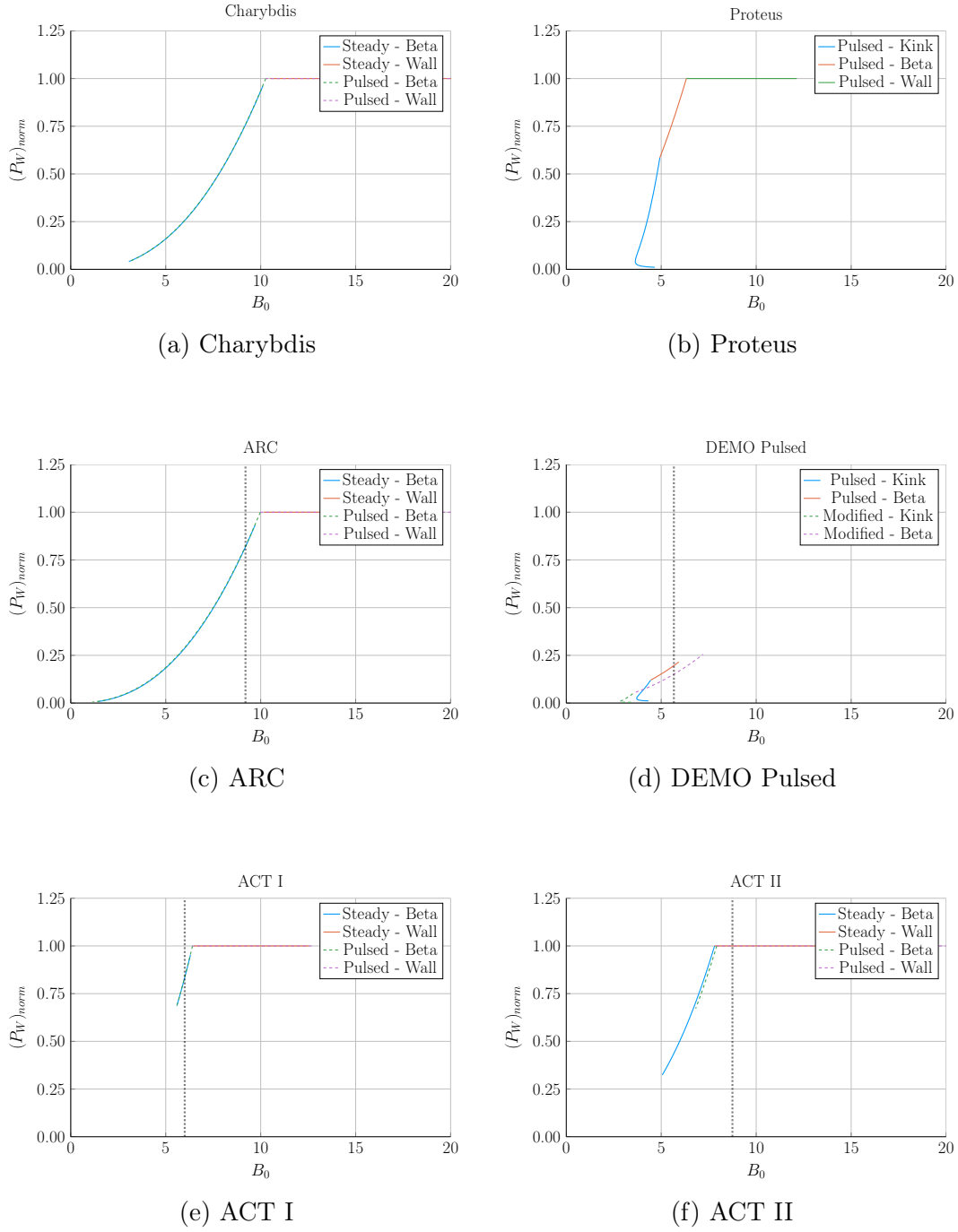
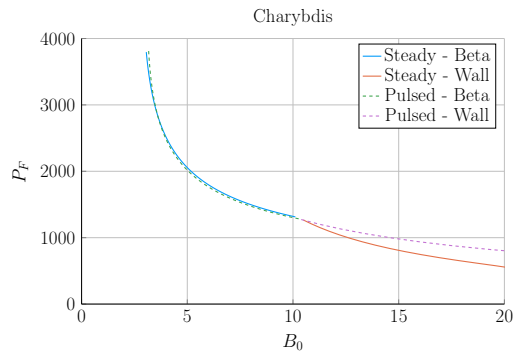
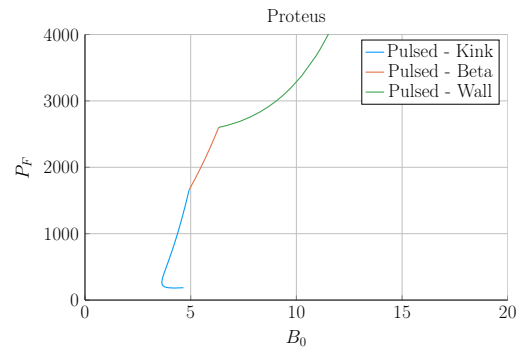


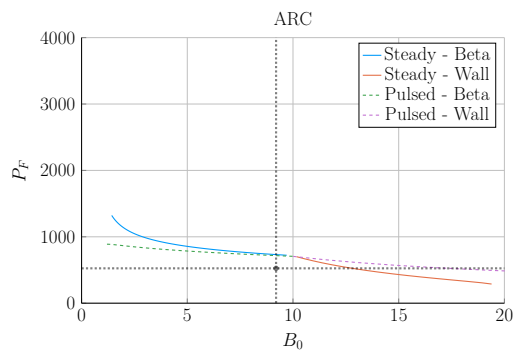
Figure H-14: Magnet Scan: $(P_W)_{norm}$ vs B_0

8.1.15 Fusion Power – P_F 

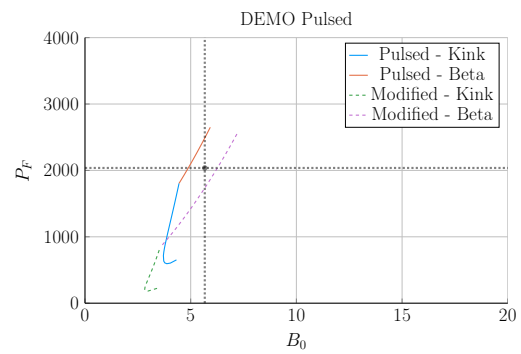
(a) Charybdis



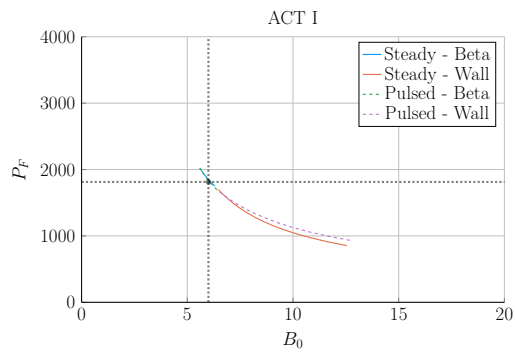
(b) Proteus



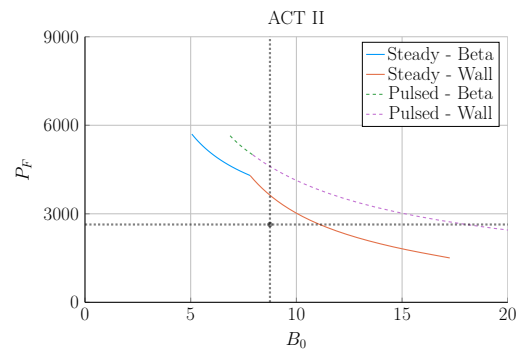
(c) ARC



(d) DEMO Pulsed



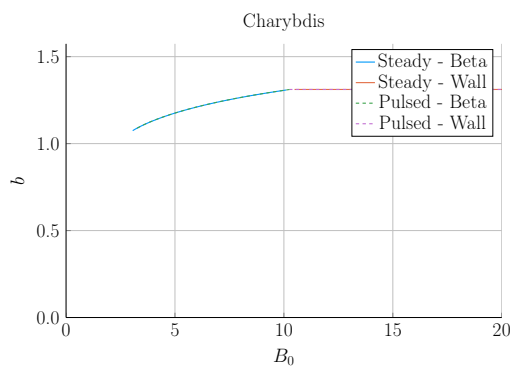
(e) ACT I



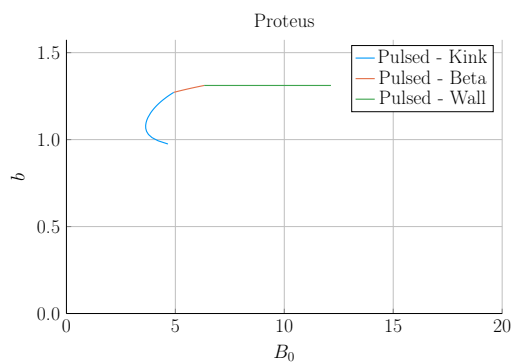
(f) ACT II

Figure H-15: Magnet Scan: P_F vs B_0

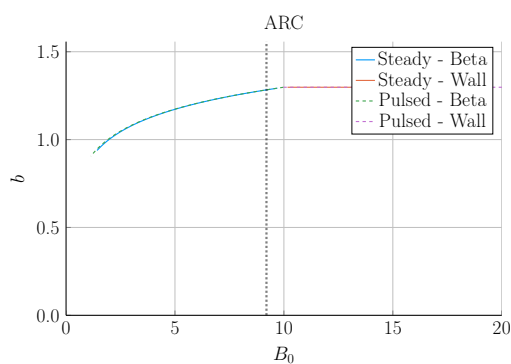
8.1.16 Blanket Thickness – b



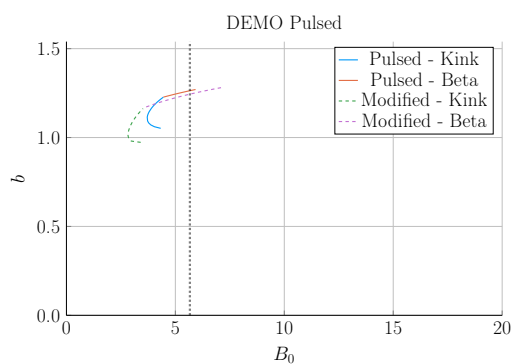
(a) Charybdis



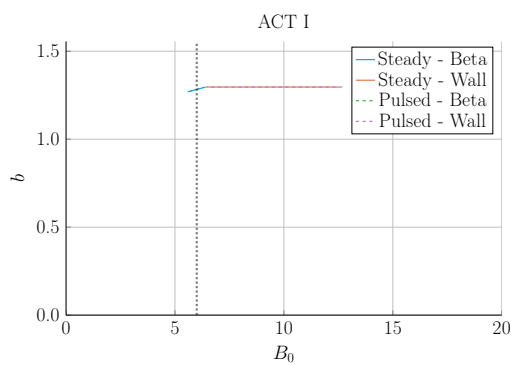
(b) Proteus



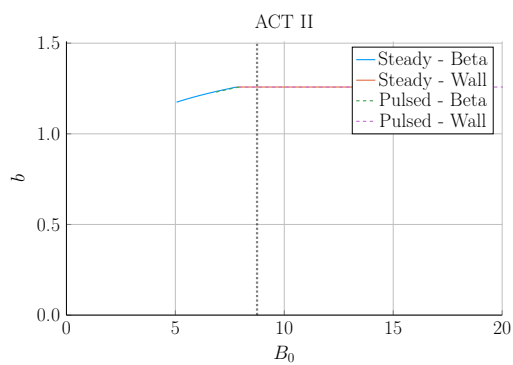
(c) ARC



(d) DEMO Pulsed

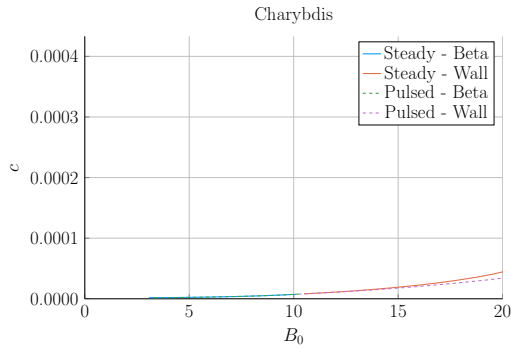


(e) ACT I

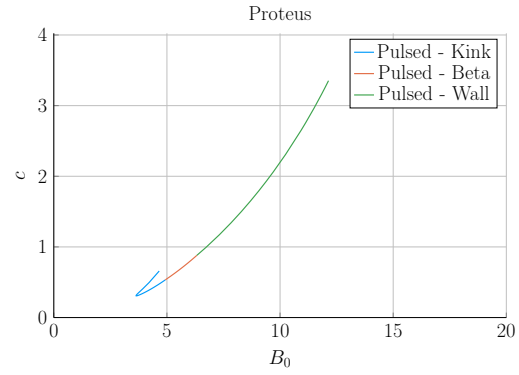


(f) ACT II

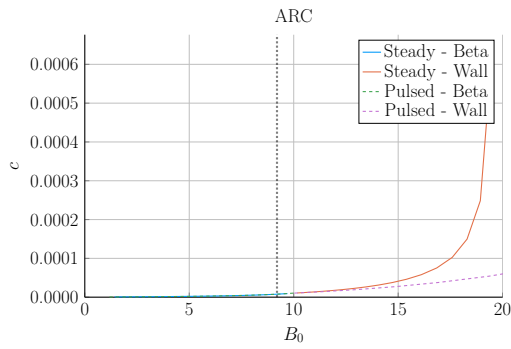
Figure H-16: Magnet Scan: b vs B_0

8.1.17 TF Coil Thickness – c 

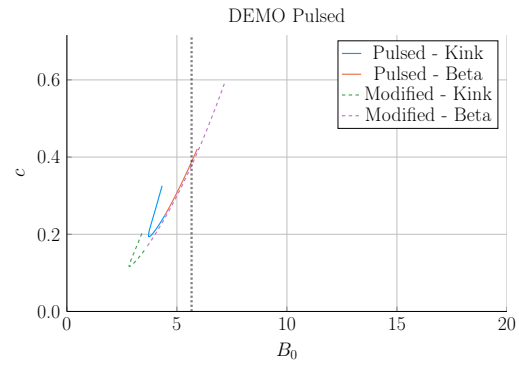
(a) Charybdis



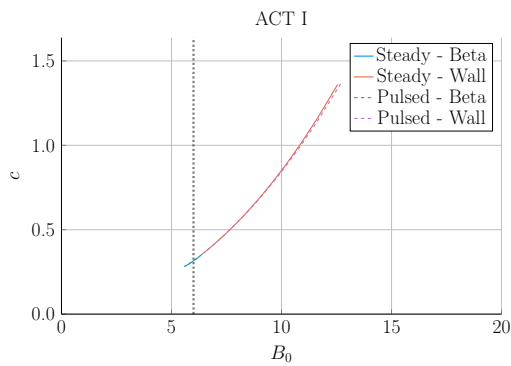
(b) Proteus



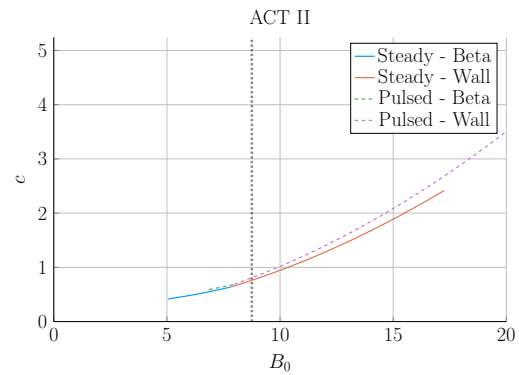
(c) ARC



(d) DEMO Pulsed



(e) ACT I



(f) ACT II

Figure H-17: Magnet Scan: c vs B_0

8.1.18 Central Solenoid Thickness – d

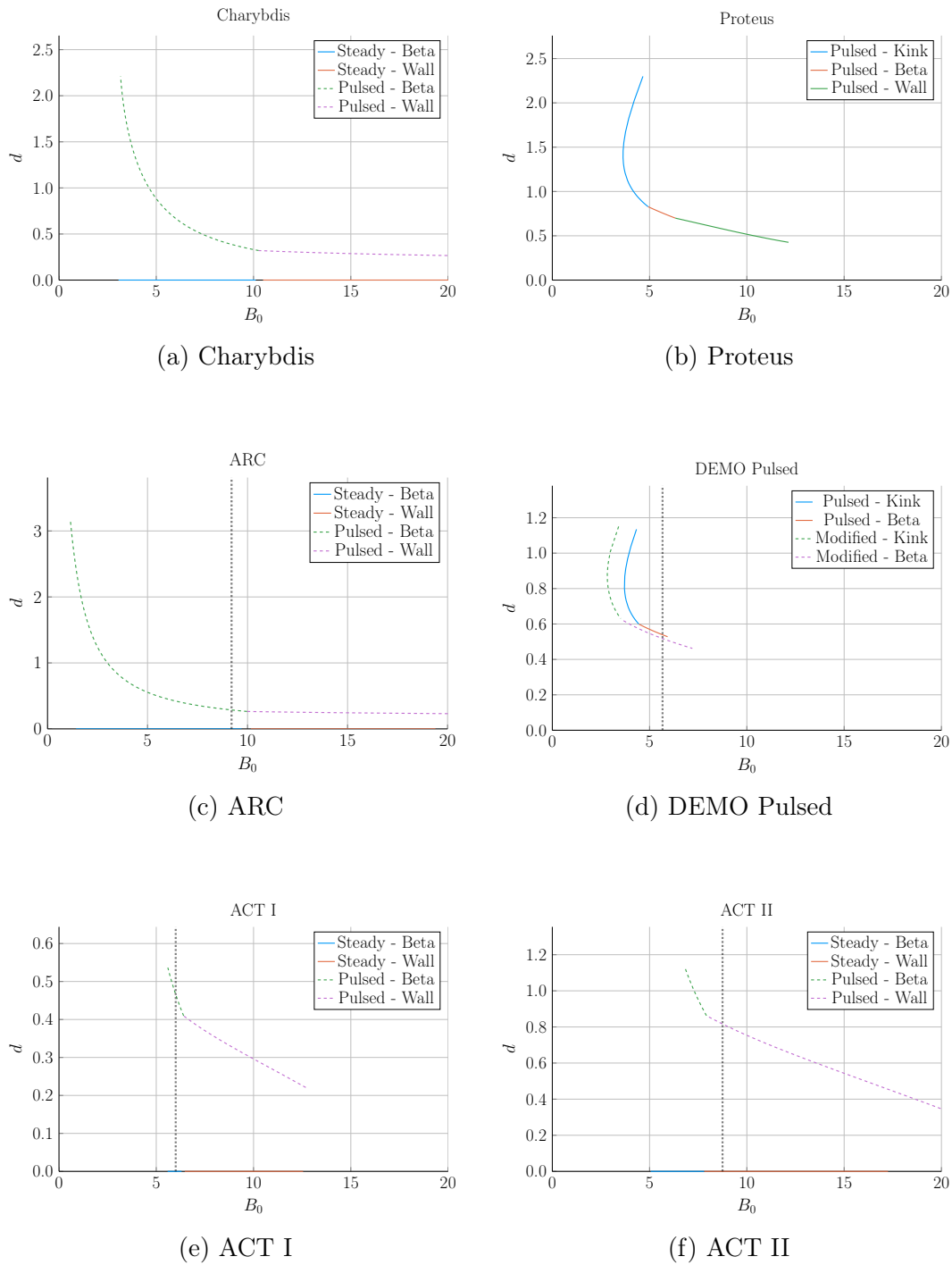
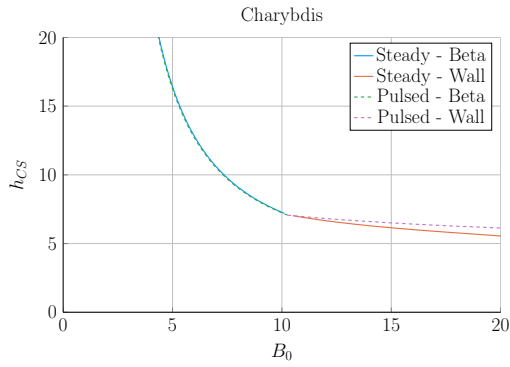
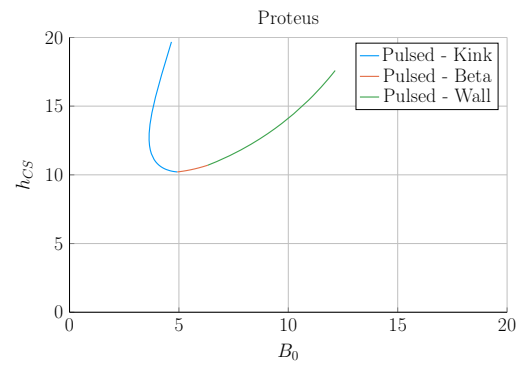


Figure H-18: Magnet Scan: d vs B_0

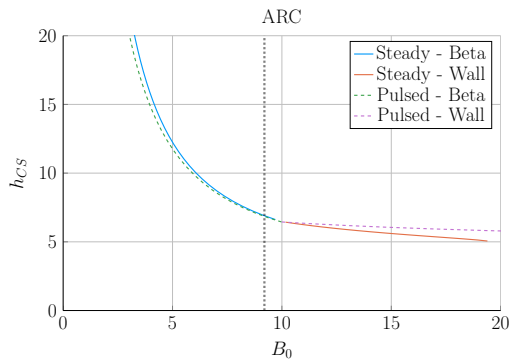
8.1.19 Central Solenoid Height – h_{CS}



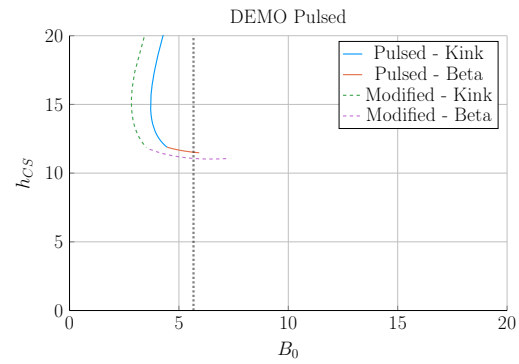
(a) Charybdis



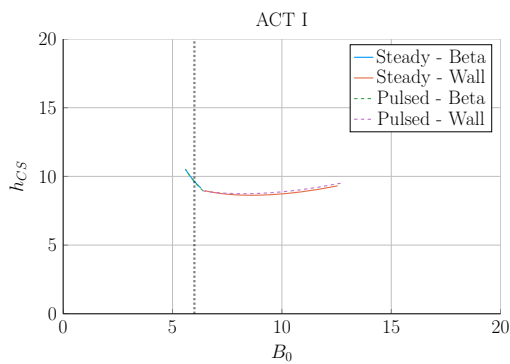
(b) Proteus



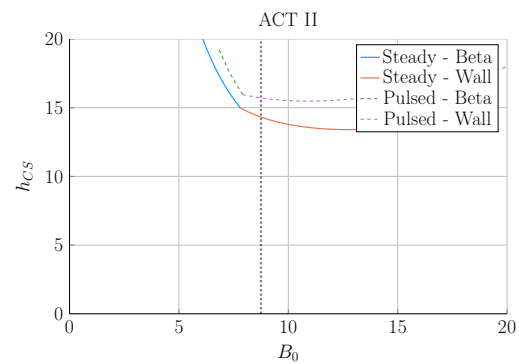
(c) ARC



(d) DEMO Pulsed



(e) ACT I



(f) ACT II

Figure H-19: Magnet Scan: h_{CS} vs B_0

8.1.20 Central Solenoid Inner Radius – R_{CS}

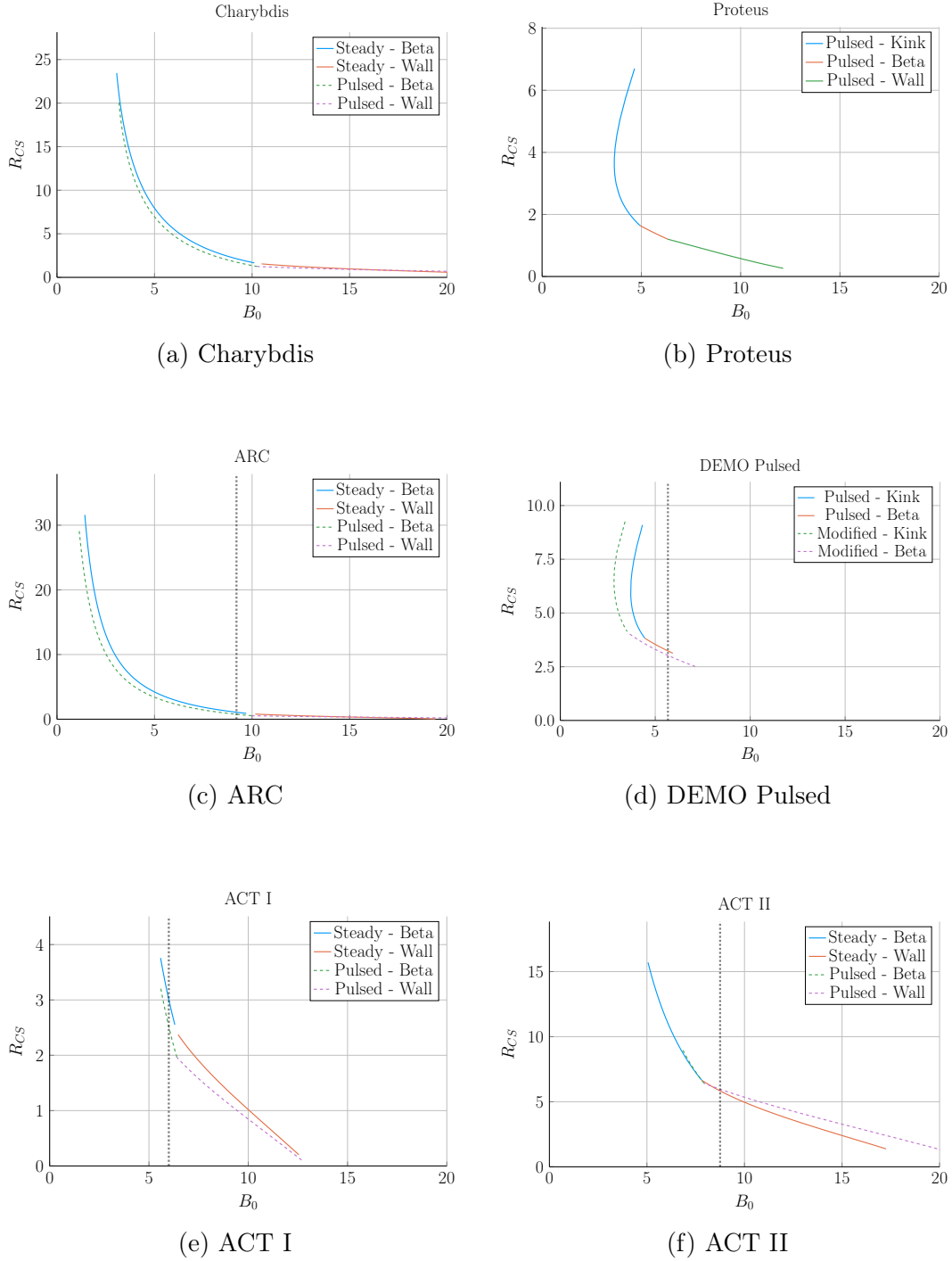


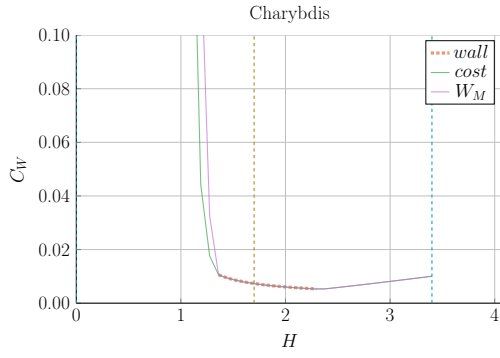
Figure H-20: Magnet Scan: R_{CS} vs B_0

2662 H.2 Cost Sensitivity Studies

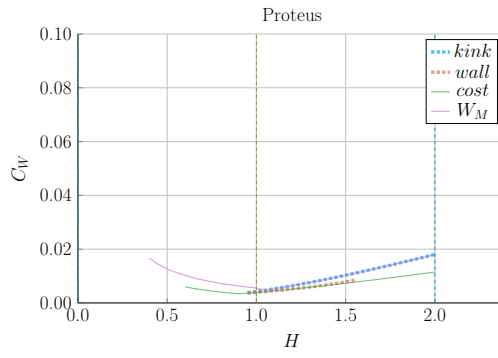
2663 This section includes the following cost sensitivity studies:

- 2664 1. Enhancement Factor – H
- 2665 2. Physics Gain – Q
- 2666 3. Flattop Duration – τ_{FT}
- 2667 4. Greenwald Fraction – N_G
- 2668 5. Dilution Factor – f_D
- 2669 6. Effective Charge – Z_{eff}
- 2670 7. Inverse Aspect Ratio – ϵ
- 2671 8. Elongation – κ_{95}
- 2672 9. Triangularity – δ_{95}
- 2673 10. Density Peaking Factor – ν_n
- 2674 11. Temperature Peaking Factor – ν_T
- 2675 12. Internal Inductance – l_i
- 2676 13. Max Beta Normal – $(\beta_N)_{max}$
- 2677 14. Max Kink Safety Factor – $(q_{95})_{max}$
- 2678 15. Max Wall Loading – $(P_W)_{max}$

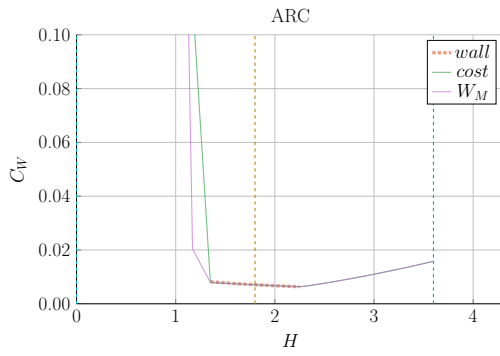
8.2.1 Enhancement Factor – H



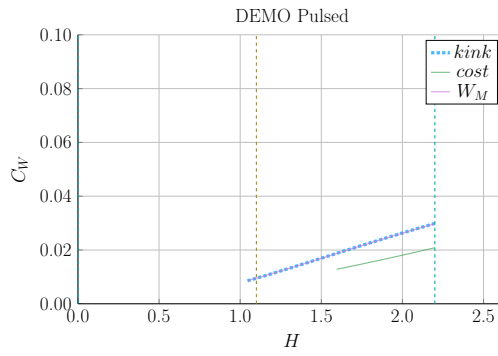
(a) Charybdis



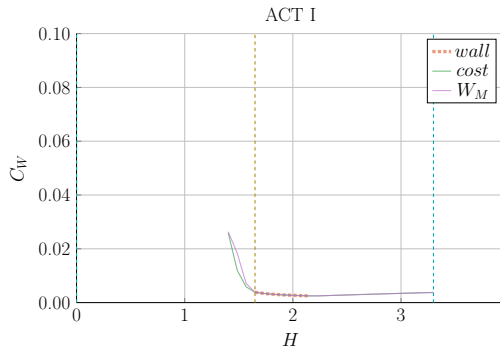
(b) Proteus



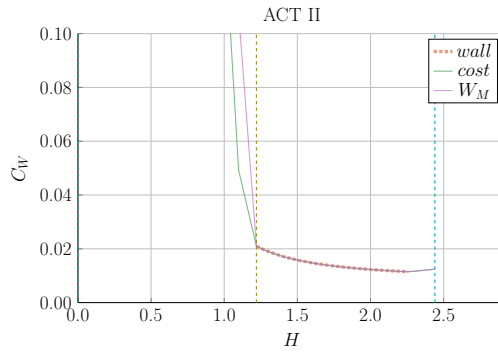
(c) ARC



(d) DEMO Pulsed



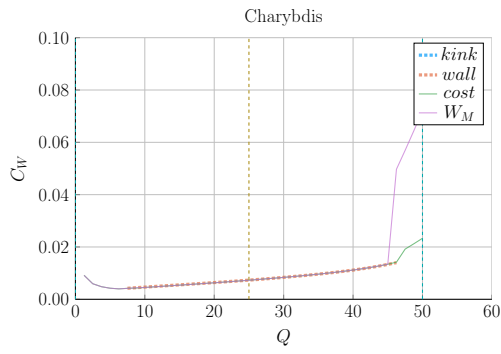
(e) ACT I



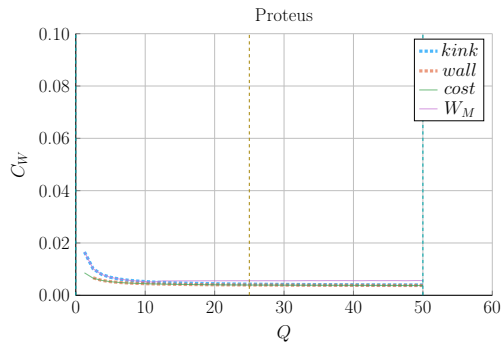
(f) ACT II

Figure H-21: Cost Sensitivity: H vs. B_0

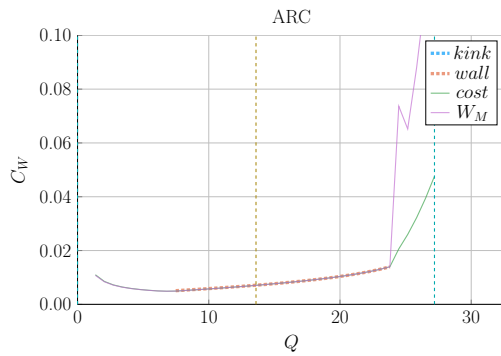
8.2.2 Physics Gain – Q



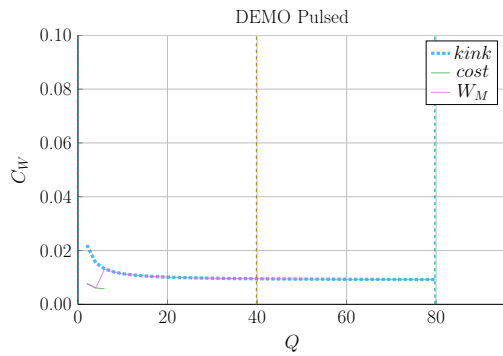
(a) Charybdis



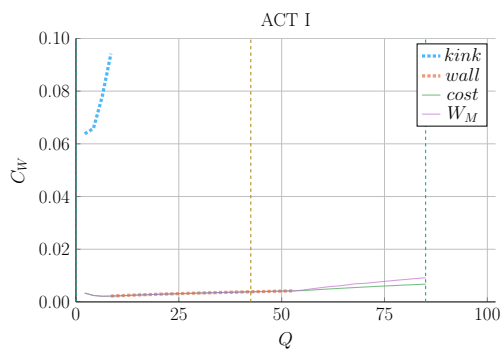
(b) Proteus



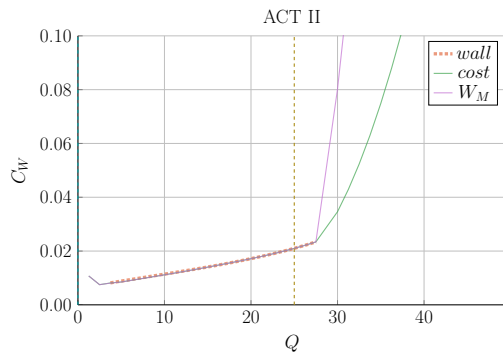
(c) ARC



(d) DEMO Pulsed



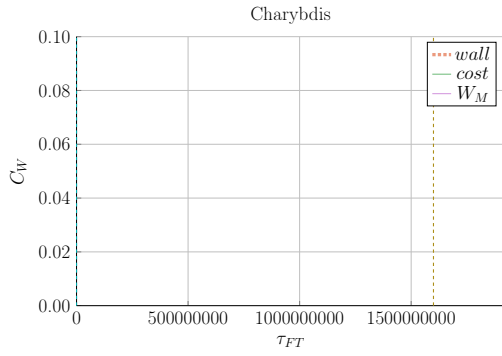
(e) ACT I



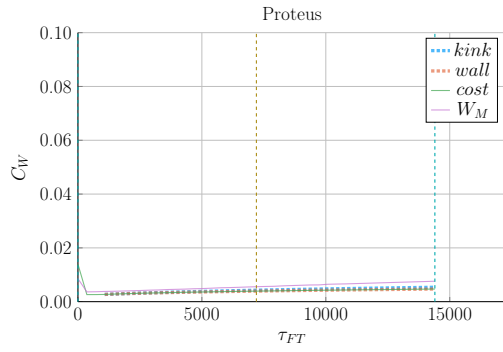
(f) ACT II

Figure H-22: Cost Sensitivity: Q vs. B_0

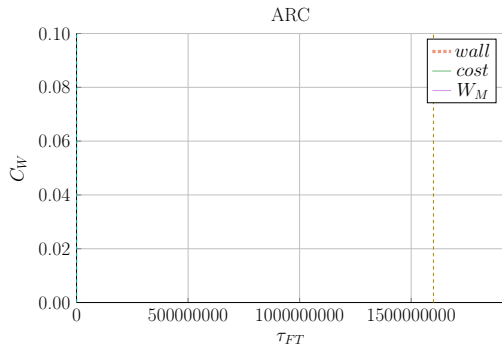
8.2.3 Flattop Duration – τ_{FT}



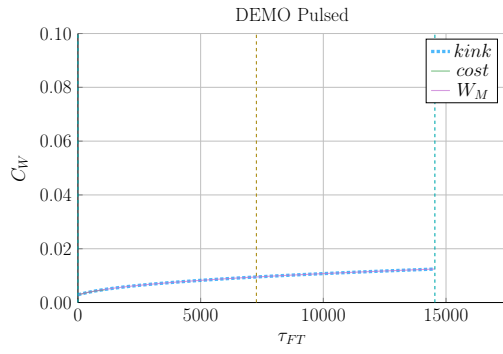
(a) Charybdis



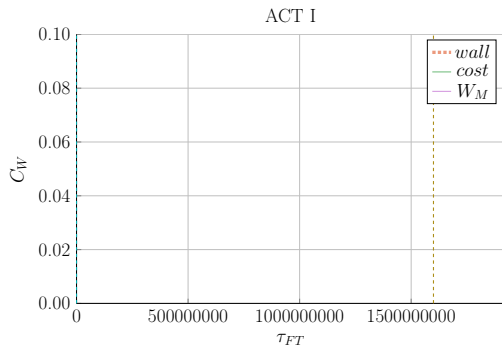
(b) Proteus



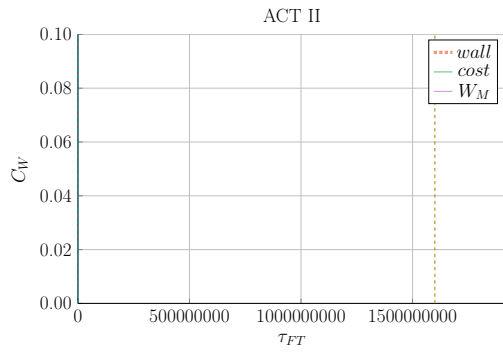
(c) ARC



(d) DEMO Pulsed

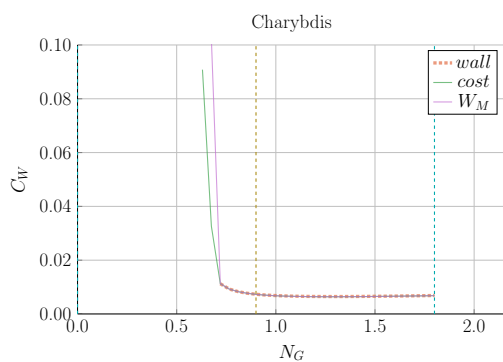


(e) ACT I

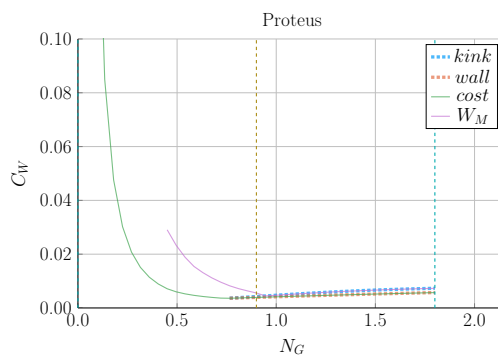


(f) ACT II

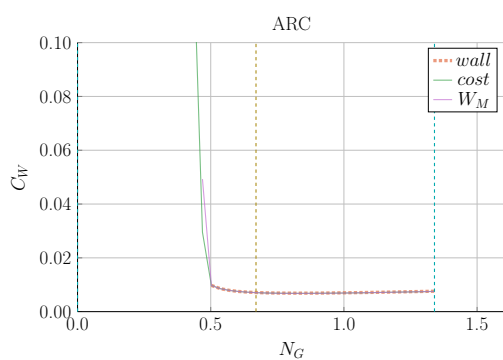
Figure H-23: Cost Sensitivity: τ_{FT} vs. B_0



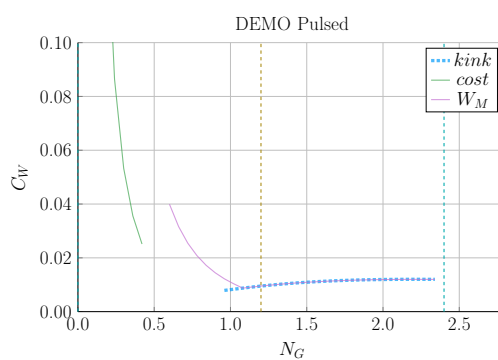
(a) Charybdis



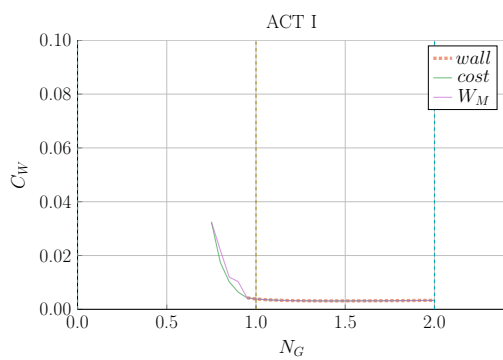
(b) Proteus



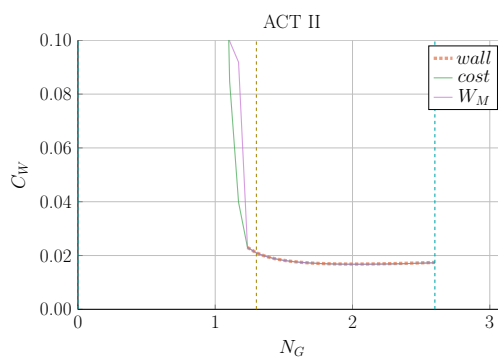
(c) ARC



(d) DEMO Pulsed



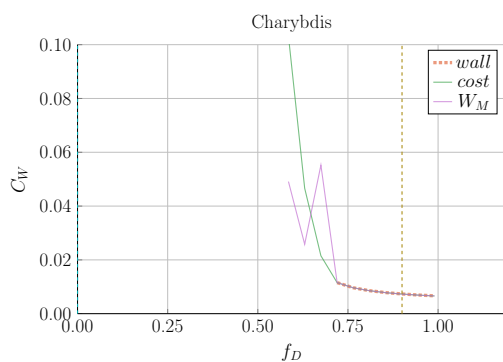
(e) ACT I



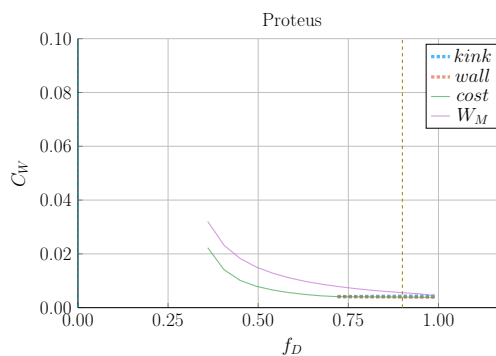
(f) ACT II

Figure H-24: Cost Sensitivity: N_G vs. B_0

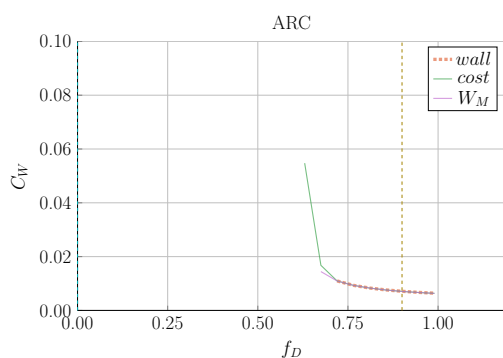
8.2.5 Dilution Factor – f_D



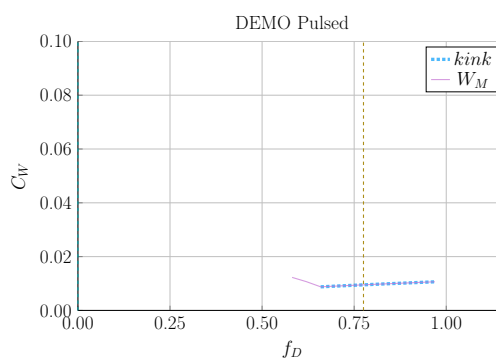
(a) Charybdis



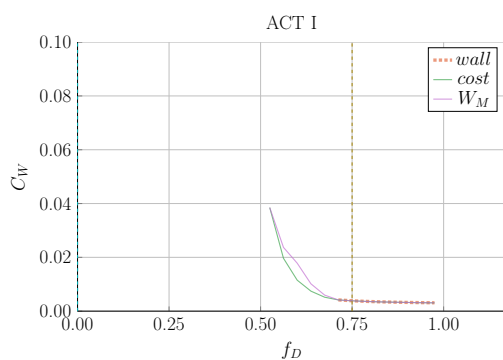
(b) Proteus



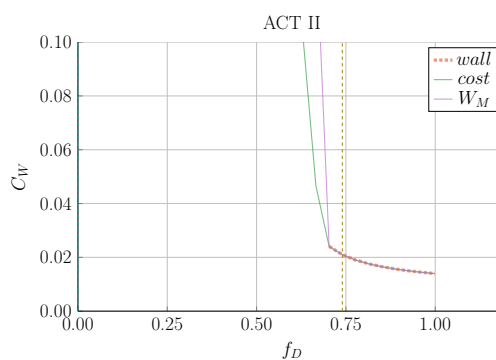
(c) ARC



(d) DEMO Pulsed



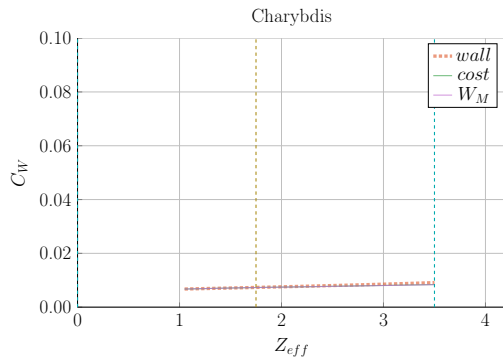
(e) ACT I



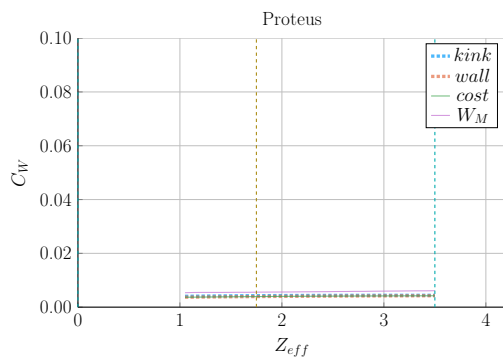
(f) ACT II

Figure H-25: Cost Sensitivity: f_D vs. B_0

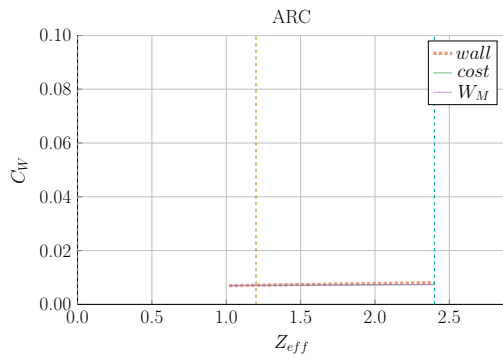
8.2.6 Effective Charge – Z_{eff}



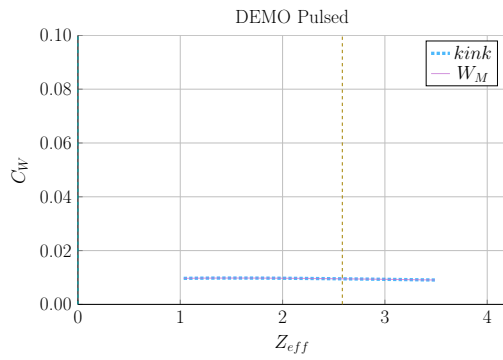
(a) Charybdis



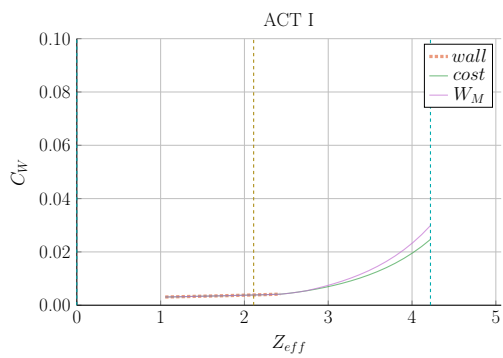
(b) Proteus



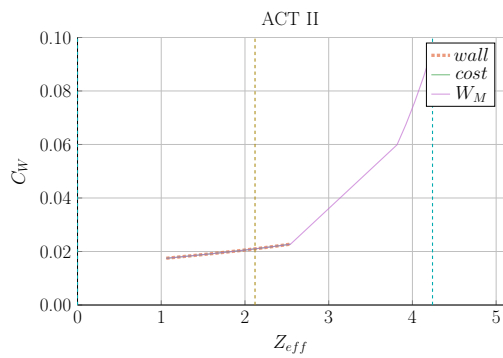
(c) ARC



(d) DEMO Pulsed



(e) ACT I



(f) ACT II

Figure H-26: Cost Sensitivity: Z_{eff} vs. B_0

8.2.7 Inverse Aspect Ratio – ϵ

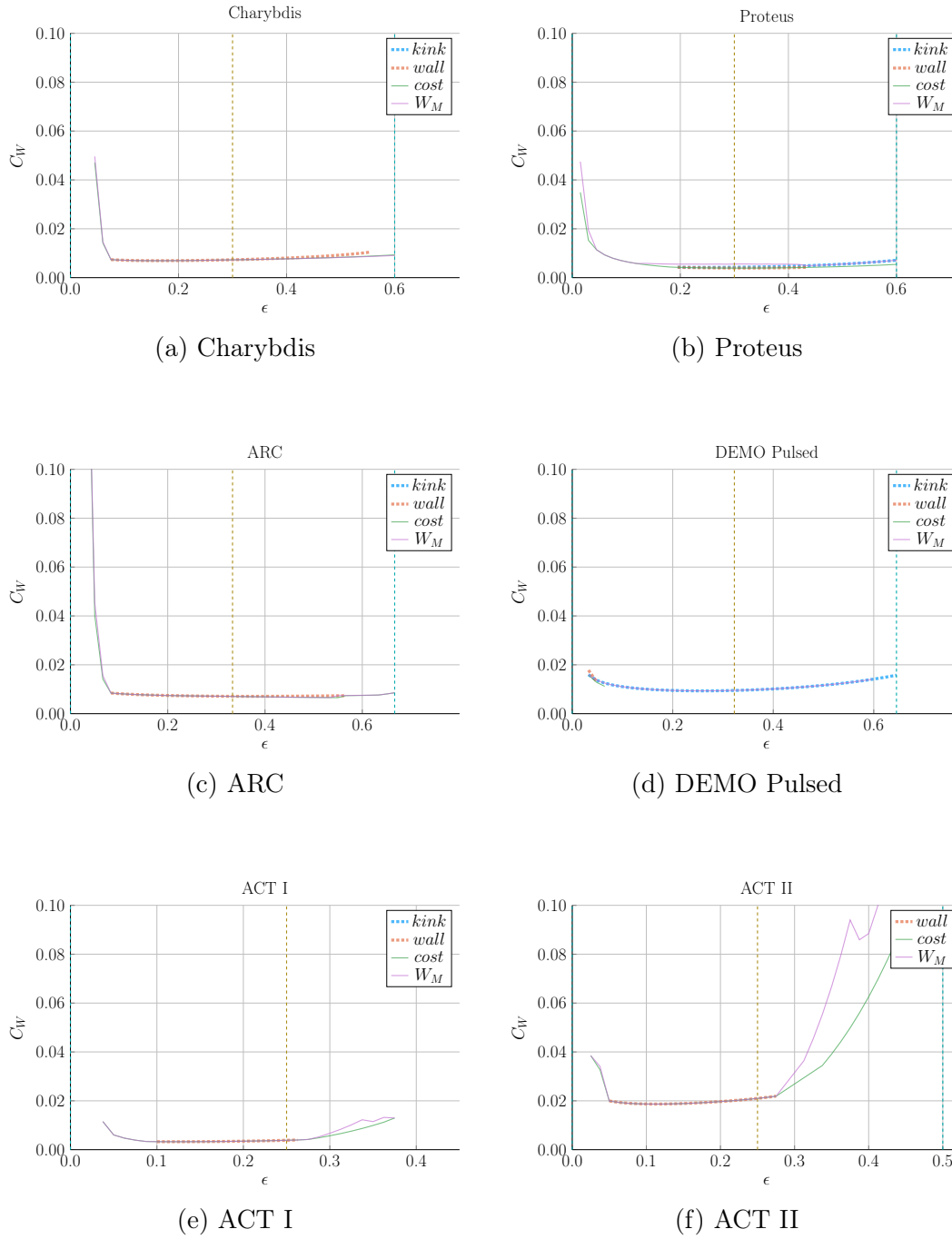
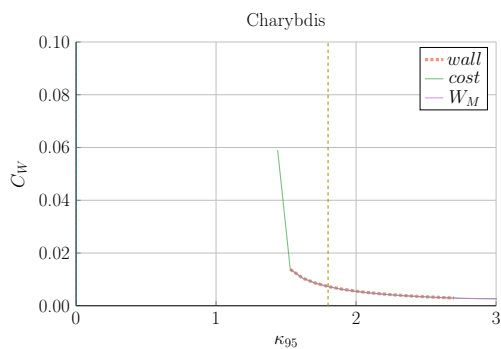
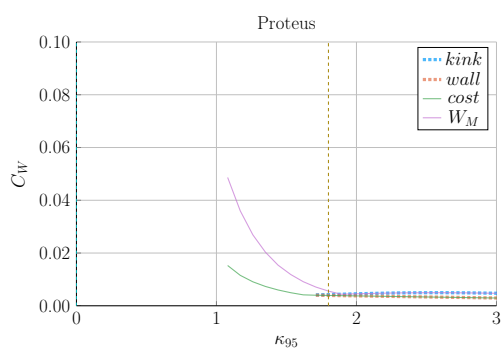


Figure H-27: Cost Sensitivity: ϵ vs. B_0

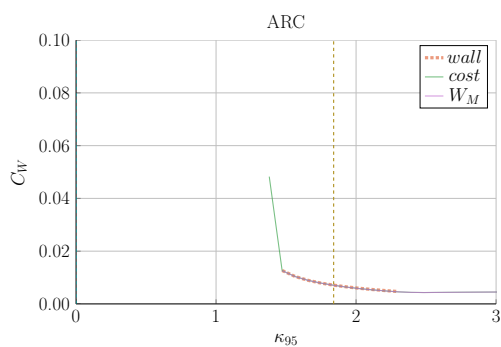
8.2.8 Elongation – κ_{95}



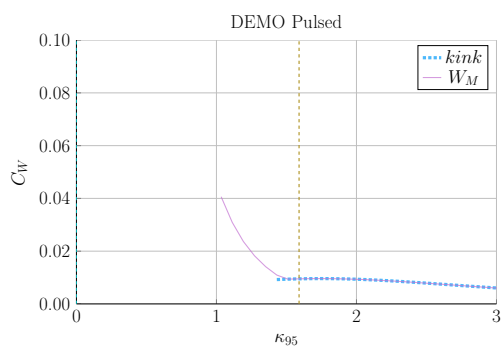
(a) Charybdis



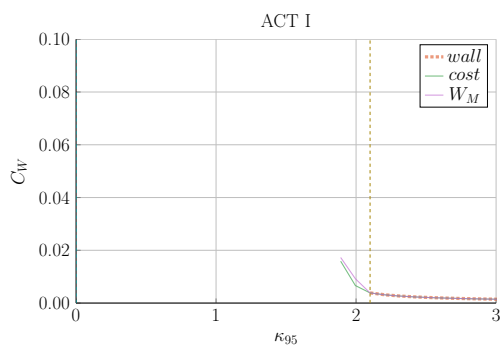
(b) Proteus



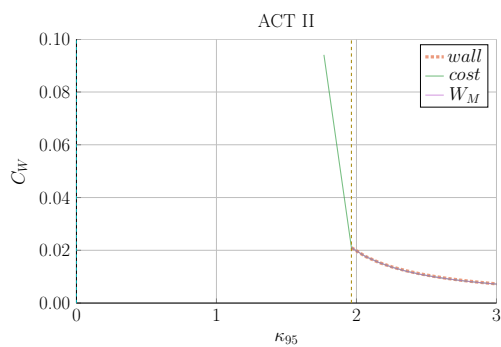
(c) ARC



(d) DEMO Pulsed

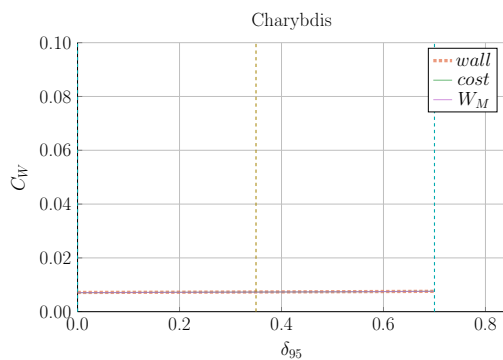


(e) ACT I

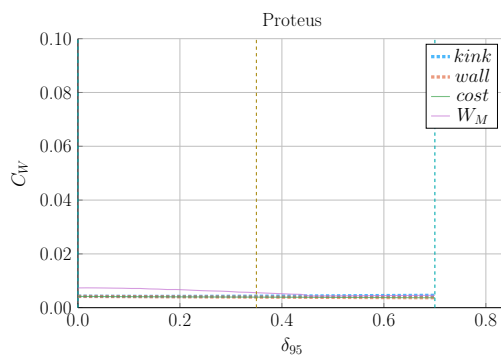


(f) ACT II

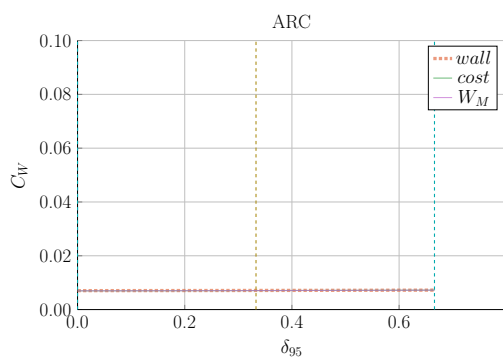
Figure H-28: Cost Sensitivity: κ_{95} vs. B_0



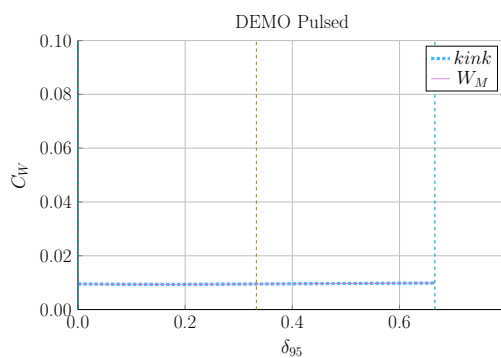
(a) Charybdis



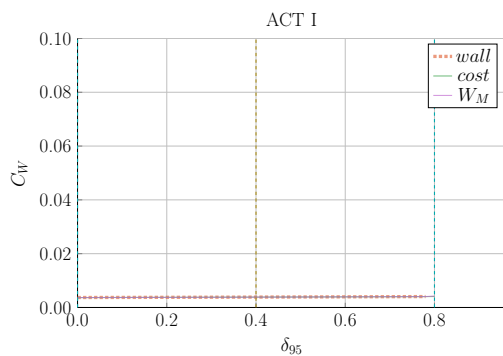
(b) Proteus



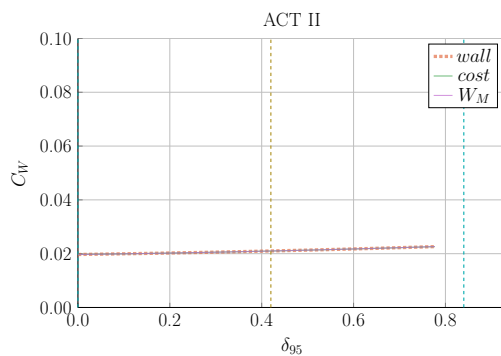
(c) ARC



(d) DEMO Pulsed



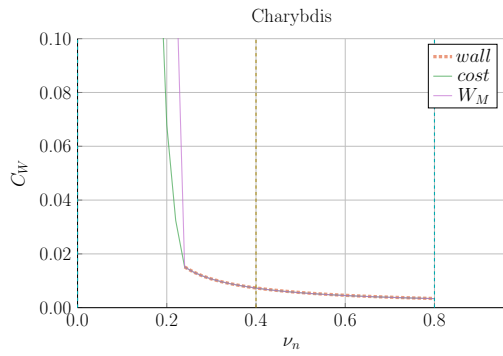
(e) ACT I



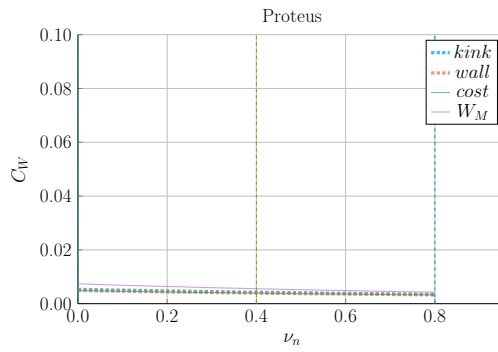
(f) ACT II

Figure H-29: Cost Sensitivity: δ_{95} vs. B_0

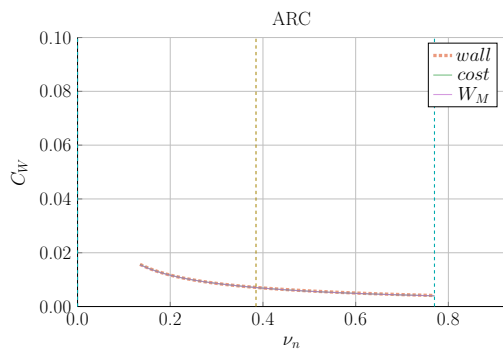
8.2.10 Density Peaking Factor – ν_n



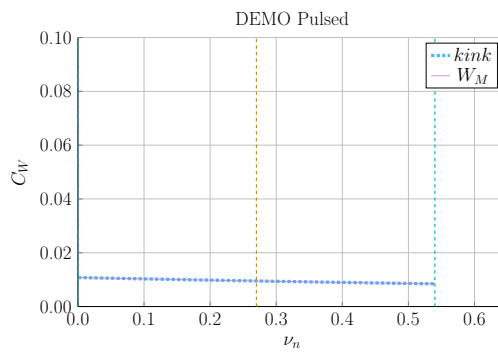
(a) Charybdis



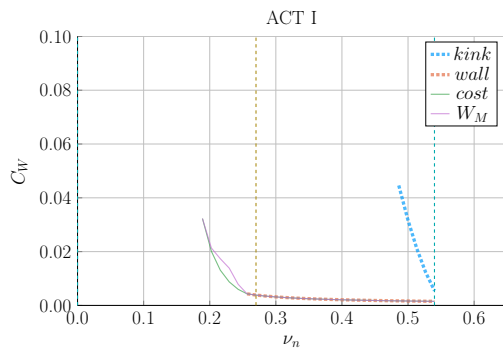
(b) Proteus



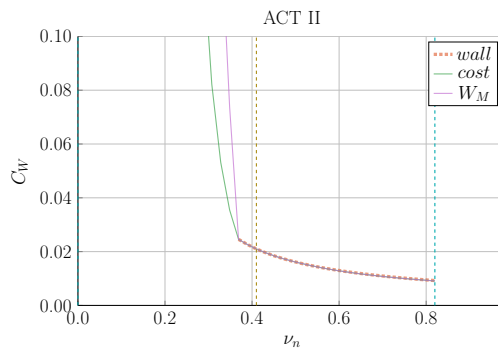
(c) ARC



(d) DEMO Pulsed



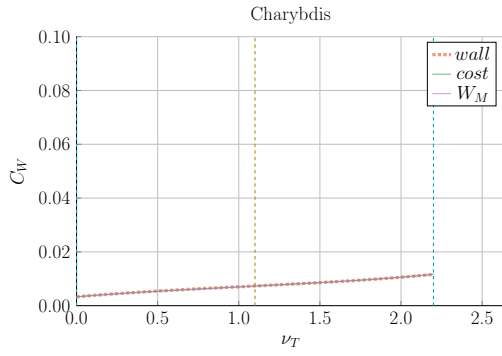
(e) ACT I



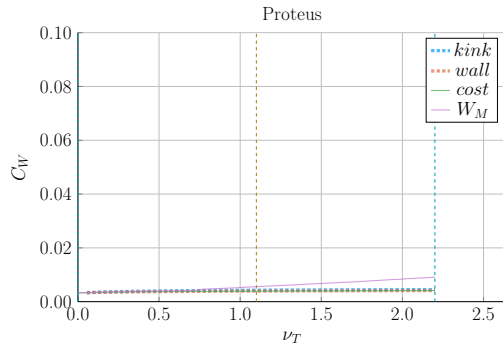
(f) ACT II

Figure H-30: Cost Sensitivity: ν_n vs. B_0

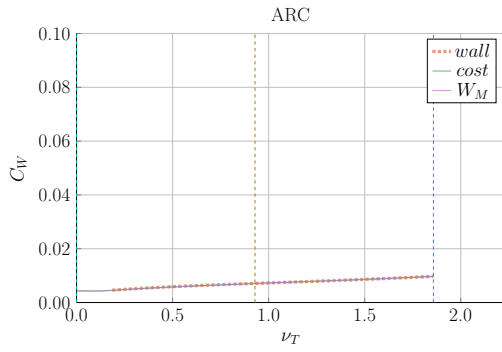
8.2.11 Temperature Peaking Factor – ν_T



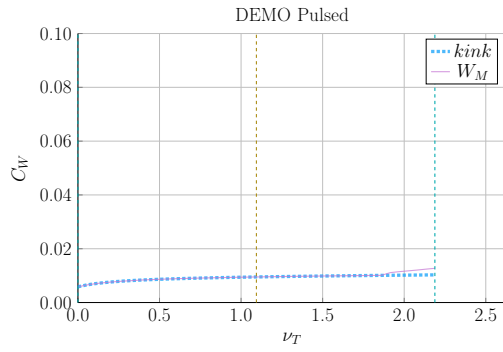
(a) Charybdis



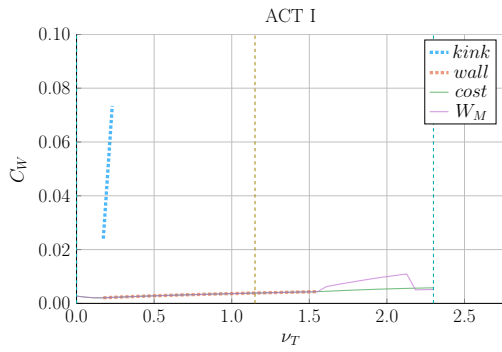
(b) Proteus



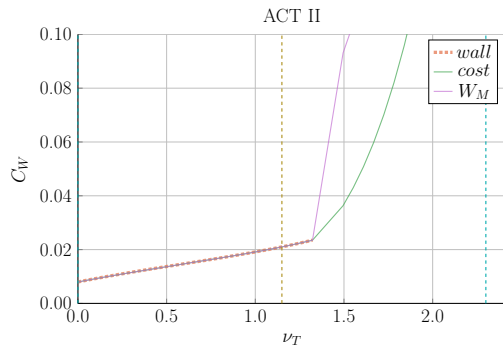
(c) ARC



(d) DEMO Pulsed



(e) ACT I



(f) ACT II

Figure H-31: Cost Sensitivity: ν_T vs. B_0

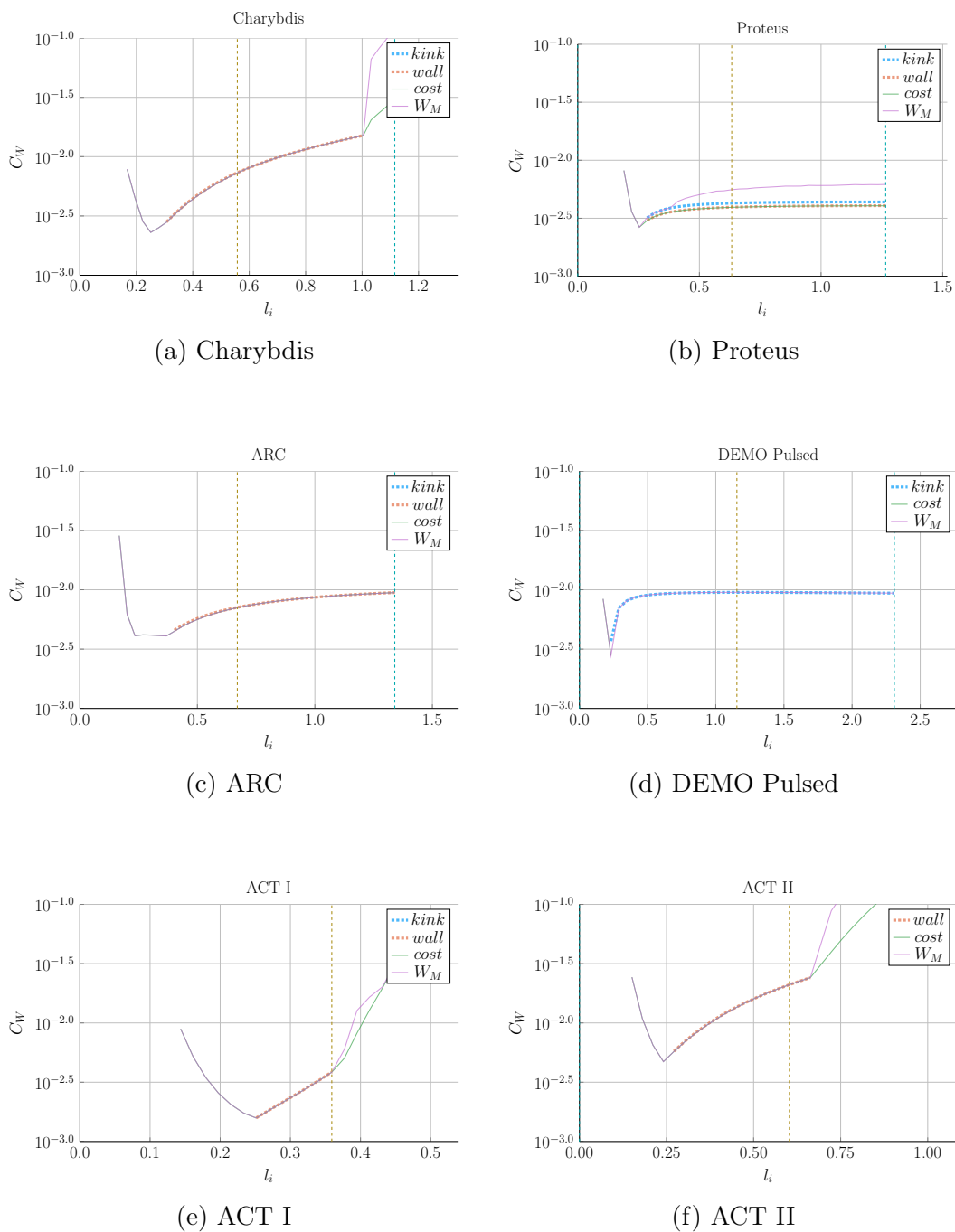
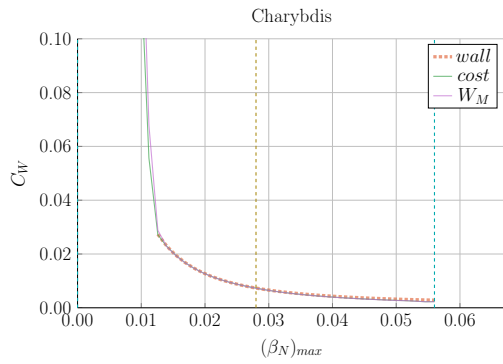
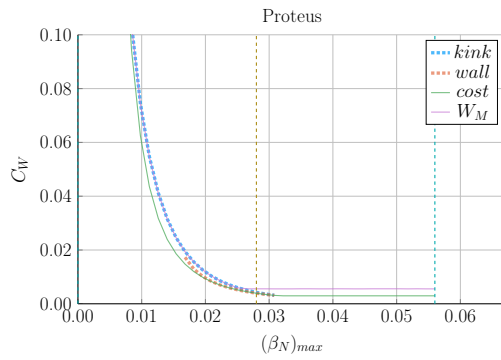


Figure H-32: Cost Sensitivity: l_i vs. B_0

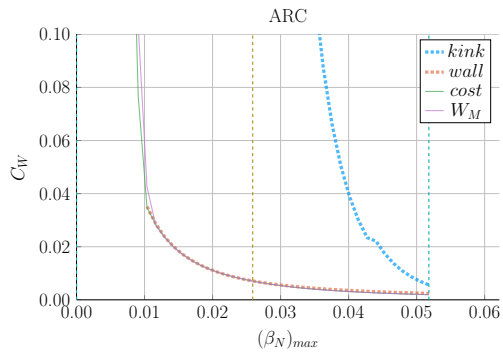
8.2.13 Max Beta Normal – $(\beta_N)_{max}$



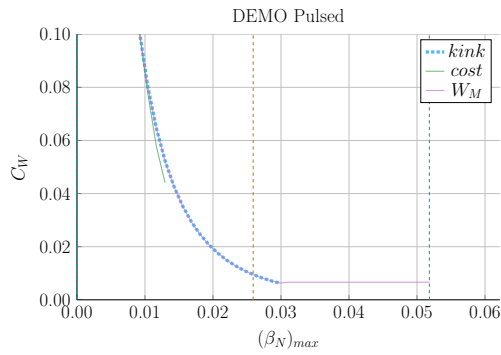
(a) Charybdis



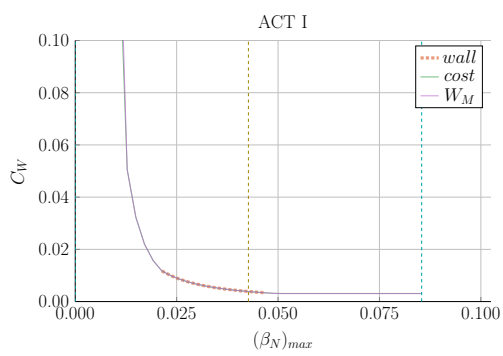
(b) Proteus



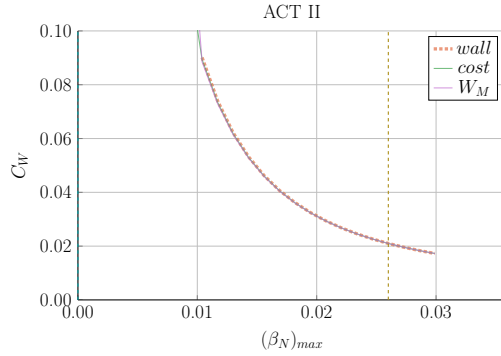
(c) ARC



(d) DEMO Pulsed



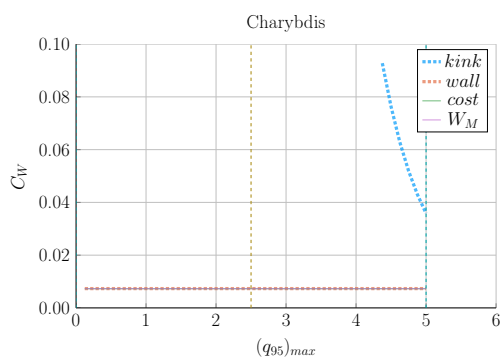
(e) ACT I



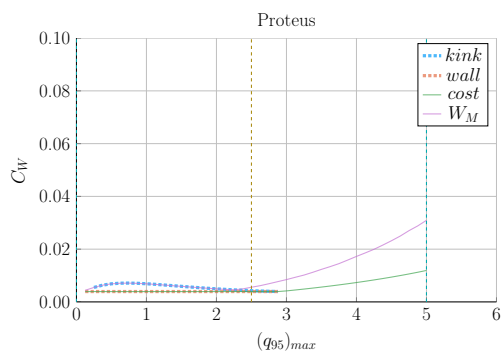
(f) ACT II

Figure H-33: Cost Sensitivity: $(\beta_N)_{max}$ vs. B_0

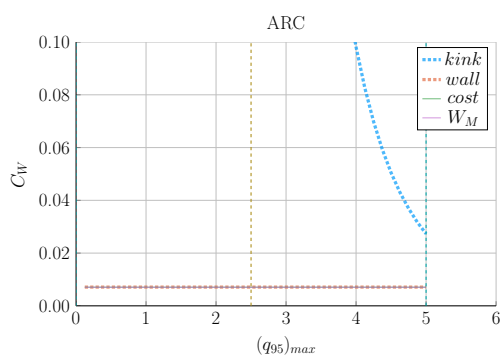
8.2.14 Max Kink Safety Factor – $(q_{95})_{max}$



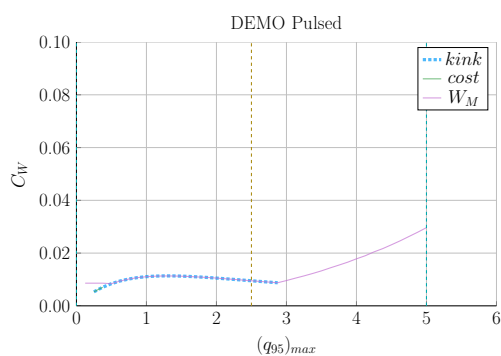
(a) Charybdis



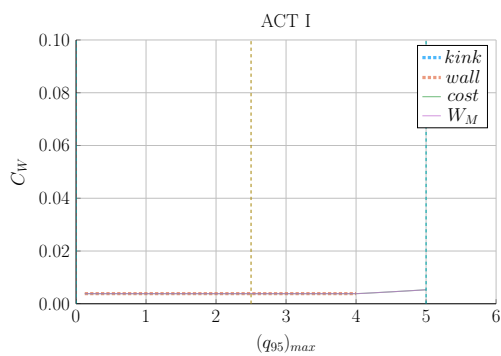
(b) Proteus



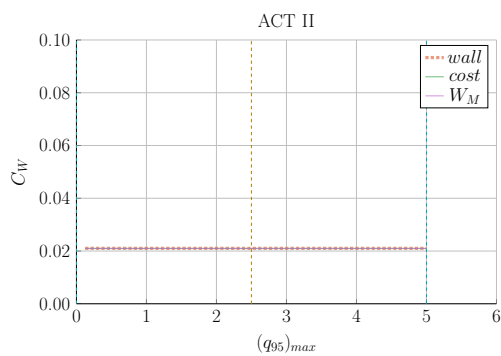
(c) ARC



(d) DEMO Pulsed

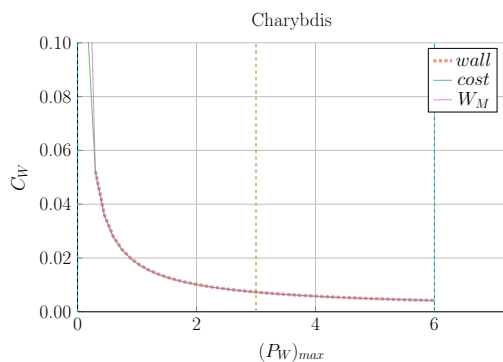


(e) ACT I

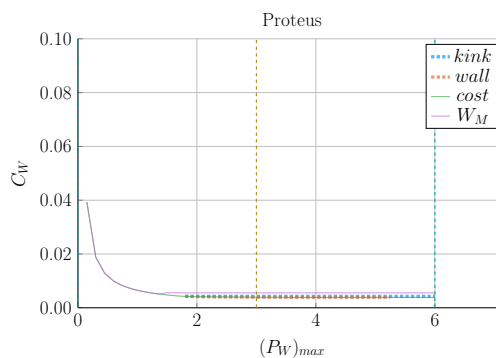


(f) ACT II

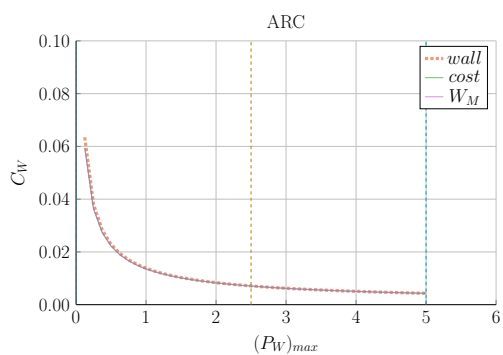
Figure H-34: Cost Sensitivity: $(q_{95})_{max}$ vs. B_0



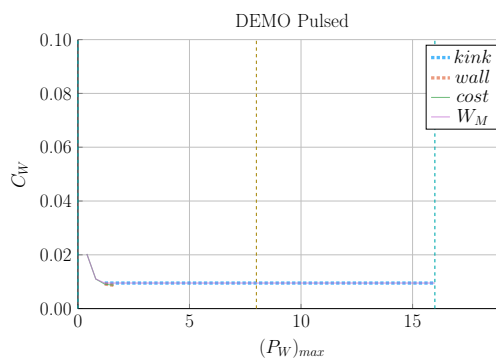
(a) Charybdis



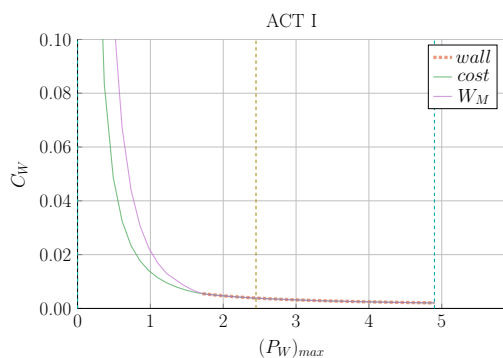
(b) Proteus



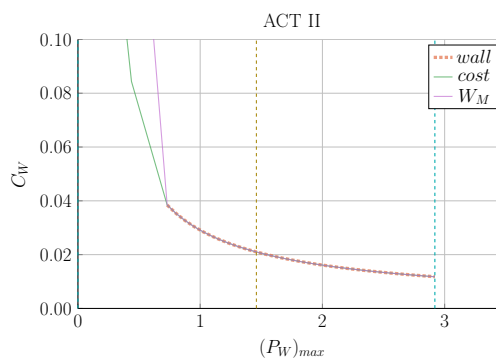
(c) ARC



(d) DEMO Pulsed



(e) ACT I



(f) ACT II

Figure H-35: Cost Sensitivity: $(P_W)_{max}$ vs. B_0

References

- [1] W. Biel, M. Beckers, R. Kemp, R. Wenninger, and H. Zohm, “Systems code studies on the optimization of design parameters for a pulsed DEMO tokamak reactor,” *Fusion Engineering and Design*, vol. 123, pp. 206–211, 2017.
- [2] G. Federici, C. Bachmann, W. Biel, L. Boccaccini, F. Cismondi, S. Ciattaglia, M. Coleman, C. Day, E. Diegele, T. Franke, *et al.*, “Overview of the design approach and prioritization of R&D activities towards an EU DEMO,” *Fusion Engineering and Design*, vol. 109, pp. 1464–1474, 2016.
- [3] C. Kessel, M. Tillack, F. Najmabadi, F. Poli, K. Ghantous, N. Gorelenkov, X. Wang, D. Navaei, H. Toudeshki, C. Koehly, *et al.*, “The ARIES advanced and conservative tokamak power plant study,” *Fusion Science and Technology*, vol. 67, no. 1, pp. 1–21, 2015.
- [4] G. Lee, J. Kim, S. Hwang, C.-S. Chang, H.-Y. Chang, M. Cho, B. Choi, K. Kim, K. Cho, *et al.*, “The KSTAR project: An advanced steady state superconducting tokamak experiment,” *Nuclear Fusion*, vol. 40, no. 3Y, p. 575, 2000.
- [5] J. P. Freidberg, *Plasma physics and fusion energy*. Cambridge university press, 2008.
- [6] B. Sorbom, J. Ball, T. Palmer, F. Mangiarotti, J. Sierchio, P. Bonoli, C. Kasten, D. Sutherland, H. Barnard, C. Haakonsen, *et al.*, “ARC: A compact, high-field, fusion nuclear science facility and demonstration power plant with demountable magnets,” *Fusion Engineering and Design*, vol. 100, pp. 378–405, 2015.
- [7] M. Kovari, R. Kemp, H. Lux, P. Knight, J. Morris, and D. Ward, “"PROCESS": A systems code for fusion power plants—Part 1: Physics,” *Fusion Engineering and Design*, vol. 89, no. 12, pp. 3054–3069, 2014.
- [8] B. Meszaros *et al.*, “DEMO Input File.” [http://ccfe.ac.uk/assets/Documents/Other/DEM01_Reference_Design_-_2015_April_\(EU_2MDKFH_v1_0.txt\)](http://ccfe.ac.uk/assets/Documents/Other/DEM01_Reference_Design_-_2015_April_(EU_2MDKFH_v1_0.txt)).
- [9] H. Fountain, “A Dream of Clean Energy at a Very High Price.” <https://www.nytimes.com/2017/03/27/science/fusion-power-plant-iter-france.html>, 2017. Accessed: 2018-12-6.

- [10] J. Tirone, “World’s Biggest Science Experiment Seeks More Time and Money.” <https://www.bloomberg.com/news/articles/2016-06-15/world-s-biggest-science-experiment-seeks-more-time-and-money>, 2016. Accessed: 2018-12-6.
- [11] D. J. Griffiths, “Introduction to electrodynamics,” 2005.
- [12] T. Hartmann, “Development of a modular systems code to analyse the implications of physics assumptions on the design of a demonstration fusion power plant,” 2013.
- [13] J. Freidberg, F. Mangiarotti, and J. Minervini, “Designing a tokamak fusion reactor—How does plasma physics fit in?,” *Physics of Plasmas*, vol. 22, no. 7, p. 070901, 2015.
- [14] J. Jean, “HELIOS: a zero-dimensional tool for next step and reactor studies,” *Fusion Science and Technology*, vol. 59, no. 2, pp. 308–349, 2011.
- [15] C. Reux, L. Di Gallo, *et al.*, “DEMO reactor design using the new modular system code SYCOMORE,” *Nuclear Fusion*, vol. 55, no. 7, p. 073011, 2015.
- [16] C. Bustreo, G. Casini, G. Zollino, T. Bolzonella, and R. Piovan, “FRESCO, a simplified code for cost analysis of fusion power plants,” *Fusion Engineering and Design*, vol. 88, no. 12, pp. 3141–3151, 2013.
- [17] Z. Dragojlovic, A. R. Raffray, F. Najmabadi, C. Kessel, L. Waganer, *et al.*, “An advanced computational algorithm for systems analysis of tokamak power plants,” *Fusion Engineering and Design*, vol. 85, no. 2, pp. 243–265, 2010.
- [18] E. Fable, C. Angioni, M. Siccino, and H. Zohm, “Plasma physics for fusion reactor system codes: Framework and model code,” *Fusion Engineering and Design*, vol. 130, pp. 131–136, 2018.
- [19] P. Knight, “A user’s guide to the PROCESS systems code,” *UKAEA Fusion*, vol. 2, no. 0, 1996.
- [20] C. Angioni, H. Weisen, O. Kardaun, M. Maslov, A. Zabolotsky, C. Fuchs, *et al.*, “Scaling of density peaking in H-mode plasmas based on a combined database of AUG and JET observations,” *Nuclear Fusion*, vol. 47, no. 9, p. 1326, 2007.
- [21] T. Onjun, G. Bateman, A. Kritz, and G. Hammett, “Models for the pedestal temperature at the edge of H-mode tokamak plasmas,” *Physics of Plasmas*, vol. 9, no. 12, pp. 5018–5030, 2002.
- [22] A. E. Hubbard, “Physics and scaling of the H-mode pedestal,” *Plasma Physics and Controlled Fusion*, vol. 42, no. 5A, p. A15, 2000.
- [23] M. Greenwald, “Density limits in toroidal plasmas,” *Plasma Physics and Controlled Fusion*, vol. 44, no. 8, p. R27, 2002.

- [24] C. Roach, M. Walters, R. Budny, F. Imbeaux, T. Fredian, M. Greenwald, *et al.*, “The 2008 public release of the international multi-tokamak confinement profile database,” *Nuclear Fusion*, vol. 48, no. 12, p. 125001, 2008.
- [25] J. D. Lawson, “Some criteria for a power producing thermonuclear reactor,” *Proceedings of the Physical Society. Section B*, vol. 70, no. 1, p. 6, 1957.
- [26] J. Jacquinet, S. Putvinski, G. Bosia, A. Fukuyama, R. Hemsworth, S. Konovalov, W. Nevins, F. Perkins, K. Rasumova, F. Romanelli, *et al.*, “Plasma auxiliary heating and current drive,” *Nuclear Fusion*, vol. 39, no. 12, pp. 2495–2539, 1999.
- [27] D. Ehst and C. Karney, “Approximate formula for radiofrequency current drive efficiency with magnetic trapping,” *Nuclear fusion*, vol. 31, no. 10, p. 1933, 1991.
- [28] I. H. Hutchinson, “Principles of plasma diagnostics,” *Plasma Physics and Controlled Fusion*, vol. 44, no. 12, p. 2603, 2002.
- [29] J. Cordey, K. Thomsen, A. Chudnovskiy, O. Kardaun, T. Takizuka, J. Snipes, M. Greenwald, L. Sugiyama, F. Ryter, A. Kus, *et al.*, “Scaling of the energy confinement time with β and collisionality approaching ITER conditions,” *Nuclear fusion*, vol. 45, no. 9, p. 1078, 2005.
- [30] N. Uckan, “ITER physics design guidelines at high aspect ratio,” tech. rep., Oak Ridge National Lab., 1991.
- [31] B. LaBombard, E. Marmar, J. Irby, J. Terry, R. Vieira, G. Wallace, D. Whyte, S. Wolfe, *et al.*, “ADX: a high field, high power density, advanced divertor and RF tokamak,” *Nuclear Fusion*, vol. 55, no. 5, p. 053020, 2015.
- [32] O. Mitarai, S. W. Wolfe, A. Hirose, and H. M. Skarsgard, “Alternating current tokamak reactor with long pulses,” *Fusion technology*, vol. 15, no. 2P1, pp. 204–213, 1989.
- [33] S. Hirshman and G. Neilson, “External inductance of an axisymmetric plasma,” *The Physics of fluids*, vol. 29, no. 3, pp. 790–793, 1986.
- [34] P. Libeyre, N. Mitchell, D. Bessette, Y. Gribov, C. Jong, and C. Lyraud, “Detailed design of the ITER central solenoid,” *Fusion Engineering and Design*, vol. 84, no. 7-11, pp. 1188–1191, 2009.
- [35] J. P. Freidberg, A. Cerfon, and J. Lee, “Tokamak elongation—how much is too much? Part 1. Theory,” *Journal of Plasma Physics*, vol. 81, no. 6, 2015.
- [36] L. Giancarli, V. Chuyanov, M. Abdou, M. Akiba, B. Hong, *et al.*, “Breeding blanket modules testing in ITER: an international program on the way to DEMO,” *Fusion Engineering and Design*, vol. 81, no. 1-7, pp. 393–405, 2006.
- [37] E. Doyle, W. Houlberg, Y. Kamada, V. Mukhovatov, T. Osborne, A. Polevoi, G. Bateman, J. Connor, J. Cordey, T. Fujita, *et al.*, “Plasma confinement and transport,” *Nuclear Fusion*, vol. 47, no. 6, p. S18, 2007.

- [38] H. Lux, R. Kemp, E. Fable, and R. Wenninger, “Radiation and confinement in 0D fusion systems codes,” *Plasma Physics and Controlled Fusion*, vol. 58, no. 7, p. 075001, 2016.
- [39] G. Giruzzi, J. Artaud, M. Baruzzo, T. Bolzonella, E. Fable, L. Garzotti, I. Ivanova-Stanik, R. Kemp, D. King, M. Schneider, *et al.*, “Modelling of pulsed and steady-state DEMO scenarios,” *Nuclear Fusion*, vol. 55, no. 7, p. 073002, 2015.
- [40] R. Maingi, A. Lumsdaine, S. Barish, A. White, L. Chacon, S. Gourlay, *et al.*, “Fusion Energy Sciences Advisory Committee Report: Transformative Enabling Capabilities for Efficient Advance Toward Fusion Energy,” tech. rep., 2018.
- [41] M. Mauel, M. Shochet, C. A. Back, R. Betti, I. Chapman, C. Forest, T. K. Fowler, J. Freidberg, R. Gilgenbach, W. Heidbrink, M. Herrmann, F. Jenko, *et al.*, *Final Report of the Committee on a Strategic Plan for U.S. Burning Plasma Research*. Washington, DC: The National Academies Press, 2018.
- [42] J. Menard, S. Gerhardt, M. Bell, J. Bialek, A. Brooks, J. Canik, J. Chrzanowski, M. Denault, L. Dudek, D. Gates, *et al.*, “Overview of the physics and engineering design of NSTX upgrade,” *Nuclear Fusion*, vol. 52, no. 8, p. 083015, 2012.
- [43] U. Stroth, M. Murakami, R. Dory, H. Yamada, S. Okamura, F. Sano, and T. Obiki, “Energy confinement scaling from the international stellarator database,” *Nuclear Fusion*, vol. 36, no. 8, p. 1063, 1996.
- [44] L. Giannone, J. Baldzuhn, R. Burhenn, P. Grigull, U. Stroth, F. Wagner, R. Brakel, C. Fuchs, H. Hartfuss, K. McCormick, *et al.*, “Physics of the density limit in the W7-AS stellarator,” *Plasma physics and controlled fusion*, vol. 42, no. 6, p. 603, 2000.
- [45] D. Whyte, A. Hubbard, J. Hughes, B. Lipschultz, J. Rice, E. Marmor, M. Greenwald, I. Cziegler, A. Dominguez, T. Golfinopoulos, *et al.*, “I-mode: an H-mode energy confinement regime with L-mode particle transport in Alcator C-Mod,” *Nuclear Fusion*, vol. 50, no. 10, p. 105005, 2010.
- [46] H. Bosch and G. Hale, “Improved formulas for fusion cross-sections and thermal reactivities,” *Nuclear fusion*, vol. 32, no. 4, p. 611, 1992.
- [47] Z. Hartwig and Y. Podpaly, “The magnetic fusion energy formulary,” 2012.
- [48] J. D. Huba, “NRL plasma formulary,” tech. rep., Naval Research Lab Washington DC Plasma Physics Div, 2006.
- [49] J. Wesson and D. J. Campbell, *Tokamaks*, vol. 149. Oxford University Press, 2011.
- [50] C. Kessel, “Bootstrap current in a tokamak,” *Nuclear Fusion*, vol. 34, no. 9, p. 1221, 1994.